

FAU Studies Mathematics & Physics 1

Daniel Niesner

Two-Photon Photoemission Studies of Graphene and Topological Insulators

FAU
UNIVERSITY
P R E S S

Two-photon photoemission studies of graphene and topological insulators

Zweiphotonen-Photoemission an Graphen
und topologischen Isolatoren

Der Naturwissenschaftlichen Fakultät
der Friedrich-Alexander-Universität Erlangen-Nürnberg
zur Erlangung des Doktorgrades Dr. rer. nat.

vorgelegt von
Daniel Niesner
aus Nürnberg

Als Dissertation genehmigt von
der Naturwissenschaftlichen Fakultät
der Friedrich-Alexander-Universität Erlangen-Nürnberg

Tag der mündlichen Prüfung:	16. Mai 2013
Vorsitzender der Prüfungskommission:	Prof. Dr. Johannes Barth
Erstberichterstatter:	Prof. Dr. Thomas Fauster
Zweitberichterstatter:	Prof. Dr. Ulrich Höfer

FAU Studies Mathematics & Physics

Band 1

Herausgeber der Reihe:

Prof. Dr. Karl-Hermann Neeb und Prof. Dr. Klaus Mecke

Daniel Niesner

**Two-photon photoemission
studies of graphene and
topological insulators**

**Erlangen
FAU University Press
2013**

Bibliografische Information der Deutschen Nationalbibliothek
Die Deutsche Nationalbibliothek verzeichnet diese Publikation in der Deutschen Nationalbibliografie; detaillierte bibliografische Daten sind im Internet über <http://dnb.ddb.de> abrufbar.

Der vollständige Inhalt des Buchs ist als PDF über den OPUS Server der Friedrich-Alexander-Universität Erlangen-Nürnberg abrufbar.
Kopien und Ausdrücke dürfen nur zum privaten und sonstigen eigenen Gebrauch angefertigt werden.

Verlag und Auslieferung:
FAU University Press, Universitätsstraße 4, 91054 Erlangen

Textsatz durch den Autor mit \LaTeX
Druck: docupoint GmbH

ISBN: 978-3-944057-07-1
ISSN: 2196-7482

Contents

1. Motivation	1
2. Physical properties of graphene	5
2.1. Atomic and electronic structure of free-standing graphene	5
2.2. Fabrication and interaction with the substrate	7
3. Physical properties of topological insulators	13
3.1. Theoretical concept	13
3.2. Experimental verification	16
4. Photoelectron spectroscopy	23
4.1. General description	23
4.2. Circular dichroism	25
4.3. Two-photon photoemission	27
4.4. Image-potential states	30
4.5. Experimental setup	31
5. Graphene on noble-metal and on silicon-carbide substrates	35
5.1. Experimental details	36
5.1.1. Sample preparation	36
5.1.2. Sample characterization by low-energy electron diffraction	38
5.1.3. Details of photoemission experiments	40
5.2. Surface states of graphene on iridium	41
5.2.1. Surface band structure of graphene/Ir(111)	41
5.2.2. Dynamics of image-potential states of graphene/Ir(111)	45
5.2.3. π -band structure of graphene/Ir(100)	47
5.2.4. Image-potential states of graphene/Ir(100)	49
5.3. Graphene on various substrates	50
5.3.1. Changes in work function and doping of graphene by the substrate	52
5.3.2. Screening of the metal substrate from the external charge of the image-potential state	54
5.4. Discussion	58
6. Unoccupied surface states of topological insulators	59
6.1. Experimental details	59
6.1.1. Sample preparation	59
6.1.2. Details of photoemission experiments	62

6.1.3.	Sample characterization by angle-resolved photoemission	62
6.1.4.	Sample degradation after cleaving	62
6.1.5.	n-type doping of Bismuth Chalcogenides	64
6.2.	Higher-lying topological surface states of bismuth chalcogenides	65
6.2.1.	Identification by spectroscopic methods	65
6.2.2.	Dynamics of the unoccupied surface states of $\text{Bi}_2\text{Te}_2\text{Se}$	70
6.3.	Electron dynamics of SnSb_2Te_4 , an intrinsic p-type topological insulator	73
6.4.	Discussion	77
7.	Summary	79
A.	Appendix	83
A.1.	Graphene	83
A.1.1.	Characterization of graphene on iridium by Raman spectroscopy	83
A.1.2.	Energy distribution curves of graphene on Ir(111) and graphene on SiC(0001)	87
A.2.	Topological insulators	89
A.2.1.	Survey spectra of the unoccupied part of the band structure of bismuth chalcogenides	89
A.2.2.	Circular dichroism patterns of bismuth chalcogenides	90
A.2.3.	Time-resolved bichromatic 2PPE on $\text{Bi}_2\text{Te}_2\text{Se}$	91
A.3.	Fit Functions	93
A.3.1.	Optical Bloch equations	93
A.3.2.	Rate equations	93
A.4.	Correlation between photoemission matrix elements of linearly and circularly polarized light	94
	List of figures	95
	Bibliography	99

1. Motivation

After Konrad Zuse's creation of the first digital computer, the "Z3", in 1941, a technological revolution set in that is still continuing and without which today's society would be unimaginable (Rojas 1997). In his early device Zuse used relays for circuit switching, which were soon replaced by semiconductor devices, i. e. transistors (Shockley 1952; Shockley 1956). Nowadays those are processed in vast arrays together with other components on integrated circuits. Their miniaturization forms the basis of increasing computing capacities at decreasing costs of production as described by Moore's rule which was formulated in 1965: "The complexity for minimum component costs has increased at a rate of roughly a factor of two per year [...] this rate can be expected to continue, if not to increase (Moore 1998)." In the course of these advances, the material-specific limitations of the most common semiconductor, silicon, will be reached within the next decades (International Technology Roadmap for Semiconductors 2011). One limiting factor are parasitic resistances in contacts and wirings, which will exceed the gate resistance at the 20 nm technology node at the end of the current silicon technology road map (Thompson 2006; Meindl 2001).

In search for alternative materials for gates and interconnects graphene plays a major role (Iwai 2009). Although the electronic properties of this hexagonally close-packed, single carbon layer had already been calculated in 1947 (Wallace 1947), its isolation and characterization was first successfully carried out in 2004 (Novoselov 2004; Geim 2010). Apart from its quasi two-dimensional structure, one of the most intriguing properties of graphene is a high carrier mobility of more than $15000 \text{ cm}^2/\text{Vs}$ (Wu 2009; Li 2010). It is a result of the two carbon atoms within a unit cell, each contributing one electron to the conduction band and the valence band, respectively: The two atoms are equivalent under inversion symmetry, and this symmetry leads to an additional conserved quantity, the pseudospin, which links electronic states to one of the two sublattices. The resulting linearly-dispersive bands of opposite pseudospin cross at a Dirac point as sketched in Figure 1.1 (a). This spectrum is similar to the one of relativistic massless particles (conduction electrons) and antiparticles (holes) and gives rise to phenomena like the half-integer quantum Hall effect (Sharapov 2004; Gusynin 2005; Zhang 2005; Novoselov 2005b) and Klein tunneling (Katsnelson 2006; Stander 2009): An electron can penetrate arbitrarily deep into a seemingly repulsive barrier by coupling to hole states in the forbidden region. Backscattering is suppressed and the high carrier mobility arises.

Low-energy excitations and carrier transport in graphene are well studied, and large-scale growth on silicon carbide (Emtsev 2009) and metal substrates (e. g. nickel (Reina 2009) and copper (Han 2011)) pave the way for applied research: Transferring graphene onto 15 mm silicon wafers allows parallel processing of 100 GHz transistors (Lin 2010) and "barristors" (Yang 2012), triode-like switches with a today's on-off-ratio of 10^5 . Despite all those achievements, basic research questions still remain open: What higher-energy

excitations are possible in graphene and what are the dynamics of those excitations? To what degree does contact to neighboring material and metal wirings influence the electronic properties, and to what extent does charge transfer set in? Chapter 5 deals with these topics by comparing the work function of graphene in contact with different metal substrates. Two-photon photoemission is employed in order to study the ability of graphene to screen an external charge, which is formed by an electron in an image-potential state in front of the surface. The image-potential states of free-standing graphene were predicted to exhibit an energetic splitting as a result of the mirror symmetry with respect to the graphene sheet (Silkin 2009). Is a remanescence of this splitting observable in the presence of a metallic or semiconducting substrate? In order to shed some light on those issues, the energetics and dynamics of surface states of a well-characterized system, graphene on iridium(111), are studied in Section 5.2.1 and 5.2.2. In contrast, graphene on square substrates has not been the subject of extended scientific effort. This system will be characterized by photoemission experiments in Sections 5.2.3 and 5.2.4. Subsequently, in Section 5.3 the results are extended to different metal substrates as well as epitaxially grown graphene on silicon carbide.

An alternate route towards dissipationless transport is making use of the spin degree of freedom of the electron (Murakami 2003; Rashba 2003). In topological insulators (Kane 2005) and Rashba-systems (Rashba 1965) spin-orbit interaction lifts the spin degeneracy of electronic states and electronic bands with spin-momentum locking arise. In the vicinity of certain high-symmetry points in the Brillouin zone, the Kramers points, where spin degeneracy is conserved, the emerging spectrum is formally similar to the one of graphene as illustrated in Figure 1.1 (b). However, in these systems an orientation of the real spin is the origin and not a pseudospin like in graphene (Hasan 2010). As scattering events which are able to flip the spin orientation and hence the orientation of the momentum of the electron are rare, backscattering is suppressed also in topological insulators (Roushan 2009). Moreover, spin-momentum locking allows manipulation of the spin of the electron by electric fields, as illustrated e. g. in Figure 1.1 (c). Theoretical concepts of a quantum computer based on a combination of topological insulators and superconductors have been proposed (Fu 2008; Collins 2006).

The discrimination between a Rashba-system and a topological insulator is a result of the underlying bulk band structure. From the knowledge of the symmetry of the bulk states a systems can be predicted to be a topological insulator or not. The spin-split branches of a Rashba-split surface state are slightly shifted respect to each other in momentum space. Like in the absence of Rashba-splitting, they may have any electronic filling level from empty to full. The topological surface state is caused by a symmetry break at the surface of a bulk insulator and necessarily metallic. The bulk band needs to have a symmetry-inversion, as it was first predicted (Volkov 1985; Pankratov 1987; Bernevig 2006) and found (König 2007) in the case of HgTe and $\text{Hg}_{1-x}\text{Cd}_x\text{Te}$ quantum well structures: With increasing cadmium concentration x the conduction band with Γ_8 -symmetry shifts towards lower energy until it finally drops below the Fermi level and turns into the valence band. At the interface between two layers of different concentration a topological interface state forms connecting bands of the same symmetry across the band gap.

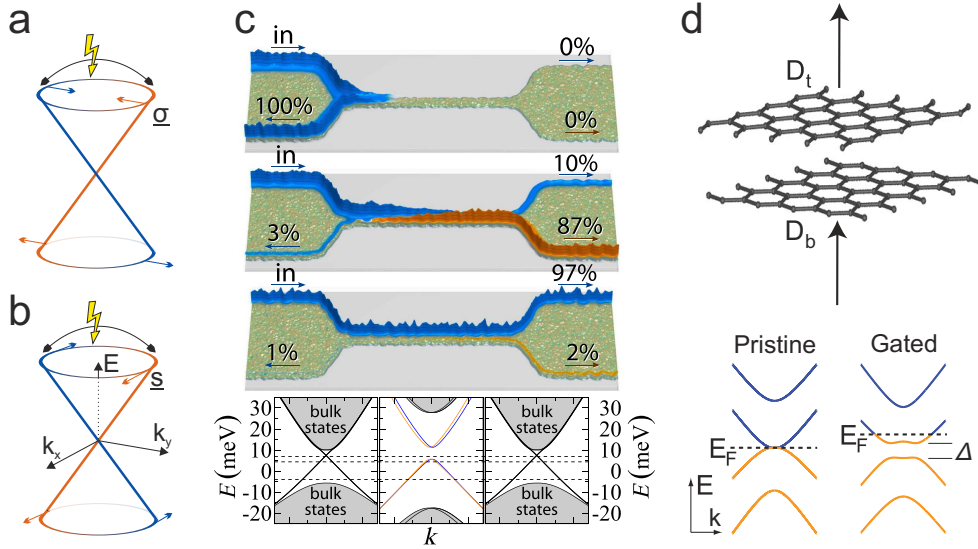


Figure 1.1: Schematic band structure of (a) graphene and (b) a topological insulator in the proximity of the Fermi level. Backscattering is suppressed by the conservation of quasispin σ and spin s . Forming a barrier is thus not easily achieved by gating, but requires e. g. confinement (c) (Krueckl 2011) or, in the case of graphene, asymmetric charging of a double-layer (d) (Zhang 2009b). In the topological state, control over the spin is achieved (c) which is depicted by the blue (spin up) and orange (spin down) color in (a - c).

The present work focuses on three-dimensional topological insulators with a topological surface state at the interface to the vacuum (Fu 2007a; Fu 2007b). Shortly after the experimental verification of the presence of these states on $\text{Bi}_{1-x}\text{Sb}_x$ (Hsieh 2008), bismuth chalcogenides (Bi_2Te_3 (Chen 2009b), Bi_2Se_3 (Hsieh 2009a)) were found to have a model-like band structure and band gaps of several hundreds of meV. This finding triggered the breakthrough of the field. Those materials are intrinsically electron doped, and often the level of doping is high enough to shift the Fermi level into the conduction band (Bianchi 2010). Measurements on electron and spin dynamics become very challenging, and in applications spin currents at the surface would be masked by the bulk conductivity. For technical applications, contributions of the bulk may be suppressed by the use of thin layers and application of a bias voltage. In addition, doping by foreign atoms like magnesium is possible and allows also for pump-and-probe experiments (Sobota 2012). Chapter 6 presents two alternative routes making spectroscopic measurements possible: On the one hand, Section 6.2 deals with higher-excited topological states in the unoccupied part of the band structure of $\text{Bi}_2\text{Te}_n\text{Se}_{3-n}$ ($n=0,2,3$). Their energetics are investigated using monochromatic two-photon photoemission, and circular dichroism effects together with comparison to calculations give insight into the spin structure. Those states can serve as model systems for the dynamics of excitations in this new class of materials. As their optical excitation is possible, they might be utilized as a source of spin-polarized electrons for spin injection into semiconductors. On the other hand, in Section 6.3 the electronic dispersion and electron dynamics of an intrinsically hole-doped topological insulator, SnSb_2Te_4 , is discussed.

2. Physical properties of graphene

Graphene, a two-dimensional, isolated single layer of graphite, was first characterized in 2004 by Andre Geim and Konstantin Novoselov (Novoselov 2004), who were awarded the Nobel prize in 2010 for this research (Geim 2010). Possible applications of the material include logical electronics (Lin 2010; Waldmann 2011; Hertel 2012; Yang 2012) and transparent electrodes (Wang 2008; Kim 2009; Bae 2010; Wu 2010). The suitability of graphene for such devices is closely related to its electronic structure, which will be the subject of Section 2.1. Section 2.2 will give attention to practical issues like production methods and effects arising from the interaction with the supporting substrate.

2.1. Atomic and electronic structure of free-standing graphene

The unit cell of graphene is spanned by two lattice vectors with a length of $a = 2.46 \text{ \AA}$ and an angle of 60° between them (Wallace 1947). It includes two atoms, located at $(0, 0)$ and $(1/3, 1/3)$. The resulting honeycomb or chicken wire structure of C_{6v} symmetry is illustrated in Figure 2.1 (a), where the sixfold rotational axis is indicated as well as dashed lines representing the mirror axes m_1 and m_2 .

For completeness, the phonon dispersion of graphene is shown in Figure 2.1 (b) (Dresselhaus 2010). Characteristic for the two-dimensional structure is a significant softening of the out-of-plane modes (σ TO and σ TA) compared to in-plane vibrations. The equivalence of the two atoms in the unit cell results in degeneracies at the \bar{K} and \bar{M} high symmetry points. Characteristic of free-standing graphene is the softening of the highest optical branch by Kohn anomalies at the $\bar{\Gamma}$ and \bar{K} points (Piscanec 2004), which arises from efficient screening of the atomic cores by the π electron system at these k values (nesting) (Kohn 1959). The Kohn anomalies are lifted when graphene is strongly bound to a substrate, like e. g. for graphene/Ni(111) (Allard 2010; Aizawa 1990; Shikin 1999).

The electronic structure in the vicinity of the Fermi level is well-described by a nearest-neighbor tight-binding approximation including a single p_z basis function (Wallace 1947; Saito 1998; Reich 2002):

$$E^\pm(\mathbf{k}) = \frac{\epsilon_{2p} \mp \gamma_0 \sqrt{3 + 2 \cos(2\pi a k_1) + 2 \cos(2\pi a k_2) + 2 \cos(2\pi a (k_1 - k_2))}}{1 \mp s_0 \sqrt{3 + 2 \cos(2\pi a k_1) + 2 \cos(2\pi a k_2) + 2 \cos(2\pi a (k_1 - k_2))}} \quad (2.1)$$

The resulting band structure for a transfer matrix element $\gamma_0 = 2.79 \text{ eV}$ and vanishing overlap matrix element s_0 is displayed in Figure 2.1 (c), where ϵ_{2p} is set to zero. The

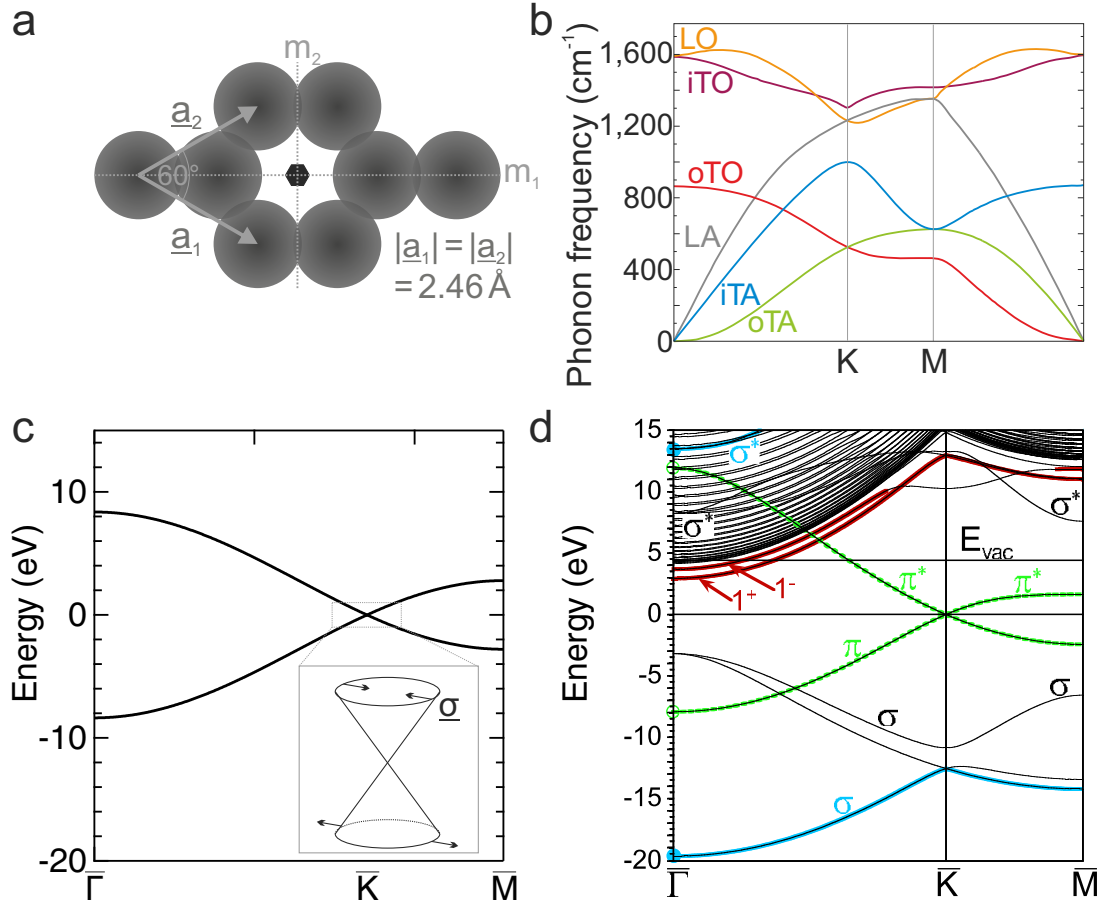


Figure 2.1.: Atomic (a), vibronic (b) (Dresselhaus 2010) and electronic structure of graphene within a tight-binding scheme (Wallace 1947) (c) and a density functional theory calculation (d) (Silkin 2009). The inset in (c) illustrates the helical structure of the Dirac cone. In contrast, the full band structure is given in (d).

three remaining valence electrons of carbon do not contribute to the Fermi surface, but can be modeled by sp^2 hybrid orbitals which are assumed to form deep lying σ bands, as confirmed by the full density functional theory calculation shown in Figure 2.1 (d).

Considerable interest has been attracted by the conical dispersion in the energy region ± 1 eV around the Fermi level at the \bar{K} high symmetry point and its mirror image, the \bar{K}' point. The resulting "Dirac cone" is sketched in the inset of Figure 2.1 (c). Since the dispersion is formally similar to the solution of the Dirac equation for massless Fermions of spin 1/2 (Dirac 1928), it can be described by the corresponding formalism after introducing a pseudospin $\underline{\sigma}$ (Novoselov 2006; McCann 2006). The bands evolve a chiral spin structure, with $\underline{\sigma} \cdot (\underline{k} - \underline{k}_{\bar{K}}) / |\underline{\sigma}| \cdot |\underline{k} - \underline{k}_{\bar{K}}| \in \{1, -1\}$. Note, however, that chirality is a result of the symmetry between the two equivalent carbon atoms within the unit cell, and hence relates the bands to one of the two sublattices but not to the spin. The bands remain spin-degenerate. Nevertheless, $\underline{\sigma}$ forms an additional conserved quantity which is rarely flipped during scattering events, resulting in chiral tunneling (Katsnelson 2006; Stander 2009), the

suppression of backscattering and ultimately ballistic charge transport (Novoselov 2004). This makes graphene a relevant material for future logical devices (Lin 2010; Waldmann 2011; Hertel 2012; Yang 2012). Besides a high carrier mobility (Wu 2009; Li 2010), the linear dispersion gives rise to an universal optical conductance, resulting in a constant light transmittivity $T = (1 + 0.5\pi\alpha)^{-2} = 97.7\%$, where $\alpha = 1/137$ is the fine structure constant, for low-frequencies and up to the complete visible range (Ando 2002; Gusynin 2006; Falkovsky 2007; Kuzmenko 2008). Together with its mechanical flexibility, this makes graphene an attractive material also for a variety of photonic applications (Bonaccorso 2010), and especially for transparent electrodes (Wang 2008; Kim 2009; Bae 2010; Wu 2010).

Two-photon photoemission experiments focus on unoccupied electronic states between the Fermi level and the vacuum level in the proximity of the $\bar{\Gamma}$ point. Two bands of free-standing graphene within this energy window are marked in red in Figure 2.1 (d), labeled 1^+ and 1^- . They originate from the first image-potential state, which exhibits a symmetry-related splitting: The graphene sheet itself forms a horizontal mirror plane, which results in a double-series of image-potential states of even and odd symmetry (Silkin 2009). However, this symmetry is necessarily broken when graphene is bound to a substrate, leaving only the state of odd symmetry (Lehmann 1999; Niesner 2012a). On the other hand, optical pumping of those unoccupied surface states becomes possible only in the presence of a substrate, since the applied photon energies of about 4.6 eV are not suitable to perform \vec{k} -conserving optical excitations from occupied initial states of graphene at $\bar{\Gamma}$. The latter would require photon energies of more than 6 eV, which would exceed the work function of graphene and give rise to a single-photon photoemission background.

2.2. Fabrication and interaction with the substrate

First graphene specimens were obtained by micromechanical cleavage of highly-oriented pyrolytic graphite (Novoselov 2004). Remarkably, due to interference phenomena the thickness of "few layer graphene" flakes deposited on 300 nm SiO_2 can be estimated using optical microscopy (Novoselov 2005a). In the same setup, single layer graphene is subsequently identified by Raman spectroscopy (Ferrari 2006). Indeed this method yields highest-quality graphene for basic research (Graphene Industries Limited 2012), but it is not scalable to wafer-size production cost-efficiently.

This problem may be overcome by the growth of graphene by decomposition of hydrocarbons at metal surfaces (Bae 2010; Wintterlin 2009; Batzill 2012). After deposition of an organic film on top and subsequent etching of the metal, graphene can be transferred to arbitrary substrates (Reina 2009; Li 2009). The transfer process as well as the underlying growth mechanisms of graphene are sketched in Figure 2.2 (Bae 2010) and 2.3 (N'Diaye 2004). Depending on the solubility of carbon in the metal, two main growth modes emerge. Its high solubility in e. g. nickel (Shelton 1974), palladium (Hamilton 1980) and ruthenium (Massalski 1990) causes carbon to dissolve in the surface-near region during the chemical decomposition of a hydrocarbon precursor at elevated temperature. Subsequent

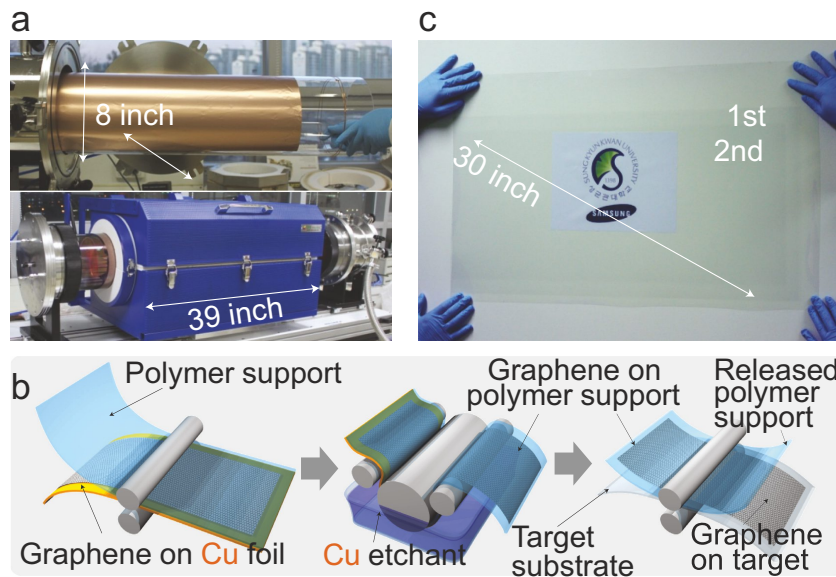


Figure 2.2.: Industrial fabrication of graphene by (a) growth on copper foil and (b) subsequent transfer to a target substrate (Bae 2010). (c) Resulting graphene sheets with an absorbance of 2.3% per layer (Bae 2010; Kuzmenko 2008).

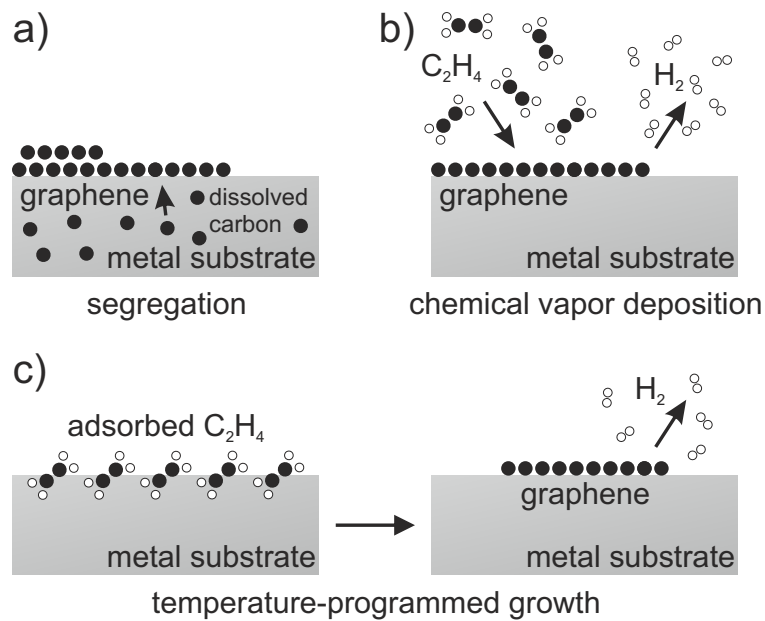


Figure 2.3.: Growth mechanisms of graphene on metal substrate referring to N'Diaye 2004. Carbon is formed by catalytic decomposition of hydrocarbon precursors at elevated temperature. Graphene forms either by (a) segregation of dissolved carbon or (b) by CVD-like growth at the surface. (c) Graphene islands are formed by temperature-programmed growth, a modification of CVD.

cooling reduces the solubility, and graphene is formed by segregation (Shelton 1974; Yu 2008; Liu 2011b; Hamilton 1980; Marchini 2007; McCarty 2009). In contrast, carbon is hardly soluble e. g. in iridium or platinum (Gland 1980; Conrad 1977). Thus chemical vapor deposition (CVD)-like growth of graphene at the surface is dominant (Gastel 2009; Sutter 2009b; Gao 2011). In contrast to segregation, CVD-like growth is self-limiting to monolayer graphene, since the carbon layer, which forms at the surface, inhibits the catalytic dissociation of successively impinging precursor molecules on the metal surface. Moreover, a modification of CVD, temperature-programmed growth (TPG), opens the possibility to produce partially graphene-covered surfaces (Coraux 2009): By adsorption of precursor molecules to a well-defined saturation coverage at room temperature, a fixed amount of carbon is introduced to the system. Following dissociation at elevated temperature results in a known graphene coverage, if either no molecules or a known fraction of them desorb during heating. The TPG cycle can be repeated several times in order to cover the surface with graphene in a stepwise manner. Thus, studies on electron localization (Kralj 2011; Niesner 2012a; Altenburg 2012), confinement (Hämäläinen 2011; Subramaniam 2012; Phark 2012) and edge states (Phark 2012) become possible.

The interaction between graphene and metals is not only a technologically relevant issue during growth. Graphene-based electronic devices will necessarily contain metallic contacts on graphene. Hence, binding between the two will directly affect the device performance. Phenomenologically, two kinds of binding can be distinguished. On e. g. Ni(111) (Nagashima 1994; Bertoni 2005), Pd(111) (Kwon 2009), Co(0001) (Varykhalov 2009) or Ru(0001) (Marchini 2007; Sutter 2008; Sutter 2009a) the distance between the graphitic adlayer and the metal surface is short ($< 3 \text{ \AA}$) and the π bands are strongly hybridized with metal d states. The two carbon atoms within the graphene unit cell become inequivalent, the symmetry is reduced to C_{3v} and the dispersion of the π bands in the proximity of the Fermi level changes from linear to parabolic. Furthermore, a significant band gap of several eV opens as shown for the case of graphene/Ni(111) in Figure 2.4 (a).

In contrast, the bonding between graphene and inert noble metal surfaces of e. g. gold, iridium or platinum is predominantly van-der-Waals type (Khomyakov 2009; Brako 2010; Busse 2011; Hamada 2010) resulting in graphene-metal distances of more than 3 \AA (Busse 2011; Sutter 2009b; Varchon 2007; Filleter 2008; Sławińska 2012). The linear dispersion of the π bands is mostly conserved (Varykhalov 2008; N'Diaye 2006; Pletikosić 2009; Sutter 2009b) as illustrated in Figure 2.4 (b, c). Graphene on a monolayer of silver, copper or gold on Ni(111) exhibits band gaps of 0.32 eV, 0.18 eV and 0 eV (Varykhalov 2010). However, more subtle effects are caused by the remaining hybridization between electronic states of graphene and the metallic surface: In case of graphene/Ir(111), the Dirac cone is located in a projected bulk band gap of the substrate, and electronic interaction is mediated by surface states within this gap (Pletikosić 2010; Starodub 2011). As shown in Figure 2.4 (e), umklapp processes due to the resulting superstructure induce the formation of mini cones and mini gaps of 0.1...0.2 eV (Pletikosić 2009). In case of graphene/Au/Ni(111), the spin-orbit splitting of gold (LaShell 1996) translates to the Dirac cone of graphene *via* hybridization with the gold d states (Marchenko 2012). The resulting spin-orbit splitting of the π states by 100 meV was observed by spin-resolved photoemission experiments

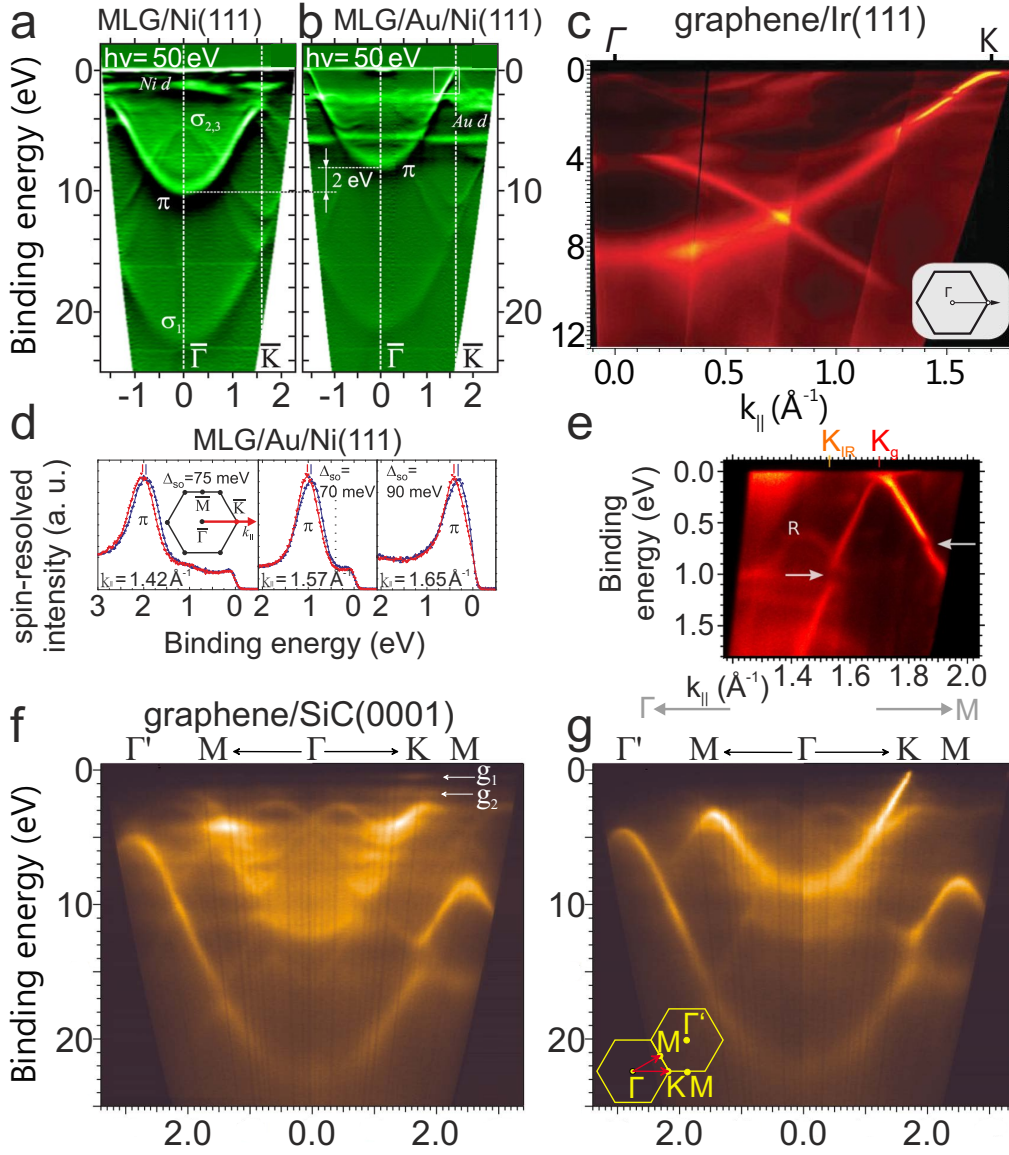


Figure 2.4.: Electronic structure of covalently-bound graphene/Ni (a) (Varykhalov 2008) as well as van-der-Waals bound graphene on Au/Ni(111) (b) (Varykhalov 2008) and Ir(111) (c) (Kralj 2011). The panels in the central row illustrate effects of the remaining substrate interaction: Rashba-type splitting of the π band of graphene/Au/Ni(111) (d) (Marchenko 2012) and backfolding and mini gap opening on graphene/Ir(111) (e) (Pletikosić 2009). Graphene/SiC(0001) shows a sharp, linearly dispersive π band in photoemission (g), while the buffer layer is covalently bond to the substrate (f) (Emtsev 2008).

as shown in Figure 2.4 (d). While modifying its electronic structure on the one hand, interaction of graphene with the substrate is on the other hand required in order to induce a preferred orientation of the adlayer during growth. Thereby the formation of growth nuclei of identical orientation becomes possible, which can merge without creating a high concentration of defects. While substrate interaction is exceptionally weak in case of graphene/Pt(111), a variety of relatively small rotational domains is formed during growth (Sutter 2009b; Gao 2011). Ordered graphene on weakly-interacting substrate like gold, the inertness of which inhibits even the catalytic decomposition of hydrocarbon precursors, is achieved in a two-step process: A strongly bound and atomically well-ordered graphitic adlayer is initially prepared on e. g. Ni(111) (Shelton 1974), Co(0001) (Hamilton 1980) or SiC(0001) (Van Bommel 1975). Gold is subsequently deposited on top and intercalated during a thermal annealing step (Varykhalov 2008; Sánchez-Barriga 2010; Gierz 2010).

An alternative fabrication technique is the thermal decomposition of silicon carbide, a commercially available, wide band gap semiconductor (Philipp 1960). At elevated temperature silicon evaporates from the wafer and at $\approx 1000^\circ\text{C}$ a carbon-rich $6\sqrt{3} \times 6\sqrt{3}$ R30° superstructure is formed on the (0001) crystal face (Van Bommel 1975; Emtsev 2008). The atomic structure of this buffer layer is close to the one of free-standing graphene, but covalent sp^3 bonds between every third carbon atom and the underlying silicon layer destroys the linear π band structure (Mattausch 2007), as shown in Figure 2.4 (f) (Emtsev 2008). Due to remaining dangling bonds, the reconstructed surface is nevertheless metallic (Emtsev 2008; Ristein 2012). When the temperature is increased above $\approx 1200^\circ\text{C}$, these bonds are broken and additional silicon evaporates from the following layer, which thereby turns into the buffer layer (Emtsev 2008). The first, topmost graphitic layer is lifted, becomes van-der-Waals bound and exhibits the π band structure of graphene as shown in Figure 2.4 (g). When the process is conducted under argon atmosphere instead of UHV conditions, growth at higher temperature and hence an improvement of the crystalline quality is possible (Emtsev 2009). Alternatively, the buffer layer is decoupled from the substrate by the intercalation of hydrogen, which breaks the covalent bonds to the silicon atoms and saturates additional dangling bonds, thus minimizing the interaction between the resulting graphene layer and silicon carbide (Riedl 2009; Speck 2010). Graphene/SiC(0001) is attractive for semiconductor applications, since the supporting silicon carbide can be structured previously as well as directly after growth of graphene without any additional transfer (Waldmann 2011; Hertel 2012).

Independent of the fabrication technique, in practice graphene is always at least partly supported by a substrate, which gives rise to charge transfer (Martin 2008; Khomyakov 2009; Bostwick 2007; Ristein 2012). In free-standing graphene, the Fermi level is intrinsically located at the Dirac point, as each of the two carbon atoms in the unit cell contributes one electron to the π bands (Wallace 1947). The dominant driving force of charge transfer is the occurring work function difference when connecting free-standing graphene to a substrate in a Gedanken experiment. The work function of graphene on a metallic substrate can be calculated within a phenomenological model, treating the graphene-metal interface as a capacitor (Giovannetti 2008; Khomyakov 2009):

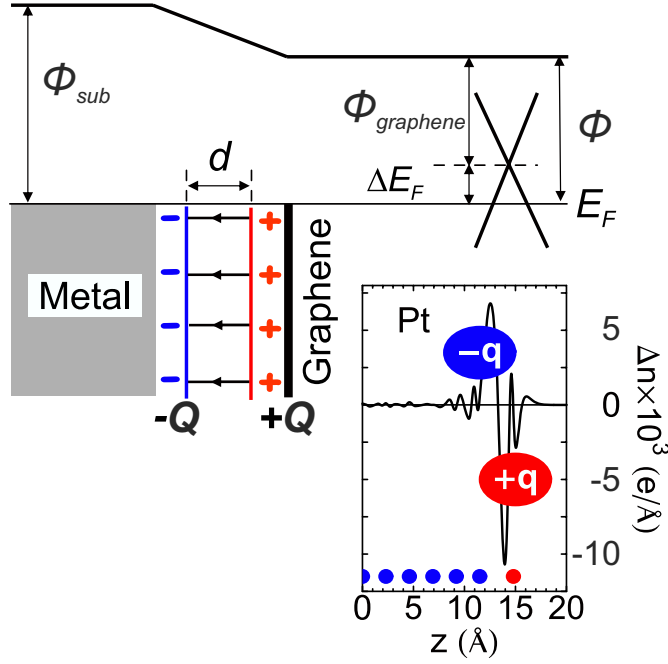


Figure 2.5.: The work function difference $\Phi_{sub} - \Phi_0$ drives a charge transfer Q , which is proportional to $\Phi_{graphene} - \Phi_0$ via the capacitance of the system. Φ_0 is the work function of graphene $\Phi_{graphene}$ plus the shift of the Fermi level caused by hybridization. The linear dispersion of graphene relates Q to a shift of the Fermi level. Adapted from Reference Giovannetti (2008).

$$\Phi = \Phi_{graphene} + \frac{C'}{d \cdot \nu} \left(\sqrt{1 + 2\nu \cdot d/C' |\Phi_{sub} - \Phi_0|} - 1 \right) \frac{(\Phi_{sub} - \Phi_0)}{|\Phi_{sub} - \Phi_0|} \quad (2.2)$$

Where C'/d is the capacitance, Φ , $\Phi_{graphene}$ and Φ_{sub} are the work functions of graphene on metal, free-standing graphene and the bare metal substrate. $\nu = 2e^2 / (\pi \hbar^2 v_F^2) = 0.09 \text{ V}^{-2}$ correlates the charge on the capacitor Q to a shift of the Fermi level of graphene ΔE_F by $Q = \nu |\Delta E_F|^2 / (2e)$, where v_F is the Fermi velocity in graphene. The driving force of the charge transfer is assumed to be $\Phi_{sub} - \Phi_0$, when $\Phi_0 \neq \Phi_{graphene}$. Deviations account for modifications of the band structure of the combined system due to the overlap of the graphene π bands with the metal d bands (Giovannetti 2008; Khomyakov 2009).

The doping levels and work functions of graphene on noble-metal surfaces calculated by the analytical model are in agreement with the ones from density functional theory, when "chemically-induced" charge transfer is accounted for by substituting $\Phi_0 - \Phi_{graphene} = 0.9 \text{ eV}$ (Giovannetti 2008; Khomyakov 2009).

3. Physical properties of topological insulators

Topological insulators are bulk insulators with a topological state on their surface (TSS) or at an interface to a "topologically trivial" material (Hasan 2010). The effect was first predicted (Volkov 1985; Pankratov 1987; Bernevig 2006) and experimentally found (König 2007) in two-dimensional CdTe/HgTe quantum wells. The following section will focus on three-dimensional topological insulators (Fu 2007a; Fu 2007b) which exhibit band gaps of several hundred meV (Hsieh 2008; Chen 2009b; Hsieh 2009a; Hsieh 2009b). A brief introduction will be given to the theoretical concepts and the electronic structure of topological insulators in Section 3.1. Experiments giving proof of some of the theoretical implications will be discussed in Section 3.2.

3.1. Theoretical concept

In Figure 3.1 (a) dispersion and spin structure of a topological state in a bulk band gap are sketched in the vicinity of $\bar{\Gamma}$. It forms a helical Dirac cone similar to the π band structure of graphene, except for the fact, that a polarization of the conventional electron spin instead of a pseudospin sets in (Kane 2005).

The helical spin structure is a result of the topological properties of the bulk material, which are described by a set of integer numbers, the topological invariants Z_2 (Hasan 2010). For three-dimensional materials, four Z_2 invariants exist, which are related to the bulk band structure. They can be evaluated from the symmetry of the bulk valence bands at the Kramers points, also called time-reversal invariant momenta (TRIM) (Fu 2007a; Moore 2007). If the material has inversion symmetry, the analysis is simplified and requires only the parity eigenvalues (Fu 2007b). The Kramers points are determined by the translation symmetry of the crystal and constitute those high symmetry points Γ_i at the edge of the Brillouin zone, which can be connected into $-\Gamma_i$ by a reciprocal lattice vector. The zone center obviously fulfills this requirement and therefore also forms a TRIM. In $d \in \{1, 2, 3\}$ dimensions, 2^d TRIM exist. The TRIM of a two-dimensional rectangularly and hexagonally-shaped Brillouin zone are shown in Figure 3.1 (b) for illustration. The name "time-reversal invariant momenta" is connected to the fact, that time-reversal symmetry has to be fulfilled at these points. For a particle of spin 1/2, as an electron is, this translates to the band structure as $E(\underline{k}, \underline{s}) = E(-\underline{k}, -\underline{s})$, if $\underline{k}=\underline{0}$ is the Kramers point.

The Z_2 topological invariant which characterizes the strong topological insulator, that is the class of topological insulators, which experiments will focus on, is the $\nu_0 = 1$ invariant. $\nu_0 \bmod 2$ determines whether the Fermi surface of the surface (Fermi circle) encloses an even or odd number of surface states. E. g. the surface band structure of graphene is formed

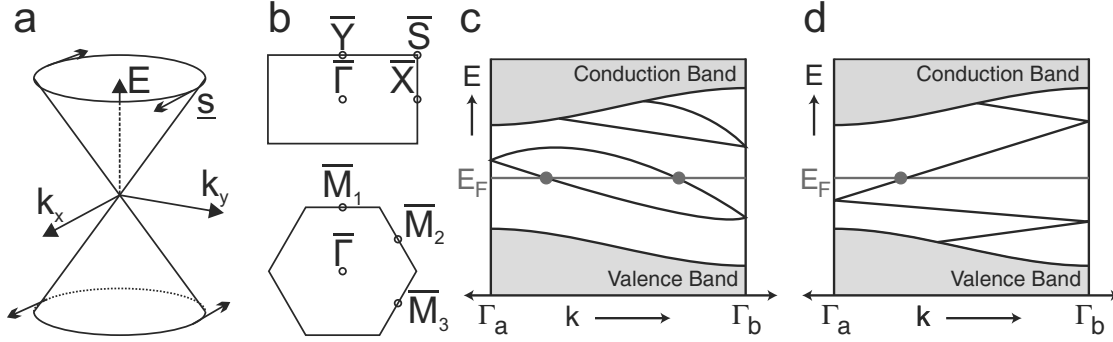


Figure 3.1.: Dispersion and helical spin structure of a topological state in the vicinity of a Kramers point (a). Kramers points (TRIM) of a rectangular and a hexagonal two-dimensional unit cell (b). The topological surface state (d) has an odd number of Fermi level crossings between two Kramers points, which requires it to connect to bulk bands there (Fu 2007a; Hasan 2010). Due to its even number of Fermi level crossings, a topologically trivial state can be connected to its Kramers partner at TRIM (c).

by four states, two spin-degenerate ones forming the two Dirac cones at \bar{K} and \bar{K}' . ν_0 is even, graphene is topologically trivial and the time-reversal symmetry with respect to the $\bar{\Gamma}$ and \bar{M} Kramers points is satisfied as a result of spin-degeneracy. The pseudospin of graphene is a result of spatial symmetry and not flipped upon time reversal. Hence the two Dirac cones have opposite helicity. In contrast, time-reversal has more serious consequences if ν_0 is odd. In the simplest case, which is realized in the systems under investigation, the Fermi circle is formed by a single and consequently not spin-degenerate topological state. For reasons of symmetry, the resulting single Kramers degenerate point is located at $\bar{\Gamma}$, where Kramers degeneracy means energetic degeneracy at the Kramers point, since $E(\underline{0}, \underline{s}) = E(-\underline{0}, -\underline{s})$. For $\underline{k} \neq \underline{0}$, time-reversal symmetry requires a reversed spin orientation at \underline{k} as compared to $-\underline{k}$. Consequently, a Dirac cone with a helical spin structure as depicted in Figure 3.1 (a) arises.

Even or odd ν_0 are equivalent to an even or odd number of Fermi-level crossings of the surface state between two TRIM, as illustrated in Figure 3.1 (c, d) (Fu 2007a; Hasan 2010). In the presence of spin-orbit coupling, the band structure with an even number of Fermi level crossings depicted in (c) is the one of a Rashba-split surface state like e. g. observed on Au(111) (LaShell 1996). The two branches are Kramers degenerate at the TRIM because of time-reversal symmetry. Bands disperse smoothly between $\bar{\Gamma}$ and the Brillouin zone boundary, and the two branches can merge into each other there, resulting in an even number of Fermi level crossings. Realizing an odd number of Fermi level crossings requires the topological state in (d) to find its Kramers partner amongst the bulk valence and conduction bands. Therefore the topological surface state bridges the bulk band gap and is necessarily metallic.

Remarkably, dispersion and spin-polarization are purely results of the symmetry of the bulk electronic structure and time-reversal symmetry. The TSS therefore occurs at

every surface or interface to a topologically trivial material, independent of details of the interface. This fact is referred to as topological protection, since other surface states are in general sensitive to e. g. surface roughness, impurities or adsorbates.

The finding that the topological state bridges the band gap suggests conditions for bulk materials to be a topological insulator. First, significant spin-orbit interaction is required in order to lift spin-degeneracy. As spin-orbit coupling (SOC) is proportional to the potential gradient acting on the electrons, topological insulators often contain heavy elements with a high atomic number like bismuth, antimony or lead. Second, a symmetry-inverted band can support a surface or interface state which restores symmetry across the surface or interface. A symmetry-inversion means a change in the energetic order of bands of different symmetry across the interface. E. g. in the first two-dimensional topological insulator, consisting of $\text{Hg}_{1-x}\text{Cd}_x\text{Te}$ quantum wells, bands of Γ_6 and Γ_8 symmetry switch from valence to conduction bands and *vice versa* as a function of cadmium content x (Volkov 1985; Pankratov 1987; Bernevig 2006; König 2007) as shown in Figure 3.2 (a). In a heterostructure, the topological state forms across the interface between layers of different cadmium content, connecting bands of identical symmetry. In present three-dimensional topological insulators, the band inversion is a result of spin-orbit coupling. Figure 3.2 (b) and (c) show the band structure of Bi_2Se_3 within functional theory without including SOC (a) and including SOC (b) (Zhang 2009a). Switching on SOC introduces avoided

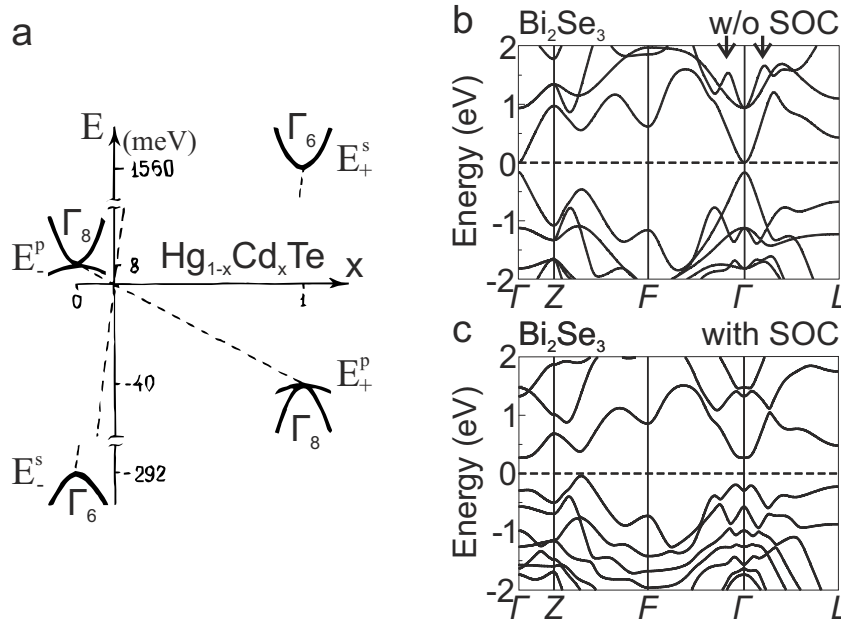


Figure 3.2.: Band inversion, which gives rise to topological non-triviality, is realized by changing the cadmium content x in $\text{Hg}_x\text{Cd}_{1-x}\text{Te}$ quantum wells (a) (Pankratov 1987). The topological state arises at the interface between an inverted and not inverted layer. In the three-dimensional topological insulator Bi_2Se_3 the band inversion is a result of spin-orbit coupling (SOC) (b, c) (Zhang 2009a). Switching on SOC changes the energetic order of the bands, which occurs as a lifting of the band crossings which are marked by vertical arrows (b).

crossings close to Γ , marked by vertical arrows in (b), indicating that the sequence of bands has changed. The band inversion is confirmed by a detailed symmetry analysis (Zhang 2009a; Fu 2007b). Since Bi_2Se_3 without SOC is topologically trivial, actual Bi_2Se_3 with SOC is a topological insulator.

Various phenomena related to the topological state were predicted. An electric current which is carried by the TSS is necessarily connected to a spin current, making topological insulators potential materials for spintronic devices (Datta 1990; King 2011). As a result of spin-momentum locking, an electron will not only maintain its spin orientation, but also its momentum in the absence of spin-flipping scattering events. Thus ballistic, dissipationless electron and spin currents may be driven (Kane 2005). Moreover, electrons in the topological regime are protected from Anderson localization (Anderson 1958), since the time-reversed of every trajectory, which describes a round-trip, is formed by states of opposite spin orientation. The two trajectories interfere destructively, which can be described in a Berry's phase of π (Fu 2007a; Hikami 1980). Phenomena of rather fundamental physical interest are the formation of magnetic monopoles, which arise from the screening of an external charge (Qi 2009), or of Majorana Fermions as a result of superconducting proximity effects (Fu 2008).

3.2. Experimental verification

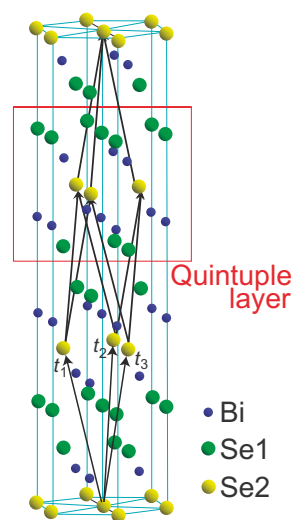


Figure 3.3.: Atomic structure of Bi_2Se_3 (Zhang 2009a).

The first experimentally confirmed topological insulator, $\text{Bi}_{1-x}\text{Sb}_x$ ($x > 0.07$), has a complex surface band structure with five Fermi level crossings between the Kramers points and will not be discussed here in detail (Hsieh 2008). In 2009, the most simple possible surface band structure consisting of a single Dirac cone was predicted by calculations (Zhang 2009a) and found by photoemission studies (Xia 2009; Chen 2009b; Hsieh 2009a; Hsieh 2009b) on several materials, including Bi_2Se_3 , Bi_2Te_3 and Sb_2Te_3 . All of them form layered crystals of covalently-bound quintuple-layers, which are separated by a van-der-Waals gap as illustrated in Figure 3.3 (Zhang 2009a). The structure is hexagonal with a threefold symmetry axis along the c axis and the central bismuth atom constitutes an inversion center. Photoemission data of these systems are shown in Figure 3.4 (a - c) (Xia 2009; Wang 2010; Hsieh 2009a), as well as spin-resolved data from Bi_2Te_3 (d) (Hsieh 2009a). The experimental dispersion of Bi_2Se_3 and Bi_2Te_3 in the proximity of the $\bar{\Gamma}$ Kramers point is in agree-

ment with the theoretical predictions presented in Section 3 and the expected spin structure is observed. In contrast to case of graphene, where the Fermi level E_F is intrinsically located at the Dirac point, since the two p_z electrons in the unit cell just occupy the π band, the Dirac point lies below E_F in Bi_2Se_3 and Bi_2Te_3 , but above E_F in Sb_2Te_3 . Hence the Dirac point of Sb_2Te_3 is not accessible in ARPES. The relative position of the Dirac

point to the bulk band gap and the filling level of the TSS are material dependent, and the experimental findings are in qualitative agreement with calculations (Xia 2009; Zhang 2009a; Park 2009). On Bi_2Se_3 , the Fermi level lies 0.2 eV higher than in the calculation (Xia 2009) due to doping of the surface (Bianchi 2010; Analytis 2010a; King 2011) by selenium vacancies (Benia 2011). The resulting band bending is strong enough to support the formation of a quasi-free electron gas at the surface (Bianchi 2010) and to partially occupy the conduction band. In Bi_2Te_3 the Dirac point is below the valence band maximum, thus bulk states exist at the same energy but higher k_{\parallel} values.

Due to the bulk band gap of a few hundred meV and the presence of bulk states at the energy of the Dirac cone or the Fermi level, surface-sensitive experiments are inevitable for studies on the characteristic electron and spin dynamics in the TSS. In transport measurements on bulk crystals, surface currents are overlaid by the bulk conductivity (Qu 2010; Analytis 2010b; Ren 2010). Surface transport becomes clearly observable in flakes or stripes of Bi_2Se_3 thinner than 30 nm at low temperature (< 20 K) by electric gating (Peng 2010; Steinberg 2010; He 2011; Liu 2011a; Checkelsky 2011; Sacépé 2011; Kim 2012; Hong 2012). Experiments confirm the characteristic Landau level quantization of massless Dirac Fermions (Sacépé 2011). Weak localization is found, unless magnetic adatoms are introduced, which break time-reversal symmetry (He 2011).

Distinct scattering channels can be identified by scanning tunneling spectroscopy of defective surfaces. dI/dV maps show standing wave patterns, which are the result of interferences of Bloch waves that are scattered by defects. The k_{\parallel} vectors of the underlying scattering events are obtained by a Fourier transformation (FT-STs). Figure 3.5 (a) shows a dI/dV map at the Fermi level of the surface of $\text{Bi}_{0.92}\text{Sb}_{0.08}$ (Roushan 2009), the initially mentioned topological insulator which exhibits five Fermi level crossings in its surface band structure (Hsieh 2008). In the top right panel the Fourier transform is given. A cut from $\bar{\Gamma}$ to \bar{M} , which are the Kramers points, is shown in (c).

In the absence of any restrictions, scattering occurs between all electronic states at the Fermi level, which are illustrated in (e). In this case the FT-STs pattern would resemble the joint density of states (JDOS) which is depicted in (b). In the experiment, the scattering events with a momentum transfer q_2 , q_4 and q_8 are observed, while the scattering channels A and B are suppressed. Comparison to the spin orientation of the TSS at the Fermi level crossings in (e) reveals, that A and B require an inversion of the spin orientation. q_2 , q_4 and q_8 connect bands of identical spin orientation. Thus, FT-STs gives experimental evidence that the helical spin structure of the TSS protects electrons on a disordered surface from backscattering, although no current flows along the surface.

More direct access to electron and spin dynamics in the topological state is achieved by following the response to an optical excitation. Three examples are presented in Figure 3.6 (McIver 2012; Hsieh 2011; Sobota 2012). (a) illustrates photo current measurements which make use of circular dichroism (CD). As shown in (b), the photo currents excited by left- and right-handed circularly polarized light differ. Different handedness corresponds to opposite orientation of the spin of the photon $\underline{s}_{h\nu}$, either parallel or antiparallel to the direction of propagation. $\underline{s}_{h\nu}$ and the orbital-angular momentum of the electron form a total angular momentum, which is conserved in electron-photon interaction. Hence

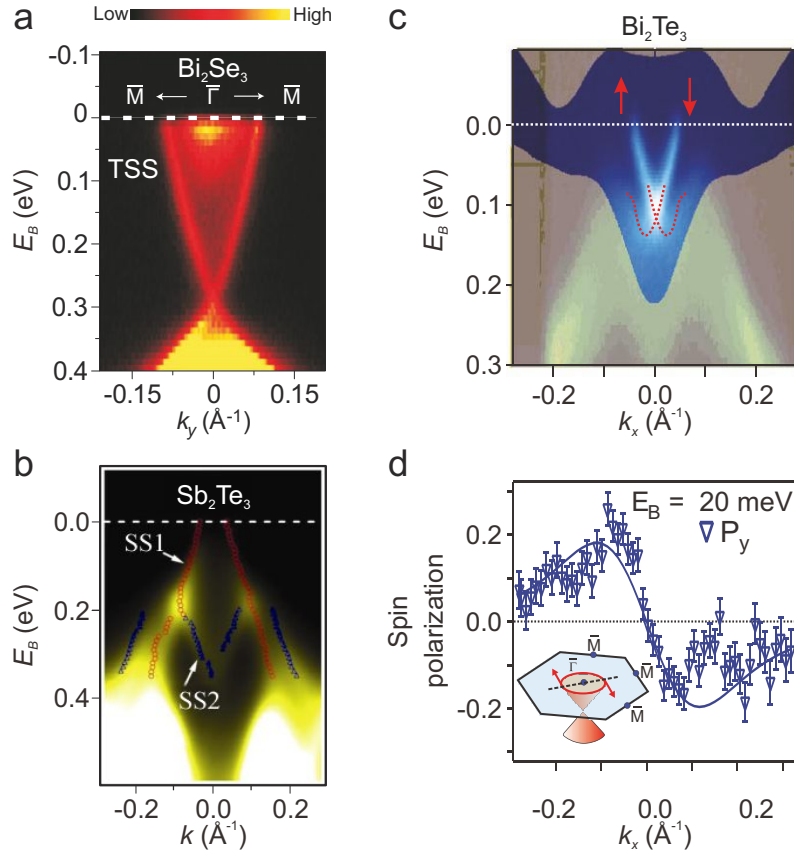


Figure 3.4.: Results of photoemission experiments on Bi_2Se_3 (a) (Xia 2009), Sb_2Te_3 (b) (Wang 2010) and Bi_2Te_3 (c) (Hsieh 2009a) and are consistent with the existence of a single topological surface state. The helical spin structure is confirmed by spin-resolved data (d) (Hsieh 2009a). In case of Bi_2Se_3 , in addition the bulk conduction band is partially filled due to n-type doping. The Dirac point of Sb_2Te_3 is not accessible in ARPES (b).

distinct selection rules for left- and right-handed light apply e. g. to optical transitions in atoms. The effect is also utilized in x-ray photoemission. In case of the surface state of a topological insulator, the spin-momentum locking of the Dirac cone results in a locking of the spin of the electron \underline{s}_{e^-} to its orbital-angular momentum (Park 2012b). Therefore, electron-photon coupling becomes dependent on $\underline{s}_{h\nu} \cdot \underline{s}_{e^-}$, or the rotational direction of the circularly polarized light, respectively. The asymmetric spin and momentum distribution of the holes, which remain in the TSS under illumination with circularly polarized light, gives rise to a spin-polarized current as sketched in Figure 3.6 (a).

Electron dynamics are observed directly in the time domain by pump-and-probe experiments, namely time-resolved second-harmonic generation (TR-SHG) and two-photon photoelectron spectroscopy. Moreover, these techniques offer surface sensitivity or the possibility to separate surface from bulk contributions. In both methods, an initial electronic excitation is induced by a femtosecond pump laser pulse, which is probed by a second pulse after an adjustable time delay.

In TR-SHG, the induced changes in the nonlinear susceptibility are probed by monitoring the intensity of the second-harmonic frequency of the pump pulse. Changes can be attributed to electric polarization caused by electronic excitations at the surface, since bulk crystals with inversion symmetry do not contribute to SHG. Switching the linear light polarization of the probe pulse from s to p allows to follow fields within or perpendicular to the surface. A spectrum recorded from Bi_2Se_3 with a s polarized probe beam is shown in red in Figure 3.6 (c) (Hsieh 2011). The decay time of 1.2 ps is shorter than the one in the bulk (2.3 ps), which is obtained from transient reflectivity measurements (gray curve). The faster cooling rate of the surface carriers may be explained by enhanced surface electron-phonon scattering or diffusion of hot carriers to the bulk (Hsieh 2011). The spectrum in Figure 3.6 (d) was recorded with p polarized probe beam and measures the fields normal to the surface. The corresponding dynamics takes place on a longer timescale of 21 ps. It was attributed to the recovery of the space-charge layer, which creates a band bending towards semiconductor surfaces. This band bending had been lifted by the photovoltage, which was induced by the pump pulse. Using circularly-polarized light, the experiment did not find a spin current in the topological surface state. Thus, the spin coherence time of the TSS of Bi_2Se_3 is shorter than the experimental resolution of ≈ 100 fs, probably because of scattering to the conduction band at the same energy.

Finally, 2PPE resolves energy and the momentum of the excited electrons. Photo-emission spectra of Bi_2Se_3 , which was p-doped by magnesium, recorded at time delay of 0.7 ps and 2.5 ps after the initial optical excitation are shown in Figure 3.6 (f, g) (Sobota 2012). In addition to the valence band below the Fermi level, the transient occupation of the conduction band and the TSS are accessed. At 2.5 ps, practically all excited bulk carriers, that have not recombined yet, have relaxed to the conduction band minimum

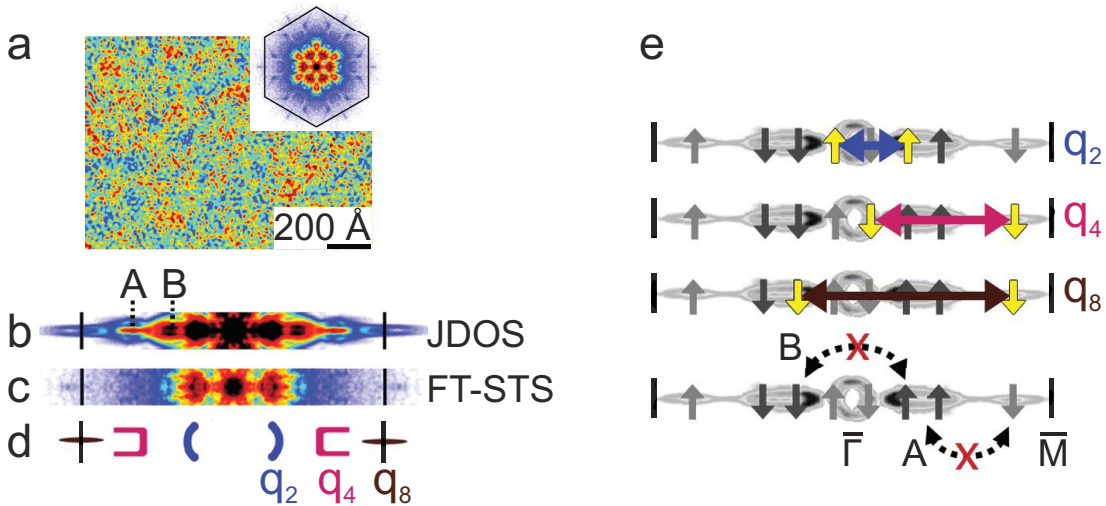


Figure 3.5.: dI/dV map of $\text{Bi}_{0.92}\text{Sb}_{0.08}$ (a) and its Fourier transform (a, c). Comparison to the spin structure of the TSS (e) demonstrates that spin-conserving scattering events (q_2, q_4, q_8) occur, while those which require a spin-flip (A, B) are suppressed (Roushan 2009).

(CBM) at ≈ 0.25 eV. The topological state remains filled only at energies below this value, indicating that refilling from the conduction band is the dominant occupation pathway. Actually, the time-resolved spectra of the TSS (4, red curve) in Figure 3.6 (e) closely resembles the one of the conduction band (3, black curve). Both traces are delayed with respect to the cross-correlation trace of the laser pulses (blue curve), indicating indirect occupation of the CBM and ultimately of the TSS by initially higher-excited electrons. By this mechanism, a transient occupation is supported even ≈ 10 ps after the optical excitation.

Furthermore, 2PPE studies were conducted on electron cooling in nominally undoped Bi_2Te_3 (Hajlaoui 2012) and Bi_2Se_3 (Wang 2012a; Crepaldi 2012). Qualitatively, all studies find a delayed occupation of the TSS which is attributed to indirect population from bulk states. The undoped materials are degenerate semiconductors, with their Fermi level located in the bulk conduction band. In case of Bi_2Te_3 , besides the occupied part of the TSS, bulk bands exist at the same energy but higher k_{\parallel} (Zhang 2009a). In the experiment, different rise times of the unoccupied and the occupied part the TSS population are observed as shown in Figure 3.7 (Hajlaoui 2012) (a, b). The applied rate-equation model yields scattering times of the surface electrons with bulk electrons (holes) of 0.34 fs (0.14 fs).

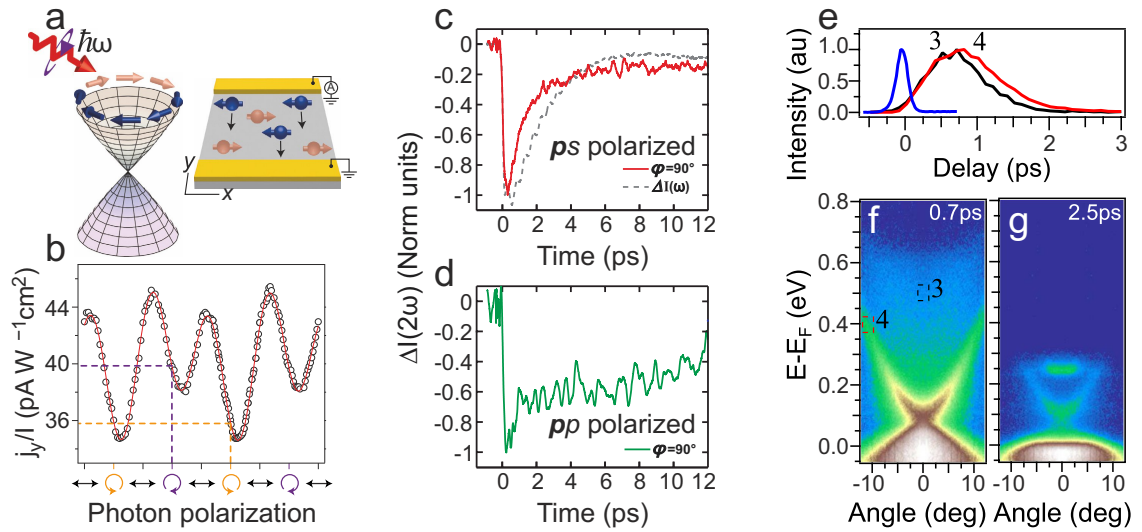


Figure 3.6.: Optical response of Bi_2Se_3 : The helical structure of the TSS allows to drive photo-generated spin currents by circularly-polarized light (a) (McIver 2012). A different current flow under illumination with left- and right-handed circular polarization arises (b). TR-SHG using s (c) and p (d) polarized probe beams measures the electric polarization along the surface and normal to it (Hsieh 2011). The decay time of the former (1.2 ps, red curve) is the result of carrier cooling at the surface, which is two times faster than in the bulk (gray curve, transient reflectivity). The latter (green curve, 21 fs decay time) arises from the collapsing photovoltage. 2PPE spectra after a time delay of 0.7 ps (f) and 2.5 ps (g) indicate refilling of the TSS from the conduction band (CB) (Sobota 2012). Consistently, the time-resolved spectra of the CB and the TSS resemble each other (e). Significant delay compared to the cross correlation trace (blue curve) indicates an indirect occupation pathway.

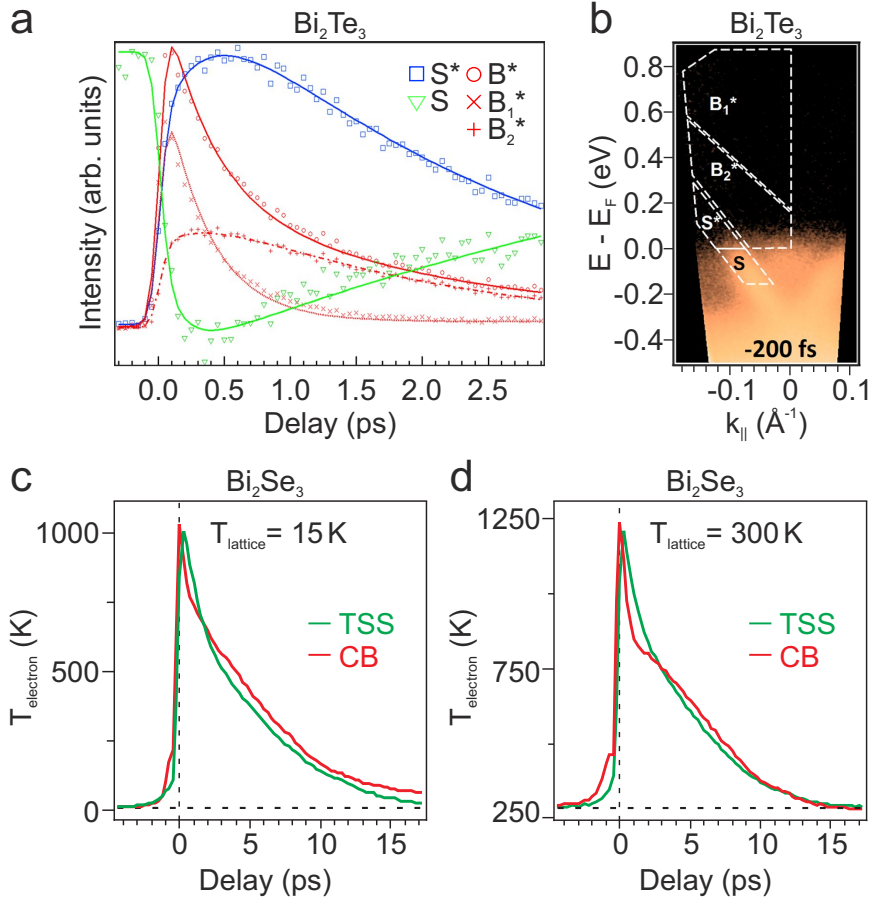


Figure 3.7.: Electron cooling in the conduction band (CB) and the topological surface (TSS) state of Bi_2Te_3 (a, b) (Hajlaoui 2012) and Bi_2Se_3 (c, d) (Wang 2012a). Time-resolved spectra in (a) are integrated over the regions indicated in (b). The occupied (S) and unoccupied part (S^*) of the Dirac cone are both populated indirectly, but with different scattering rates. In Bi_2Se_3 , CB and TSS temperatures are balanced after 15 ps at room temperature (d) but not at 15 K (c), indicating phonon-mediated interaction.

From an analysis of the probing depth, these scattering events are found to take place within a depth of $< 5\text{nm}$ below the surface. Thermalization of the topological state of Bi_2Te_3 lasts $\approx 1\text{ps}$, and electron relaxation has a time constant of $\approx 2\text{ps}$.

In contrast, in Bi_2Se_3 thermalization within the TSS and the bulk conduction band is faster than the experimental resolution (200...300 fs) (Wang 2012a; Crepaldi 2012). Energy-distribution curves were fitted by modeled thermal distributions, thus yielding the electron temperature as a function of time delay which is shown in Figure 3.7 (c, d) at two different temperatures. Thermalization of the TSS with the conduction band is slowed down at lower temperature and was therefore ascribed to phonon-mediated scattering (Wang 2012a). At low temperature, the cooling rate was found to depend on the position of the Fermi level E_F relative to the Dirac point as E_F^3 . This relation is characteristic for the cooling of two-dimensional Dirac Fermions *via* acoustic phonons (Bistritzer 2009).

4. Photoelectron spectroscopy

Photoelectron spectroscopy provides a valuable tool for studies on the band structure of solids and especially surfaces. The following chapter will treat UV photoemission (ARPES) and two-photon photoemission (2PPE). After a theoretical description of the photoemission process in Section 4.1, attention will be paid to circular dichroism in Section 4.2. Particular effects in 2PPE are the subject of Section 4.3. Finally, the experimental setup is presented in Section 4.5.

4.1. General description

When a surface is illuminated by light with a photon energy $h\nu$ larger than the work function Φ , absorption of a photon can excite an electron from below the Fermi level into a state which is energetically above the vacuum level as sketched in Figure 4.1. If the direction of propagation is suitable, the electron can escape from the surface. It is ultimately detected by an analyzer in a free-electron state which is characterized by a momentum \underline{p} and a kinetic energy $E_{kin} = p^2/2m_0$. The detector determines E_{kin} and the direction of emission, thus \underline{p} . Conservation of energy gives the binding energy E_B of the initial state:

$$E_B = h\nu - \Phi - E_{kin}$$

The systems under investigation have crystalline translation symmetry in the bulk, which is reduced to the symmetry parallel to the surface for the emission process. Therefore, the total parallel crystal momentum $\underline{k}_{||}$ is a conserved quantity except for a reciprocal surface lattice vector. The momentum of the photons in the visible and UV spectral range of $\approx 10^{-3} \text{ \AA}^{-1}$ is negligible compared to the experimental resolution. Thus the modulus of $\underline{k}_{||}$ is given by

$$k_{||} = \frac{p \sin \theta}{\hbar} = \frac{\sqrt{2m_0}}{\hbar} \sqrt{E_{kin}} \sin \theta \quad (4.1)$$

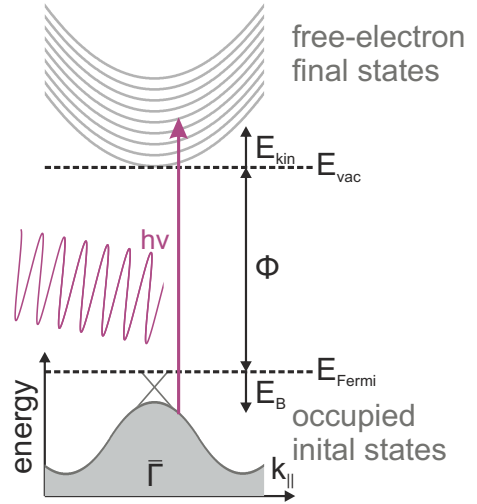


Figure 4.1.: Energy diagram of the photoemission process.

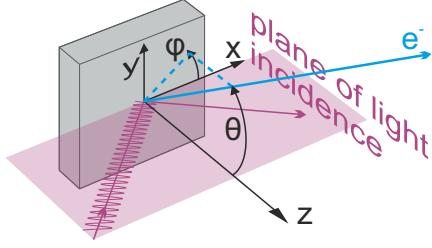


Figure 4.2.: Reference frame.

with respect to the reference frame depicted in Figure 4.2. Hence the full surface band structure $E_B(\underline{k}_{\parallel})$ is contained in the energy- and angle-resolved photoemission data. The reconstruction of the bulk band structure $E_B(\underline{k}_{\parallel}, k_z)$ is more problematic, since k_z is not conserved due to the symmetry break in the z direction at the surface. Determining the full \underline{k} vector requires a variation of the photon energy in combination with assumptions of the involved bands or

measurements on several crystal faces. This is not in the scope of the present work.

Perturbation theory allows to calculate relative photoemission intensities. The light field is assumed as a plane wave of the form $\underline{A} = \underline{A}_0 \exp(i(\underline{q}r - \omega t))$, $\Phi = 0$ satisfying a Coulomb gauge ($\nabla \cdot \underline{A} = 0$) when $\underline{A}_0 \cdot \underline{q} = 0$. The direction of \underline{A}_0 gives the polarization of light, since $\underline{E} = -\partial \underline{A} / \partial t$. The perturbation V is found by substituting $\hat{p} \rightarrow \hat{p} - e\underline{A}$ in the Hamiltonian:

$$V = \frac{1}{2m} (-e\underline{A}\hat{p} - e\hat{p}\underline{A} + e^2 \underline{A}^2) = \frac{1}{2m} (-2e\underline{A}\hat{p} + ei\hbar(\nabla \cdot \underline{A}) + e^2 \underline{A}^2) \approx -\frac{e}{m} \underline{A}\hat{p} \quad (4.2)$$

where the quadratic term in \underline{A} was neglected. Integrating the periodical time dependence reproduces conservation of energy, and results in the photoemission probability w according to Fermi's golden rule

$$w = -\frac{2\pi e}{m\hbar} |M_{f,i}|^2 \delta(E_f - E_i - h\nu), \quad M_{f,i} = \langle \psi_f | \tilde{V}(\underline{A}) | \psi_i \rangle \quad (4.3)$$

$$\tilde{V}(\underline{A}) = \underline{A}_0 \exp(i\underline{q}r) \hat{p}$$

where ψ_i and ψ_f are the initial and final state, corresponding to the energy eigenvalues E_i and E_f , respectively. In general, a numerical evaluation requires detailed knowledge of these states.

However, when the plane of light incidence ($y=0$) matches a mirror plane of the sample, electrons which are emitted along the $y=0$ plane are subject of distinct selection rules for $\underline{A}_s \parallel \underline{e}_y$ (s polarization) and $\underline{A}_p \perp \underline{e}_y$ (p polarization). In the former case, \tilde{V} is odd under the unitary mirror operation \mathcal{O} : $y \rightarrow -y$, in the latter it is even. The plane-wave electron final states ψ_f within the plane are necessarily even ($k_y = 0$), and initial states obey $\mathcal{O}\psi_{i\pm} = \pm\psi_{i\pm}$. Hence

$$M_{f,i+} = \langle \psi_f | \mathcal{O}^\dagger \tilde{V}(\underline{A}_s) \mathcal{O}^\dagger | \psi_{i+} \rangle = \langle \mathcal{O}\psi_f | \tilde{V}(\underline{A}_s) \mathcal{O}^\dagger | \psi_{i+} \rangle = -M_{f,i+} = 0$$

$$M_{f,i-} = \langle \psi_f | \mathcal{O}^\dagger \tilde{V}(\underline{A}_p) \mathcal{O}^\dagger | \psi_{i-} \rangle = \langle \mathcal{O}\psi_f | \tilde{V}(\underline{A}_p) \mathcal{O}^\dagger | \psi_{i-} \rangle = -M_{f,i-} = 0$$

and using p (s) polarized light, only transitions from even (odd) initial states to the even final states are observed. Similar selection rules apply for s polarization and p polarized light at grazing incidence, when the mirror plane and the direction of photoelectron emission are both within the yz plane.

4.2. Circular dichroism

Circular dichroism (CD) in general describes the differing response of a system to light of left-handed and right-handed circular polarization. Circularly polarized light is helical with a parity of -1 , meaning that the electromagnetic wave, in which the fields wind around the direction of propagation in clockwise direction is the mirror image of its oppositely turning counterpart. The different helicities correspond to either parallel or antiparallel orientation of spin and momentum. The appearance of photons of opposite spin gives rise to distinct optical selection rules in the interaction with electrons in a system with rotational symmetry. Thus circular dichroism effects are widely observed in spectroscopic experiments on atoms, inner shell electrons and to some degree in molecules, where the helicity of the photon couples to the orbital angular momentum.

Rotational symmetry is broken in crystals, which are characterized by anisotropy. However, in case of topological insulators, significant spin-orbit coupling (SOC) induces the helical surface state with its spin-momentum locking. As a result of SOC, spin is not a good quantum number, but pseudospin, similar to the total angular momentum of atoms (Fu 2009; Park 2012b; Cao 2012). In the helical structure of the pseudospin, the orbital angular momentum (OAM) is thus locked to the spin (Jung 2011; Park 2012b; Cao 2012). An OAM can be assigned to the crystal eigenstates phenomenologically by expanding the Bloch states in terms of atomic orbitals, which are eigenstates of the OAM. The helical structure which arises from the application of this scheme to a density functional theory calculation of Bi_2Se_3 is sketched in Figure 4.3 (a) (Park 2012b). Remarkably, experiments using linearly polarized light indicate a switch of the p_x, p_y orbital composition of the TSS at the Dirac point as illustrated in Figure 4.3 (b, c) (Cao 2012). Although the orientation of the OAM is not directly accessible in this configuration, a changing composition of p_x, p_y orbitals, which are linear combinations of the p_1, p_{-1} orbitals, is consistent with a change in the helicity of the OAM across the Dirac point.

Strict selection rules like in the case of optical transitions in atoms do not apply in the CD of photoemission from crystals. However, the distinct coupling of photons of opposite

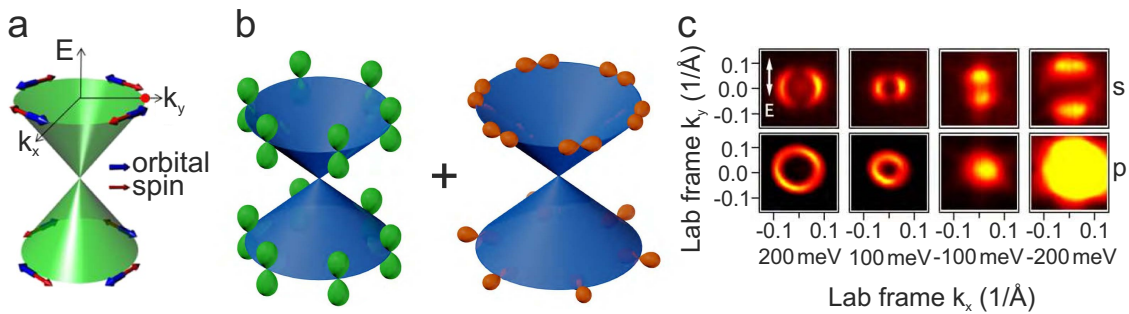


Figure 4.3.: (a) Helical structure of the orbital angular momentum of the TSS of Bi_2Se_3 within a density functional theory calculation (Park 2012b). (b) Symmetry of the orbital composition of the TSS as reconstructed from the polarization dependence of the photoelectron distribution in (c), where $\underline{k}_y = \underline{0}$ is the plane of light incidence (Cao 2012).

spin orientation to the orbital momentum of the TSS results in asymmetric photoemission patterns even in a highly symmetric experimental geometry (Park 2012b; Wang 2012a; Mirhosseini 2012; Park 2012a). The highly symmetric geometry is realized when the mirror plane of the sample coincides with the mirror plane of the experimental setup, i. e. the plane of light incidence. In this case, the circular dichroism asymmetry ΔI , which is the difference of the photoemission patterns recorded with left- and right-handed circularly polarized light, is antisymmetric with respect to the mirror axis, which forms a zero line as illustrated in Figure 4.4 (Wang 2012a; Wang 2012b; Park 2012b). Perpendicular to the mirror axis, two features of opposite CD asymmetry and opposite slope appear in the two-dimensional $E(\underline{k})$ versus \underline{k} cuts. They exhibit the group velocity of the TSS and a crossing point at the Dirac point, as expected from the orbital momentum structure in Figure 4.3 (a). The CD patterns observed in this geometry are hardly affected by variations in the photon energy, as illustrated in Figure 4.4 (c - e).

A theoretical description of the CD patterns requires evaluation of the photoemission matrix elements in Equation 4.3 for the case of circularly polarized light, which is given by $A_0 = (-iA_x, A_y, -iA_z)$. The two rotational directions are transformed into each other by $A_y \rightarrow -A_y$. For topological insulators, an analytical evaluation is possible within the $\underline{k} \cdot \underline{p}$ approximation (Wang 2012a). Within this approximation, the states in the vicinity of the expansion point at $\underline{k} = \underline{0}$ are expanded in terms of the degenerate eigenfunctions $|\psi_+\rangle$ and $|\psi_-\rangle$ at $\underline{k} = \underline{0}$, which are eigenfunctions of the pseudospin (Fu 2009). Assuming spin-degeneracy of the final states, most of the terms in the dipole transition element vanish

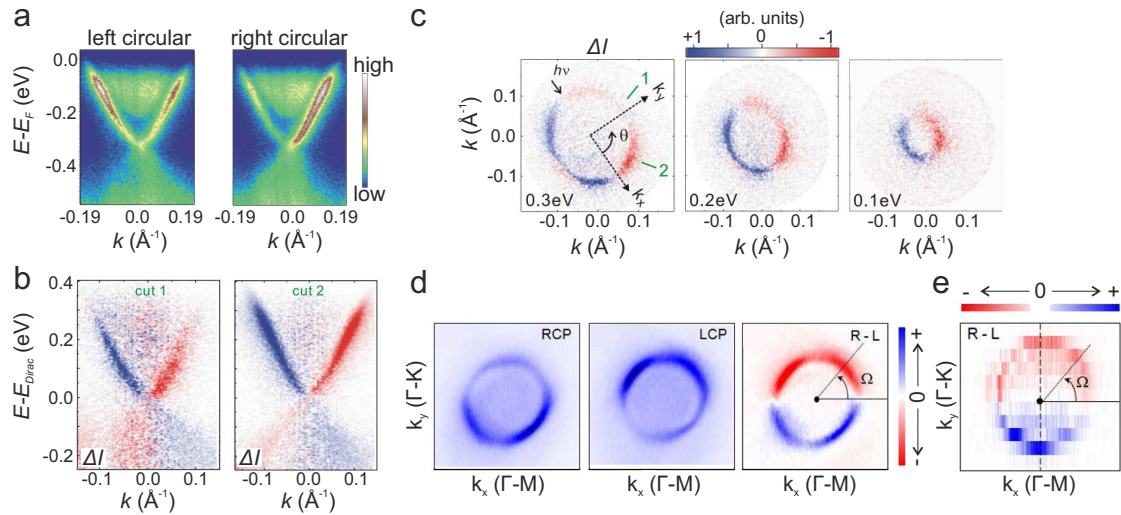


Figure 4.4.: Photoemission studies of the conventional Dirac cone of Bi₂Se₃ in a highly-symmetric setup using left-handed (LCP) and right-handed (RCP) circularly polarized light. **(a)** Intensity distribution for both polarizations as measured at a photon energy of 6.2 eV and **(b)** difference of the two (Wang 2011a; Wang 2012b). The cut was recorded along the green lines labeled 1 and 2 in the momentum distribution patterns in (c). Energies in **(b)** and **(c)** refer to the Dirac point. **(d, e)** Circular dichroism patterns recorded at **(d)** 13 eV and **(e)** 10 eV photon energy at the Fermi level, which is located 0.3 eV above the Dirac point (Park 2012b).

due to the threefold rotational axis, the mirror plane and the fact that $|\psi_+\rangle$ and $|\psi_-\rangle$ are Kramers partners (Wang 2011b). The CD asymmetry ΔI is related to the spin orientation parallel $\langle S_x \rangle_{\underline{k}}$ and perpendicular $\langle S_z \rangle_{\underline{k}}$ to the surface by subtracting the dipole matrix elements for left- and right-handed circularly polarized light:

$$\Delta I = |M_{f,i}^{LCP}|^2 - |M_{f,i}^{RCP}|^2 = a^2 \text{Im}(A_x A_y^*) \langle S_z \rangle_{\underline{k}} - 4ab \text{Im}(A_z A_y^*) \langle S_x \rangle_{\underline{k}}$$

where a , b are real constants. The spin orientation reconstructed from the CD patterns of Bi_2Se_3 within this approximation resembles the one of DFT calculations, including increasing $\langle S_z \rangle_{\underline{k}}$ components at higher \underline{k} values (Wang 2012a).

An issue of discussion are the CD patterns which evolve when the symmetry is broken, e. g. when the mirror plane of the sample is oriented perpendicular to the plane of light incidence. Ishida *et al.* demonstrated, that in a purely two-dimensional system, the xz and the yz plane both form zero lines when the mirror axis of the sample is perpendicular to the plane of light incidence. They observe the corresponding zero lines in the CD patterns of copper-doped Bi_2Se_3 but also of SrTiO_3 , which is not a topological insulator (Ishida 2011). On the other hand, a complex and asymmetric CD pattern of Bi_2Te_3 was observed along the xz plane in this geometry, including a change of the sign of CD asymmetry along one of the bands (Jung 2011). A change of the sign of the complete CD pattern was found upon variation of the photon energy (Sánchez-Barriga 2012b). Density-functional calculations which did not only take into account the helical spin structure of the initial state, the TSS, but evaluated the photoemission matrix elements, were able to reproduce the CD patterns (Sánchez-Barriga 2012b; Mirhosseini 2012). However, for the highly symmetrical setup, the CD asymmetry computed within the same calculation remains necessarily symmetric and resembles the spin structure of the TSS (Mirhosseini 2012). Consequently, in general and especially when mirror symmetry is broken by the experimental setup, final-state effects have to be taken into account for a quantitative analysis of the measured CD patterns.

The conducted 2PPE experiments focus on measurements in the highly symmetrical geometry. In this case, both initial and final states have a well-defined symmetry with respect to the $y \rightarrow -y$ mirror operation, giving rise to antisymmetric CD patterns along the y direction. A fingerprint of the helical pseudospin structure of the TSS then is an inversion of the CD asymmetry at the Dirac point (Cao 2012; Wang 2012a; Mirhosseini 2012; Park 2012b; Jung 2011). Additional inversion points due to final-state effects cannot be fully excluded (Sánchez-Barriga 2012b; Mirhosseini 2012), but are unlikely to coincide with the Dirac point.

4.3. Two-photon photoemission

By conventional ARPES, occupied bands below the Fermi level E_F are probed. In two-photon photoemission an additional optical pump pulse excites a measurable non-equilibrium occupation of electronic states above E_F , which is probed by a second pulse.

The probability of this process is proportional to the product of both pump and probe intensity, and hence 2PPE is a nonlinear process. Therefore short and tightly focused light pulses have to be applied. Suppression of "single-photon" photoemission makes the use of photon energies smaller than the work function desirable. Thus 2PPE usually probes the electronic structure between E_F and the vacuum level in the proximity of the $\bar{\Gamma}$ point.

The energy diagram of 2PPE is shown in Figure 4.5 (a). For reasons of simplicity, two-photon absorption in a continuous wave (cw) light field will be discussed first. Second-order perturbation theory yields the transition matrix element (Jha 1966; Göppert-Mayer 1931):

$$M_{f,i} = \langle \psi_f | \tilde{V}^*(\underline{A}_{pump}, \underline{A}_{probe}) | \psi_i \rangle + \sum_m \left[\frac{\langle \psi_f | \tilde{V}(\underline{A}_{probe}) | \psi_m \rangle \langle \psi_m | \tilde{V}(\underline{A}_{pump}) | \psi_i \rangle}{(E_m - E_i - h\nu_{pump})^{-1}} + \left(\begin{matrix} pump \\ \downarrow \\ probe \end{matrix} \right) \right] \quad (4.4)$$

The intensity is again proportional to $|M_{fi}|^2 \delta(E_f - E_i - h(\nu_{pump} + \nu_{probe}))$.

$\tilde{V}^*(\underline{A}_{pump}, \underline{A}_{probe})$ contains the sum of the quadratic and product terms in the vector potentials \underline{A}_{pump} and \underline{A}_{probe} , which were neglected in Equation 4.2, as well as the sum-frequency and second-harmonic fields of \underline{A}_{pump} , \underline{A}_{probe} , which are generated at the surface.

Together with general symmetry consideration, the following implications are obtained:

(i) Parallel momentum is conserved in each absorption step except for a reciprocal lattice vector. In the absence of scattering at defects or other quasiparticles, the initial state ψ_i , the intermediate state ψ_m and the final state ψ_f correspond to the same $k_{||}$ quantum number.

(ii) In monochromatic 2PPE ($\nu_{pump} = \nu_{probe}$) the two terms in the square brackets are identical. In bichromatic 2PPE each the pump and probe photons may be provided by any of the two incoming laser beams. Only the photon energy of two IR photons is usually not sufficient to overcome the work function of the surface and to extract photoelectrons. Notably, the overall absorbed photon energy is independent of the pump-probe sequence for $\nu_{pump} \neq \nu_{probe}$. As both processes take simultaneously, the resulting signals are overlaid in the spectra. Determining the pump-probe sequence requires time-resolved experiments or a variation of the photon energy as described in the following.

(iii) Energy is conserved in the overall 2PPE process. However, the energy of the intermediate state and the initial state are not necessarily separated exactly by the pump photon energy $h\nu_{pump}$. If they are, optical transitions between ψ_i and ψ_m become possible and resonances occur. The denominator is reduced and the 2PPE intensity is enhanced, as illustrated in Figure 4.5 (b) (Giesen 1986; Steinmann 1989). When the photon energy is slightly detuned, two distinct peaks are observed in 2PPE. They are the result of initial-state effects where $E_f = E_i + h(\nu_{pump} + \nu_{probe})$ and intermediate-state effects with $E_f = E_m + h\nu_{probe}$, as described by the two summands in Equation 4.4. Direct transitions from the initial state to the final state as well as the probe photon in bichromatic 2PPE can thus be identified from the photon-energy dependence.

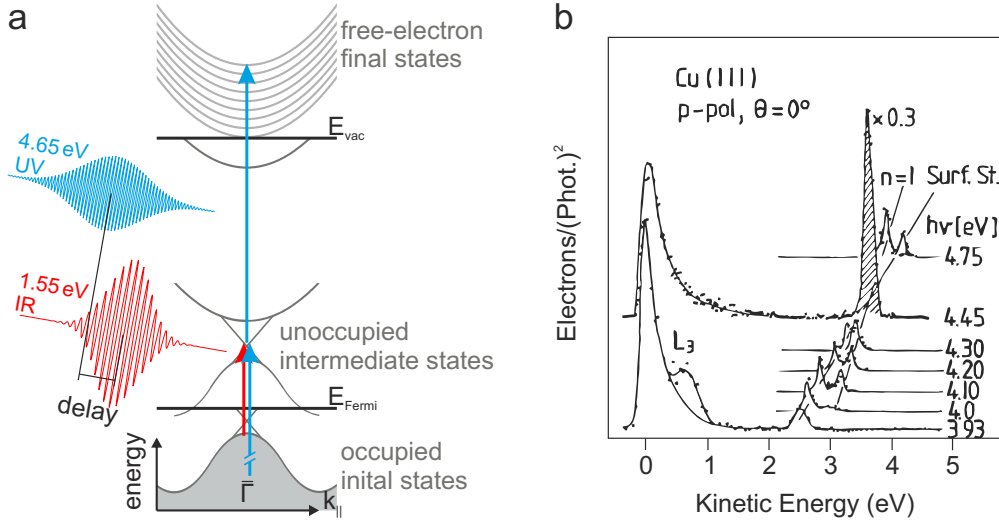


Figure 4.5.: (a) Energy diagram of two-photon photoemission. (b) From their photon-energy dependence, initial-state (Shockley-type surface state, Surf. St.) and intermediate-state (image-potential state, $n = 1$) effects are distinguished. When both peaks coincide, the photoemission intensity is enhanced due to resonance effects (Giesen 1986; Steinmann 1989).

(iv) The sum in Equation 4.4, which describes transitions through an intermediate state, contains matrix elements of the form $\langle \psi_2 | \tilde{V}(\underline{A}) | \psi_1 \rangle$, which is identical to the case of single-photon photoemission. Therefore, the selection rules discussed in Section 4.1 hold for the individual steps. Especially, when the plane of light incident, the direction of photoemission and the mirror plane of the crystal coincide, p polarized light induces transition between states of the same symmetry, s polarized light between states of opposite symmetry. As the free electron final state is again symmetric, the polarization dependence allows conclusions on the symmetry of both initial and intermediate state if they are isolated from the continuum.

In addition to the mapping of the unoccupied part of the surface band structure, the pump-and-probe scheme of 2PPE enables time-resolved experiments. For this purpose a time-delay between the two pulses is introduced and the photoelectron distribution is measured after an adjustable time-delay. The obtained time-resolved spectra reflect the evolution of the transient population, energetic relaxation and dephasing of the excited electronic states as well as the shape of the optical pulses. Depending on the details of electron dynamics in the system under investigation, different approaches for data modeling have been suggested. Two main regimes can be distinguished:

(i) If the excited electrons lose their phase coherence within the observed time interval, classical rate equations can be applied (Weinelt 2002; Petek 1997; Zhu 2002; Kirchmann 2008; Hajlaoui 2012). The approach is mathematically relatively simple and especially useful, when the underlying scattering mechanisms include a variety of contributing channels (Hotzel 2000). It gives a set of coupled inhomogeneous linear differential equations. To some degree, analytical evaluation is possible. In the general case, they are solved

numerically. Alternatively, ensemble properties are modeled, i. e. the evolution of the thermal distribution of the electrons, which allows to follow carrier cooling in metals (Fann 1992a; Fann 1992b; Schmuttenmaer 1994; Cao 1997) and semiconductors (Goldman 1994; Schmuttenmaer 1996; Ramakrishna 2004; Wang 2012a; Crepaldi 2012).

(ii) The full coherent response of the system is modeled by the optical Bloch equations. They use the Liouville-von Neumann formalism to describe the temporal evolution of the quantum-mechanical density matrix within the rotating-wave approximation. Analytic evaluation is possible in the presence of a single decay channel in the limits of overlapping and separated pulses (Boger 2002). In general, the resulting differential equations have to be solved numerically. A detailed discussion of the mathematical treatment as well as resulting implications is given in Reference Boger (2004). The formalism explains e. g. the time-dependent line shape in energy-resolved 2PPE (Ogawa 1997; Boger 2002) and allows to separate between direct coherent excitation at the surface and incoherent excitation mechanisms, which involve e. g. bulk states (Hertel 1996; Ogawa 1997; Shumay 1998; Wolf 1999; Boger 2004). An approximation to the optical Bloch equations, including a single decay channel, is given in Appendix A.3.1 and was used to fit time-resolved spectra of energetically isolated states.

Both mathematical models yield an identical minimal interpretation of time-resolved spectra in agreement with experiments. (i) If the lifetime of the intermediate state is short (< 20 fs), the shift of the maximum in the time-resolved spectra resembles the lifetime (Hertel 1996; Wolf 1999). (ii) The longest-lived observed decay channel dominates the spectra at long pump-probe delays and gives rise to an exponential decay. The time constant reflects the decay time of this long-lived state. If two decay channels with significantly different decay rates are involved, a biexponential decay is observed.

4.4. Image-potential states

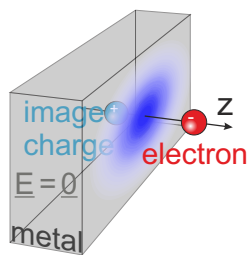


Figure 4.6.: Screening of an external charge by a surface charge redistribution (blue).

A model system for studies of dynamics in a two-dimensional quasi-free electron gas is provided by image-potential states (IPs) in front of metallic surfaces (Fauster 1994; Osgood 1997; Echenique 2004). When an electron is brought in front of the surface at a distance z , a charge redistribution at the surface sets in, which screens the bulk metal from the external field. The resulting potential in front of the surface is described by adding a positive elementary image-charge at $-z$ inside the metal as sketched in Figure 4.6. Thus electron and image-charge form a one-dimensional hydrogen-like system. Parallel to the surface, the electron can move almost freely, since the resulting image-potential state usually has its maximum several Ångström in front of the surface. The resulting energy eigenvalues of the IPS form a Rydberg-like series (Echenique 1978):

$$E_n(k_{||}) = E_{vac} - \frac{0.85 eV}{(n + a)^2} + \frac{\hbar^2}{2m^*} k_{||}^2, \quad n \in \mathbb{N} \setminus \{0\} \quad (4.5)$$

The series limit is the vacuum energy E_{vac} , n is the quantum number, m^* is the effective mass of the IPS band. a is the quantum defect, a correction which arises from the matching of the IPS to the bulk states (Echenique 1978; Smith 1985; Giesen 1987). In order to ensure localization at the surface, the IPS has to be located in a projected bulk band gap. The quantum defect is then determined by the relative position of the IPS to the band edges. It evolves monotonously from $1/2$ at the bottom of the band gap to zero at the top.

With increasing n , and hence decreasing binding energy, the maximum of the charge density of the IPS moves further away from the surface (Loudon 1959; Haines 1969). According to the virial theorem the kinetic energy decreases hereby. The period T which a classical particle takes for a round-trip in an $1/r$ potential is proportional to $(E_0 - E)^{3/2}$. Here E_0 is the minimum of the energy of the unbound states. Application of the equation to the IPS electron gives the period $T = \frac{h}{2.085 \text{ eV}}(n + a)^3$ (Echenique 1991; Fauster 2000). In this classical picture, the electron is subject to scattering to bulk bands at the turning point at the surface. When the probability of scattering to bulk states is independent of energy and momentum, the resulting lifetime is proportional to $(n + a)^3$. This classical limit is usually reached for $n \geq 2$, e. g. in case of Cu(100) (Reuß 1999; Echenique 2004).

2PPE of image-potential states was e. g. applied to study lateral electron localization (Fischer 1993; Fischer 1996; Wallauer 1995) and confinement in z direction (Fischer 1995; Wallauer 1995; Chiang 2009; Chiang 2010). The latter was also accessed by 2PPE studies of quantum well structures (Kirchmann 2007; Kirchmann 2008; Kirchmann 2010; Mathias 2010b; Mathias 2010a; Chiang 2009; Chiang 2010). CO adsorption was shown to enhance the dephasing rate of the IPSs drastically (Wolf 1999; Reuß 1999), while Cu adatoms dominantly cause elastic scattering between states of different momentum (Boger 2004). Remarkably, higher-lying IPS with a narrow energy spacing can be excited coherently due to the spectral width of the optical pump. The interference caused by the distinct temporal evolution of the states results in quantum beats in the time-resolved spectra (Höfer 1997). The decay of the oscillations allows to observe their loss of phase coherence directly in the time domain (Reuß 1999).

4.5. Experimental setup

Two-photon photoemission experiments were conducted in two experimental setups. The corresponding laser systems and possibilities of sample preparation are similar, but the available electron analyzers constitute a major difference.

Optical setup

As a light source acts a titanium:sapphire oscillator with a repetition rate of 90 MHz. It is pumped by a frequency-doubled Nd:YVO laser (Spectra-Physica Millennia) with a wavelength of 532 nm and a power of 4.3 W. The duration of the generated pulses is about 35 fs and the central wavelength can be tuned from 760 nm to 820 nm, corresponding to photon energies between 1.51 eV and 1.63 eV. The resulting average power ranges from 480 mW to 600 mW with a maximum at a wavelength of 800 nm. If not stated otherwise,

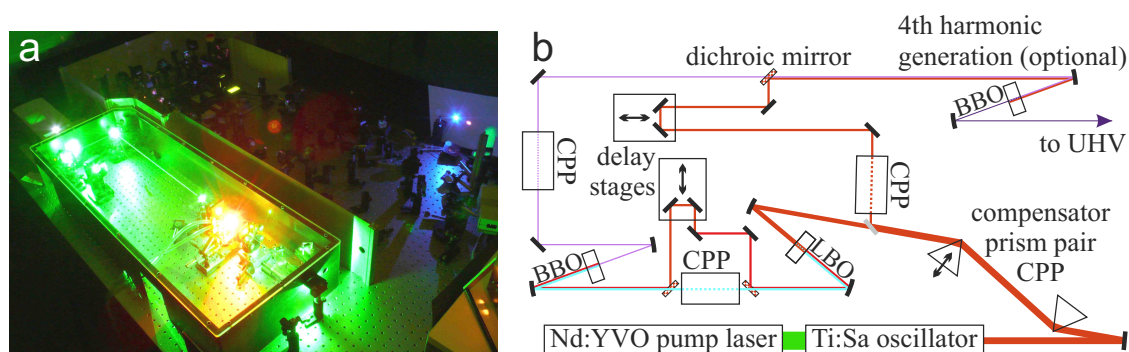


Figure 4.7.: Laser setup, (a) real-space image and (b) schematic drawing.

this photon energy was applied. A spectrometer and an autocorrelator are used to determine central wavelength and duration of the pulses. A schematic drawing of the system is shown in Figure 4.7. A detailed description of the system and the underlying working principles like e. g. the Kerr lens effect in the titanium:sapphire crystal or the pulse compression in prisms can be found in Reference Wang (2005).

For bichromatic 2PPE, 30% of the laser output are deflected by a beam splitter, which is removed in monochromatic experiments. Subsequently, the beam is focussed onto lithium triborate (LBO) and β -barium borate (BBO) crystals, which generate the second harmonic and mix the third harmonic of the fundamental laser frequency in nonlinear optical processes (Boyd 2008). $\lambda/2$ or $\lambda/4$ wave plates in the fundamental IR and the third harmonic UV path are used to adjust the light polarization. If not stated otherwise, experiments were conducted with p polarized beams. The pulse duration is minimized by compressor prism pairs in the IR, the UV and the second-harmonic beampath. Assuming Gaussian lineshapes, the pulse duration of the third harmonic as reconstructed from the cross-correlation trace of IR and UV pulse in 2PPE is typically about 60 fs. Angle-resolved photoemission (ARPES) measurements become possible by additional sum frequency generation of UV and IR beam in a BBO crystal, which results in a photon energy of about 6.2 eV. For bichromatic 2PPE experiments, the UV beam and the initially withdrawn IR light are joined by a dichroic mirror. An adjustable time delay is introduced in the IR beampath by a delay stage. The beam is brought into the ultrahigh vacuum chamber through a quartz glass window. The angle of light incidence is $\alpha = 33^\circ$ with respect to the sample normal in the display analyzer setup and $\alpha = 45^\circ$ at normal emission in experiments on topological insulators in the hemispherical analyzer setup. In the latter setup, experiments on graphene were conducted at $\alpha = 80^\circ$ at normal emission.

In addition, 2PPE of graphene on iridium was conducted in the display analyzer setup using a commercial titanium:sapphire oscillator (Coherent Mira 900 F), which is pumped by a argon ion laser (13 W, multiline). The optical setup is similar, but specifications of the laser differ. The average fundamental power is 1.3 W at 800 nm while the central wavelength can be tuned from 740 nm to 820 nm. The system is equipped with a 10% beam splitter for bichromatic 2PPE experiments. Frequency tripling is achieved in a commercial device (Inrad frequency tripler) which results in longer pulse durations due to the thicker

optical crystals. On the other hand, the third harmonic is more intense with an average power of about 30 mW. Only the IR beampath contains compressor prisms. The width of the cross-correlation trace is about 150 fs.

Ultrahigh-vacuum chamber

Sample preparation and photoemission experiments were conducted under ultrahigh-vacuum (UHV) conditions at a base pressure below 10^{-9} Pa, which is achieved by a combination of turbomolecular, ion getter and titanium sublimation pumps. In the display analyzer setup, the analyzer is protected from contaminating gases, which are present during sample preparation, by a gate valve. Both chambers are equipped with the same systems of sample holders (Dr. Lutz Hammer and workshop of Lehrstuhl für Festkörperphysik) allowing quick sample transfer through a load lock. The sample holder is electrically isolated from the chamber and offers electric contacts for direct current heating (≤ 25 A) and a Chromel/Alumel[®] thermocouple. Sample temperatures above 900 K were additionally checked using a pyrometer. Both setups contain a sputter gun for ion bombardment, the possibility to cool samples to 90 K using liquid nitrogen, a thermal gold evaporator (Potenz 2012) as well as optics and an electron gun for low-energy electron diffraction (ErLEED). In addition to a conventional gas inlet, a "doser" is available, which is a capillary tube on a linear motion drive, providing a gas inlet closely (≈ 1 cm) in front of the sample surface. In this geometry, the pressure of the inserted gas in front of the surface is enhanced by two to three orders of magnitude with respect to the average pressure in the UHV chamber (Gubo 2010).

Hemispherical analyzer

In this analyzer concept, electrons are forced onto circular paths by an electric field between two hemispheres (Hadjarab 1985). Energy-resolution is achieved by the dependence of the radius on the kinetic energy. In the utilized Omicron EA125 analyzer seven channeltrons serve as detectors, which are arranged along the radial direction and hence receive electrons of slightly different energy. The applied pass energy of 2 eV results in an energy-resolution of 34 meV and an energetic spacing of 50 meV between the single channels. The angular resolution amounts to 1.6° . The resolution was determined in Reference Boger (2004), where the apparatus is described in detail. The analyzer is spatially fixed and angle-resolved photoemission experiments are performed by rotating the sample with respect to the analyzer. The polar angle around one axis within the sample plane is varied in order to select a definite emission angle θ and hence the modulus of k_{\parallel} via Equation 4.1. The direction of k_{\parallel} is chosen by an additional rotational axis around the sample normal. Varying θ changes also the angle of light incidence on the sample, thus changing the dipole matrix element in Equation 4.3 and hence the relative photoemission intensities. Notably, in the geometry at hand the detectable emission direction remains within the plane of light incidence when rotating the sample. This direction forms a zero line of circular dichroism.

Ellipsoidal display-type analyzer

In the second setup, the sample is located in one of the focal points of a metallic ellipsoid during photoemission experiments as illustrated in Figure 4.8. A finite voltage $-E_{pass}/e$ is applied to the ellipsoid, which serves as a lowpass and reflects photoelectrons of kinetic energy smaller than E_{pass} onto the second focal point, where they pass an exit slit.

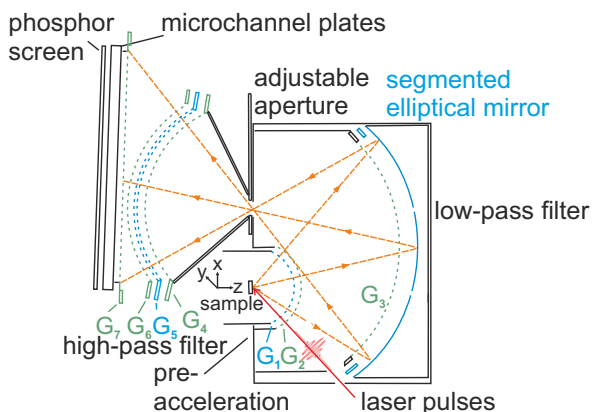


Figure 4.8.: Schematic drawing of the ellipsoidal display-type analyzer

grounded in order to confine the electric fields. The present setup is described in detail in References Gubo (2006) and Rieger (1983), including the reconstruction of the angular photoelectron distribution from the camera image. The apparatus is the first application of this analyzer concept to 2PPE (Gubo 2006). It permits measurements of the circular dichroism of 2PPE, which are not feasible in the hemispherical analyzer setup.

For 2PPE experiments, a pass energy of 5 eV was chosen, which results in an energy resolution of 50 meV for a single emission angle and 90 meV over the entire ellipsoid. The difference is a result of the off-normal incidence of the photoelectrons on the ellipsoid. As the reflection at the repulsive potential sorts electrons with respect to their momentum perpendicular to the surface, the resolution gets worse from the poles of the ellipsoid towards the direction of normal emission. Tribute was paid to this fact by segmenting the ellipsoid into three electrically isolated parts. Hence, three voltages are adjusted separately depending on the emission angle. However, a significant improvement does not occur as also found in Reference Düttemeyer (2001).

The recorded two-dimensional momentum-distribution patterns (MDCs) exhibit inhomogeneities, i. e. dark areas, which are independent of the system under investigation but presumably arise from inhomogeneities of the micro-channel plates. Therefore MDCs were normalized to the ones of features, which may be assumed to be isotropic. The latter are provided by image-potential states. This procedure improves the angular resolution from about 5° (Gubo 2006; Niesner 2010) to 3° . MDCs which are isotropic within the angular resolution were averaged along the direction of the azimuth ϕ . Corresponding algorithms were implemented in the course of a replacement of the data acquisition hard- and software.

The following double grid G_5 forms a retarding field analyzer which acts as a highpass. Electrons are finally detected by a combination of micro-channel plates, a phosphor screen and an amplifying camera. By the resulting bandpass, energy-resolution is realized, and the full two-dimensional angular photoemission pattern within an acceptance cone of 88° is imaged simultaneously (Eastman 1980). The detected energy is varied by biasing the sample and G_1 . The additional grids G_2, G_3, G_4, G_6, G_7 which are depicted in green in Figure 4.8 are

5. Graphene on noble-metal and on silicon-carbide substrates

Electronic surface states of graphene supported by different substrates will be the subject of this section. While the properties of the π -band electrons have been studied in great detail (Wallace 1947; Reich 2002; Novoselov 2004; Geim 2007; Bostwick 2007; Dedkov 2008c; Varykhalov 2008; Pletikosić 2009), here two-photon photoemission is applied to access the image-potential states of graphene close to the vacuum level. In addition, the influence of the graphene adlayer on substrate-induced surface states closely below the Fermi level in the vicinity of the $\bar{\Gamma}$ high symmetry point is investigated.

In case of free-standing graphene, a splitting of the series of IPS into states of even and odd symmetry with respect to the mirror plane formed by the graphene sheet was predicted (Silkin 2009). Although this symmetry is broken by the substrate, a two-peak structure of the first IPS of graphene/SiC(0001) appears in scanning tunneling spectroscopy (Bose 2010). The momentum resolution of 2PPE gives additional information to clarify the situation. By 2PPE, a double series of image-potential states was also found on graphene/Ru(0001) (Armbrust 2012). From their distinct dispersion, the splitting was assigned to the occurrence of localized and delocalized states on the corrugated surface in agreement with scanning tunneling spectroscopy (Parga 2008) and calculations (Borca 2010). Moreover, significant hybridization between the IPS and substrate-induced surface states was found in this system (Borca 2010) due to the short graphene-ruthenium distance (Moritz 2010). In contrast, the graphene-substrate distances in the systems which will be discussed in the following are much larger (Busse 2011; Sutter 2009b; Varchon 2007; Filleter 2008; Sławińska 2012) and close to the graphite interlayer distance of 3.354 Å (Baskin 1955). Therefore the resulting electronic interaction is considerably weaker (Pletikosić 2009; Nobis 2013a; Bostwick 2007; Sutter 2009b; Varykhalov 2008).

After addressing some experimental details in Section 5.1, surface states of graphene on iridium will be described in detail in Section 5.2. Subsequently, in Section 5.3 the energetics and dynamics of image-potential states of graphene on different substrates, including Pt(111), Au/Ni(111) and SiC(0001), will be compared. In addition, work functions of the different surfaces are directly measured in 2PPE. Changes in the work function will be related to charge transfer between graphene and the substrate in Section 5.3.1. The experimental findings are compared to the theoretical model proposed in Reference Giovannetti (2008).

5.1. Experimental details

5.1.1. Sample preparation

Graphene on metal substrates was synthesized under ultrahigh vacuum conditions by decomposition of ethene on the hot clean metal surfaces. This method leads to the formation of well-aligned large-area monolayer graphene (MLG) films on Ir(111) in a chemical vapor deposition (CVD) like process (Nieuwenhuys 1976; N'Diaye 2006; Gastel 2009; Hattab 2011; Hattab 2012). By a similar approach, graphene can be grown on Pt(111) (Sutter 2009b; Gao 2011) and Ir(100) (Gubo 2009; Ferstl 2010). The graphene/Au/Ni(111) system was established by deposition of gold on graphene/Ni(111) and subsequent intercalation of the adatoms (Shikin 2000).

Preparation parameters are summarized in Table 5.1. Clean metal surfaces were prepared by repeated cycles of bombardment with argon ions of the kinetic energies E_{ion} followed by annealing at T_{metal} . Platinum and iridium crystals were then cooled from T_{metal} to T_{O_2} and exposed to oxygen atmosphere in order to remove carbon impurities. The oxygen pressure in the UHV chamber was p_{O_2} but locally enhanced by $10^2 \dots 10^3$ (Gubo 2009) using a "doser" as described in Section 4.5. In case of Ni(111), oxygen treatment was conducted at significantly lower temperature and pressure without the use of a doser for two reasons (Potenz 2012). On the one hand, chemisorbed carbon is dissolved in bulk Ni(111) at temperatures as low as 500...660 K and segregates back to the surface at room temperature (Nakano 2002; Nakamura 1989). At temperatures above 1180 K even the inert MLG/Ni(111) is dissolved and is reformed after cooling (Shelton 1974). Moreover, nickel is rapidly oxidized when a surplus of oxygen is offered (Rieder 1978), while the platinum and iridium noble metal surfaces are far more stable against oxidation (Conrad 1977; Gland 1980).

LEED diffraction patterns from the clean surfaces except Ir(100) show the periodicity and symmetry of the bulk-terminated single crystals without additional diffraction spots. In case of Ir(100), a (5×1) -superstructure is observed which can be attributed to the hexagonally reconstructed topmost iridium layer (Ignatiev 1972; Veen 1980). In this layer the packing density is increased. However, at elevated temperatures as they are needed for the growth of graphene, the reconstruction is lifted and the additional iridium atoms diffuse to step edges as they become mobile (Gubo 2010).

Prior to graphene growth, ethene was adsorbed to saturation coverage at 90 K on iridium and platinum. Subsequent heating to T_{TPG} leads to the formation of initial graphene islands. This growth mode, which will be referred to as temperature-programmed growth (TPG), was studied in detail on Ir(111) using STM (Coraux 2009; N'Diaye 2009), low-energy electron microscopy (N'Diaye 2009; Gastel 2009) and photoemission (Kralj 2011). After one TPG cycle at 1400 K, 19% of the surface is covered by graphene islands of >20 nm diameter which exhibit sharp zigzag edges (Coraux 2009; Kralj 2011). These well-ordered structures of low density (10^{-5} islands/site (Coraux 2009)) serve as nucleation seeds during the following continuous CVD-like growth (N'Diaye 2009). Alternatively, the TPG step was repeated several times in order to adjust the graphene coverage in a stepwise way, as

Table 5.1.: Preparation conditions of graphene on Ir(111), Ir(100), Pt(111) (Nobis 2011) and Ni(111) (Potenz 2012). Ion energies are given in keV, temperatures in K, pressures in Pa and times in minutes. * indicates the use of a doser.

substrate	E_{ion}	T_{metal}	T_{O_2}	p_{O_2}	T_{TPG}	T_{CVD}	p_{CVD}	t_{CVD}
Ir(111)	3	1500	1230	$*2 \cdot 10^{-7}$	1450	1270	$5 \cdot 10^{-7}$	20
Ir(100)	3	1500	1230	$*2 \cdot 10^{-7}$	1450	1270	$5 \cdot 10^{-7}$	15
Pt(111)	1.5	1280	1150	$*2 \cdot 10^{-7}$	1130	1130	$5 \cdot 10^{-7}$	20
Ni(111)	1	1280	580	$1 \cdot 10^{-7}$	-	980	$*1 \cdot 10^{-6}$	5

81% of the previously bare substrate remain uncovered after each cycle. The respective graphene coverages reached per TPG step on Ir(100) and Pt(111) are unknown. However, photoemission experiments on graphene/Pt(111) indicate a significantly lower growth rate than on Ir(111) (Nobis 2011), which is possibly caused by desorption of ethene during heating (Davis 1985). On Ni(111), the TPG approach does not lead to the formation of graphene. Carbon is preferentially chemisorbed in a $c(2 \times 2)$ structure at low coverage, whereas graphene is formed only at higher carbon coverage (Nakamura 1989). Monolayer graphene/Ni(111) was achieved in a single, continuous growth step.

A closed layer of MLG was grown by heating the surface to T_{CVD} under ethene atmosphere (p_{CVD}) during a time interval t_{CVD} . In case of iridium and platinum, this step was performed immediately after the initial TPG cycle, consequently the sample temperature was decreased from T_{TPG} to T_{CVD} . A surplus of ethene was then offered at relatively low pressure during a long time interval in order to allow the growth of large, aligned graphene single crystals from the TPG-induced nucleation seeds. On Ni(111), the alignment of the graphitic adlayer is ensured by the interaction with the substrate (Shelton 1974). However, in order to avoid dissolving excess carbon in nickel, the ethene dose was reduced compared to the noble-metal surfaces.

The preparation of graphene/Au/Ni(111) was completed by gold intercalation. One monolayer of gold, referring to bulk-terminated Au(111), was deposited on graphene on Ni(111) from a thermal evaporator. The intercalation process was triggered by subsequent annealing at 630 K.

Epitaxial graphene/SiC(0001) was produced by thermal decomposition of 6H-SiC(0001) under argon atmosphere (Emtsev 2009) in the group of Prof. Thomas Seyller, Lehrstuhl für Technische Physik. Samples were characterized by x-ray photoemission ensuring monolayer (bilayer) coverage, by atomic force microscopy revealing micrometer-sized flat terraces and by Raman spectroscopy which measured an insignificant intensity of the defect-induced mode relative to the graphitic optical mode (Fromm 2011). Details of the sample characterization can be found in Reference Gugel (2011). After transfer through air, graphene/SiC(0001) samples were annealed in vacuum at 670...850 K for at least 20 minutes in order to desorb hydrocarbons and water which adsorb or intercalate under ambient conditions (Emtsev 2009).

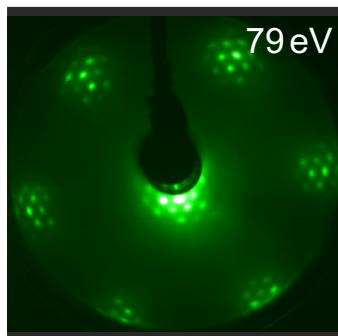
The quality of all surfaces was checked by low-energy electron diffraction and results are discussed in the following section.

5.1.2. Sample characterization by low-energy electron diffraction

In the following, low-energy electron diffraction (LEED) patterns of graphene grown *in situ* in UHV (a-e) will be presented (Niesner 2012a; Nobis 2013a) as well as of the bare Ni(111) substrate (f) (Potenz 2012) and of epitaxial graphene on silicon carbide (g, h) (Gugel 2011). A brief discussion on each of the systems will be given.

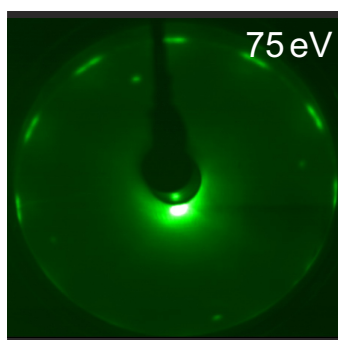
(a) Graphene/Ir(111)

In the LEED pattern of MLG/Ir(111), the graphene lattice vectors are aligned with the ones of the substrate. In addition, a large supercell is observed which is consistent with the 9.32×9.32 moiré structure modeled in Reference N'Diaye (2008). Sharp LEED spots and the absence of diffuse background indicate a low concentration of defects as expected under the used growth conditions (Gastel 2009; N'Diaye 2009). This interpretation is supported by the finding, that after exposition of the specimen to ambient conditions the LEED pattern can be recovered by mild thermal treatment in UHV.



Graphene growth on Ir(111) at low temperatures leads to the formation of misaligned domains which are rotated by 30° with respect to the substrate (Loginova 2009; Starodub 2011; Hattab 2011). Growth of bilayer graphene is also accompanied by the occurrence of rotated domains (Nie 2011). In the present LEED data, no additional spots are found, neither is the graphitic optical phonon ("G-Peak") observed in Raman spectra as shown in Section A.1.1, which would be another fingerprint of second-layer growth or the presence of rotated graphene domains (Starodub 2011; Nie 2011).

(b) Graphene/Ir(100)



Besides the original square unit mesh of the clean Ir(100) substrate, twelve broad additional spots with a double-peak structure are found in the LEED pattern of graphene/Ir(100). The lattice constant found from the distance to the (00) reflex matches the one of graphene. The splitting into two peaks indicates the presence of two symmetry-equivalent domains which are rotated by $\pm 2.7^\circ$ with respect to the (011) direction of the iridium substrate. Due to the fourfold symmetry of the (100) crystal face, the graphene adlayer causes twelve additional double-spots instead of six, a result of the superpositions of the diffraction patterns of 90° rotated but yet symmetry-equivalent graphene domains.

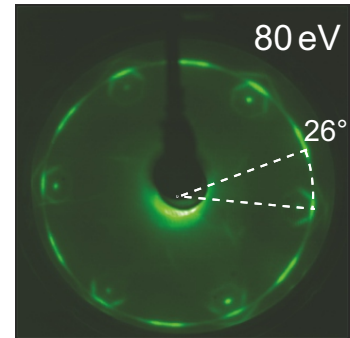
Under slightly different preparation conditions, a complex moiré structure is found in addition, as observed earlier in the LEED patterns of graphene on (100) noble metal surfaces (Hamilton 1980). In scanning tunneling microscopy, areas of flat graphene are found next to regions with a stripe-like one-dimensional structure that has an apparent height

of several Ångström and a periodicity of 22 Å (Ferstl 2011). These strongly-corrugated regions can be found in STM independent of details of the sample preparation, while the intensity of the LEED moiré spots varies strongly depending on the growth temperature (Ferstl 2010). To what extent atomic rearrangement is connected to this superstructure can only be a subject of speculation. Nevertheless, the large height differences observed in STM and the different thermal expansion coefficients of graphite (Tsang 2005) and iridium (Singh 1968) seem to be consistent with the occurrence of atomic corrugation in the reconstructed areas.

Two-photon photoemission will focus on the "low-temperature phase" (Ferstl 2010) without pronounced LEED moiré spots. Although strongly-corrugated graphene may be expected to cover only a small fraction of surface, it is probably nevertheless present (Ferstl 2011).

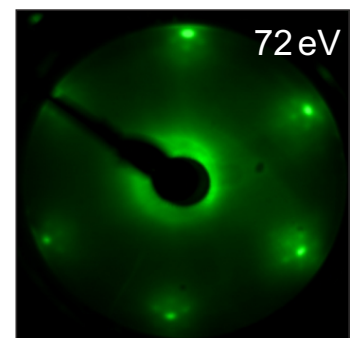
(c) Graphene/Pt(111)

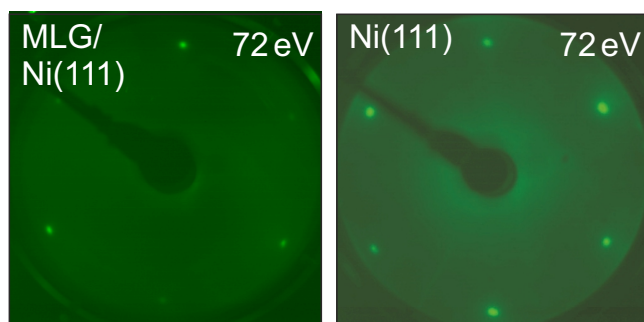
LEED patterns of graphene/Pt(111) indicate the formation of various domains which exhibit different rotational orientations as observed before (Sutter 2009b; Gao 2011). Although the distribution of rotational domains does not measurably affect the two-photoemission results, parameters of the sample preparation, namely growth temperature and ethene pressure, were varied in order to achieve a relatively narrow distribution (Nobis 2011). In the LEED pattern, preferential orientations of 0° and 26° with respect to the $(01\bar{1})$ direction of the substrate are found.



(d) Graphene/Au/Ni(111)

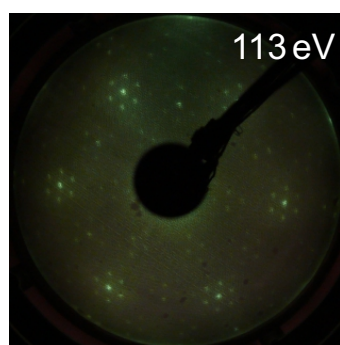
After annealing one monolayer of gold on graphene/Ni(111), a $\approx 10 \times 10$ moiré structure appears in the LEED pattern (Potenz 2012) as also found in STM topographic images of MLG/Au/Ni(111) (Varykhalov 2008). Conclusively, gold has actually intercalated between graphene and nickel. Gold forms a similar superstructure on bare Ni(111) (Umezawa 1999), thus indicating only weak interaction between gold and graphene. However, the alignment of MLG/Ni(111) is transferred to graphene/Au/Ni(111). The diffuse background in the LEED pattern is more intense than in case of MLG/Ir(111), most probably because of imperfect ordering of the intercalated gold layer.



(e, f) Graphene/Ni(111) and Ni(111)

Graphene forms a commensurate 1×1 structure on Ni(111), which is why its LEED pattern shows the same periodicity as the one of Ni(111). Still, the spot intensities in the LEED patterns of MLG/Ni(111) and Ni(111) differ, and thus allow to distinguish between the two phases (Dedkov 2008b; Dedkov

2008a). Photoemission experiments focus on graphene on noble-metal surfaces and silicon carbide, hence graphene/Ni(111) serves mainly as an intermediate during the preparation of graphene/Au/Ni(111).

(g) Graphene/SiC(0001)

The interface between graphene and the silicon-terminated crystal face of SiC is formed by a carbon-rich "buffer layer" which gives rise to the $6\sqrt{3} \times 6\sqrt{3}$ R30° superstructure (Van Bommel 1975; Mattausch 2007; Emtsev 2008; Starke 2009) observed in the LEED pattern. As MLG/SiC(0001) is formed by a lift-off of this buffer layer, it is commensurate with the superstructure (Ohta 2008). This leads to the growth of an ordered and well-aligned graphene adlayer as observed in the LEED pattern which is in agreement with the sample characterization by the complementary methods listed in Section 5.1.

5.1.3. Details of photoemission experiments

The unoccupied part of the band structure of graphene on noble-metal surfaces was examined by bichromatic two-photon photoemission. In addition, UV photoemission was conducted at photon energies of ≈ 6.2 eV. Experiments on each of the surfaces were conducted in both setups described in Section 4.5 giving consistent results. Graphene on iridium was grown in the "display analyzer" setup and 2PPE in the "hemispherical analyzer" setup was conducted after transfer of the sample through air and subsequent annealing at 1150 K in order to avoid adsorbed or intercalated species. After retransfer to the display-analyzer setup and annealing again, the original LEED patterns and photoemission data can be reproduced. MLG/Pt(111) and MLG/Au/Ni(111) were always prepared *in situ* prior to photoemission experiments. In the display-analyzer setup, 2PPE experiments on graphene/iridium were conducted using a commercial laser setup consisting of a Coherent Mira 900 F Titanium:Sapphire oscillator and an Inrad frequency tripler.

On graphene/SiC(0001) additional 2PPE experiments were carried out at Max-Born-Institut Berlin together with the group of Prof. Martin Weinelt, now Freie Universität

Berlin. The laser system is based on a Titanium:Sapphire laser and a Coherent RegA 9050 amplifier which drives two optical parametric amplifiers (Coherent OPA 9450, Coherent OPA 9850). It allows to tune the photon energy of a UV pulse from 3.26 eV to 5.46 eV and that of a visible pulse between 1.6 eV and 2.25 eV independently. The corresponding ultrahigh vacuum system is equipped with a Specs Phoibos 100 hemispherical electron analyzer. A detailed description of the setup can be found in Reference Eickhoff (2010).

Complementary monochromatic 2PPE experiments on Ir(111) were also performed by the group of Prof. Richard Osgood, Columbia University, New York (Niesner 2012a). UV photon pulses were generated by frequency-doubling the output of an optical parametric amplifier driven by a titanium:sapphire laser, resulting in photon energies between 3.8 eV and 4.9 eV. Photoelectrons are collected using a spherical-sector energy analyzer with 50 meV energy resolution. In this setup, the angle of light incidence stays constant, while the polar angle is varied during angle-resolved experiments by changing the position of the analyzer. Details of the setup are given in Reference Hao (2010).

Angle-resolved photoelectron spectroscopy (ARPES) on graphene/Ir(100) was conducted at beamline U125/2-SGM at BESSY II of Helmholtz-Zentrum Berlin in collaboration with the groups of Prof. Thomas Seyller and Dr. Lutz Hammer, both Universität Erlangen-Nürnberg. The endstation was equipped with a toroidal electron analyzer as described in Reference Broekman (2005), which measures two-dimensional photoemission intensity distributions as a function of polar angle and energy. An automated five-axis manipulator allows to vary the sample azimuth quickly and therefore to precisely identify and orientate the high-symmetry directions of the surface.

ARPES on graphene/Ir(111) was conducted at APE (ELETTRA) by Marin Petrović and Dr. Marko Kralj, Institut za fiziku, Zagreb. Experiments were performed using a photon energy of 55 eV and a Scienta SES 2002 hemispherical electron analyzer with an energy resolution of 20 meV and an angular resolution of 0.2° .

5.2. Surface states of graphene on iridium

5.2.1. Surface band structure of graphene/Ir(111)

The unoccupied part of the band structure of Ir(111) as obtained from two-photon photoemission and the occupied part as measured by angle-resolved photoemission are shown in Figure 5.1 (a) and (b) (Niesner 2012a). The as-measured energy distribution curves of the 2PPE data can be found in Figure A.4. A series of states is found, whose final-state energy exhibits a one-to-one correspondence to changes in the IR photon energy as illustrated in Figure 5.2 (b), where a slope of one is sketched by dashed lines. Because the determined work function of graphene/Ir(111) amounts to 4.65 eV, these states are UV-pumped and located energetically 0.83 eV, 0.19 eV and 0.09 eV below the vacuum level. Their dispersion is the one of free electrons with an effective mass of 0.9 free-electron masses. The bands are only observed when the IR-beam is *p*-polarized consistent with even symmetry under mirror operation with respect to the plane of light incidence. Conclusively

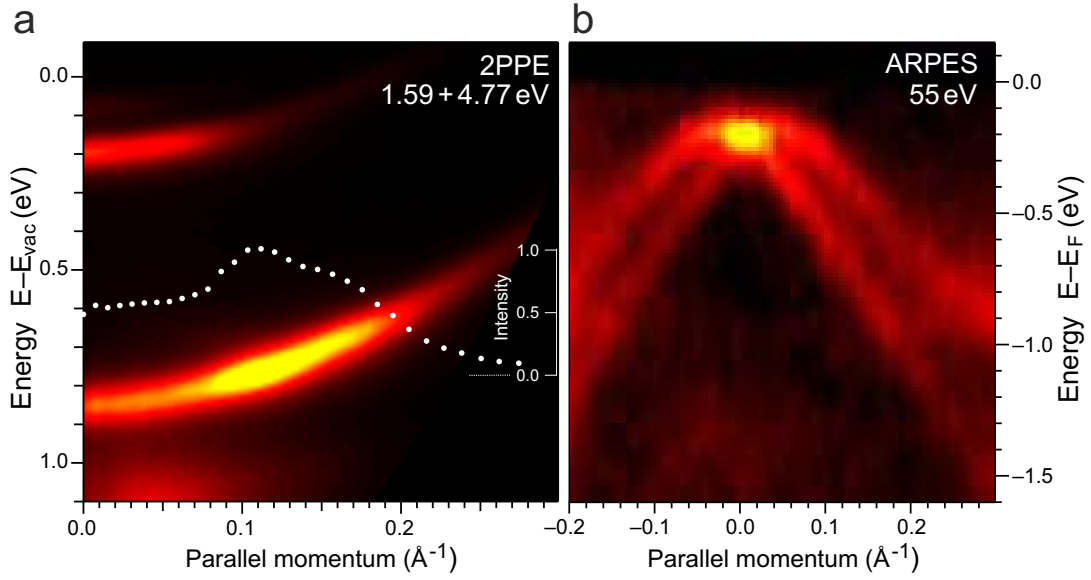


Figure 5.1.: (a) Image-potential states of Ir(111). The intensity distribution along the first IPS is indicated by white circles. The double-peak structure is a result of the resonance between the IPS and the two branches of the downward dispersive, Rashba-split surface state below the Fermi level (b) (Niesner 2012a).

these states are attributed to the series of image-potential states which occur in front of metallic surfaces (Echenique 1978; Fauster 1995).

Below the Fermi level, two downward-dispersing surface states are observed with a binding energy of 190 meV. Their maxima are shifted away from the $\bar{\Gamma}$ -point in parallel momentum by $\pm 0.033 \text{ \AA}$, resembling the dispersion of a Rashba-type spin-split surface state (Rashba 1960). It is attributed to a substrate-induced Shockley-type surface state as it is observed at 0.2 eV higher binding energy also on the bare Ir(111) surface (Pletikosić 2010). The difference in binding energy is a result of charge transfer between graphene and the substrate, which is the subject of Section 5.3.1, and which modifies the potential at the iridium surface.

From a band structure calculation (Niesner 2012a), which is based on a nonrelativistic parametrized tight-binding scheme (Papaconstantopoulos 1986), the total density of bulk states projected onto the (111) direction of iridium (right-hand side of Figure 5.2 (a)) as well as contributions which originate from basis functions of sp symmetry (left-hand side of the same figure) were extracted along the $\bar{\Gamma} \bar{K}$ direction. Starting from the $L_{2'}$ and L_1 band edges, which are formed by states of pure sp symmetry at $\bar{\Gamma}$, the position of the Shockley-type surface state as well as the ones of the image-potential states were calculated within a scattering model (Fauster 1995). The work function was adjusted to the experimental value for MLG/Ir(111). As relativistic effects and spin-orbit coupling are not included in the calculation, the surface state was shifted in parallel momentum by $\pm 0.033 \text{ \AA}$ in order to account for the experimental Rashba-type spin splitting.

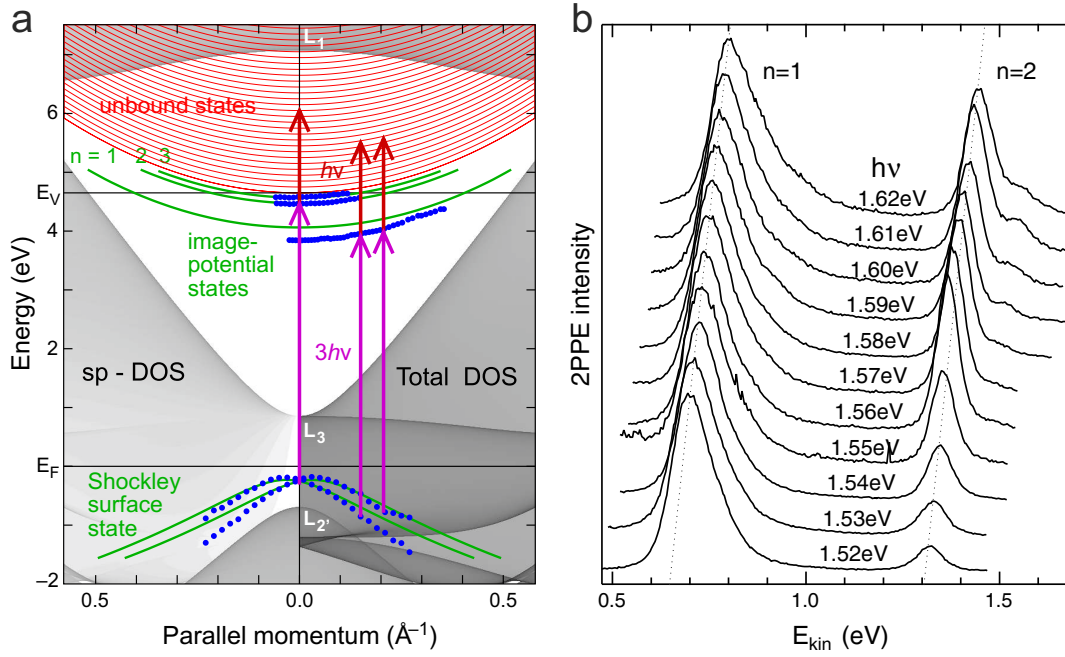


Figure 5.2.: (a) Total projected density of states (Total DOS) and density of states with sp symmetry (sp -DOS) of Ir(111) within a tight-binding calculation (Niesner 2012a). A downward-dispersing, Rashba-split surface state (green lines) is located in the symmetry band gap, giving rise to the resonances indicated by arrows for a photon energy of $h\nu = 1.59$ eV. Blue dots depict experimental data. Changing the photon energy, the second and third image-potential states are shifted into or out of resonance (b). Dashed lines indicate a slope $\partial E_{kin}/\partial h\nu = 1$.

While the calculated and the experimentally found binding energies of the higher-lying image-potential states are in agreement, the binding energy of the first image-potential state, which is located closely in front of the surface, is significantly increased by the graphene adlayer. Experiments on weakly-bound graphene on different substrates give similar results. The screening of the IPS electron by the graphene sheet and resulting implications on the detailed binding energies of the IPSs will be the subject of Section 5.3. The Shockley state lies in a projected sp symmetry band gap of iridium and is degenerate with the bulk d states.

As it inherits the sp symmetry, optical transitions between the surface state and the image-potential states are possible under irradiation by p -polarized light. These transitions give rise to resonance effects in 2PPE which occur as an intensity enhancement in the spectra (Giesen 1986). In the calculation in Figure 5.2 (a) the resonant transitions at a pump photon energy of $3h\nu = 4.77$ eV are indicated by pink arrows. The experimentally found intensity distribution along the first image-potential state is depicted by white circles in Figure 5.1 (a). It exhibits a double-peak structure resulting from the Rashba-splitting of the occupied surface state, while the positions of the intensity maxima are shifted to slightly smaller $k_{||}$ values as compared to the calculation. The latter finding is explained by the overlaid intensity distribution resulting from non-resonant excitation, which decreases monotonically from $\bar{\Gamma}$ towards larger $k_{||}$ values (Güdde 2007).

Additional evidence of the consistence of the model surface band structure is given by the photon-energy dependence of the higher-lying IPSs as illustrated in Figure 5.2 (b). Energy-distribution curves at normal emission were recorded at different photon energies $h\nu$ in the ellipsoidal display analyzer setup and were normalized to the peak intensity of the first IPS. Consistent with the preceding discussion, the intensity of the second (third) IPS rises drastically when the pump photon energy $3h\nu$ reaches the energy difference of 4.65 eV (4.75 eV) between the image-potential state and the Shockley-state.

In conclusion, a comprehensive picture of the electronic bands under investigation is obtained for a closed monolayer of graphene on Ir(111). In order to study the influence of confining graphene islands on the concerning image-potential states, experiments were conducted on the partially covered surface (Niesner 2012a). Therefore repeated cycles of temperature-programmed growth were used to cover 19% of the surface not covered by graphene per step (Coraux 2009) with graphene as described in Section 5.1.1.

The evolution of the work function and the binding energies of the lowest three image-potential states as a function of coverage is illustrated in Figure 5.3. The work function decreases linearly from 5.79 eV, which is in agreement with literature values for clean Ir(111) (Strayer 1973; Nieuwenhuys 1974), to the value of 4.65 eV for MLG/Ir(111). Photoemission measures the work function averaged over bare substrate and graphene islands (Fischer 1993). Hence the linear relation between coverage and work function confirms the underlying calibration of the coverage $\theta = 1 - 0.81^n$, where n is the number of applied TPG cycles.

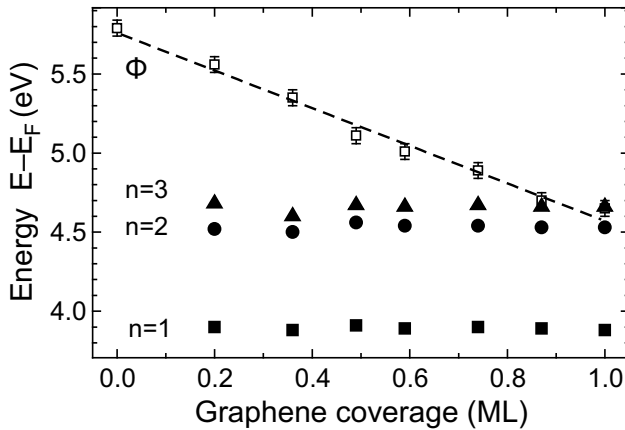


Figure 5.3.: Coverage-dependence of the work function Φ and the lowest three image-potential states $n = 1, 2, 3$ of graphene/Ir(111) (Niesner 2012a).

is suppressed, as these states are not accessible because of the high work function of Ir(111). The constant energy of the image-potential states indicates that, under the applied preparation conditions, the local work function of graphene islands reflects the value of the closed layer independent of their size which is about $(35 \text{ nm})^2$ after the first TPG cycle (Kralj 2011). Energy shifts caused by confinement in a potential well of this size are $\ll 1 \text{ meV}$ and are therefore negligible compared to experimental uncertainties.

In contrast, the image-potential states appear at the same energetic positions as on MLG/Ir(111) for all coverages $\theta > 0$. As the IPSs are energetically pinned to the vacuum level (Echenique 1978), this finding implies that they are localized on graphene islands and pinned to their local work function. This behavior is expected when island sizes exceed the lateral extension of the surface charge distribution which screens the IPS electron (Fischer 1993). The latter is given by the distance of the probability density maximum of the image-potential state from the surface, which is of the order of nanometers.

5.2.2. Dynamics of image-potential states of graphene/Ir(111)

Lifetimes of the image-potential states were determined by bichromatic two-photon photoelectron spectroscopy. A series of time-resolved measurements of the first four states recorded at normal emission is shown in Figure 5.4 (a). Note that the fourth IPS is not resolved in the energy distribution curves, hence the spectrum was acquired at the energetic position calculated from Equation 4.5. Lifetimes were extracted by fitting equation A.1 to the data. The resulting fitting curves are given in gray. All data sets are well-described by a single-exponential decay at long pump-probe delays with lifetimes of 35 fs, 114 fs, 270 fs and 437 fs. The relation between lifetime and binding energy is illustrated in Figure 5.4 (b). As described in Section 4.4, lifetimes are expected to decrease $\propto E^{-3/2}$ within a classical model based on a one-dimensional Kepler problem, whereas an $\propto E^{-1}$ relation is found in the present case. One possible reason for deviations are scattering processes taking place dominantly in two dimensions (Petek 1997). However, a similar $\propto E^{-1}$ dependence was also found on copper surfaces (Echenique 2004). A comprehensive theoretical description of the underlying scattering events is necessary in order to assign them to a distinct spatial dimensionality.

On closer examination the time-resolved spectrum of the fourth IPS is periodically modulated at delays < 300 fs. The modulation is a result of quantum beats between higher-lying states which are separated in energy only by a few tens of meV (Höfer 1997). Due to the spectral width of the laser pulse, these states can be excited coherently. The fast decay of the quantum beats indicates a fast loss of the phase coherence of the excited states (Reuß 1999). The pure dephasing rate of the first IPS was determined from a line width analysis

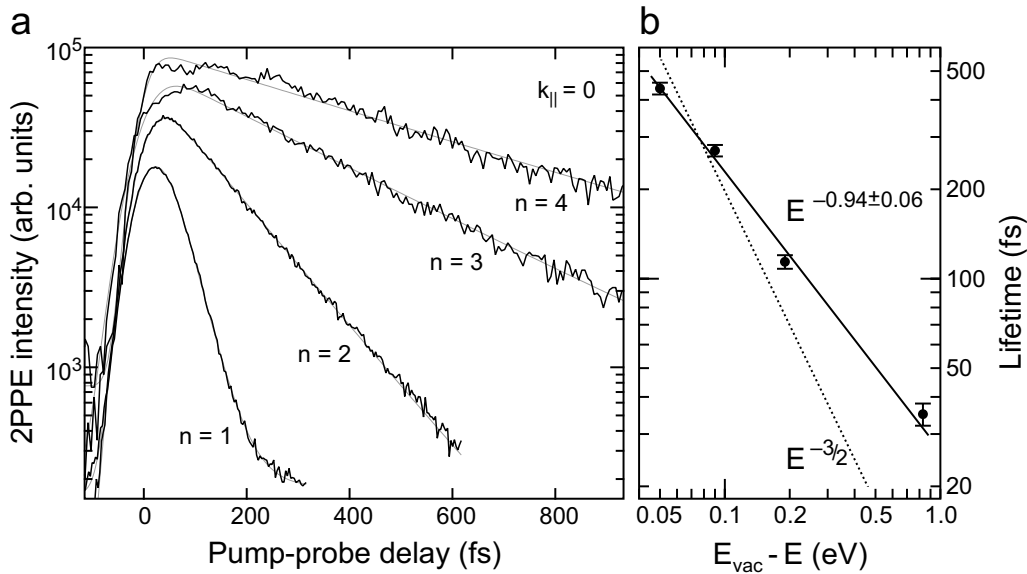


Figure 5.4.: (a) Time-resolved spectra of image-potential states of graphene/Ir(111) (black) and fits to the data (gray). (b) Extracted lifetimes are inversely proportional to the binding energy (Niesner 2012a).

as illustrated in the inset of Figure 5.5 (a). The peak shapes were deconvolved into a Gaussian contribution representing an experimental resolution of 58 meV and a Lorentzian contribution which depends on the pump-probe delay in 2PPE (Wolf 1999; Boger 2002). From comparison to a simulation based on the optical Bloch equations (Boger 2005) a pure dephasing rate of ≈ 10 meV is found, which is a factor 2...3 larger than the one of the $n = 1$ state of Cu(100), although the decay rates are similar in both systems (Weinelt 2002; Boger 2005). Consistently, quantum beats between higher-lying IPSs of Cu(100) are observed even picoseconds after the initial excitation (Höfer 1997). The faster loss of the phase coherency of the IPS of graphene/Ir(111) compared to Cu(100) may be attributed to the presence of the periodic superstructure on the one hand and to the presence of an additional band at a similar energy on the other hand. The mean free path of an electron in the image-potential state is $\frac{1}{\hbar} \langle \frac{dE}{dk} \rangle_k \tau \approx 35 \text{ \AA}$, where $\langle \dots \rangle_k$ denotes the average over k values within the first moiré Brillouin zone. This value is similar to the size of the supercell (25 Å (N'Diaye 2008)). Thus within its lifetime the image-potential electron passes about one single high and one low area of the superstructure, which act as defects and can reduce the phase coherence. In addition, quasi-elastic scattering may occur between the first image-potential state and an additional band, which will be the subject of the following paragraph.

As shown in Figure 5.5 (a), the decay rate of the first IPS increases steeply with energy within the lowest 100 meV from the band minimum, corresponding to a k_{\parallel} range of $\approx 0.15 \text{ \AA}^{-1}$. At higher energies the slope is decreased significantly. The additional scattering channel in the proximity of the minimum can be attributed to a second, flat unoccupied band in this energy region. The lineshape of the $n=1$ image-potential state at $\approx 0.7...1.3$ eV kinetic energy in the EDCs in Figure 5.5 (b) becomes increasingly asymmetric at polar angles $\theta \geq 20^\circ$. At $\theta=40^\circ$ a second peak is resolved. At polar angles below 15° , corresponding to $k_{\parallel}=0.15 \text{ \AA}^{-1}$, the feature merges into the $n = 1$ state. Monochromatic 2PPE observes the unoccupied state at a similar binding energy (Dadap 2011), supporting the interpretation as an intermediate state.

A possible origin of the flat band is the localization of image-potential states on corrugated regions of the surface as observed on graphene/Ru(0001) (Armbrust 2012). However, the corrugation of graphene/Ir(111) is significantly smaller than on Ru(0001) (Busse 2011; Moritz 2010). Moreover, the periodic potential of the superstructure is expected to give rise to umklapp processes. No indication of a resulting band gap opening is observed within the experimental uncertainties. A splitting of the IPS series into states of even and odd symmetry like expected in case of free-standing graphene (Silkin 2009; Bose 2010) may also be considered, but seems very unlikely, as the underlying symmetry is broken by the metal substrate. Revealing the nature of the additional band is a concern of ongoing research (Nobis 2013b).

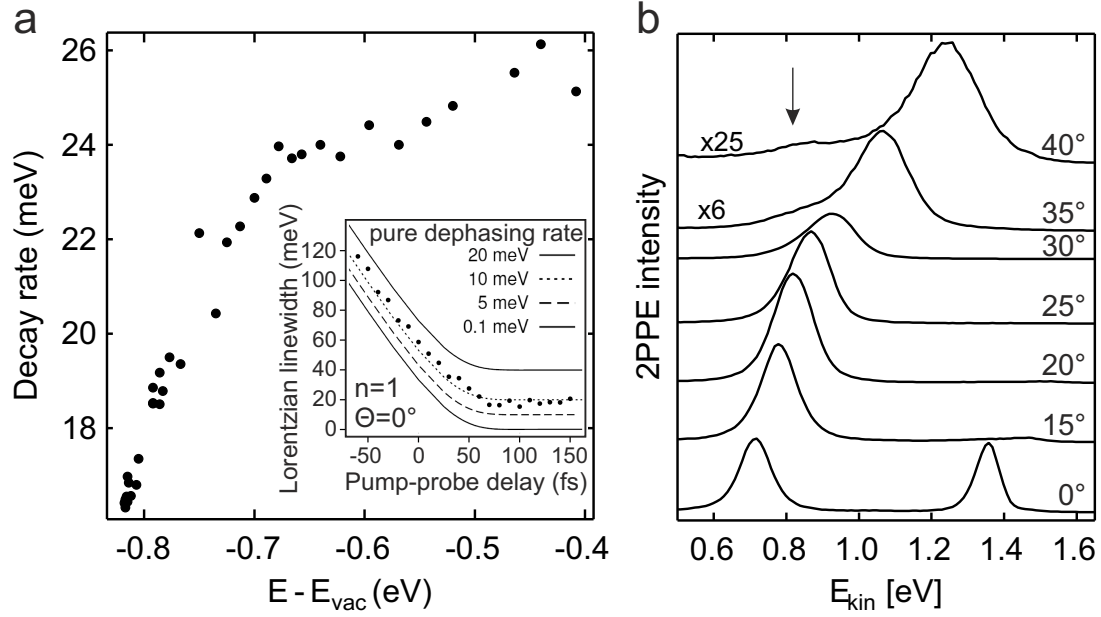


Figure 5.5.: (a) The observed decay rate of the first IPS of graphene/Ir(111) increases steeply in energy in the proximity of the band minimum. (b) The additional flat band marked by the arrow is observed at polar angles $>20^\circ$ in the energy distribution curves. The large slope in (a) is either caused by the superposition of signal from both states or by scattering between them on the surface. The inset in (a) illustrates the line width analysis of the first IPS. From comparison to the simulation (Boger 2004) a dephasing rate of ≈ 10 meV is estimated.

5.2.3. π -band structure of graphene/Ir(100)

While the growth of graphene/Ir(111) is a well-understood process (Nieuwenhuys 1976; N'Diaye 2006; Gastel 2009; Hattab 2011; Hattab 2012) and the resulting, almost defect-free graphene was studied using various techniques (Coraux 2009; Pletikosić 2009; Gastel 2009; Busse 2011; Langer 2011), only little preliminary work has been performed on graphene/Ir(100) (Ferstl 2010; Ferstl 2011). A key method giving information on the electronic structure is angle-resolved photoelectron spectroscopy (ARPES). The experimental band structure recorded at a photon energy of 55 eV is shown in Figure 5.6 (a), whereas in (b) the first derivative of the spectra with respect to energy is given. The square symmetry of the (100) crystal face results in the formation of two symmetry-equivalent domains, which are rotated by 90° with respect to each other. Hence, contributions of the ΓM direction of one and the ΓK direction of the second domain are overlaid in the data. Fits to energy distribution curves find the minimum of the prominent band at -8.03 eV at Γ and a local maximum at -2.45 eV at about 1.54 \AA^{-1} . In the proximity of the Fermi level E_F it develops a narrow lineshape and a linear dispersion, until it crosses E_F at $\approx 1.65 \text{ \AA}^{-1}$. The dispersion is the same at a photon energy of 40 eV (not shown). Thus the band is assigned to a surface feature, namely to the π band of graphene.

As a model dispersion, the tight-binding band structure of Equation 2.1 (Wallace 1947) was fitted to the $\bar{\Gamma}$ and \bar{M} high symmetry points. Fixing the lattice constant to the literature

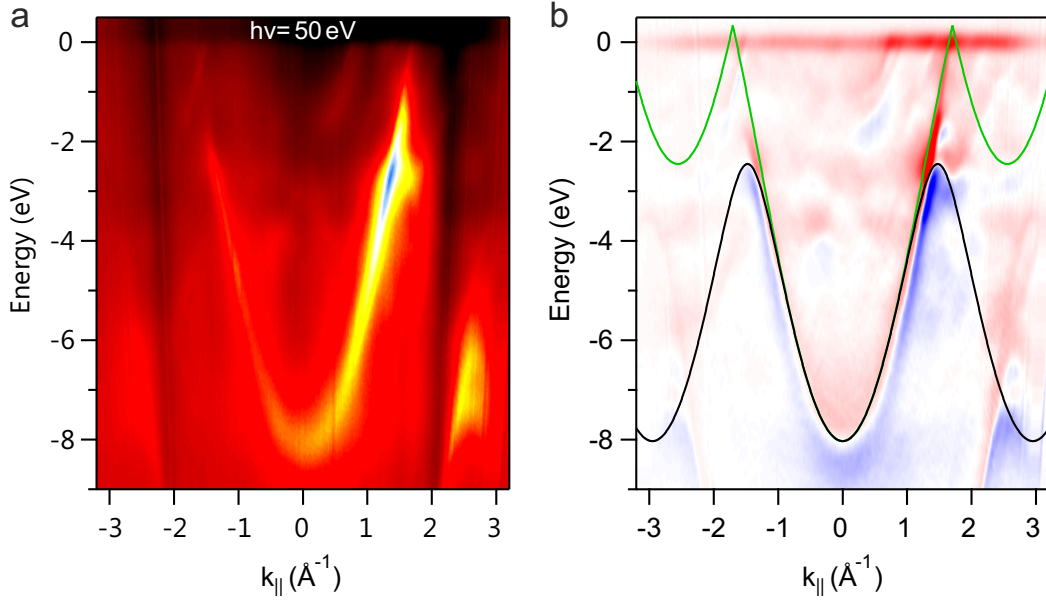


Figure 5.6.: (a) In ARPES data of graphene/Ir(100) signals from the ΓK and ΓM high symmetry directions are overlaid because of the fourfold symmetry of the substrate. The tight-binding band structure (Wallace 1947) along both directions is shown together with the first derivative of the spectra in (b). The crossing between the additional linearly dispersive feature and the original π band at 1.58 \AA^{-1} is assigned to the zone boundary of the moiré supercell.

value (Geim 2007) and neglecting the overlap matrix element results in a transfer matrix element of 2.79 eV, in agreement with previously reported values (Reich 2002). The Dirac point is found 0.34 eV above the Fermi level. P -doping occurs also in graphene/Ir(111), where the Dirac point is located at 0.1 eV (Pletikosić 2009). Due to the p-type doping, the Dirac point is not accessible by ARPES. Its position at 0.34 eV therefore gives an upper limit of a possible band gap occurring in MLG/Ir(100). Nevertheless, the linearity of the π band up to the Fermi level suggest a smaller value.

The tight-binding π bands along the ΓK and ΓM direction are plotted as green and black curves in Figure 5.6 (b). There is reasonable agreement for $E - E_F < -2$ eV and the linearly upward-dispersing branch just below the Fermi level is well described. However, an additional branch of opposite slope that crosses the π band at 1.58 \AA^{-1} (0.12 \AA^{-1} from the K point) appears at photon energies of both 40 eV and 50 eV. No surface states or downward-dispersing bulk bands of Ir(100) are expected at this energy (Lerch 2006). The feature can rather be assigned to an umklapp of the original π band at the zone boundary which arises from the superstructure of graphene/Ir(100). The estimated periodicity of $\pi/0.12 \text{ \AA}^{-1} = 26 \text{ \AA}$ is consistent with the value of 22 \AA found in scanning tunneling microscopy (Ferstl 2011), since the relative error in each of the experiments amounts to 10%. Moiré structures of graphene on other metal surfaces cause similar umklapp effects (Pivetta 2005; Pletikosić 2009; Marchenko 2012; Ulstrup 2012; Katsiev 2012; Sánchez-Barriga 2012a). No minigap opens at the zone boundary within the experimental resolution of 90 meV.

The occurrence of a second Dirac cone of different periodicity is supported by the massive corrugation of the moiré structure observed in STM (Ferstl 2011). In a speculative model, the corrugation could arise from thermal stress, causing a bending of graphene perpendicular to the stripes of the moiré, which would ultimately result in reduced periodicity along the surface.

5.2.4. Image-potential states of graphene/Ir(100)

Angle-resolved two-photon photoemission data of graphene/Ir(100) which were recorded using the display analyzer are shown in Figure 5.7. The first two image-potential states are resolved. The bands seem broadened, and experiments using the hemispherical analyzer with better resolution reveal an asymmetric lineshape, as shown by the energy distribution curves in Figure 5.8 (a). Despite two distinct peaks are not resolved, the EDCs are well described by a sum of two Voigtian functions with an equidistant spacing of 0.14 eV almost independent of k_{\parallel} .

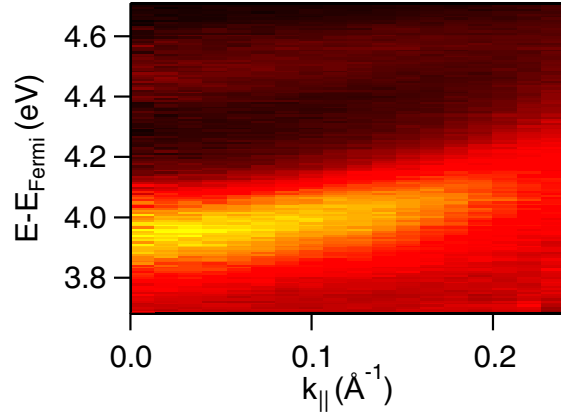


Figure 5.7.: 2PPE intensity map of the image-potential states of graphene/Ir(100).

Furthermore, the work function varies from preparation to preparation between 4.75 eV and 4.92 eV. A reliable position of the vacuum level can not be extracted, and energies of the IPSs are therefore given with reference to the Fermi level. From fits to the data, two $n = 1$ parabolas are found at 4.00 eV and 3.86 eV with effective masses of 0.9 free electron masses as displayed in Figure 5.8 (b).

The appearance of two image-potential states and the varying work functions are indications of the presence of two different surface modifications. Actually scanning tunneling microscopy (STM) images show areas of flat graphene as well as areas with a one-dimensional, stripe-like moiré (Ferstl 2011). The latter have a periodicity of 22 Å and the apparent corrugation is several Ångström. Although the intensity of the resulting superstructure spots in LEED patterns depends strongly on details of the sample preparation, flat and corrugated regions are always found side by side in STM images (Ferstl 2010). Hence, the surfaces under investigation are presumably composed of slightly varying contributions of both modifications. The different work functions observed in the photoemission experiment are an average over the entire illuminated surface of slightly varying composition (Fischer 1993). The image-potential states on the other hand are localized on individual patches and pinned to the referring local work function (Fischer 1993), giving rise to the observed double series. Consistently, the $n = 2$ state exhibits a qualitatively similar line shape as the $n = 1$ state, although a reliable quantitative line shape analysis is complicated by the lower photoemission intensity.

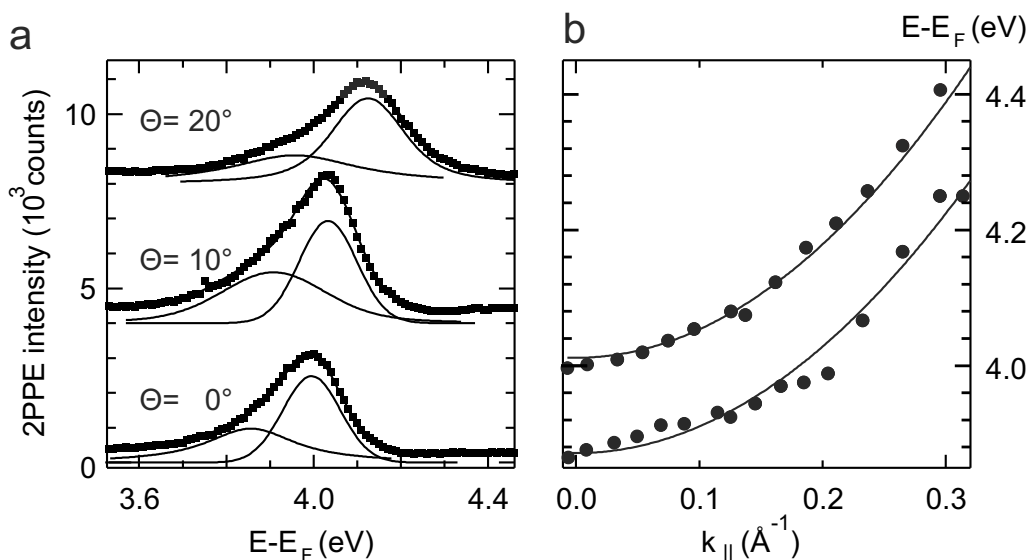


Figure 5.8.: (a) The asymmetric line shape in energy distribution curves of the first image-potential state of graphene/Ir(100) are described by two Voigtian functions of equidistant spacing. The resulting dispersion is shown in (b).

Attempts to prepare the pure phases were not successful. Therefore the determination of the local work functions as well as an assignment of the two members of the double series to one of the phases is not possible. Nevertheless, the absence of clear moiré superstructure spots in the LEED patterns under the applied preparation conditions suggests minor contributions from corrugated areas. Hence the assignment of the dominant high-energy peak to flat graphene is plausible.

5.3. Graphene on various substrates

The doping level of the graphene on different substrates and its influence on the binding energies of image-potential states will be studied systematically in this chapter by a comparison of bichromatic two-photon photoemission data from monolayer graphene grown on different substrates.

The dispersion of the image-potential states of several systems are shown in Figure 5.9. Experiments on (a) graphene/Pt(111) were conducted using the Omicron hemispherical analyzer (Nobis 2013a; Nobis 2012; Nobis 2011), on (b) graphene/Au/Ni(111) with the ellipsoidal display analyzer (Nobis 2013a; Potenz 2012) and (c) 2PPE on MLG/SiC(0001) was performed in the setup at Max-Born-Institut, Berlin (Gugel 2011; Gugel 2011). For experimental details see Section 5.1.3 and corresponding References. In the first two setups pump and probe photon energies of 4.65 eV and 1.55 eV were applied, in the latter they amounted to 4.13 eV and 2.1 eV. The two-dimensional momentum distribution patterns recorded with the display analyzer were averaged along the azimuthal direction.

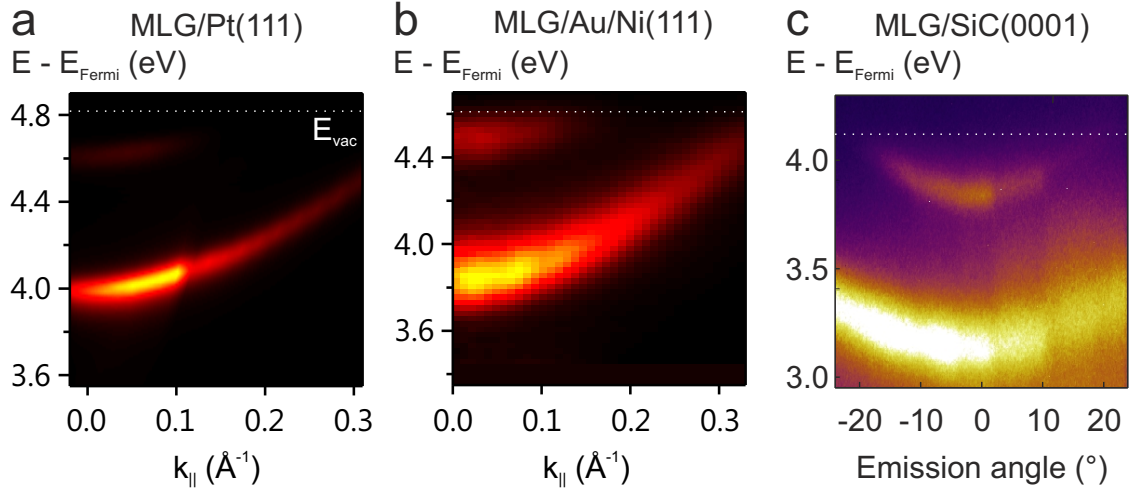


Figure 5.9.: Image-potential states of graphene on (a) Pt(111), (b) Au/Ni(111) and (c) SiC(0001). Data were recorded in different experimental setups.

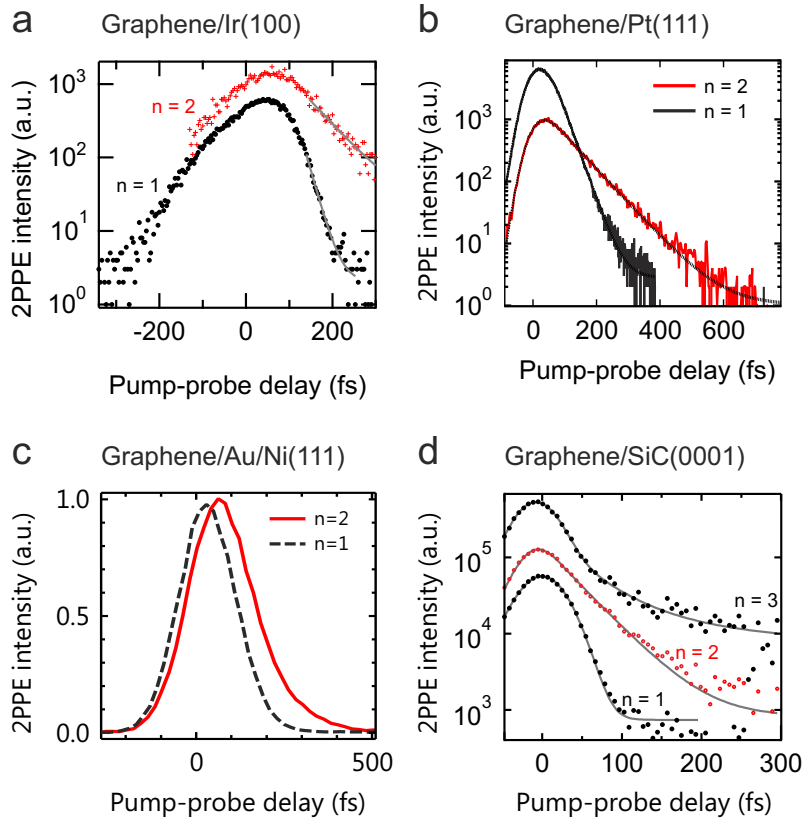


Figure 5.10.: Time-resolved 2PPE spectra of the first two (three) image-potential states of graphene on (a) Ir(100), (b) Pt(111), (c) Au/Ni(111) and (d) SiC(0001). Relative intensities were modified for reasons of clarity. Data are fitted by Equation A.1. The extracted lifetimes are listed in Table 5.2.

Peak positions were determined by fitting a single Voigtian function to each IPS in the energy distribution curves. By this approach, all EDCs are well-described including the ones recorded on graphene/SiC(0001). No low-energy shoulder of the image-potential state like in case of graphene/Ir(100) is observed, see also Figure A.5. The resulting dispersion curves are well described by a single parabolic band. The intensity distribution of the $n = 1$ state of Pt(111) is dominated by a resonance between the IPS and a bulk sp band edge, yet without significant influence on the parabolic dispersion (Nobis 2013a). Binding energies, effective masses and work functions are summarized in Table 5.2.

Time-resolved spectra of the first image-potential states of the systems under investigation are given in Figure 5.10. Spectra from graphene/Ir(100) were recorded with the hemispherical analyzer, for the other materials the same experimental setups were used as for the energy-resolved data. Except for graphene/Ir(100), lifetimes were extracted by fitting Equation A.1 to the data. In case of graphene/Au/Ni(111) and graphene/Ir(100), spectra of the $n = 1$ image-potential state are overlaid by a background resulting from IR-pumped processes. The IR-pumped contributions in the spectrum of graphene/Au/Ni(111) were accounted for by a corresponding component in the fit. The time-resolved spectrum of the $n = 1$ state of graphene/Ni(111) is dominated by the IR-pumped process. Moreover, the pulse shape is not Gaussian as assumed in Equation A.1. Therefore lifetimes were determined by fitting a single-exponential decay to the data at pump-probe delays ≥ 140 fs. The lifetimes obtained from the fits are listed in Table 5.2.

5.3.1. Changes in work function and doping of graphene by the substrate

The work function of the different surfaces is directly obtained from the low-energy cutoff of the photoemission spectra. The measured work functions of graphene on various substrates are displayed in Figure 5.11. As the work function of Au/Ni(111) was not measured and is not available in the literature, the value of Au(111) (Reuß 1996) is assumed. This value may be considered as a good approximation, since the difference between the work functions of Au(111) and Ni(111) is only 0.2 eV. However, gold on Ni(111) grows in a 9×9 superstructure (Jacobsen 1995) which may slightly modify the work function compared to the herringbone-reconstructed clean Au(111) surface (Perdereau 1974; Wöll 1989).

When free-standing graphene is attached to a metal substrate in a gedanken experiment, the work function difference $\Phi_{\text{Substrate}} - \Phi_{\text{graphene}}$ between the two systems drives a charge transfer, which ultimately determines the work function Φ of the combined system. The phenomenological capacitor model described in Section 2.2 relates the charge transfer to work function differences in a classical approach resulting in Equation 2.2 (Giovannetti 2008; Khomyakov 2009). Within the model, the energetic difference between the vacuum level and the Dirac point is the work function of free-standing graphene (Giovannetti 2008).

Table 5.2.: Work function Φ , Dirac point energies E_D and energies E_n of image-potential states relative to the vacuum level E_{vac} and the Dirac point E_D for various graphene-covered surfaces. All energies are given in eV. Lifetimes τ_n in fs and effective masses (in units of the free-electron mass). Values for the substrates are included for comparison.

Surface	Φ	E_1	E_2	E_3	m_1	τ_1	τ_2	τ_3	$E_D - E_F$	$E_1 - E_D$
MLG/SiC(0001) ^a	4.12	0.96	0.27	0.15	0.76	9	45	108	-0.45 (Emtsev 2009)	3.61
0L/SiC(0001) ^c	—	—	—	—	—	—	—	—	—	—
MLG/Ir(111)	4.65	0.83	0.19	0.09	0.9	35	114	270	0.1 (Pletikosić 2009)	3.72
Ir(111)	5.79	—	—	—	—	—	—	—	—	—
MLG/Ir(100) ^e	4.82	4.00	4.54	—	0.85 (0.90) ^f	19	65	—	0.34	3.66
Ir(100)	5.85	(3.86) ^{e,f}	—	—	—	—	—	—	—	—
MLG/Au/Ni(111) ^h	4.56	0.73	0.14	—	1.03	23	75	—	0.1 (Varykhalov 2008)	3.73
Au(111) ^j	5.55	0.8	—	—	1.0 ^k	—	—	—	—	—
Ni(111) ^l	5.35	0.80,	0.25	—	1.12	7	—	—	—	—
MLG/Pt(111) ^m	4.81	0.82	0.21	—	0.8	30	79	—	0.30 (Sutter 2009b)	3.69
Pt(111) (Link 2001a)	5.97	0.65	0.16	—	—	26	62	—	—	—

^aReferences Gugel (2011) and Gugel (2011)

^c0L/SiC(0001) refers to the covalently carbon-rich buffer layer on SiC(0001) (Mattausch 2007; Emtsev 2009). Values from Reference Wiets (2003) and Wiets (2004)

^eAs discussed in Section 5.1.2 and 5.2.4, the work function is an average over two occurring surface modifications. Therefore IPS binding energies are given with respect to the Fermi level instead of the vacuum level.

^fFirst number corresponds to the dominant high-energy component, numbers in parenthesis to the low-energy shoulder (see Section 5.2.4).

^gThe value was determined on the thermodynamically stable (5×1)-reconstructed surface.

^hReferences Nobis (2013a) and Potenz (2012)

^jReference Reuß (1996), recorded on the herringbone-reconstructed Au(111) surface. On bare Au(111) the IPS is degenerate with bulk bands and forms an image-potential resonance rather than a surface state.

^kReference Woodruff (1986)

^lReferences Giesen (1986), Link (2001b), Schuppler (1990) and Passek (1992)

^mReferences Nobis (2013a), Nobis (2012) and Nobis (2011)

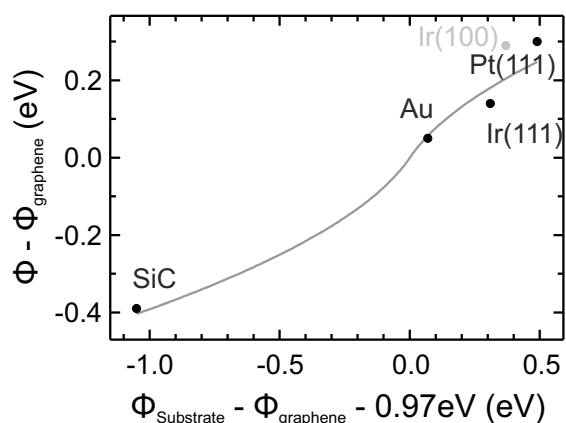


Figure 5.11.: Work function Φ of the graphene-covered surfaces as a function of the work function of the bare substrate Φ_{sub} . The gray line indicates a calculation using the capacitor model (Giovannetti 2008; Khomyakov 2009).

to $\Phi_{\text{Substrate}} - (\Phi_{\text{graphene}} + 0.97\text{eV})$ as a result of hybridization between the graphene π bands and the metal d states (Giovannetti 2008). The value of 0.97 eV is in good agreement with 0.9 eV obtained from density functional theory calculations (Giovannetti 2008; Khomyakov 2009). The capacitor distance $d = 2.5 \pm 0.6 \text{ \AA}$ is significantly shorter than the average graphene-metal distance of $\approx 3.4 \text{ \AA}$ (Busse 2011; Sutter 2009b; Varchon 2007; Filleter 2008; Sławińska 2012), as expected from the localization of the charge between graphene and the substrate (Giovannetti 2008; Khomyakov 2009).

It may seem surprising that graphene/SiC(0001) is described by the capacitor model, as charge accumulation on such a short length scale is usually not possible in semiconductors. However, on SiC(0001) graphene is placed on top of a graphitic buffer layer (Mattausch 2007; Emtsev 2009), which is metallic (Emtsev 2008) and can assimilate enough charge to reduce the band bending at the surface by 1.3 eV (Ristein 2012). The buffer layer can therefore be assumed to serve as the second plate of the capacitor.

5.3.2. Screening of the metal substrate from the external charge of the image-potential state

On metal surfaces, the image-potential states are energetically pinned to the vacuum level, resulting in a binding energy of 0.85 eV of the first image-potential state (Echenique 1978). Matching of the IPS to the bulk bands of a distinct metal results in modifications of the probability density distribution and ultimately in a decrease of this binding energy by a factor $1/(1+a)^2$. Here, a denotes the quantum defect, which varies between zero if the IPS is energetically located at the upper edge of a projected bulk band gap and one half at the lower edge. As a result, binding energies of 0.65 eV (Link 2001a), 0.8 eV (Reuß 1996) and 0.73 eV are observed on Pt(111), Au(111) and Ir(100). Experimental values for Ir(111) and SiC(0001) are not available, but within a scattering model (Fauster 1995) binding

Subtracting the position of the Dirac cones (Bostwick 2007; Varykhalov 2008; Sutter 2009b; Pletikosić 2009) from the work functions of graphene/metal gives the work function of free-standing graphene $\Phi_{\text{graphene}} = \langle E_{\text{vac}} - E_D \rangle = 4.51 \pm 0.05 \text{ eV}$ in agreement with the calculated value of 4.5 eV (Wehling 2008; Giovannetti 2008; Silkin 2009). $\langle \dots \rangle$ denotes the average over the individual systems. Starting from this value, a fit of Equation 2.2 to the data was performed which is depicted by the gray line in Figure 5.11. The work function of graphene/Ir(100) was disregarded because of the experimental uncertainties described in Section 5.2.4. Notably, the driving force of charge transfer is modified

energies of 0.59 eV and 0.65 eV are expected when the work function of the graphene-covered surfaces is included in the calculation. As silicon carbide is distinguished from the metallic surfaces by being a wide band-gap semiconductor (Philipp 1960), an additional decrease of the work function by a factor $\left(\frac{\epsilon-1}{\epsilon+1}\right)^2$ arises from the large screening length in the system (Echenique 1978), where $\epsilon \approx 10$ is the dielectric constant of silicon carbide (Patrick 1970). Within the scattering model, the decrease in work function caused by the graphene adlayer is expected to lead to reduced binding energies also on the other surfaces, as the image-potential states are energetically shifted towards the lower band edge.

Before proceeding to a quantitative discussion of the results, one may consider the influence of the graphene sheet in a classical approach. Doped graphene is metallic with a high carrier mobility of more than $15000 \text{ cm}^2/\text{Vs}$ (Wu 2009; Li 2010), and electronic delocalization is ensured by Klein tunneling (Stander 2009), which inhibits Anderson localization (Anderson 1958). Hence, an electron localized in front of the sheet is expected to be screened efficiently by a charge redistribution within the graphene as sketched in Figure 5.12.

The resulting surface charge density, which is depicted in blue, is similar to the one on the surface of a bulk metal filling the half-space to the left-hand side, since in metals an external charge is also screened on a length scale close to the interatomic distance. The electric fields are the same as described in Section 4.4 for the latter case: While the electric field in the half-space to the right-hand side can be described by the presence of an image charge, the space to the left-hand side becomes field-free. A metal placed on this side will hence not undergo a charge redistribution. The metal is screened from the external charge by the graphene layer.

Binding energies of the $n = 1$ state E_1 , work functions Φ and the position of the respective Dirac points E_D (Bostwick 2007; Pletikosić 2009; Sutter 2009b; Marchenko 2011) are depicted in Figure 5.13. In all investigated systems, the binding energy of the image-potential state with respect to the vacuum level $E_{vac} - E_1$ is increased after deposition of graphene. In contrast, a slight decrease due to the reduced work function is expected within a scattering model that matches the IPS to the bulk bands (Fauster 1995). Except for graphene/SiC(0001), the experimental values for $E_{vac} - E_1$ are close to the average of 0.77 eV, which is indicated by the blue dotted line in Figure 5.13. This finding suggests that the image-potential state is widely decoupled from the bulk band structure of the substrate by the graphene adlayer.

In addition, the average energetic position of the $n = 1$ state with respect to the Dirac point $E_1 - E_D$ is indicated by the red solid line. With respect to this reference level, the first image-potential state of graphene on the metal substrates has a fixed energy of 3.70 ± 0.03 eV. In MLG/SiC(0001), the energy of the $n = 1$ state is slightly lower ($E_1 - E_D = 3.61$ eV). Its constant energy independent of the metal substrate indicates that

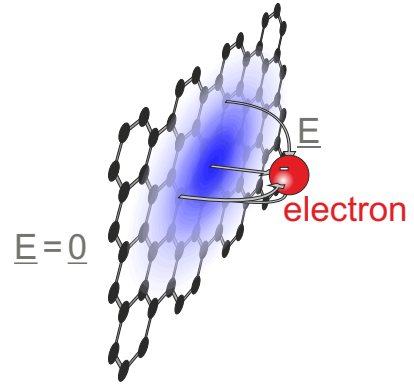


Figure 5.12.: Screening of an external charge by a two-dimensional metallic sheet.

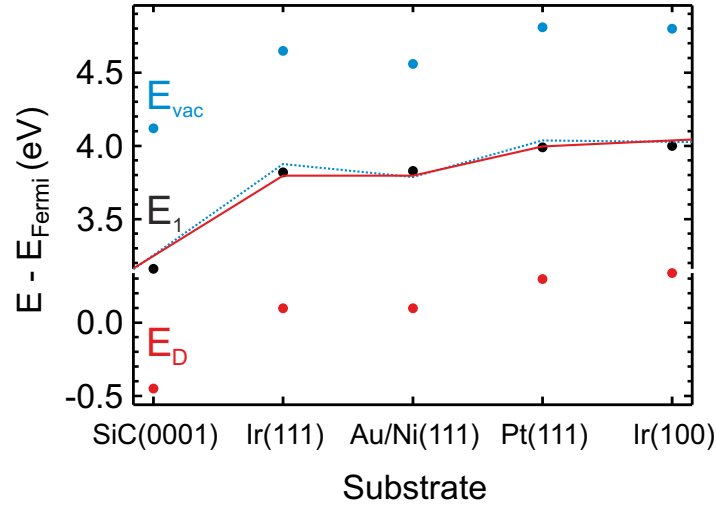


Figure 5.13.: Dirac point energy E_D , binding energy of the first IP state E_1 and work function Φ of graphene on different substrates. Blue and red lines depict an energetic distance $\Phi - E_1 = 0.77$ eV and $E_1 - E_D = 3.70$ eV.

the image-potential state is pinned to the band structure of the graphene layer. The energy difference to E_D of 3.7 eV is between the calculated positions of the symmetric 1^+ and the antisymmetric 1^- state of free-standing graphene (Silkin 2009). In the presence of the metal substrate, the mirror symmetry which gives rise to the double-series of image-potential states of free-standing graphene is broken, and the IPS of graphene/metal is a superposition of the states of both parities. At a graphene/metal spacing of ≈ 3.4 Å only the linear combination which is dominated by contributions of 1^+ keeps a binding energy close to the case of free-standing graphene (Borca 2010). The 1^- state, which is located farther from the graphene sheet, is strongly affected by spatial confinement and exists no longer as a bound state as it is shifted above the vacuum level (Borca 2010). Symmetric and antisymmetric combinations of the 1^+ -derived state are also the origin of the interlayer state and the image-potential state of graphite (Posternak 1983; Lehmann 1999; Silkin 2009), on which the $n = 1$ image-potential state is also located 3.7 eV above the touching point of the π and π^* bands (Fauster 1983; Reihl 1986; Schäfer 1987; Lehmann 1999).

The interpretation of the image-potential states as graphene-induced states is further supported by the measured lifetimes. They are listed in Table 5.2, time-resolved spectra are shown in Figure 5.10. IPS lifetimes of graphene on Pt(111), Au/Ni(111) and Ir(100) are similar ($\tau_2 = 65$ fs...75 fs) despite the different underlying bulk band structures. In graphene/Ir(111), which forms well-ordered domains of more than $1 \mu\text{m}$ size (N'Diaye 2009), even longer lifetimes are observed ($\tau_2 = 114$ fs). These findings are consistent with an efficient screening of the external charge and suggest decoupling of the IPS from the substrate, whereas scattering is enhanced by defects in the graphene layer. Data for the bare substrates are only partly available. As far as there are, e. g. for Pt(111) and Ni(111), lifetimes are increased in the graphene/metal system compared to the ones on the bare metal surface.

A slightly deviating binding energy is found for graphene/SiC(0001), and also the lifetimes of the image-potential states are significantly reduced in this system as compared to graphene on metal substrates. Imperfect screening of an external charge in front of graphene/SiC(0001) was observed in scanning tunneling spectroscopy (Sandin 2010), and attributed to charged-impurity scattering, which is the dominant scattering channel in graphene (Jang 2008; Chen 2008; Chen 2009a). The unique binding energy of graphene/SiC(0001) and the high decay rate of the image-potential states support this interpretation. In contrast, in the presence of metal substrates, charged impurities are screened on a length scale given by the distance between the metal surface and the graphene adlayer (News 1969; Lang 1973; Echenique 1978), which is $\approx 3.4 \text{ \AA}$ (Busse 2011; Sutter 2009b; Varchon 2007; Filletter 2008; Sławińska 2012).

The finding, that the metal substrate is screened efficiently from the external charge by the graphene layer is supported by theoretical considerations. The Thomas-Fermi length λ_{TF} , which is the characteristic screening length of an external Coulomb potential in a Fermi liquid, is given by the density of states of a three-dimensional metal at the Fermi level $D(E_F)$ as $\lambda_{TF}^{-2} = 4\pi e^2 D(E_F)$ and amounts to 0.55 \AA in copper (Kittel 2005). In case of undoped graphene at zero temperature, the vanishing $D(E_F)$ is expected to inhibit screening of external charges, and the $1/r$ dependence of the external Coulomb potential is maintained (Ando 2006; Terekhov 2008; Neto 2009; Kotov 2012). When the Fermi level does not coincide with the Dirac point, however, screening occurs on a length scale $\lambda_{TF}^{-1} = 4\alpha E_F / v_F$ as long as the external charge does not exceed a critical magnitude, which is not the case for a single elementary charge (Terekhov 2008). Here, $\alpha = \frac{e^2}{4\pi\epsilon_0 v_F} = 2.2$ is the "fine structure constant of graphene" and $v_F \approx 6.5 \text{ eV \AA}$ is the Fermi velocity. Doping levels in the range $|E_D - E_F| = 0.45 \dots 0.1 \text{ eV}$ give $\lambda_{TF} = 1.6 \dots 7.4 \text{ \AA}$. Although these values are one order of magnitude larger than in case of copper, they are close to the distance of $\approx 2 \text{ \AA}$ between the maximum of the $n = 1$ wave function and the graphene layer (Silkin 2009). The latter defines the lateral screening length of the external charge in a classical model, which can be reached within the graphene sheet. Calculations (Visscher 1971) and experiments (Sun 2010) on "multilayer graphene" indicate that the charge screening length perpendicular to the surface coincides with the interlayer spacing, and that the external charge is hence mostly screened within the first graphene layer.

5.4. Discussion

2PPE experiments of image-potential states of van-der-Waals bound graphene on Ir(111), Ir(100), Au/Ni, Pt(111) and SiC(0001) indicate efficient screening of the metal substrate from an external charge by a graphene layer. The result is the constant energetic position of the $n = 1$ state 3.7 eV above the Dirac cone, almost independent of the substrate. Slight deviations occur only in case of graphene/SiC(0001), probably as a result of incomplete screening as also observed in STS (Sandin 2010).

As a result of the symmetry breaking by the substrate, a single series of image-potential states is found, differently to the case of free-standing graphene (Silkin 2009). In contrast to 2PPE measurements, STS dI/dV spectra of graphene/SiC show an additional feature energetically close to the $n = 1$ IPS (Bose 2010; Sandin 2010). However, it does not give rise to a clear peak in dI/dZ spectra (Lauffer 2009), as would be expected from the localization of an IPS in front of the surface (Bose 2010). The absence of an energetic splitting due to the corrugation of the graphene layer caused by graphene-substrate interaction as observed on graphene/Ru(0001) (Armbrust 2012) supports the assumption of weak binding. This interpretation is also confirmed by the observed charge transfer between graphene and the substrate. The doping level of graphene is described within a classical capacitor model (Giovannetti 2008), giving a "chemically induced" shift of the work function of $\Delta_c = 0.97$ eV and an effective capacitor distance of 2.5 Å. These values are independent of the individual substrate in agreement with calculations (Khomyakov 2009), giving evidence of the absence of significant covalent bonding. Moreover, the lifetimes of image-potential states are similar in all systems under investigation ($\tau_2 = 65 \dots 75$ fs), but significantly reduced in graphene/SiC(0001), resembling the imperfect screening in this system. Furthermore, the underlying buffer layer is known to exhibit a higher surface roughness compared to the other substrates (Lauffer 2008).

Particular attention was paid to graphene on Ir(111) and Ir(100). Growth on the former substrate leads to the formation of large and well-ordered graphene domains of macroscopic size (Gastel 2009) and TPG be used to cover the surface with nanometer-sized graphene islands (Coraux 2009; N'Diaye 2009). From the coverage-dependence of the work function and the $n = 1$ binding energy, localization of the IPS on the islands was demonstrated. Probably as a result of high crystalline quality, lifetimes of IPSs are enhanced compared to the other systems under investigation. Thus the lifetimes of image-potential states seem rather affected by the quality of graphene than by the band structure of the underlying substrate. In addition to the $n = 1$ state, an additional flat band is observed at similar energy. Its origin is not fully clarified and subject of recent research (Nobis 2013b).

In contrast, few studies deal with the growth of graphene on the square Ir(100) surface. Two distinct structures occur in LEED and STM experiments. One of them is characterized by a strong corrugation of the graphene adlayer (Ferstl 2011; Ferstl 2010). In 2PPE, preparation-dependent variations in the work function and two series of IPSs were found, supporting the presence of two different surface modifications. ARPES measurements show the characteristic π -band structure of graphene. The dispersion is linear in the proximity of the Fermi level, the Dirac point is not observed due to p-type doping. An additional linearly dispersive feature is observed in the proximity of the Fermi level, which is attributed to umklapp processes in the periodic potential of the superstructure.

6. Unoccupied surface states of topological insulators

As described in Section 3, topological insulators form a new quantum state of matter: While they are bulk insulators, they exhibit a metallic, spin-polarized surface state forming a Dirac cone (Kane 2005; Fu 2007a). Two-photon photoemission (2PPE) may prove to be the ideal tool to study the dynamics of charge and spin carriers in this characteristic state. Like angle-resolved photoelectron spectroscopy (ARPES), 2PPE provides access to the dispersion of surface states. The low photon energies which are typically used result in a good momentum resolution even if the experimental setup provides only moderate angular resolution. In addition, through the pump-and-probe scheme described in Section 4.3, 2PPE allows to detect electrons in excited states and to follow their dynamics in the time domain.

Most topological insulators available at present are intrinsically electron-doped (Zhang 2009a). This fact allows detailed studies on their equilibrium electronic structure using ARPES. However, only hole excitations, but no electron excitations are possible in the proximity of the Dirac point. For investigations on the dynamics of the spin-polarized Dirac electrons it is essential to have systems exhibiting no or p-type doping. Scattering rates extracted from such experiments and insight into the underlying mechanisms may also be of interest for future applications.

In this chapter, two complementary routes giving access to unoccupied topological surface states will be presented. After commenting on specific experimental details in Section 6.1, bismuth chalcogenides will be the topic of Section 6.2. In these systems, a second Dirac cone is found approximately 1.4 eV above the Fermi level in addition to the occupied conventional one. The topological character of this state is clarified by circular dichroism and comparison to density functional theory calculations. Second, in Section 6.3 experiments on a p-type topological insulator, SnSb_2Te_4 , will be presented. Thus, time-resolved experiments on the dynamics of electrons in the topological surface states become possible and first results will be presented.

6.1. Experimental details

6.1.1. Sample preparation

As described in Section 3.2, the topological insulators under investigation have a layered atomic structure which is made up of covalently-bound quintuple or septuple layers which are separated by a van-der-Waals gap. This allows simple preparation of well-defined clean surfaces by cleaving.

The single steps of the cleaving process are illustrated in Figure 6.1. Usually the material was received as a part of a cylinder as shown in Figure 6.1 (a) with a diameter of ≈ 1 cm and a length of several centimeters. This shape is the result of growth in an ampoule in a modified Bridgman-method, see e. g. References Kokh (2005), Bekker (2005) and Bianchi (2010). The c -axis is aligned perpendicular to the cylinder axis. The surface with a minimum density of macroscopic steps, which is usually oriented normal to the c -axis, has to be identified. Using a scalpel, the face side of the cylinder is then slightly penetrated parallel to this surface and single slices of ≈ 1 mm thickness as shown in Figure 6.1 (b) are broken off. These slices are cut into pieces with lateral dimensions of $\approx 6 \times 6$ mm². The resulting samples are fixed on a copper baseplate using conductive epoxy glue (Epo-Tek E4110) and mounted on a sample holder as illustrated in Figure 6.1 (c). The baseplate allows for *ex-situ* azimuthal alignment after the initial orientation has been determined using low-energy electron diffraction (LEED). This kind of orientation is necessary for circular dichroism measurements in the display analyzer setup as discussed in Section 6.2.1. In the second photoemission setup, azimuthal alignment is possible *in situ*.

The ultimate cleaving step is conducted under vacuum conditions using adhesive tape. Therefore the sample holder is mounted onto the cleaving mechanism shown in Figure 6.1 (e) containing a linear motion drive. Adhesive tape (Tesafilm 57329) is fixed to the sample surface and a stationary part of the cleaving mechanism as shown in Figure 6.1 (d). After installation to the load lock of the ultrahigh vacuum (UHV) chamber it is evacuated to a pressure below 10^{-5} Pa in case of the display-analyzer setup and 10^{-6} Pa in case of the hemispherical analyzer setup. These numbers were estimated from the rise of the base pressure in the UHV chamber when opening the load lock. Finally the sample is cleaved by retracting the linear shift and drawing off the adhesive tape with the topmost layers of the topological insulator material sticking to it. Transfer to UHV (base pressure below 10^{-8} Pa) where the sample is cooled to 90 K for measurements takes place within less than one minute.

Within the scope of this work, Bi₂Se₃ crystals from three different collaborating groups were obtained. In Figure 6.2 LEED patterns recorded on different samples are presented. All samples (Group of Prof. Dr. Philip Hofmann, Aarhus, Denmark, not shown; Prof. Dr. Oleg E. Tereshchenko, Novosibirsk, Russia, Figure 6.2 (a); Prof. Dr. Nazim Mamedov, Baku, Azerbaijan, Figure 6.2 (b)) delivered almost identical photoemission results, apart from slightly different levels of doping. As cleaving of the samples from Novosibirsk usually resulted in the most homogeneous macroscopic surfaces, most experiments were carried out on them and the presented data were measured on these samples.

In addition, LEED patterns of Bi₂Te₃, Bi₂Te₂Se and Sb₂SnTe₄ are shown in Figure 6.2 (c-e). All materials exhibit a single-crystalline structure with a hexagonal surface mesh of threefold symmetry. The $\overline{M} \overline{\Gamma} \overline{M}'$ mirror plane can immediately be identified from the LEED patterns.

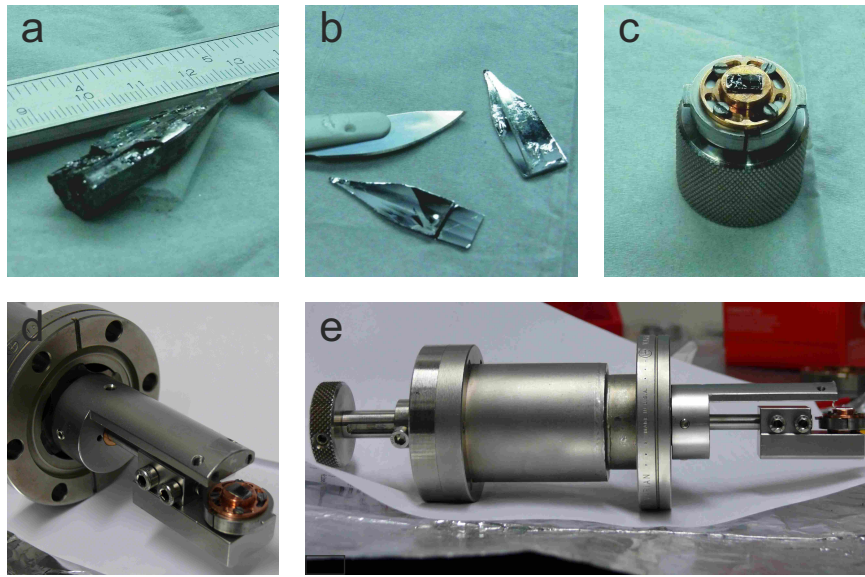


Figure 6.1.: Different stages of sample preparation. (a) The as-grown crystal exhibits a slate-like structure that allows to break off slices as shown in (b). After segmenting into smaller pieces and gluing to a rotatable copper-baseplate (c), samples are cleaved under vacuum conditions after attaching adhesive tape (d) using the cleaving mechanism shown in (e).

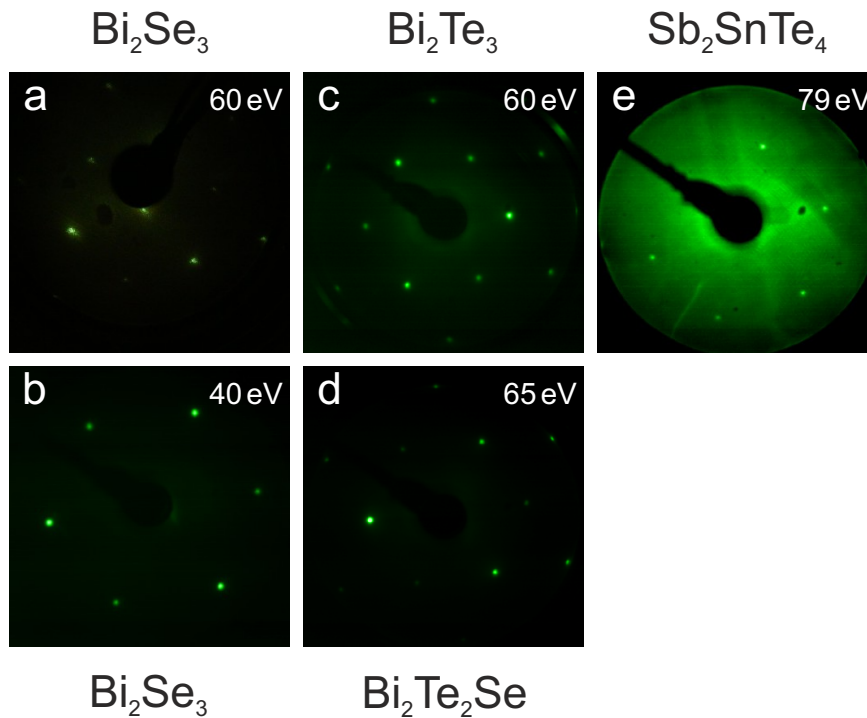


Figure 6.2.: (a, b) LEED diffraction patterns from different specimens of Bi_2Se_3 (see text). (c, d) Diffraction patterns of the additional bismuth chalcogenide crystals under investigation. (e) Sb_2SnTe_4 , a ternary p-type topological insulator.

6.1.2. Details of photoemission experiments

Experiments on all systems under investigation were carried out in both experimental setups introduced in Section 4.5 resulting in consistent photoemission data.

The display-type analyzer allows to monitor the dispersion of surface states through the complete accessible range of the Brillouin zone quickly and without any changes in the geometry of the setup. It was used to check the occupied part of the band structure of bismuth chalcogenides for the conventional Dirac cone close to the Fermi level. If necessary, surfaces were scanned for regions consisting of a single crystal domain giving rise to a single Dirac cone in ARPES. Due to the large acceptance cone, tilts in sample mounting can be determined after identifying the direction of normal emission in the two-dimensional momentum distribution patterns. The respective tilts were accounted for during data evaluation. Moreover, two-dimensional circular dichroism patterns were recorded containing the crucial direction of parallel momenta of photoelectrons perpendicular to the plane of incidence of the laser beam. Apart from rotating the polarization of the laser light, no changes in the setup have to be performed during these experiments, i. e. the angle of incidence of the the laser beam and the illuminated sample area do not change.

High-resolution measurements were conducted using the hemispherical-analyzer setup. Besides the improved angle and energy resolution, the associated laser system is equipped with thinner optical crystals and additional prism compressors resulting in a shorter cross correlation trace of 70 fs as compared to the display-analyzer setup (≈ 200 fs) improving also the temporal resolution. On the other hand, care has to be taken of sample alignment due to the narrow entrance slit (1.2°) of the analyzer. For angle-resolved measurements covering a wide range of the surface Brillouin zone, the wanted high-symmetry direction was oriented parallel to the plane of measurements according to LEED diffraction patterns. For close-ups of the cone-shaped surface state, samples were rotated stepwise along the azimuthal direction and ARPES data were recorded thus ensuring that the $\bar{\Gamma}$ high symmetry point is included in the measurements. 2PPE experiments were subsequently performed in the identical experimental geometry.

Monochromatic photoemission experiments were performed on bismuth chalcogenides. Photon energies were 4.65 eV with a respective wavelength of 267 nm in 2PPE and 6.2 eV (200 nm) during ARPES measurements. On p-type topological insulators bichromatic 2PPE was conducted at photon energies of 1.63 eV and 4.89 eV. All beams were *p*-polarized if not stated otherwise. Circular polarization was achieved by inserting a $\frac{\lambda}{4}$ -waveplate into the path of the UV-beam.

6.1.3. Sample characterization by angle-resolved photoemission

6.1.4. Sample degradation after cleaving

Bismuth chalcogenides are known to exhibit intrinsic n-type doping (Xia 2009; Chen 2009b). Indeed, the amount of doping in the surface region may increase after exposure to air or, in some cases, to residual gas under UHV conditions. The effect is most pronounced

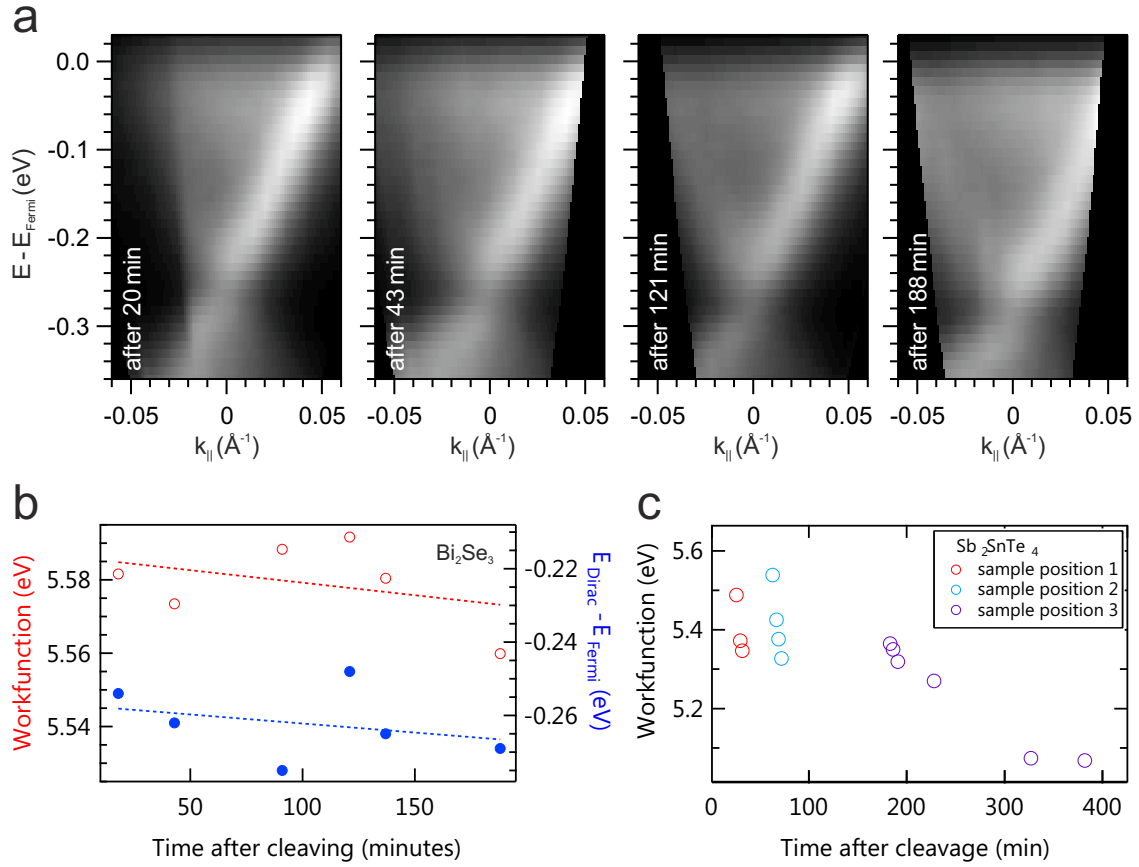


Figure 6.3.: (a) Evolution of the Dirac cone of Bi_2Se_3 after cleaving. Differences in the photoemission spectra are within the statistical variations between various areas of the sample as shown in (b). (c) Changes in the work function of p-type samples after cleavage. Photoemission experiments were usually performed after saturation of these initial effects.

and was studied in detail on Bi_2Se_3 (Bianchi 2010; Analytis 2010a). Initial doping was attributed to Se vacancies (Horák 1990). Water was shown to dissociate at the selenium-terminated surface, forming hydrogen diselenide gas which leads to an increase in the density of selenium vacancies (Benia 2011). Formation of bismuth oxide was suggested as another source of surface degradation (Kong 2011).

In order to monitor these effects, the evolution of the occupied Dirac cone of Bi_2Se_3 during several hours after cleavage is shown in Figure 6.3 (a), resembling the typical time interval for two-photon photoemission experiments. Note, that the sample azimuth was varied between the experiments. This may change photoemission intensities, and the $\bar{\Gamma}$ point is not necessarily included in the measurements. Irrespective of this, work function and position of the Dirac point do not change during the three hours of measurements as demonstrated in Figure 6.3 (b). Small variations are within statistical errors and can be attributed to slightly inhomogeneous doping of the sample. At most, a shift of the Fermi level and a decrease of work function by ≤ 10 meV takes place as estimated by linear fits to their temporal evolution.

This situation is qualitatively the same in case of Bi_2Te_3 and $\text{Bi}_2\text{Te}_2\text{Se}$. No detectable changes in the photoemission spectra from these tellurium-terminated surfaces were observed during several hours of measurements. Only after one day under UHV conditions, the work function decreased by ≤ 100 meV and a downshift of the surface state by ≤ 20 meV was found (Hermann 2012). In conclusion, 2PPE experiments were performed on stable bismuth chalcogenide surfaces.

However, the surfaces of the studied p-type topological insulators based on antimony and tellurium constituents are not as stable. Figure 6.3 (c) demonstrates the evolution of the work function after preparation. Within a few hours, it decreases by at least 0.5 eV. Corresponding changes in the p-doping of the surface states can hardly be tracked because of the longer measuring time of 2PPE compared to conventional ARPES. Notably, the laser beam tends to accelerate or even causes the changes in case of Sb_2SnTe_4 as can be deduced from Figure 6.3 (c): Focusing to positions of the sample that had not been illuminated before leads to an increase of the observed work function, which is quickly settled after irradiation. In order to ensure stable conditions during 2PPE measurements, they were conducted after saturation of the initial changes. This occurs within a few hours after cleavage, while the exact time constants depend on the experimental setup utilized and variations from cleave to cleave.

6.1.5. n-type doping of Bismuth Chalcogenides

Figure 6.4 shows ARPES data from $\text{Bi}_2\text{Te}_2\text{Se}$ (a), Bi_2Se_3 (b) and Bi_2Te_3 (c) together with results of density functional theory (DFT) calculations (d-f) on these systems (Niesner 2012b). Details of the calculations can be found in Reference Niesner (2012b). In the proximity of the Fermi level, the experimental band structures reveal two linearly dispersing branches with a crossing point at the $\bar{\Gamma}$ point. As displayed in Figure 6.4 (g), two-dimensional momentum distribution patterns (MDCs) show an isotropic dispersion with slight hexagonal warping several hundred meV above the crossing point. These findings are in agreement with the literature (Chen 2009b; Hsieh 2009a; Ren 2010; Miyamoto 2012; Neupane 2012) and the present calculations, thus indicating that the samples exhibit the topological surface state giving rise to the observed linearly dispersive feature.

The energetic positions of the Dirac points in experiment and calculation differ especially in case of Bi_2Se_3 because of intrinsic n-type doping by defects (Bianchi 2010), see also Section 6.1.4. Distinct levels of doping are found for the different Bi_2Se_3 crystals, namely the Dirac point is found at $E_{occ} = -0.39$ eV (-0.29 eV) on sample c (d) referring to the labeling in Figure 6.2 in Section 6.1.1. In case of $\text{Bi}_2\text{Te}_2\text{Se}$ an inhomogeneous level of doping within the same macroscopic crystal was found with E_{occ} varying from cleave to cleave between -0.1 eV to -0.4 eV in agreement with Reference Neupane (2012). The position of the Dirac point of Bi_2Te_3 at -0.13 eV is highly reproducible and in good agreement with the calculations.

In order to account for varying doping levels, ARPES was always used after sample preparation to determine E_{occ} individually prior to two-photon photoemission experiments.

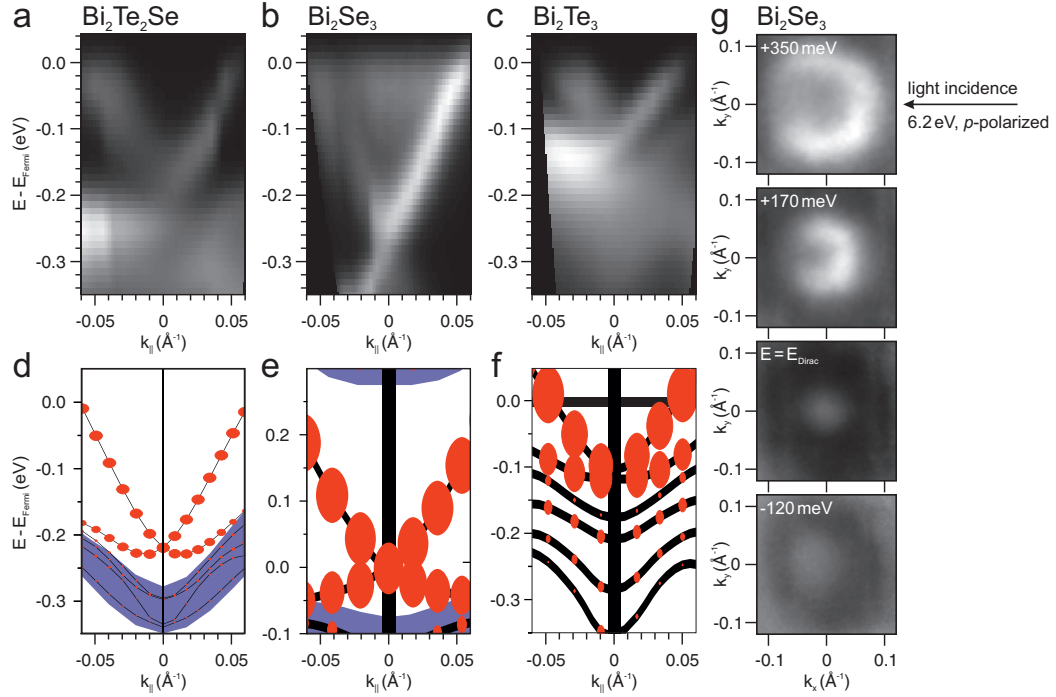


Figure 6.4.: ARPES data recorded at 6.2 eV photon energy on the conventional, occupied Dirac cone of the bismuth chalcogenides under investigation (**a-c**) and comparison to the calculated band structure (**d-f**) (Niesner 2012b; Chulkov 2012). While the surface band structure of Bi_2Te_3 and $\text{Bi}_2\text{Te}_2\text{Se}$ are well reproduced by calculations, additional band bending occurs on the surface of Bi_2Se_3 (Bianchi 2010). (**g**) demonstrates the evolution of the Dirac cone of Bi_2Se_3 with energy.

The discrepancy between experiment and theory due to doping can be accounted for by a rigid shift of the calculated band structure in order to match the positions of the Dirac points. In the given figures, the original energetics of the calculation are reflected.

6.2. Higher-lying topological surface states of bismuth chalcogenides

6.2.1. Identification by spectroscopic methods

Figure 6.5 (a) illustrates the result of monochromatic two-photon photoemission experiments on $\text{Bi}_2\text{Te}_2\text{Se}$ covering a wide range of energy and parallel momentum. For comparison, the related parts of the unoccupied and occupied part of the calculated band structure (Niesner 2012b) are given in Figure 6.5 (b) and (c). Therein purple-shaded regions represent bulk bands, whereas red dots mark electronic states with an increased localization in the topmost atomic quintuple layer. Energies of the initial states in Figure 6.5 (c) were shifted by the pump photon energy (4.65 eV) in order to match the energy scales of (a) and (b).

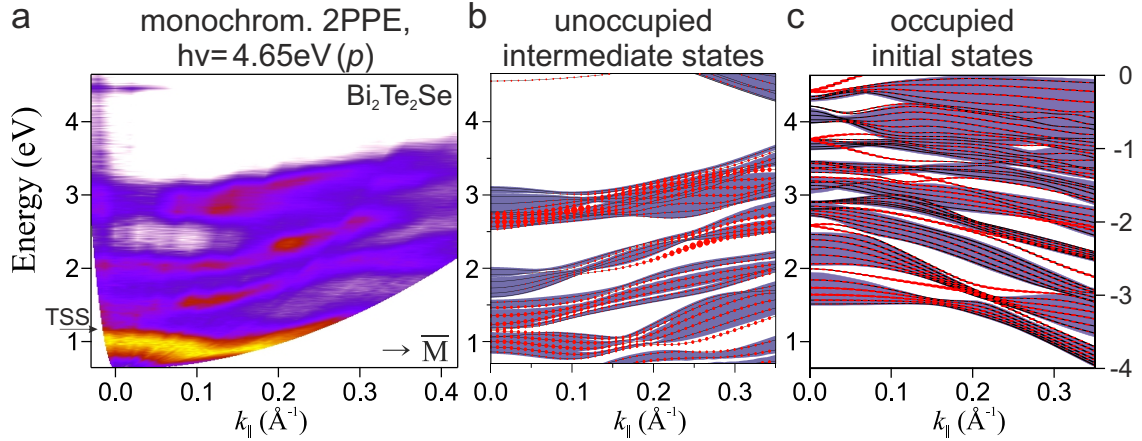


Figure 6.5.: (a) Monochromatic 2PPE survey spectrum of the unoccupied part of the band structure of $\text{Bi}_2\text{Te}_2\text{Se}$ recorded at 4.65 eV photon energy. Four conduction bands as well as an image-potential state (IPS) or IPS-derived interlayer state are found in agreement with the calculations in (b) (Niesner 2012b). The position of the unoccupied topological surface state is indicated by the arrow labeled "TSS". Comparison to the occupied part of the band structure (c) demonstrates that the dispersion of the initial states does not significantly influence the 2PPE spectra. The energy scale to the left-hand side of (c) was shifted by the pump photon energy in order to match the energy scale of the experiment.

All features observed in experiment can be attributed to corresponding unoccupied bands in the calculation. The predominantly downward dispersing initial states are not observed in the spectra. Hence, 2PPE probes intermediate states in the unoccupied part of the band structure rather than initial states below the Fermi level. Notably, surface states and resonances in the calculation coincide widely with regions of enhanced intensity in the measured data. This fact may be considered as an indication of high surface sensitivity in the 2PPE experiment as was also found in earlier experiments (Wallauer 1995; Knoesel 1995). The agreement between the angle-resolved 2PPE data and the calculated band structure is of similar agreement for the other topological insulators under investigation, see Figures A.6 and A.7.

In the following, the discussion will focus on the energetic region $\approx 1...2$ eV above E_F in the close proximity of the $\bar{\Gamma}$ point. Attention is drawn to the state marked by the arrow labeled "TSS" in Figure 6.5 (a). It will be found to be an empty topological surface state residing in a local bulk band gap. In Figure 6.6 (b) high-resolution data of the corresponding part of the Brillouin zone are shown. From the calculated band structure in Figure 6.6 (a) a bulk band gap is expected at the $\bar{\Gamma}$ point at $E - E_F = 1.55$ eV with a total size of ≥ 100 meV. In experiment, no indication of a band gap is observed within the best available experimental resolution of 23 meV. Instead, the 2PPE spectra can be explained taking into account the surface electronic structure as obtained from slab calculations. It reveals a linearly dispersing surface state forming a Dirac cone around the center of the Brillouin zone. As observed in experiment, this surface state bridges the bulk band gap and evolves into a surface resonance as it approaches bulk conduction bands at higher and lower energies.

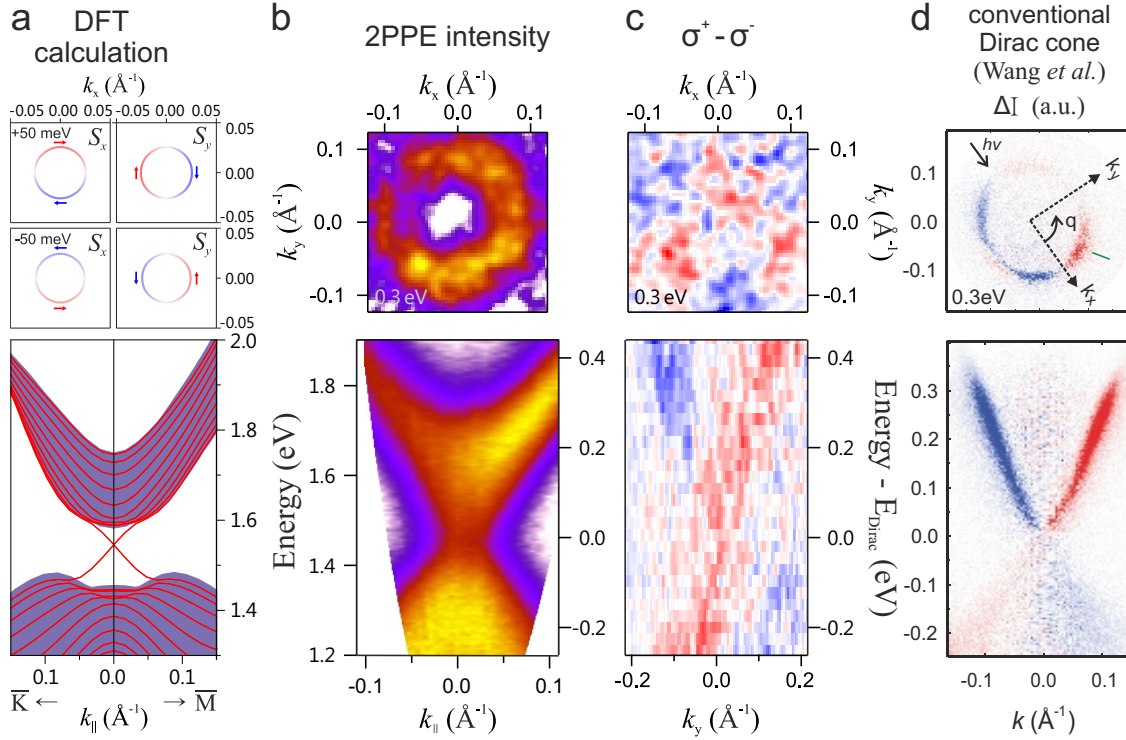


Figure 6.6.: Comparison between monochromatic 2PPE data of Bi₂Se₃ (b) and calculations (a) (Niesner 2012b) demonstrates that the bulk band gap ≈ 1.5 eV above the Fermi level is bridged by a surface state. The circular dichroism pattern (c) exhibits a crossing point at the Dirac point as expected for a topological surface state and as also found in the calculation, see upper panel of (a). As can be seen in the upper panel of (c), the circular dichroism pattern evolves into a trigonal shape at higher energies. A similar dichroism pattern results from the conventional, occupied Dirac cone (d) (Wang 2011a).

Besides this linear dispersion, a fingerprint of a TSS is the lifting of spin degeneracy which leads to a helical spin structure with an inversion of the spin orientation at the Dirac point as pointed out in Section 3. This characteristic is found in calculations as sketched in the upper panel of Figure 6.6 (a). Experimental evidence is achieved by measuring circular dichroism using circularly polarized light as described in Section 4.2. Therefore photoelectron momentum distributions patterns (MDCs) resolving both components of the two-dimensional parallel momentum were measured with both left- (σ^-) and right-handed (σ^+) polarization of the laser beam. The sample was aligned with its $\bar{\Gamma}\bar{M}$ mirror plane parallel to the plane of light incidence which also forms a mirror plane of the electron-analyzer setup. In Figure 6.6 (c) the difference $\sigma^+ - \sigma^-$ between the resulting MDCs is shown. Because of symmetry reasons, the mirror plane ($k_y=0$ in the figure) causes a zero line as displayed in the upper panel which shows a difference MDC at an energy far (0.3 eV) above the Dirac point. In contrast, the selective excitation of electrons of different in-plane spin component is observed in the direction perpendicular to the mirror plane.

The lower panel of Figure 6.6 (c) shows a cut through the data set along the direction perpendicular to the mirror plane ($k_x=0$). Two bands of opposite slope are observed which give opposing contributions to circular dichroism. The intensities of the two branches are slightly asymmetric possibly because of asymmetries in the experimental setup, e. g. a tilt of the sample or elliptical polarization of the laser beam after passing through the quartz glass window of the UHV chamber. The maximum observed normalized dichroism amounts to $(\sigma^+ - \sigma^-)/(\sigma^+ + \sigma^-) = \pm 12\%$, which is smaller than the values of 30...40% observed in ARPES on Bi_2Se_3 (Park 2012b) and $\text{Bi}_2\text{Te}_2\text{Se}$ (Jung 2011; Scholz 2011). As both the pump and probe pulses in monochromatic 2PPE are circularly polarized, both excitation steps underly circular dichroism effects. Since amplitude and sign of the measured signals depend on the excitation energy (Sánchez-Barriga 2012b), the combination of the two transitions can cause a decreased intensity due to contrarian contributions. In fact, in bichromatic 2PPE with only one circularly polarized beam, significantly stronger circular dichroism is observed when exciting electrons from the occupied Dirac cone to an image-potential state as illustrated in Section 6.2.2. To date, only few experimental studies on circular dichroism in 2PPE exist which are limited to ferromagnetic systems (Hild 2009; Nakagawa 2009; Chiang 2009). A comprehensive theoretical description of the phenomenon is not available. Nevertheless, the intensity distribution observed in the present experiment is consistent with that of a topological surface state, with its spin-momentum locking leading to a helical orbital-angular momentum (Park 2012b). In contrast, the initial states at a pump photon energy of 4.65 eV are located in a continuum of spin-degenerate bulk states far from the Fermi level as illustrated in Figure 6.5 (b), and are therefore not expected to give rise to circular dichroism.

In the upper panel of Figure 6.6 (c) a MDC shows the circular dichroism pattern at an energy 0.3 eV above the Fermi level. As the surface state approaches the bulk bands and turns into a surface resonance, the pattern develops from a twofold into a threefold shape resembling the symmetry of the bulk states.

This behavior is expected for a TSS. It is in agreement with the calculations and qualitatively similar to the results of laser-ARPES experiments performed on the conventional occupied Dirac cone close to the Fermi (Wang 2011a) level as illustrated in Figure 6.6 (d). Therefore it can be concluded that the observed feature actually originates from an unoccupied topological surface state.

After establishing the existence of a high-lying TSS on Bi_2Se_3 , the discussion will move on to other bismuth chalcogenides, namely $\text{Bi}_2\text{Te}_2\text{Se}$ and Bi_2Te_3 . Figure 6.7 (a, b) show angle-resolved 2PPE data of the projected bulk band gaps under investigation together with the respective calculated band structures (c, d) (Niesner 2012b). The calculated band gaps of ≤ 80 meV are considerably smaller than in case of Bi_2Se_3 . Nevertheless, the experiment is expected to be able to resolve this band gap if present. Instead, a linearly dispersive surface state is found on $\text{Bi}_2\text{Te}_2\text{Se}$. In calculations (Chulkov 2012), this state exhibits the characteristic helical spin structure of a TSS and circular dichroism gives results similar to the ones from Bi_2Se_3 as shown in Figure A.8. Consequently it is attributed to the same topological origin.

The situation is less clear in case of Bi_2Te_3 . In the 2PPE spectra, a small band gap appears to be present. The presence of the surface state in theory depends strongly on the details of the calculations including the exact lattice constant (Niesner 2012b). Different density functional theory approaches were applied and the results are summarized in Table 6.1. Based on these findings, the existence of the TSS on Bi_2Te_3 may be sensitive to the details of sample growth and preparation. Although no clear evidence for its appearance is found in the present data, it cannot be excluded that the TSS may be observed on crystals of different parameters of growth or within the first minutes after preparation of a clean surface.

In Table 6.1 the energetic positions of the unoccupied topological surface states are summarized together with the work functions and the position of the occupied Dirac cone. Doping levels of Bi_2Se_3 may vary by up to 0.1 eV as discussed in Section 6.1.5. Apart from this, all experimentally found values are in agreement with the calculations (Niesner 2012b). The possibility to perform time-resolved monochromatic two-photon photoemission on the dynamics of the new-found TSS is not implemented in the experimental setup yet. Instead, bichromatic 2PPE was applied to tackle this issue and results will be discussed in the following section.

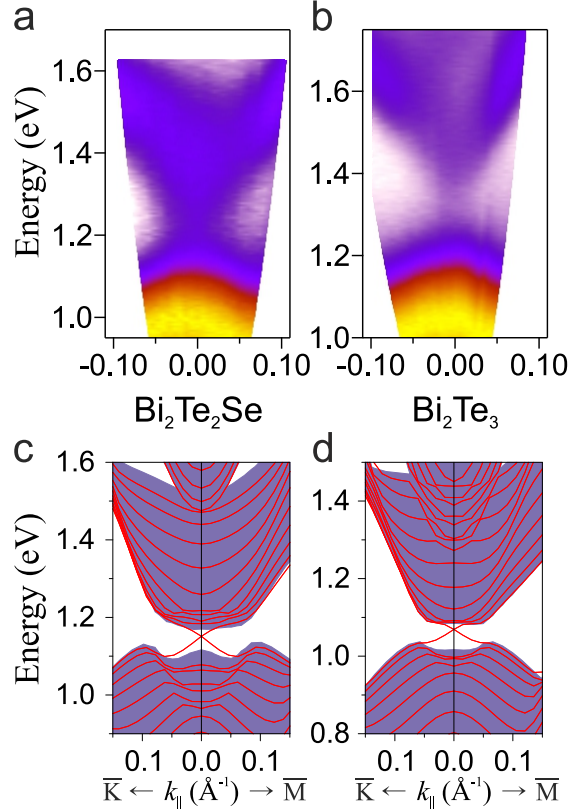


Figure 6.7.: While the comparison between the 2PPE experiment (a) and theory (c) (Niesner 2012b) demonstrates the presence of the unoccupied topological surface state of $\text{Bi}_2\text{Te}_2\text{Se}$, the calculated surface band structure (d) (Niesner 2012b) of Bi_2Te_3 is sensitive to details of the calculations. The experiment (b) does not clearly resolve a linearly dispersing feature in the latter case.

Table 6.1.: Work function Φ and energies of Dirac points with respect to the Fermi energy (in eV). Group velocity v_{unocc} of the unoccupied Dirac cone in eV \AA .

	Φ		E_{occ}		exp.	E_{unocc}			v_{unocc} exp.
	exp.	calc.	exp.	calc.		VASP (PBE)	VASP (vdW-DF)	FLEUR	
Bi_2Se_3	5.61	5.42	-0.30	0	1.46	1.52	1.56	1.55	2.5 ± 0.3
$\text{Bi}_2\text{Te}_2\text{Se}$	5.23	4.92	-0.25	-0.22	1.21	1.15	1.18	1.15	3.4 ± 0.5
Bi_2Te_3	5.33	4.87	-0.13	-0.15	(1.28)	-	1.03	1.07	-

6.2.2. Dynamics of the unoccupied surface states of $\text{Bi}_2\text{Te}_2\text{Se}$

In order to gain access to the dynamics of the unoccupied surface states, time-resolved bichromatic 2PPE was conducted at photon energies of 1.55 eV and 4.65 eV. In this experiment, the two introduced laser pulses can each act both as a pump or as a probe, and signals resulting from the different possible processes are included in the data.

Comparison to monochromatic 2PPE and knowledge of the symmetry of the involved states can serve to identify the underlying processes as described in Section 4.3. Therefore energy distribution curves (EDCs) from $\text{Bi}_2\text{Te}_2\text{Se}$ were recorded with p and s linearly polarized laser beams. The plane of incidence of the laser beam was matched to the $\overline{M}\overline{\Gamma}\overline{M}'$ mirror plane of the sample and EDCs were measured close to normal emission at a polar angle of $\approx 3^\circ$.

As shown in Figure 6.8 (a), four peaks are observed in monochromatic 2PPE at final-state energies between 5 eV and 8 eV. They can be attributed to the four bulk conduction bands in this energy region as illustrated earlier in Figure 6.5. This interpretation is supported by their appearance being independent of polarization, which indicates that bulk states of both even and odd symmetry under mirror operation contribute to these features. In contrast, the less intense peak at 9.04 eV is present only at p -polarization. Assuming mirror-symmetric free-electron like final states, it originates from a surface state of even symmetry. Together with its energetic position 0.84 eV below the vacuum level and its effective mass of $0.86 m_0$, this is consistent with the interpretation as an image-potential state (IPS).

In bichromatic 2PPE, three main features are found as illustrated in Figure 6.8 (b). From comparison to the monochromatic data, the peaks at final-state energies of 5.55 eV and 6.16 eV can immediately be related to bulk conduction bands which are populated by the IR pulse. Consequently, they are present at arbitrary polarization of the laser beams. The higher-lying conduction band at 6.16 eV appears more intense when the UV probe pulse is p -polarized, indicating the presence of a surface resonance at this energy in agreement with the calculations in Figure 6.5 (b).

Located energetically between the two bulk states, an additional feature is found in bichromatic 2PPE. A fit to the data by Voigtian functions reveals that it consists of two components which are not clearly separated in the EDCs. The two states also exhibit a distinct polarization dependence: The low-energy component at 5.93 eV is observed only when the IR beam is p -polarized, as expected for an UV-pumped intermediate state of even symmetry. The difference in final-state energy to the IPS at 9.04 eV in the monochromatic 2PPE spectra in Figure 6.8 (a) coincides closely with the difference in probe photon energies of 3.1 eV. In conclusion, both features have the same origin.

The high-energy component at 5.99 eV behaves in a different way: While the UV pulse is p -polarized, it occurs independent of the IR polarization and vanishes when both beams are s -polarized. As it coincides in final-state energy with the unoccupied topological surface state discussed in Section 6.2, the feature is attributed to this state. This interpretation is in agreement with the polarization dependence discussed so far when assuming even symmetry of the TSS. However, in this case the resulting photoemission intensity is

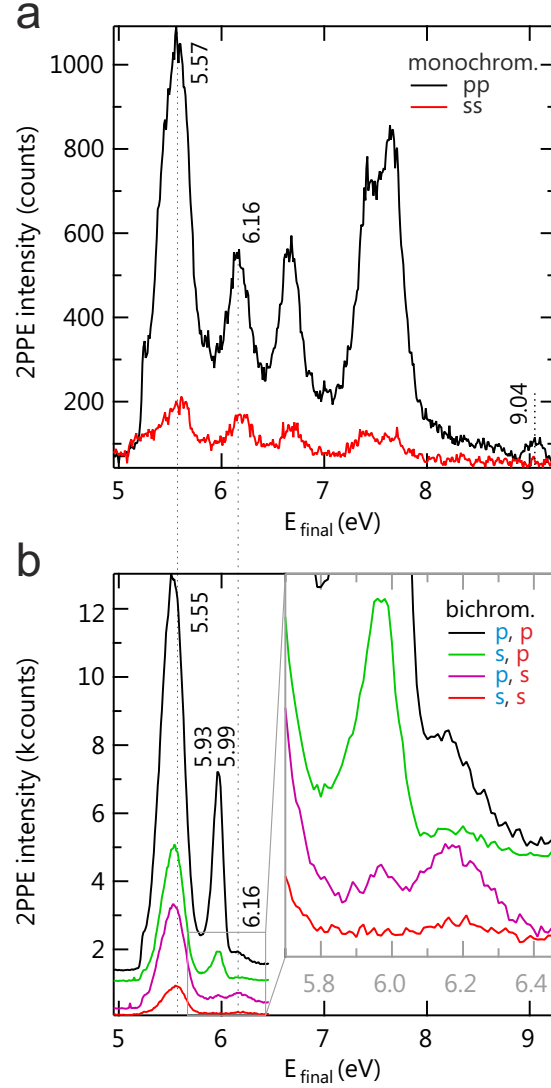


Figure 6.8: Polarization dependent measurements of $\text{Bi}_2\text{Te}_2\text{Se}$ show four bulk conduction bands in monochromatic 2PPE (a). Two of them are also found in bichromatic 2PPE (b). The low-energy component of the additional feature in bichromatic 2PPE results from the IPS also found in the monochromatic data, while the high-energy component can be attributed to the TSS.

expected to vanish when the UV probe beam is switched from p - to s -polarization. In the experiment, it decreases only by one order of magnitude as can be seen from the topmost two curves in Figure 6.8 (b). In fact, a complex orbital composition of the conventional Dirac cone of Bi_2Se_3 was observed, in which p_z and $p_{x,y}$ -like orbitals are mixed, resulting in a switch of the mirror symmetry at the Dirac point (Cao 2012). Calculations indicate that the higher-lying surface state also contains contributions of p_x, p_y and p_z orbitals (Eremeev 2012) and hence does not necessarily retain its symmetry within the energy resolution of the experiment. In addition, a slight tilt of the sample in the experiment might introduce a symmetry break, as the sample surface remains no longer perpendicular to the plane of incidence. In addition, the TSS would not be probed at normal emission in this case. As the local band gap, which it is located in, amounts only to ≈ 70 meV, the surface state might be overlapped by bulk states of different symmetry.

After the identification of the underlying processes, discussion will turn to the dynamics of the unoccupied states. In Figure 6.9 the results of a series of time-resolved bichromatic

2PPE measurements are illustrated. Both pump- and probe laser pulses were p -polarized during the experiment. In Figure 6.9 (a) photoemission intensities are given as a function of final-state energy and pump-probe delay, which will be referred to as a "lifetime map". The long-lived IR-pumped conduction band in the low-energy region below 5.8 eV exhibits a lifetime ≥ 100 fs. This band is refilled in an indirect and complex way, which will not be discussed in detail. Lifetimes τ were determined by an exponential fit to the decay at long pump-probe delays. The single time-resolved spectra are given in Figure A.10, the resulting decay rates are plotted as a function of energy in Figure 6.9 (c). The decay rate \hbar/τ within the conduction band rises linearly in energy over a wide range with a slope of 0.014. The linear increase is characteristic for layered materials and was also found in graphite (Xu 1996), whereas a quadratic relation is expected in three-dimensional systems (Petek 1997).

In contrast, the transitions in the high-energy region above 5.8 eV are coherently optically excited. In the lifetime map in Figure 6.9, both IR-pumped and UV-pumped processes are observed, as also indicated by angle-resolved data shown in Figure A.9. The data were modeled by fitting a sum of the two different contributions. As fit function

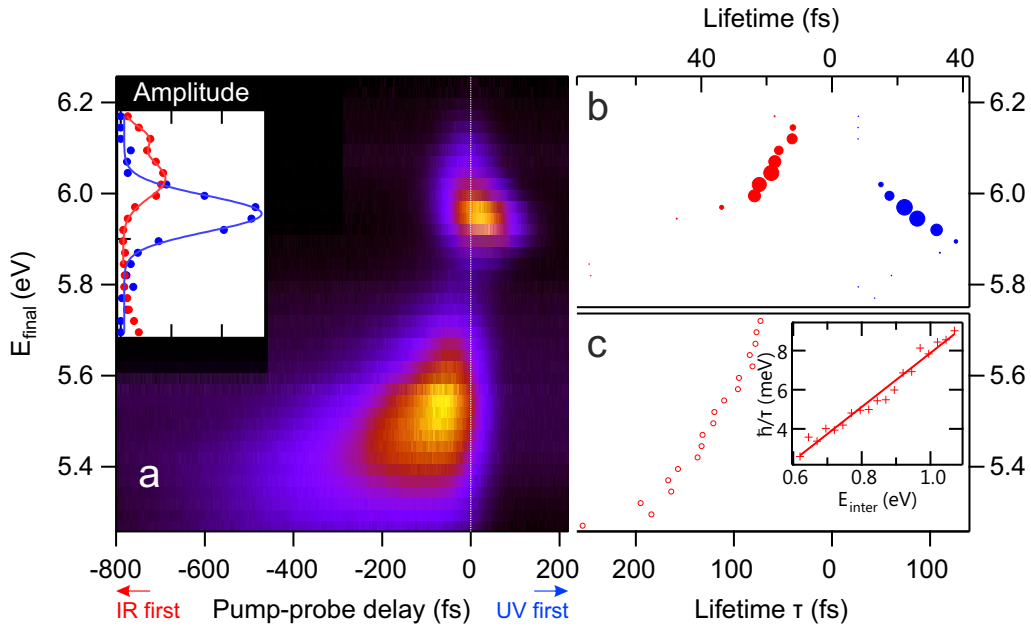


Figure 6.9.: Energy-dependent time-resolved bichromatic 2PPE measurements ("lifetime map") of $\text{Bi}_2\text{Te}_2\text{Se}$ (a). The signal from the band in the low-energy region shows a lifetime ≥ 100 fs (c). In the high-energy region, several features overlap. The inset of (a) shows the 2PPE intensities of the UV-pumped (blue symbols) and IR-pumped (red symbols) transitions as extracted from a fit to the data. The two IR-pumped components, which also appear in polarization-dependent measurements, are found by the fits. In (b) the corresponding lifetimes are given, spot sizes reflect the fit amplitudes. The weighted average results in a lifetime of the topological surface state (image-potential state) of 22 fs (25 fs).

serves as an approximation to the optical Bloch equations including a single decay channel dominating each of the processes (Boger 2004). The resulting fit function is given in Appendix A.3.1 and the fitting curves are depicted together with the single time-resolved spectra in Figure A.10. In the inset of the lifetime map, the resulting amplitudes are given as a function of final-state energy, where blue (red) filled circles indicate UV- (IR-)pumped contributions. The maximum of 2PPE intensity arising from UV-pumped processes at 5.96 eV found by this procedure coincides well with the one from preceding polarization-dependent measurements. Moreover, the amplitudes of the IR-pumped transitions exhibit a double peak structure with maxima at 6.03 eV and 6.13 eV in agreement with polarization dependent experiments. In conclusion, they can be attributed to the same origin: the IPS or interlayer state 4.4 eV above the Fermi level E_F , the topological surface state ($E - E_F = 1.4$ eV) and the minimum of the conduction band above $E - E_F = 1.5$ eV.

The lifetimes obtained from the fits are given in Figure 6.9 (b). Blue (red) circles denote UV- (IR-)pumped processes. The size of the symbols depicts the amplitude of the corresponding signal. In order to extract the lifetimes at the energetic positions of the bands, lifetimes were averaged with a weighting given by their intensities as found from the fit to the peak amplitudes shown in the inset of the lifetime map. This procedure results in a value of 25 fs for the IPS, 22 fs for the topological surface state and 13 fs for the conduction band above it.

6.3. Electron dynamics of SnSb₂Te₄, an intrinsic p-type topological insulator

Antimony- and tellurium-based alloys were amongst the first systems which were proposed (Zhang 2009a) to exhibit a topological surface state. The electronic structure of quintuple-layered Sb₂Te₃ was probed by ARPES and a surface state was found in good agreement with calculations (Hsieh 2009b). However, the material is intrinsically p-doped and therefore the Dirac point cannot be accessed by this method. Alkali adatoms induce counter doping, but the spectra are significantly broadened (Seibel 2012) and complete counter doping is hard to be achieved.

Recent calculations predict the presence of a TSS on the closely-related septuple-layered SbSn₂Te₄ (Menshchikova 2012), which will be the subject of the present section. From photoemission experiments (Chulkov 2012) the material is known to be hole-doped. Two-photon photoemission can therefore not only serve as an ideal method to detect the unoccupied topological surface state, but also the electron dynamics within this state becomes accessible. For this purpose time-resolved bichromatic 2PPE was applied. As the 2PPE signal from the conventional Dirac cone should not overlap with background arising from image-potential states, a straightforward interpretation of the resulting data becomes possible.

Figure 6.10 (a, b) shows the results of an angle-resolved 2PPE measurement at photon energies of 1.63 eV and 4.89 eV with both laser beams *p*-polarized. In Figure 6.10 (c) the calculated band structure (Menshchikova 2012) is shown for comparison. In the survey

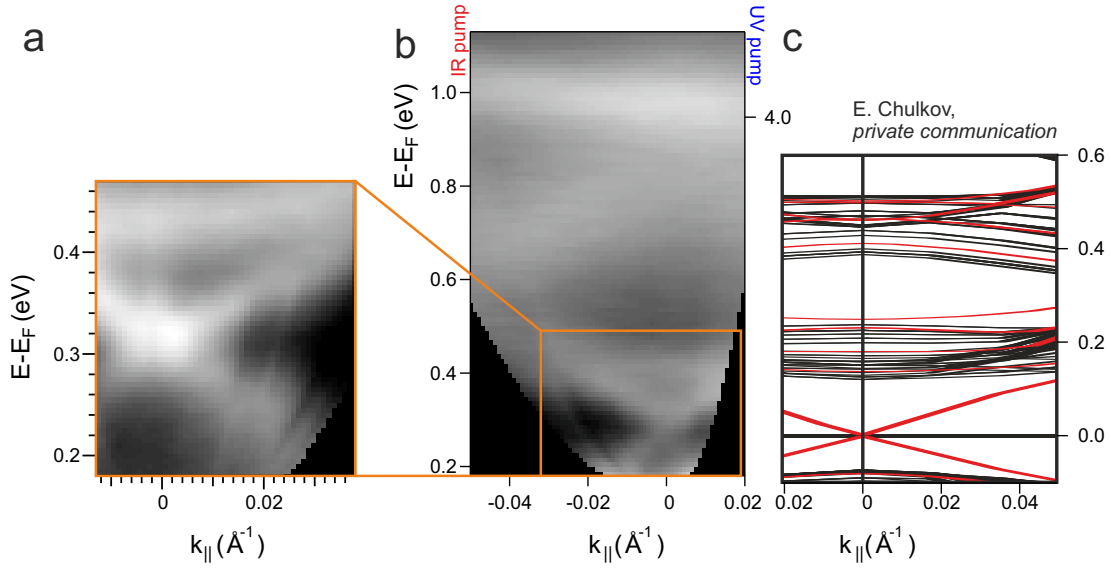


Figure 6.10.: Angle-resolved bichromatic 2PPE (photon energies: 1.63 eV, 4.89 eV) of SnSb_2Te_4 reveal two conduction bands 0.42 eV and 0.78 eV above the Fermi level (b) as well as a linearly dispersive feature. These findings are in agreement with calculations (c) (Chulkov 2012). The latter do not cover the highest-energy band, the UV-pumped image-potential state (Hermann 2012). High-resolution measurements (a) on the linearly dispersive state 0.31 eV above the Fermi level give a group velocity of 3.4 eV \AA^{-1} . The feature is attributed to the topological surface state expected from the calculation with a similar dispersion (Menshchikova 2012). The overall energy shift between experiment and theory stems from intrinsic hole doping and was also found in UV photoemission (Chulkov 2012).

spectrum in Figure 6.10 (b) four bands are found at the $\bar{\Gamma}$ -point. Concluding from time-resolved measurements (not shown) the state observed at the highest final-state energy stems from an UV-pumped intermediate state 4.25 eV above the Fermi level or 0.78 eV below the vacuum level respectively. This feature is attributed to an image-potential state with a lifetime of 15 fs (Hermann 2012). Analogous, the bands at lower energy are identified as bulk conduction bands 0.42 eV and 0.78 eV above the Fermi level in agreement with Reference Hermann (2012). In addition, a linearly dispersive feature is found at a slightly lower final-state energy. Figure 6.10 (a) shows a high-resolution measurement of the corresponding energy region. The group velocity of the band amounts to 3.4 eV \AA^{-1} . From time-resolved measurements, which will be discussed later, it is attributed to an intermediate state 0.31 eV above the Fermi level.

As illustrated in Figure 6.10 (c), the experimentally determined band structure is in agreement with calculations when taking into account the doping level of the sample. From calculations the Dirac cone is expected at the Fermi level. However, ARPES data suggest p-type doping leading to an energy shift of several hundreds of meV (Chulkov 2012). This finding is supported also by the present data. The calculation reproduces the experimental data in the energy range covered when p-type doping is accounted for by a rigid shift

of the energy scale of the calculation by 0.31 eV. Based on this agreement, the linearly dispersive band in experiment is attributed to the topological surface state found in the calculation (Menshchikova 2012).

In Figure 6.11 the results of time-resolved experiments on the topological surface state and the conduction band above it are illustrated. Time-resolved spectra were recorded at the energetic positions indicated by circles in Figure 6.11 (b) and are given together with fits based on a rate equation model in Figure 6.11 (a). The topmost, green curve shows the transient occupation of the conduction band minimum (CBM). It exhibits a large width (FWHM) of 750 fs and a plateau-like maximum that is reached only after a time delay of 210 fs which is significantly longer than the pulse duration. The population decays exponentially at long pump-probe delays with a time constant of 220 fs. This shape cannot be reproduced by optical Bloch equations taking into account only a few (≤ 4) decay channels and points to a complex refilling of the CBM from higher-excited states with a variety of decay channels involved. Similar CBM dynamics were also found for p-doped Bi₂Se₃ (Sobota 2012). 2PPE probes the transient occupation of the conduction band near (2...3 nm (Hajlaoui 2012)) the surface, which is the result of a combination of scattering events taking place at the surface, in the bulk and diffusion between the surface and the bulk (Driel 1987; Rowe 1993; Ichibayashi 2011). Unfolding the individual contributions is beyond the scope of this work. Nevertheless, note that the time constant of diffusion depends on the excitation density as well as the penetration depth of the laser beam, e. g. the excitation wavelength. This fact may partly explain the rise of the 2PPE intensity at about zero time delay in the present experiment, whereas it is delayed by several hundred femtoseconds in experiments on Bi₂Se₃ (Sobota 2012). The conduction band of SnSb₂Te₄ is at least partially populated directly by optical pumping, whereas indirect refilling is dominant in case of Bi₂Se₃.

The lower five time-resolved spectra in Figure 6.11 (a) were measured at different energetic positions along the topological surface state. The line shapes coarsely resemble the one of the CBM, indicating that the TSS is populated partially by electrons from this band. Nevertheless, the details of the individual spectra differ. Especially, distinct rise times occur and the width of the plateau-like maximum changes, which may be explained by varying contributions from direct optical pumping. The dynamics of the TSS was modeled by rate equations accounting for direct optical excitation as well as refilling from the CBM as sketched in Figure 6.11 (c). Both population pathways are incorporated as source terms into the rate equations. The resulting fit function is given in Appendix A.3.2. In order to reproduce the spectra at higher energies, UV-pumped processes overlapping with the TSS were included in the fit by adding the function given in Appendix A.3.1. However, neglecting the latter does not significantly affect the results of the fits.

The resulting fit curves consistently describe the experimental data as depicted by the gray lines in Figure 6.11 (a). No additional refilling mechanisms, such as intraband scattering within the surface state, have to be introduced. In conclusion, intraband scattering occurs on a significantly longer timescale than scattering from the CBM. The rate of refilling from the CBM can not be extracted, as the photoelectron transition probabilities of the CBM and the TSS are not known absolutely. Nevertheless, the lifetime of the TSS

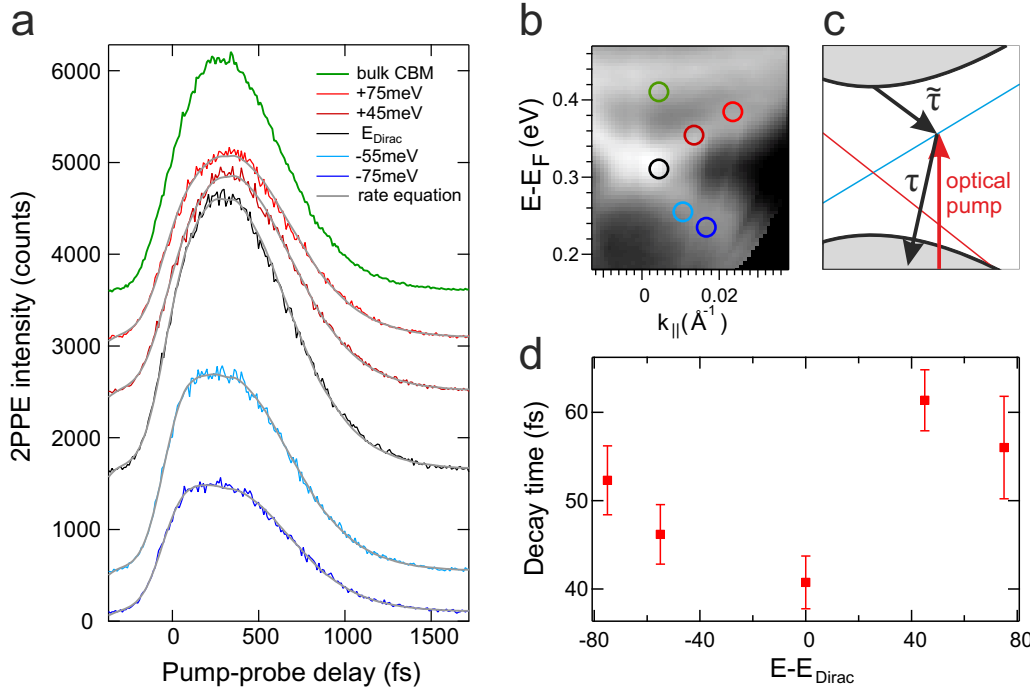


Figure 6.11.: Time-resolved 2PPE spectra (a) from the conduction band minimum (green) of SnSb_2Te_4 and several positions on the topological surface state which are marked in (b). In addition to direct optical excitation, the line shape indicates refilling of the TSS from the CBM observed similarly on Bi_2Se_3 (Sobota 2012). Fits to the data were conducted based on a simple rate-equation model as sketched in (c). Corresponding fit curves are given as gray lines in (a), the resulting lifetime of the TSS is depicted in (d).

can be determined from the model and is given in Figure 6.11 (d) as a function of energy. Considering exclusively scattering within the spin-polarized TSS, much longer lifetimes than ≈ 40 fs, which occur in the proximity of the Dirac point, might be expected. However, the comparison between theory and experiment in Figure 6.10 (b, c) demonstrates, that the bulk valence band of SnSb_2Te_4 is partially depleted at the present doping level. The emerging partially filled valence band can provide final states for electronic decay as well as for electron-hole pair creation. Thus it supports efficient relaxation of excited carriers in the topological surface state.

6.4. Discussion

A high-lying topological surface state of Bi_2Se_3 and $\text{Bi}_2\text{Te}_2\text{Se}$ in a projected bulk band gap $\approx 1.1\text{--}1.5$ eV above the Fermi level was identified by combination of angle-resolved two-photon photoemission, density functional theory calculations and utilization of circular dichroism. To date, this is the first observation of circular dichroism by 2PPE on non-magnetic systems. It demonstrates, that selective optical excitation of electrons of one preferential spin orientation to the unoccupied Dirac cone is possible. This fact may help to complete the description of photocurrents in Bi_2Se_3 which are sensitive to the direction of rotation of circularly polarized light (McIver 2012). Variation of the excitation energy may allow to pump electrons resonantly from the conventional Dirac cone to the new-found surface state giving rise to more strict selection rules in circular dichroism experiments. The occupied and the unoccupied Dirac cone are separated in energy by ≈ 1.5 eV and may be matched energetically to the valence band maximum and the conduction band minimum of a conventional semiconductor in a heterojunction, thereby allowing for efficient spin injection. In this case, coupling between both materials has to be strong enough to overcome the decay of excited electrons within the topological insulator, which results in a lifetime $\tau = 22$ fs in case of Bi_2Se_3 . The resulting mean-free path $\frac{1}{\hbar} \frac{dE}{dk} \cdot \tau \approx 8$ nm limits the use of the higher-lying TSS in applications which require charge transport. In addition, the first image-potential state was found on all TIs under investigation with lifetimes of ≈ 20 fs. Notably, the screening of an electron in the IPS in front of the surface of a TI is expected to give rise to a magnetic monopole at the surface (Qi 2009).

On SnSb_2Te_4 the predicted (Menshchikova 2012) topological surface state was detected by bichromatic 2PPE. The most important tool to study TIs is probably photoemission, and especially UV photoemission (Hsieh 2008; Chen 2009b; Hsieh 2009a; Hsieh 2009b; Xia 2009). Since this method is not able to probe states lying above the Fermi level, the extension to 2PPE will likely allow to identify and characterize upcoming p-type TIs.

The short lifetime of the TSS of SnSb_2Te_4 of 45 fs can be attributed to a high level of doping. Since no apparent intraband scattering of the TSS was found, electrons from this state must relax to the bulk valence band, which is partially depleted at the observed level of doping. The strong coupling between bulk states and the surface state is consistent with experiments (Zhang 2010) and calculations (Linder 2009) which demonstrate that the TSS reaches several quintuple layers (around 10 nm) deep into the bulk. The short lifetime of the TSS of SnSb_2Te_4 compared to e. g. Bi_2Te_3 (Hajlaoui 2012), in which the bulk valence band is fully occupied, indicates non-negligible interaction with the bulk states. In future applications, which will make use of dissipationless spin transport in TIs (Qi 2008), the Fermi level will have to be carefully adjusted to the bulk band gap in order to avoid scattering to bulk states, as also indicated by transport measurements (Checkelsky 2011).

7. Summary

Two kinds of electronic states were investigated by two-photon photoelectron spectroscopy (2PPE): Image-potential states (IPSs) of graphene on metal substrates and silicon carbide, and unoccupied surface states of topological insulators.

For van-der-Waals bound graphene on Ir(111), Ir(100), Pt(111), Au/Ni(111) and SiC(0001) binding energies and lifetimes of the image-potential states were determined. The data demonstrate, that an image-potential electron can be screened within the single graphitic adlayer, resulting in an energetic position of the $n = 1$ state 3.7 eV above the Dirac point almost independent of the substrate. Only in graphene/SiC(0001) this value is reduced by 0.1 eV as a result of incomplete screening. These findings are supported by the measured decay rates. The lifetime of the $n = 2$ state is about 70 fs in most of the systems, but significantly reduced in graphene/SiC(0001). Individual binding energies, lifetimes and work functions are summarized in Table 5.2 on page 53. In addition, the work function is directly accessed in 2PPE. Changes in the work function induced by the graphene adlayer are related to charge transfer to the substrate. The experimental values are compared to a phenomenological capacitor model (Giovannetti 2008). The parameters found from the experiment, which are an effective plate distance of 2.5 Å and a chemically-induced correction of the work-function difference by 0.97 eV, are in good agreement with density functional theory calculations. Thus, the applicability of the model to weakly-bound graphene is demonstrated and theoretical values are supplemented by an experimental set of parameters.

Special attention was paid to graphene on iridium substrates. Graphene is known to grow on Ir(111) in high quality, which is reflected in the long lifetimes of image-potential states of this system. The lifetimes of the first four IPSs do not reach the classical limit $\tau_n \propto E_n^{3/2}$, but follow an $\tau_n \propto E_n$ dependence, indicating deviations of the potential in front of graphene from the asymptotic $1/r$ dependence. Insight into the underlying scattering processes, and especially their relation to the two-dimensional band structure of graphene, require additional theoretical efforts. Furthermore an occupied, downward-dispersing Rashba-split surface state in a symmetry band-gap closely below the Fermi level is found by ARPES (Niesner 2012a). The Rashba-splitting is of similar magnitude as the one of the surface state of Au(111) (LaShell 1996). The origin of an additional, flat band at similar binding as the $n = 1$ IPS remains subject of current research (Nobis 2013b).

Graphene/Ir(100) had only been studied by LEED and STM experiments before (Ferstl 2011), which find a strong atomic corrugation on parts of the surface. ARPES experiments at BESSY II reveal the characteristic π -band structure up to the Fermi level. Graphene is p-doped, the Dirac point is located 0.34 eV above the Fermi level. The appearance of two surface modifications gives rise to preparation-dependent variations of the work function in 2PPE and to two parallel series of image-potential states which are pinned to the individual

local work functions. This is the first study demonstrating the appearance of a Dirac cone of graphene grown epitaxially on square substrate, and the arising atomic and electronic interaction are not fully understood.

The second part of the thesis concerns the unoccupied part of the band structure of topological insulators. Using monochromatic 2PPE the band structure of $\text{Bi}_2\text{Te}_{3-x}\text{Se}_x$, $x \in \{0, 1, 3\}$ up to the vacuum level was determined for the first time, and is found to be in good agreement with calculations. In addition to the first image-potential state 0.8 eV below the vacuum level, a linearly dispersive feature is found in a projected bulk band gap about 1.4 eV above the Fermi level in Bi_2Se_3 and $\text{Bi}_2\text{Te}_2\text{Se}$. Calculations indicate symmetry-inversion of the band gap, and evidence of the characteristic spin structure of a topological surface state (TSS) is given in 2PPE by making use of circular dichroism. It is the first observation of circular dichroism in 2PPE from nonmagnetic system, and the asymmetries of 10...15% are considerably smaller than in ARPES.

In addition, the existence of the conventional TSS of a new material, SnSb_2Te_4 , was proven by bichromatic 2PPE experiments. The Dirac cone is located 0.3 eV above the Fermi level and therefore not accessible by conventional photoemission. As photoemission provides a valuable method for the identification and characterization of topological insulators, the extension to 2PPE will allow studies on further upcoming p-type topological insulators. Moreover, time-resolved pump-and probe experiments allow to follow the dynamics within the topological state. They indicate an indirect population mechanism of the surface state of SnSb_2Te_4 *via* refilling by initially higher-excited electrons. Modeling of the data by rate equations yields a lifetime of the TSS of about 45 fs. Refilling from the conduction band together with the short lifetime, which can be attributed to scattering to the partly depleted bulk valence band, demonstrates significant interaction between the TSS and bulk states. The interaction may be attributed to a large spatial overlap between the two, in agreement with calculations which show an extension of the TSS several nanometers deep into the bulk (Linder 2009).

Zusammenfassung

Zwei Arten von Oberflächenzuständen wurden mittels Zweiphotonen-Photoemission (2PPE) untersucht: Bildpotentialzustände (BPZ) vor Graphen auf Metall- und Siliziumkarbid-Substrat sowie unbesetzte Oberflächenzustände von topologischen Isolatoren.

Zunächst wurden die Bindungsenergien und Lebensdauern von van der Waals-gebundenem Graphen auf Ir(111), Ir(100), Pt(111), Au/Ni(111) and SiC(0001) bestimmt. Die gewonnenen Daten zeigen, dass eine einzelne Lage Graphen in der Lage ist, eine äußere Ladung abzuschirmen, was sich in einer weitgehend vom Substrat unabhängigen energetischen Lage des ersten Bildpotentialzustandes 3.7 eV oberhalb des Diracpunktes äußert. Im Falle von Graphen/SiC(0001) wurde eine Abweichung um 0.1 eV festgestellt und einer unvollständigen Ladungsabschirmung zugeschrieben. Die Interpretation wird durch zeitaufgelöste Messungen gestützt, die eine vom Substrat unabhängige Lebensdauer des $n = 2$ -Zustandes von etwa 70 fs zeigen. Nur für Graphen/SiC(0001) ist dieser Wert deutlich geringer. Die einzelnen Messwerte sind in Tabelle 5.2 auf Seite 53 zusammengefasst. Zusätzlich wurden die Austrittsarbeiten der graphenbedeckten Oberflächen bestimmt. Austrittsarbeitsänderungen gegenüber freistehendem Graphen sind auf Ladungstransfer zum Substrat zurückzuführen. In einem phänomenologischen Modell bilden Graphen und Substrat gegenüberliegende Platten eines Kondensators (Giovannetti 2008). Die experimentellen Daten lassen sich unter Annahme eines Plattenabstandes von 2.5 Å und einer chemisch induzierten Korrektur der Austrittsarbeitsdifferenz um 0.97 eV beschreiben. Die Übereinstimmung mit theoretischen Parametern (Khomyakov 2009) unterstreicht die Anwendbarkeit des Modells, das somit um einen experimentellen Satz von Parametern ergänzt wurde.

Einen Schwerpunkt bilden die Messungen an epitaktischem Graphen auf Iridiumsubstrat. Graphen/Ir(111) ist intensiv untersucht und kann in hoher kristalliner Qualität synthetisiert werden. Diese spiegelt sich in den langen Lebensdauern der BPZ wider. Die Lebensdauern der ersten vier BPZ folgen nicht dem klassischen asymptotischen $\tau_n \propto E_n^{3/2}$ Verhalten, sondern nehmen mit $\tau_n \propto E_n$ zu. Das Potential vor dem Graphen erreicht also noch nicht den asymptotischen $1/r$ Verlauf. Einen weiteren Grund für Abweichungen könnte die Energieabhängigkeit der Streuprozesse im Graphen bilden, da die Elektron-Loch-Paarbildung durch die lineare Zustandsdichte im Energiebereich ± 1 eV um das Ferminiveau eingeschränkt ist. Eine quantitative Analyse erfordert jedoch eine detaillierte theoretische Beschreibung des Systems. Zusätzlich zu den BPZ wurde mittels ARPES ein abwärtsdispergierender besetzter Shockleyzustand in einer Symmetriebandlücke gefunden (Niesner 2012a), der eine ähnlich große Rashba-Aufspaltung wie der Oberflächenzustand vor Au(111) (LaShell 1996) zeigt. Zudem weisen 2PPE-Messungen auf das Vorhandensein eines weiteren unbesetzten Zustandes nahe dem ersten BPZ hin. Der Ursprung dieses Bandes bleibt jedoch Gegenstand aktueller Forschung (Nobis 2013b).

Im Gegensatz zu Graphen auf Ir(111) ist Graphen auf Ir(100) bisher kaum untersucht. Elektronenbeugung und Rastertunnelmikroskopie zeigen eine starke Korrugation der Graphenlage auf Teilen der Oberfläche (Ferstl 2011). Durch ARPES-Messungen am BESSY II konnte die charakteristische π -Bandstruktur von Graphen nachgewiesen werden. Der Diracpunkt ist aufgrund des Ladungsübertrags zum Substrat nicht zugänglich, die Messungen weisen jedoch auf eine energetische Position 0.34 eV oberhalb des Fermi-niveaus hin. Das Auftreten unterschiedlicher Oberflächenmodifikationen macht sich in der 2PPE durch präparationsabhängige Schwankungen in der mittleren Austrittsarbeit bemerkbar. Außerdem gibt es zwei Serien von BPZ, die an die jeweilige lokale Austrittsarbeit gebunden sind.

Der zweite Teil der Arbeit behandelt den unbesetzten Teil der Bandstruktur topologischer Isolatoren. Mittels monochromatischer Zweiphotonen-Photoemission wurde die Bandstruktur von $\text{Bi}_2\text{Te}_{3-x}\text{Se}_x$, $x \in \{0, 1, 3\}$ zwischen dem Fermi-niveau und dem Vakuumniveau vermessen. Die Ergebnisse decken sich mit Rechnungen. Neben dem ersten Bildpotentialzustand 0.8 eV unterhalb des Vakuumniveaus findet sich auf Bi_2Se_3 und $\text{Bi}_2\text{Te}_2\text{Se}$ ein Oberflächenzustand mit linearer Dispersion in einer projizierten Volumenbandlücke etwa 1.4 eV oberhalb des Fermi-niveaus. Rechnungen zeigen, dass die Bandlücke die Folge einer Bandinversion durch Spin-Bahn-Kopplung ist und dass der Oberflächenzustand die Spinstruktur eines topologischen Zustandes aufweist. Ein experimenteller Hinweis auf Letztere lässt sich aus Messungen des Zirkulardichroismus in der 2PPE herleiten. Die gemessene Asymmetrie zwischen den unter rechts- und linkszirkularer Polarisation gemessenen Intensitäten ist mit 10...15% zwar geringer als in der konventionellen Photoemission, die beobachtete Winkelverteilung ist jedoch mit der erwarteten helischen Struktur des Dirac-Konus konsistent.

Zuletzt wurde mittels bichromatischer 2PPE der topologische Oberflächenzustand eines neuen Materials, SnSb_2Te_4 , experimentell nachgewiesen. Da der Diracpunkt in diesem System 0.3 eV oberhalb des Fermi-niveaus liegt, ist ein Nachweis durch konventionelle Photoemission nicht möglich. Da die Methode der Photoemission in den bisherigen Untersuchungen an topologischen Isolatoren eine zentrale Rolle einnimmt, ist damit zu rechnen, dass die Zweiphotonen-Photoemission auch in Zukunft dazu beitragen wird, intrinsisch p-dotierte topologische Zustände zu charakterisieren. Zusätzlich eröffnet sich die Möglichkeit zeitaufgelöster Experimente. Durch zeitaufgelöste Messungen an SnSb_2Te_4 wurde gezeigt, dass der topologische Zustand größtenteils indirekt durch Elektronen bevölkert wird, die durch den Pumpimpuls ursprünglich höher angeregt wurden. Nach Relaxation zum Leitungsbandminimum streuen sie von dort in den Oberflächenzustand. Die zeitaufgelösten Spektren wurden durch Ratengleichungen modelliert, wodurch die Lebensdauer des Oberflächenzustandes zu 45 fs ermittelt wurde. Sowohl die kurze Lebensdauer, die sich durch Streuung in das teilweise entleerte Volumen-Valenzband erklären lässt, als auch das Nachfüllen aus dem Leitungsband weisen auf eine nennenswerte Wechselwirkung zwischen dem topologischen Oberflächenzustand und den Volumenbändern hin. Diese ist das Resultat einer großen Eindringtiefe des Oberflächenzustandes in das Volumen, wie sie auch durch Rechnungen bestätigt wird (Linder 2009).

A. Appendix

A.1. Graphene

A.1.1. Characterization of graphene on iridium by Raman spectroscopy

Raman spectroscopy is a widely-used technique to study layer thickness (Ferrari 2006; Röhrl 2008), strain (Hanfland 1989; Röhrl 2008; Huang 2009), doping (Casiraghi 2007; Das 2008) and defect concentration (Tuinstra 1970; Ferrari 2000; Cançado 2011) of graphene and other graphitic materials. Usually their Raman spectrum is dominated by the only Raman-active optical Γ -point phonon (G) with a frequency of 1575 cm^{-1} in graphite (Tuinstra 1970) as depicted in Figure A.3. Higher-order processes result in the defect-induced mode (D) at 1350 cm^{-1} and its overtone (2D), the line shape of which is used to identify single layers in the fabrication of graphene by micromechanical cleaving (Ferrari 2006). A description of the Raman process is given e. g. in References Kittel (1987) and Cardona (1982), while the scattering events occurring in graphene are discussed in detail in References Reich (2004), Malard (2009) and Dresselhaus (2005).

In Raman spectra of graphene on metal substrates, the otherwise prominent features are strongly suppressed and observed only after growth of a second layer or transfer to insulating substrates (Sutter 2008; Reina 2009; Li 2009; Nie 2011). In case of MLG/Ir(111) the occurrence of the D- and G-modes was also reported on 30° rotated domains (Starodub 2011), and graphene/Pt(111) exhibits these peaks when grown on thin films (Kang 2009) or in case of highly defective material (Imamura 2011).

Raman spectra of graphene/Ir(111), graphene/Ir(100) and bare iridium substrate were recorded under ambient conditions using a Jobin Yvon Horiba T64000 spectrometer and an excitation wavelength of 532 nm (Spectra Physics Millennia XS). The resolution was reduced to 1.5 cm^{-1} . A linear function was subtracted from the spectrum of Ir(111) in Figure A.2, accounting for a broad background reaching from 1200 cm^{-1} to 3500 cm^{-1} .

Raw data over a wide frequency range can be found in Figure A.1. In the survey spectrum of MLG/Ir(111) a Raman band is observed around 2430 cm^{-1} with a maximum at 2433 cm^{-1} which is attributed to combinations of the in-plane transverse optical phonon and the longitudinal acoustic phonon at the K-point of graphene (Araujo 2012). A weak feature at 2687 cm^{-1} resembles the position of the 2D mode of graphite at 2691 cm^{-1} (Vidano 1981). The additional peak at 481 cm^{-1} corresponds neither to a known Raman mode of graphene, nor to commonly adsorbed species unless taking into account sulfur- or iodine-containing compounds. It might originate from an umklapp of acoustic phonons in the presence of the moiré superstructure from $2g$ to Γ , where g denotes the lattice vector of the supercell. An alternative explanation is a lifting of the k restrictions

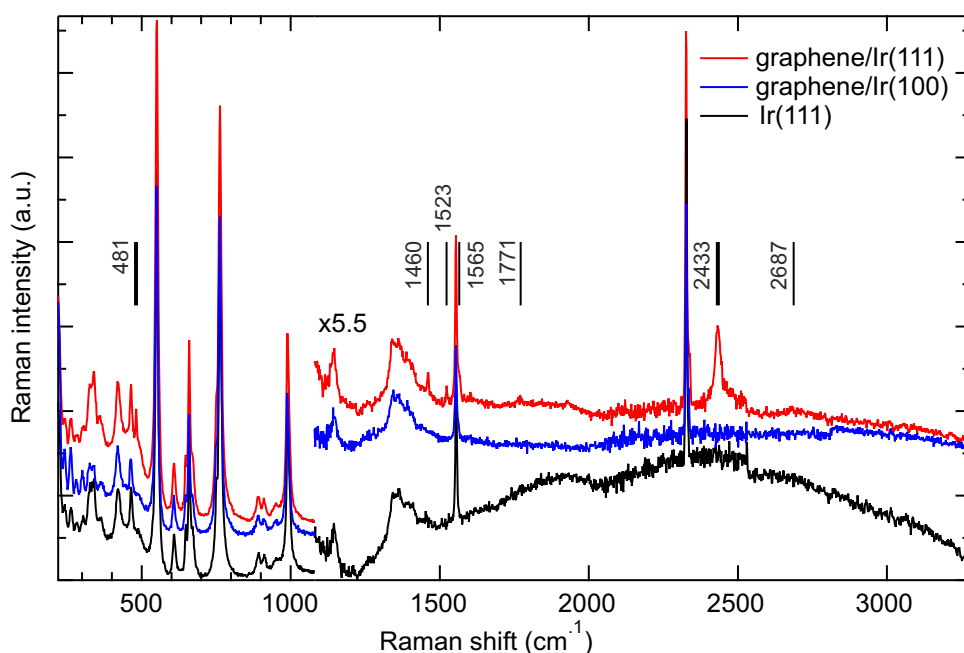


Figure A.1.: As recorded Raman survey spectra of graphene on Ir(100) and Ir(111) as well as the bare substrate. Bold vertical lines indicate prominent features, while thin lines indicate less intense peaks. As the curves are merged from four single spectra, changes in the noise level occur e. g. at 2000 cm^{-1} and 2500 cm^{-1} .

of free-standing graphene by the substrate, resulting in the occurrence of the singularity of the phonon density of states at this frequency which arises from flat branches around the M-point (Mohr 2007). A distinction between the two possibilities based on the present data is not possible. All features in the survey spectrum of MLG/Ir(100) are related to the bare iridium substrate.

Figure A.2 shows a close-up of the frequency range surrounding the energy of the optical phonon of graphene. The prominent feature at 1555 cm^{-1} is a result of adsorbed molecular oxygen as also found on MLG/Pt(111) (Imamura 2011). Oxygen was shown to intercalate between graphene and Ir(111) (Larciprete 2012). Additional peaks are observed at 1562 cm^{-1} on MLG/Ir(100) and at 1460 cm^{-1} , 1523 cm^{-1} and 1565 cm^{-1} on MLG/Ir(111). Three possible derivations of the nature of these modes will be discussed.

First, they may originate from adsorbates. The mode at 1562 cm^{-1} (1565 cm^{-1}) might be a split-off of the oxygen peak at 1555 cm^{-1} , while the feature at 1460 cm^{-1} could be related to a C-H deformation mode like observed in highly-defective graphene (Mathew 2011). However, a defect concentration as high as in Reference Mathew (2011) is not expected for MLG/Ir(111). Moreover, a distinct adsorption behavior of MLG/Ir(111) compared to MLG/Ir(100) and Ir(111) is not expected at first sight and the peak at 1523 cm^{-1} is not easily explained.

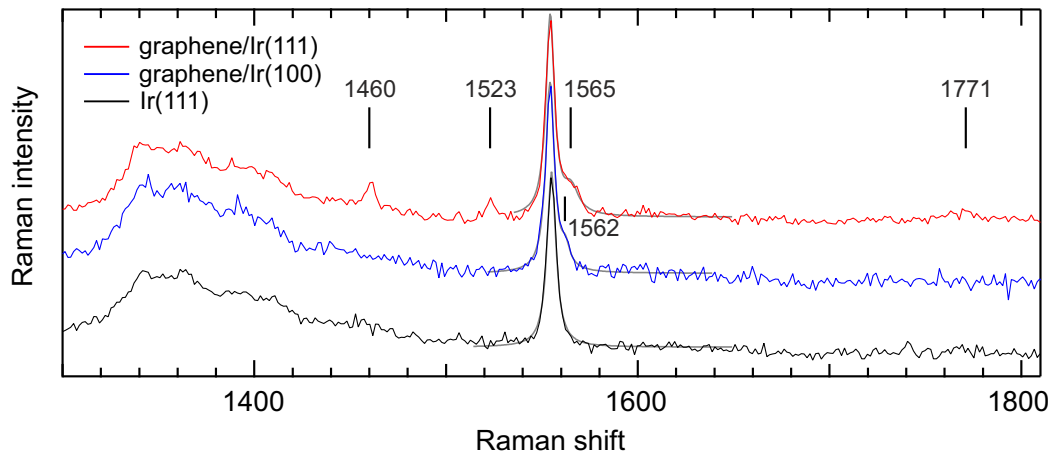


Figure A.2.: Besides the iridium or oxygen peak at 1555 cm^{-1} , Raman spectra of the G peak region show a single mode for MLG/Ir(100) (blue) and three features in case of MLG/Ir(111) (red). Although all peaks are of low intensity, they are reproducibly present on the graphene-covered surfaces.

Second, combinations of acoustic K-point modes might be observed. Referring to Figure A.3 (taken from Reference Mohr (2007)), the combination of the K5 or K2 mode with the K6 LA and ZO modes - which are non-degenerate in high-resolution electron energy loss spectroscopy on Pt(111) (Aizawa 1992; Politano 2012) - results in similar total energies. However, to the best of the author's knowledge, corresponding features have not been reported before and only the combination K5+K6 is expected to be Raman-active (Dresselhaus 2005). Furthermore, in order to explain the difference between MLG/Ir(100) and MLG/(111), different electron-phonon scattering channels have to be dominant in the two systems. The latter require significant electronic or vibronic coupling between graphene and the substrate which is not expected.

Third, the peak at 1562 cm^{-1} (1565 cm^{-1}) can be attributed to the optical phonon of graphene. A softening of the G-mode by $\approx 20\text{ cm}^{-1}$ ($\approx 80\text{ cm}^{-1}$) with respect to value of 1575 cm^{-1} of graphite (Tuinstra 1970; Röhrl 2008) is observed on MLG/Pt(111) (Aizawa 1992; Politano 2012) (MLG/Ni(111) (Aizawa 1990)) due to interaction with the substrate. The frequency of 1565 cm^{-1} of MLG/Ir(111) is close to the one of graphene/Pt(111) and differs clearly from 1598 cm^{-1} reported for 30° rotated domains (Starodub 2011). It is therefore assigned to aligned graphene. The peaks at 1523 cm^{-1} and 1460 cm^{-1} arise from umklapp processes of the TO phonon, which is Raman-active along the T direction in double resonant scattering (Malard 2009), at the moiré supercell zone boundary as illustrated in Figure A.3.

Note, that the three discussed mechanisms do not exclude each other. Hence they may partly be present side by side. Nevertheless, the latter gives a consistent explanation for all observed Raman features and is therefore preferred by the author. The umklapp processes may be a result of resonant electron-phonon scattering between the Dirac mini cones of graphene/Ir(111) (Pletikosić 2009).

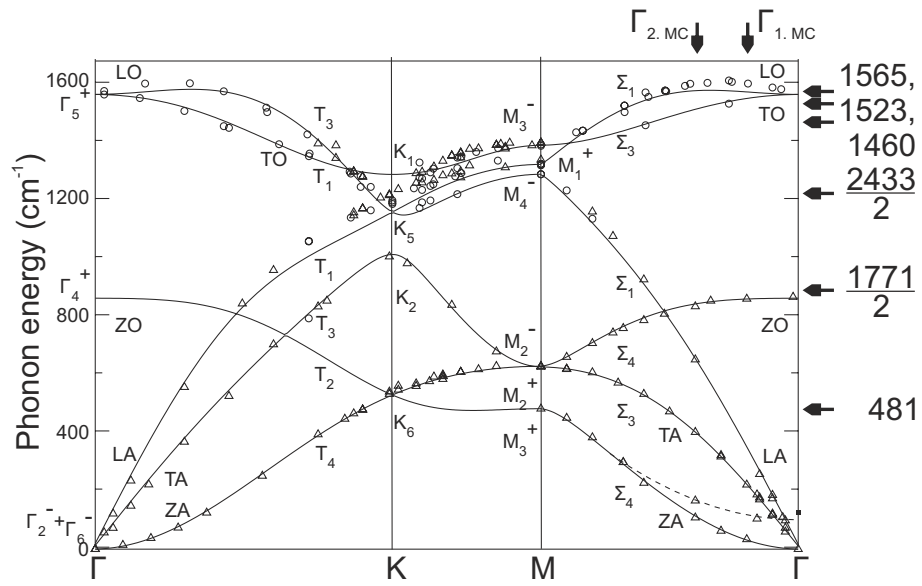


Figure A.3.: Calculated (black lines) and experimental (inelastic x-ray scattering, squares and circles) phonon dispersion of graphite (Mohr 2007). Horizontal arrows indicate peak positions in the Raman spectrum of MLG/Ir(111), vertical arrows denote lattice vectors of the moiré cell (MC).

A.1.2. Energy distribution curves of graphene on Ir(111) and graphene on SiC(0001)

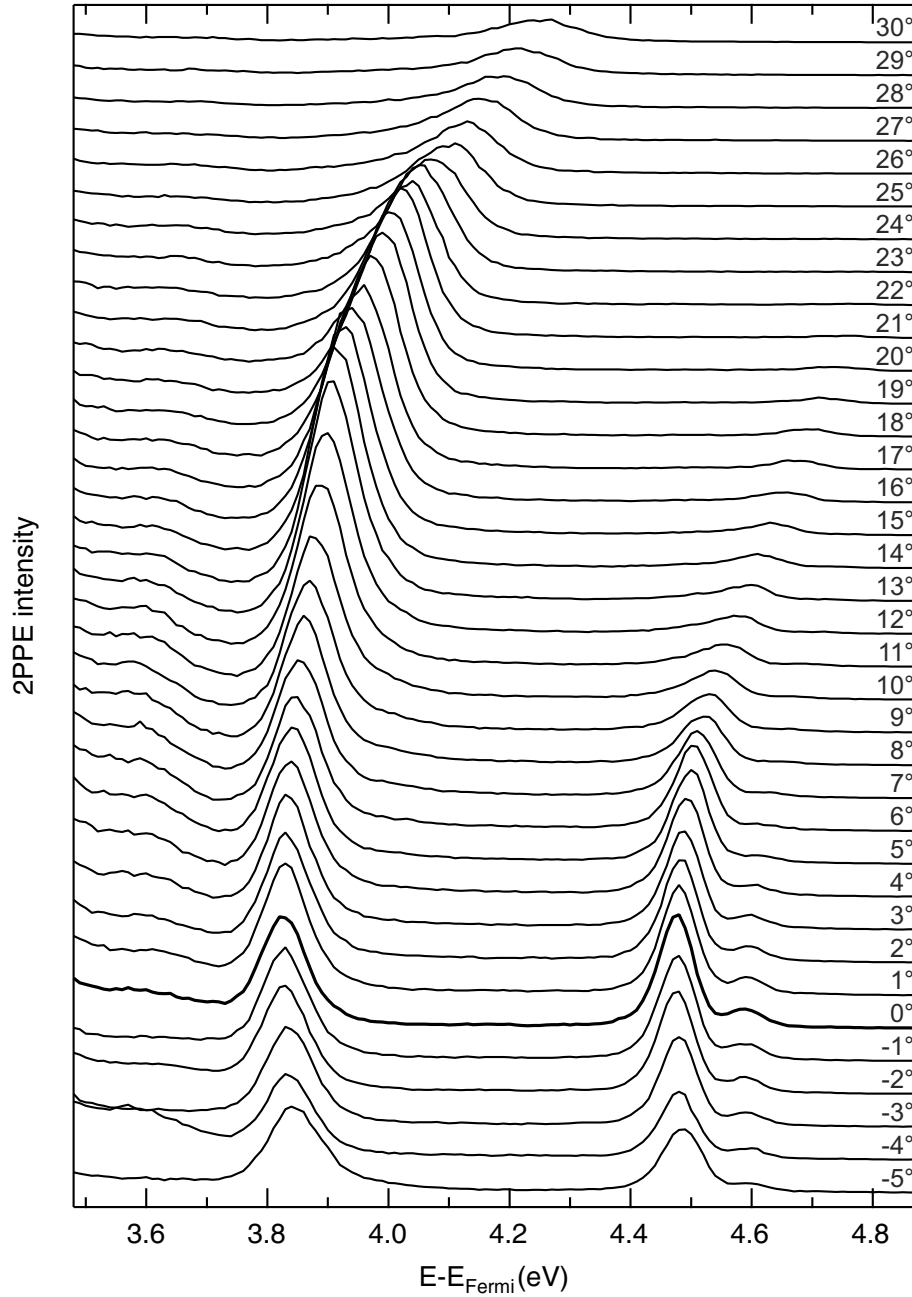


Figure A.4.: Two-photon photoemission energy-distribution curves recorded on graphene/Ir(111). The fundamental excitation wavelength is 780 nm and the time delay is close to zero. Increasing asymmetry of the $n = 1$ image-potential state at around 3.9 eV is observed at angles above 15° .

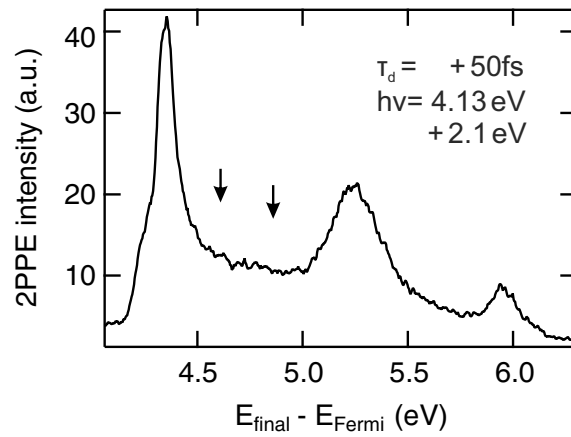


Figure A.5: 2PPE energy-distribution curve of graphene/SiC(0001) recorded at normal emission. The pump-probe delay is slightly positive (UV first). The first two image-potential states occur at final-state energies of approximately 5.3 eV and 5.9 eV. Vertical lines indicate the approximate position of the low-energy shoulder observed in Bose (2010) and Sandin (2010).

A.2. Topological insulators

A.2.1. Survey spectra of the unoccupied part of the band structure of bismuth chalcogenides

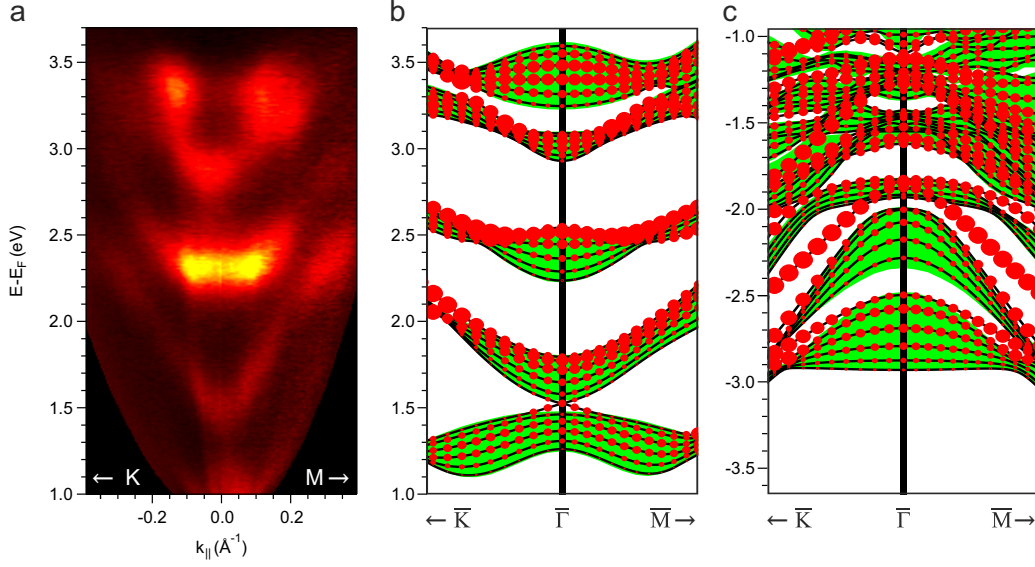


Figure A.6.: Cuts along the high-symmetry directions through 2PPE monochromatic spectra recorded on Bi_2Se_3 using the display-type analyzer (a). The plane of light incidence coincides with the $\bar{\Gamma}\bar{M}$ mirror plane. The calculated intermediate states (b) and initial states (c) for the applied photon energy of 4.65 eV are shown for comparison (Chulkov 2012).

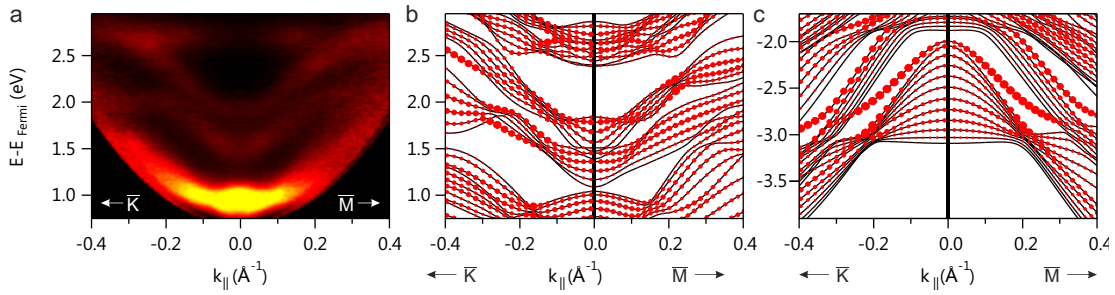


Figure A.7.: Survey spectra at the same experimental parameters like in Figure A.6 for $\text{Bi}_2\text{Te}_2\text{Se}$. Calculations from Chulkov (2012).

A.2.2. Circular dichroism patterns of bismuth chalcogenides

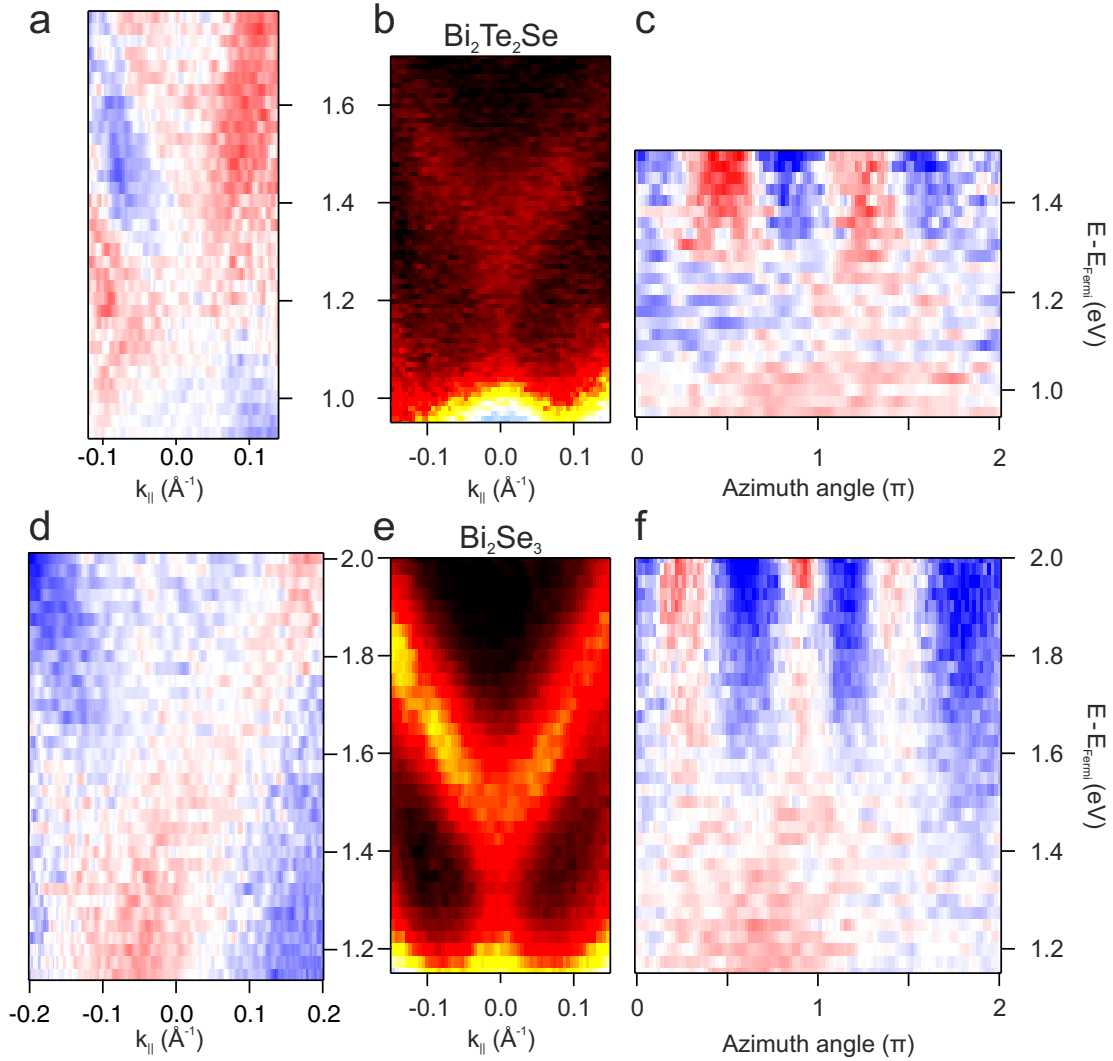


Figure A.8.: Evolution of the circular dichroism (CD) patterns of $\text{Bi}_2\text{Te}_2\text{Se}$ (top row) and Bi_2Se_3 (bottom row). **(a, d)** In both cases, two linearly-dispersive branches of opposite slope with a crossing point at the Dirac point appear in the difference between photoemission intensities recorded with left- and right-handed circularly polarized light $\sigma^+ - \sigma^-$. **(b, e)** Angle-resolved monochromatic 2PPE data in show the dispersion of the unoccupied bands for comparison. **(c, f)** As the surface state approaches the bulk conduction band above it and turns into a surface resonance, the CD pattern changes from a helical structure into a threefold shape, resembling the symmetry of the bulk bands.

A.2.3. Time-resolved bichromatic 2PPE on $\text{Bi}_2\text{Te}_2\text{Se}$

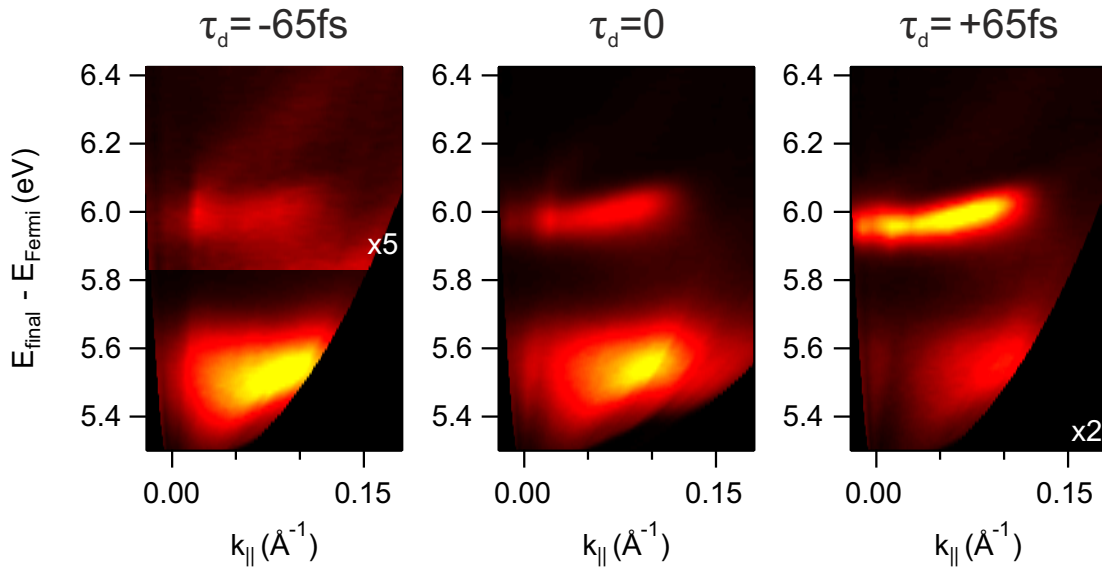


Figure A.9.: Angle-resolved bichromatic 2PPE spectra ($h\nu = 1.65 \text{ eV}, 4.65 \text{ eV}$) of $\text{Bi}_2\text{Te}_2\text{Se}$ recorded at different time delays. Parts of the intensity maps were multiplied by the given factors for better visibility.

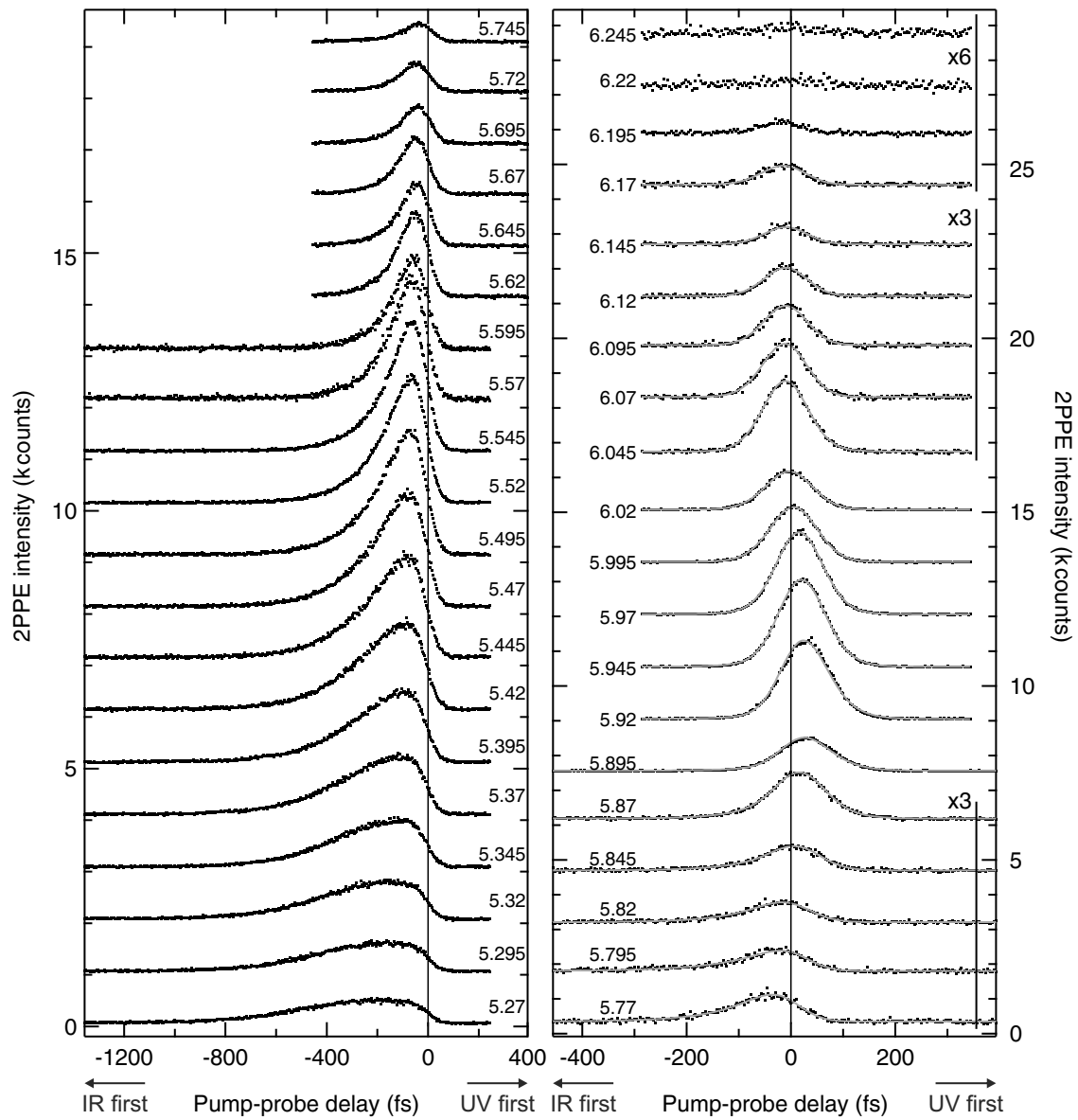


Figure A.10.: Series of the time-resolved bichromatic 2PPE spectra ($h\nu = 1.65$ eV, 4.65 eV) recorded on $\text{Bi}_2\text{Te}_2\text{Se}$ which are combined in Figure 6.9. Small numbers indicate the corresponding final-state energies referring to the Fermi level. Lifetimes of the conduction band in the left panel were extrapolated from a fit to the exponential decay at large negative pump-probe delays (not shown). Spectra in the high-energy region were fitted by a sum of two components of Function A.1. One component describes the IR-pumped processes, and the second one accounts for UV-pumped processes. The width of the cross-correlation trace was kept fixed at 78 fs.

A.3. Fit Functions

A.3.1. Optical Bloch equations

As a fit function to the transient population of an electronic state excited by a Gaussian laser pulse serves an approximation to the optical Bloch equations accounting for a single decay channel (Boger 2004):

$$n(t) = n_0 \exp\left(-\frac{t}{\tau} + 0.125 \left(\frac{Bp}{\tau}\right)^2\right) \left(1 + \operatorname{erf}\left(\sqrt{2} \frac{t}{Bp} - \frac{Bp}{(2\sqrt{2}\tau)}\right)\right) \quad (\text{A.1})$$

where Bp denotes the width of the cross correlation trace and τ the lifetime of the electronic state.

A.3.2. Rate equations

Within the rate equation model, the temporal evolution of the population n_i of the state i (i = CB: conduction band, TSS: topological surface state) is given by:

$$\frac{d}{dt} n_{TSS} = -\frac{1}{\tau} n_{TSS} + \frac{1}{\tilde{\tau}} n_{CB} + g(t)$$

τ is the lifetime of the surface state, $\tilde{\tau}$ the inverse rate of refilling from the conduction band and $g(t)$ the rate of optical pumping. The latter is proportional to the intensity of the laser pulse which will be assumed to be Gaussian-shape in time.

The 2PPE intensity I_i is proportional to the transient population *via* the transition probability $M_{i,f}^2$:

$$\left(\frac{1}{\tau} + \frac{d}{dt}\right) I_{TSS} = \frac{1}{\tilde{\tau}} \frac{M_{TSS,f}^2}{M_{CB,f'}^2} I_{CB} + M_{TSS,f}^2 g(t) =: h(t)$$

The right-hand side of the equation is treated as a source term $h(t)$, including both refilling from the conduction band and optical pumping. As the transition probabilities are unknown, the rate of refilling cannot be extracted from the rate equations.

The Green's function G of the operator on the left-hand side is given by

$$\left(\frac{1}{\tau} + \frac{d}{dt}\right) G(t) = \delta(t) = \left(\frac{1}{\tau} + \frac{d}{dt}\right) \theta(t) \exp\left(-\frac{t}{\tau}\right)$$

where $\delta(t)$ is Kronecker's delta-function and $\theta(t)$ is Heavyside's theta-function. The solution of the differential equation is given by

$$I_{TSS} = \int_{-\infty}^t \exp\left(-\frac{1}{\tau}(t-t')\right) h(t') dt' \quad (\text{A.2})$$

This expression serves as a fit function to the time-resolved data in Section 6.3.

A.4. Correlation between photoemission matrix elements of linearly and circularly polarized light

Inserting the vector potential of circularly polarized light $\underline{A}_0 = (-iA_x, A_y, -iA_z)$ into the dipole matrix element (Equation 4.3) gives

$$M_{f,i} = -i \langle \psi_f | A_x p_x | \psi_i \rangle + \langle \psi_f | A_y p_y | \psi_i \rangle - i \langle \psi_f | A_z p_z | \psi_i \rangle = -iM_{f,i}^p + M_{f,i}^s$$

where $M_{f,i}^p$ and $M_{f,i}^s$ are the matrix elements of purely p and s polarized light, respectively. $M_{f,i}^p{}^2$ and $M_{f,i}^s{}^2$ are observable, and have e. g. been measured for the conventional Dirac cone of Bi_2Se_3 (Cao 2012) as illustrated in Figure 4.3. The photoemission intensity is proportional to

$$|M_{f,i}|^2 = |M_{f,i}^p|^2 + |M_{f,i}^s|^2 + 2 \text{Im}(M_{f,i}^p M_{f,i}^{s*}) \quad (\text{A.3})$$

Switching the direction of rotation of the circularly polarized light, $A_y \rightarrow -A_y$, changes the sign of $M_{f,i}^s$ and thus of the last term in Equation A.3, which therefore gives rise to circular dichroism. Notably, a zero in $M_{f,i}^p$ or $M_{f,i}^s$ results in a zero in the circular dichroism signal, as was observed in case of Bi_2Se_3 in Reference Ishida (2011) in agreement with the orbital structure depicted in Figure 4.3 (Cao 2012). The possible occurrence of a similar switch in the orbital composition of the higher-lying Dirac cones of Bi_2Se_3 and $\text{Bi}_2\text{Te}_2\text{Se}$, which also exhibits a complex composition of p_x , p_y and p_z orbitals (Eremeev 2012), would explain the different intensities of the circular dichroism observed above and below the Dirac cone in Figure A.8.

List of Figures

1.1. Schematic band structure of graphene and a topological insulator. Scattering of the Dirac state by a narrowing. Bandgap opening in gated bilayer graphene. (c) Reprinted figure with permission from (Krueckl 2011). Copyright 2011 by the American Physical Society. (d) Reprinted by permission from Macmillan Publishers Ltd: (Zhang 2009b), copyright 2009.	3
2.1. Atomic, vibronic and electronic structure of graphene. (b) Republished with permission of Annual Reviews, Inc, from (Dresselhaus 2010); permission conveyed through Copyright Clearance Center, Inc. (d) Reprinted figure with permission from (Silkin 2009). Copyright 2009 by the American Physical Society.	6
2.2. Industrial roll-to-roll production of graphene. Reprinted by permission from Macmillan Publishers Ltd: (Bae 2010), copyright 2010.	8
2.3. Growth mechanisms of graphene on metal substrate referring to (N'Diaye 2004).	8
2.4. Experimentally measured band structure of graphene on various substrates. (a, b) Reprinted figure with permission from (Varykhalov 2008). (c) Reprinted figure with permission from (Kralj 2011). Copyright 2011 by the American Physical Society. (d) Reprinted by permission from Macmillan Publishers Ltd: (Marchenko 2012), copyright 2012. (e) Reprinted figure with permission from (Pletikosić 2009). Copyright 2009 by the American Physical Society. (f, g) Reprinted figure with permission from (Emtsev 2008). (a, b, f, g) Copyright 2008 by the American Physical Society.	10
2.5. The capacitor model relating charge transfer between graphene and the substrate to their different work functions. Reprinted figure with permission from Giovannetti (2008). Copyright 2008 by the American Physical Society.	12
3.1. Gapless topological surface state arising from time-reversal symmetry at the Kramers point. (c, d) Reprinted figure with permission from (Hasan 2010). Copyright 2010 by the American Physical Society.	14
3.2. Topological surface states arising from the inverted band gaps of $\text{Hg}_x\text{Cd}_{1-x}\text{Te}/\text{HgTe}$ quantum wells and Bi_2Se_3 . (a) Reprinted from (Pankratov 1987), Copyright 1987, with permission from Elsevier. (b, c) Reprinted by permission from Macmillan Publishers Ltd: (Zhang 2009a), copyright 2009.	15

3.3.	Atomic structure of Bi_2Se_3 . Reprinted by permission from Macmillan Publishers Ltd: (Zhang 2009a), copyright 2009.	16
3.4.	ARPES data of various topological insulators. (a) Reprinted by permission from Macmillan Publishers Ltd: (Xia 2009), copyright 2009. (b) (Wang 2010) With kind permission from Springer Science and Business Media. (c, d) Reprinted by permission from Macmillan Publishers Ltd: (Hsieh 2009a), copyright 2009.	18
3.5.	Suppression of backscattering within the Dirac cone observed by Fourier-transformed STM. Reprinted by permission from Macmillan Publishers Ltd: (Roushan 2009), copyright 2009.	19
3.6.	Time-resolved pump-and-probe measurements following the response of Bi_2Se_3 to an optical excitation. (a, b) Reprinted by permission from Macmillan Publishers Ltd: (McIver 2012), copyright 2012. (c, d) Reprinted figure with permission from (Hsieh 2011). Copyright 2011 by the American Physical Society. (e, f, g) Reprinted figure with permission from (Sobota 2012). Copyright 2012 by the American Physical Society.	20
3.7.	Electron thermalization and cooling at the surface of bismuth chalcogenides. (a, b) Reprinted with permission from (Hajlaoui 2012). Copyright 2012 American Chemical Society. (c, d) Reprinted figure with permission from (Wang 2012a). Copyright 2012 by the American Physical Society.	21
4.1.	Energy diagram of the photoemission process.	23
4.2.	Reference frame.	24
4.3.	Helical orbital angular momentum structure of the surface state of Bi_2Se_3 . (a) Reprinted figure with permission from (Park 2012b). Copyright 2012 by the American Physical Society. (b, c) (Cao 2012) With kind permission from Prof. Daniel Dessau.	25
4.4.	Circular dichroism in angle-resolved photoemission from Bi_2Se_3 . (a, b, c) With kind permission from Dr. Yihua Wang. (d, e) Reprinted figure with permission from (Park 2012b). Copyright 2012 by the American Physical Society.	26
4.5.	Photon energy dependence of the 2PPE intensity. (b) (Steinmann 1989) With kind permission from Springer Science and Business Media.	29
4.6.	Screening of an external charge by a surface charge redistribution.	30
4.7.	Laser setup, real-space image and schematic drawing.	32
4.8.	Schematic drawing of the ellipsoidal display-type analyzer	34
5.1.	Angle-resolved photoemission from image-potential states and Shockley-type surface states of graphene/Ir(111). (Niesner 2012a) Copyright 2012 by the American Physical Society.	42
5.2.	Resonance effects in 2PPE between the surface state and the image-potential states of graphene/Ir(111). (Niesner 2012a) Copyright 2012 by the American Physical Society.	43

5.3.	Coverage-dependence of the work function and the binding energies of the image-potential states of graphene/Ir(111). (Niesner 2012a) Copyright 2012 by the American Physical Society.	44
5.4.	Time-resolved 2PPE of image-potential states of graphene/Ir(111). (Niesner 2012a) Copyright 2012 by the American Physical Society.	45
5.5.	Energy dependence of the decay rate of the first image-potential state of graphene/Ir(111). (a) Inset adapted from (Boger 2004).	47
5.6.	ARPES data of graphene/Ir(100)	48
5.7.	2PPE intensity map of the image-potential states of graphene/Ir(100). . .	49
5.8.	2PPE data of graphene/Ir(100)	50
5.9.	Angle-resolved 2PPE data of graphene on Pt(111), Au/Ni(111) and SiC(0001)	51
5.10.	Time-resolved 2PPE data of graphene on Ir(100), Pt(111), Au/Ni(111) and SiC(0001)	51
5.11.	Work function of the graphene-covered surfaces and comparison to the capacitor model.	54
5.12.	Screening of an external charge by a two-dimensional metallic sheet. . . .	55
5.13.	Dirac point energy, binding energy of the first IP state and work function of graphene on different substrates.	56
6.1.	Cleaving of topological insulator crystals.	61
6.2.	LEED diffraction patterns of topological insulators.	61
6.3.	Relaxation of the electronic structure after cleaving.	63
6.4.	ARPES data of the conventional, occupied Dirac cone of the bismuth chalcogenides under investigation and comparison to theory. (d) (Niesner 2012b) Copyright 2012 by the American Physical Society. (e, f) (Chulkov 2012)	65
6.5.	2PPE survey spectrum of Bi ₂ Te ₂ Se and comparison to theory. (a) (Niesner 2012b) Copyright 2012 by the American Physical Society. (b, c) (Chulkov 2012)	66
6.6.	2PPE data of the additional high-lying topological surface state of Bi ₂ Se ₃ and comparison to theory and the conventional, occupied Dirac cone. (a, b, c) (Niesner 2012b) Copyright 2012 by the American Physical Society. (d) Reprinted figure with permission from (Wang 2011a). Copyright 2011 by the American Physical Society.	67
6.7.	Comparison between 2PPE data of the high-lying Dirac cone of Bi ₂ Te ₂ Se and Bi ₂ Te ₃ and the calculated band structure. (Niesner 2012b) Copyright 2012 by the American Physical Society.	69
6.8.	Comparison between monochromatic and bichromatic 2PPE spectra of Bi ₂ Te ₂ Se.	71
6.9.	Time-resolved 2PPE data of Bi ₂ Te ₂ Se	72
6.10.	Angle-resolved 2PPE of SnSb ₂ Te ₄ and comparison to DFT calculations. (c) (Chulkov 2012)	74
6.11.	Time-resolved 2PPE of the topological surface state of SnSb ₂ Te ₄	76

List of Figures

A.1. Raman survey spectra of graphene/iridium	84
A.2. Raman spectra of the G-Peak region of graphene/iridium.	85
A.3. Comparison of the observed Raman peak positions to the phonon dispersion of graphene. Reprinted figure with permission from (Mohr 2007). Copyright 2007 by the American Physical Society.	86
A.4. 2PPE EDCs of graphene/Ir(111).	87
A.5. 2PPE EDC of graphene/SiC(0001)	88
A.6. Monochromatic 2PPE survey spectra of Bi ₂ Se ₃ and comparison to calculations. (b, c) (Chulkov 2012)	89
A.7. Monochromatic 2PPE survey spectra of Bi ₂ Te ₂ Se and comparison to calculations. (b, c) (Chulkov 2012)	89
A.8. 2PPE circular dichroism pattern of Bi ₂ Se ₃ and Bi ₂ Te ₂ Se.	90
A.9. Angle-resolved bichromatic 2PPE spectra of Bi ₂ Te ₂ Se recorded at different pump-probe delays.	91
A.10. Time-resolved bichromatic 2PPE spectra of Bi ₂ Te ₂ Se.	92

Bibliography

- Aizawa, T., Souda, R., Ishizawa, Y., Hirano, H., Yamada, T., Tanaka, K. ichi, and Oshima, C. (1990). “Phonon dispersion in monolayer graphite formed on Ni(111) and Ni(001)”. *Surface Science* **237**, 1 - 3, pp. 194–202 (cit. on pp. 5, 85).
- Aizawa, T., Hwang, Y., Hayami, W., Souda, R., Otani, S., and Ishizawa, Y. (1992). “Phonon dispersion of monolayer graphite on Pt(111) and NbC surfaces: bond softening and interface structures”. *Surface Science* **260**, 1 - 3, pp. 311–318 (cit. on p. 85).
- Allard, A. and Wirtz, L. (2010). “Graphene on Metallic Substrates: Suppression of the Kohn Anomalies in the Phonon Dispersion”. *Nano Letters* **10**, 11, pp. 4335–4340 (cit. on p. 5).
- Altenburg, S. J., Kröger, J., Wehling, T. O., Sachs, B., Lichtenstein, A. I., and Berndt, R. (05/2012). “Local Gating of an Ir(111) Surface Resonance by Graphene Islands”. *Physical Review Letters* **108**, 20, p. 206805 (cit. on p. 9).
- Analytis, J. G., Chu, J.-H., Chen, Y., Corredor, F., McDonald, R. D., Shen, Z. X., and Fisher, I. R. (05/2010a). “Bulk Fermi surface coexistence with Dirac surface state in Bi_2Se_3 : A comparison of photoemission and Shubnikov-de Haas measurements”. *Physical Review B* **81**, 20, p. 205407 (cit. on pp. 17, 63).
- Analytis, J. G., McDonald, R. D., Riggs, S. C., Chu, J.-H., Boebinger, G. S., and Fisher, I. R. (12/2010b). “Two-dimensional surface state in the quantum limit of a topological insulator”. *Nature Physics* **6**, 12, pp. 960–964 (cit. on p. 17).
- Anderson, P. W. (03/1958). “Absence of Diffusion in Certain Random Lattices”. *Physical Review* **109**, 5, pp. 1492–1505 (cit. on pp. 16, 55).
- Ando, T. (07/2006). “Screening Effect and Impurity Scattering in Monolayer Graphene”. *Journal of the Physical Society of Japan* **75**, 7, p. 074716 (cit. on p. 57).
- Ando, T., Zheng, Y., and Suzuura, H. (05/2002). “Dynamical Conductivity and Zero-Mode Anomaly in Honeycomb Lattices”. *Journal of the Physical Society of Japan* **71**, p. 1318 (cit. on p. 7).
- Araujo, P. T., Mafra, D. L., Sato, K., Saito, R., Kong, J., and Dresselhaus, M. S. (07/2012). “Phonon Self-Energy Corrections to Nonzero Wave-Vector Phonon Modes in Single-Layer Graphene”. *Physical Review Letters* **109**, 4, p. 046801 (cit. on p. 83).
- Armbrust, N., Gütde, J., Jakob, P., and Höfer, U. (01/2012). “Time-Resolved Two-Photon Photoemission of Unoccupied Electronic States of Periodically Rippled Graphene on Ru(0001)”. *Physical Review Letters* **108**, 5, p. 056801 (cit. on pp. 35, 46, 58).
- Bae, S., Kim, H., Lee, Y., Xu, X., Park, J.-S., Zheng, Y., Balakrishnan, J., Lei, T., Ri Kim, H., Song, Y. I., Kim, Y.-J., Kim, K. S., Ozyilmaz, B., Ahn, J.-H., Hong, B. H., and Iijima, S. (08/2010). “Roll-to-roll production of 30-inch graphene films for transparent electrodes”. *Nature Nanotechnology* **5**, 8, pp. 574–578 (cit. on pp. 5, 7, 8).
- Baskin, Y. and Meyer, L. (10/1955). “Lattice Constants of Graphite at Low Temperatures”. *Physical Review* **100**, 2, pp. 544–544 (cit. on p. 35).
- Batzill, M. (2012). “The surface science of graphene: Metal interfaces, CVD synthesis, nanoribbons, chemical modifications, and defects”. *Surface Science Reports* **67**, 3 - 4, pp. 83–115 (cit. on p. 7).
- Bekker, T., Kokh, A., Popov, V., Mokrushnikov, P., and Kokh, K. (2005). “Hydrothermal crystal growth under rotation of external heat field”. *Journal of Crystal Growth* **275**, 1 - 2. Proceedings of the 14th International Conference on Crystal Growth and the 12th International Conference on Vapor Growth and Epitaxy, e1481–e1486 (cit. on p. 60).
- Benia, H. M., Lin, C., Kern, K., and Ast, C. R. (10/2011). “Reactive Chemical Doping of the Bi_2Se_3 Topological Insulator”. *Physical Review Letters* **107**, 17, p. 177602 (cit. on pp. 17, 63).

- Bernevig, B. A., Hughes, T. L., and Zhang, S.-C. (2006). “Quantum Spin Hall Effect and Topological Phase Transition in HgTe Quantum Wells”. *Science* **314**, 5806, pp. 1757–1761 (cit. on pp. 2, 13, 15).
- Bertoni, G., Calmels, L., Altibelli, A., and Serin, V. (02/2005). “First-principles calculation of the electronic structure and EELS spectra at the graphene/Ni(111) interface”. *Physical Review B* **71**, 7, p. 075402 (cit. on p. 9).
- Bianchi, M., Guan, D., Bao, S., Mi, J., Iversen, B. B., King, P. D., and Hofmann, P. (11/2010). “Coexistence of the topological state and a two-dimensional electron gas on the surface of Bi₂Se₃”. *Nature Communications* **1**, 8, p. 128 (cit. on pp. 3, 17, 60, 63–65).
- Bistritzer, R. and MacDonald, A. H. (05/2009). “Electronic Cooling in Graphene”. *Physical Review Letters* **102**, 20, p. 206410 (cit. on p. 21).
- Boger, K. (2004). *Streuung heißer Elektronen an Adatomen auf Metalloberflächen*. Doctoral thesis, Lehrstuhl für Festkörperphysik, Department für Physik der Universität Erlangen-Nürnberg (cit. on pp. 30, 31, 33, 47, 73, 93).
- Boger, K., Roth, M., Weinelt, M., Fauster, T., and Reinhard, P.-G. (01/2002). “Linewidths in energy-resolved two-photon photoemission spectroscopy”. *Physical Review B* **65**, 7, p. 075104 (cit. on pp. 30, 46).
- Boger, K., Weinelt, M., and Fauster, T. (03/2004). “Scattering of Hot Electrons by Adatoms at Metal Surfaces”. *Physical Review Letters* **92**, 12, p. 126803 (cit. on p. 30).
- Boger, K., Fauster, T., and Weinelt, M. (2005). “Elastic scattering in image-potential bands observed by two-photon photoemission”. *New Journal of Physics* **7**, 1, p. 110 (cit. on p. 46).
- Bonaccorso, F., Sun, Z., Hasan, T., and Ferrari, A. C. (09/2010). “Graphene photonics and optoelectronics”. *Nature Photonics* **4**, 9, pp. 611–622 (cit. on p. 7).
- Borca, B., Barja, S., Garnica, M., Sánchez-Portal, D., Silkin, V. M., Chulkov, E. V., Hermanns, C. F., Hinarejos, J. J., Parga, A. L., Vázquez de, Arnau, A., Echenique, P. M., and Miranda, R. (07/2010). “Potential Energy Landscape for Hot Electrons in Periodically Nanostructured Graphene”. *Physical Review Letters* **105**, 3, p. 036804 (cit. on pp. 35, 56).
- Bose, S., Silkin, V. M., Ohmann, R., Brihuega, I., Vitali, L., Michaelis, C. H., Mallet, P., Veuillen, J. Y., Schneider, M. A., Chulkov, E. V., Echenique, P. M., and Kern, K. (2010). “Image potential states as a quantum probe of graphene interfaces”. *New Journal of Physics* **12**, 2, p. 023028 (cit. on pp. 35, 46, 58, 88).
- Bostwick, A., Ohta, T., Seyller, T., Horn, K., and Rotenberg, E. (01/2007). “Quasiparticle dynamics in graphene”. *Nature Physics* **3**, pp. 36–40 (cit. on pp. 11, 35, 54, 55).
- Boyd, R. W. (04/2008). *Nonlinear Optics, Third Edition*. 3rd ed. Academic Press (cit. on p. 32).
- Brako, R., Šokčević, D., Lazić, P., and Atodiresei, N. (2010). “Graphene on the Ir(111) surface: from van der Waals to strong bonding”. *New Journal of Physics* **12**, 11, p. 113016 (cit. on p. 9).
- Broekman, L., Tadich, A., Huwald, E., Riley, J., Leckey, R., Seyller, T., Emtsev, K., and Ley, L. (2005). “First results from a second generation toroidal electron spectrometer”. *Journal of Electron Spectroscopy and Related Phenomena* **145 - 147**, 0. Proceeding of the Fourteenth International Conference on Vacuum Ultraviolet Radiation Physics, pp. 1001–1004 (cit. on p. 41).
- Busse, C., Lazić, P., Djemour, R., Coraux, J., Gerber, T., Atodiresei, N., Caciuc, V., Brako, R., N’Diaye, A. T., Blügel, S., Zegenhagen, J., and Michely, T. (07/2011). “Graphene on Ir(111): Physisorption with Chemical Modulation”. *Physical Review Letters* **107**, 3, p. 036101 (cit. on pp. 9, 35, 46, 47, 54, 57).
- Cançado, L. G., Jorio, A., Ferreira, E. H. M., Stavale, F., Achete, C. A., Capaz, R. B., Moutinho, M. V. O., Lombardo, A., Kulmala, T. S., and Ferrari, A. C. (2011). “Quantifying Defects in Graphene via Raman Spectroscopy at Different Excitation Energies”. *Nano Letters* **11**, 8, pp. 3190–3196 (cit. on p. 83).

- Cao, J., Gao, Y., Miller, R. J. D., Elsayed-Ali, H. E., and Mantell, D. A. (07/1997). “Femtosecond photoemission study of ultrafast electron dynamics on Cu(100)”. *Physical Review B* **56**, 3, pp. 1099–1102 (cit. on p. 30).
- Cao, Y., Waugh, J. A., Zhang, X.-W., Luo, J.-W., Wang, Q., Reber, T. J., Mo, S. K., Xu, Z., Yang, A., Schneeloch, J., Gu, G., Brahlek, M., Bansal, N., Oh, S., Zunger, A., and Dessau, D. S. (09/2012). *In-Plane Orbital Texture Switch at the Dirac Point in the Topological Insulator Bi₂Se₃*. arXiv:1209.1016, arXiv pre-print (cit. on pp. 25, 27, 71, 94).
- Cardona, M. (1982). *Light Scattering in Solids II: Basic Concepts and Instrumentation*. Ed. by G. Guntherodt. Springer-Verlag, Berlin - Heidelberg - New York (cit. on p. 83).
- Casiraghi, C., Pisana, S., Novoselov, K. S., Geim, A. K., and Ferrari, A. C. (12/2007). “Raman fingerprint of charged impurities in graphene”. *Applied Physics Letters* **91**, 23, p. 233108 (cit. on p. 83).
- Checkelsky, J. G., Hor, Y. S., Cava, R. J., and Ong, N. P. (05/2011). “Bulk Band Gap and Surface State Conduction Observed in Voltage-Tuned Crystals of the Topological Insulator Bi₂Se₃”. *Physical Review Letters* **106**, 19, p. 196801 (cit. on pp. 17, 77).
- Chen, J.-H., Jang, C., Adam, S., Fuhrer, M. S., Williams, E. D., and Ishigami, M. (05/2008). “Charged-impurity scattering in graphene”. *Nature Physics* **4**, 5, pp. 377–381 (cit. on p. 57).
- Chen, J.-H., Jang, C., Ishigami, M., Xiao, S., Cullen, W., Williams, E., and Fuhrer, M. (2009a). “Diffusive charge transport in graphene on SiO₂”. *Solid State Communications* **149**, 27 – 28. Recent Progress in Graphene Studies, pp. 1080 –1086 (cit. on p. 57).
- Chen, Y. L., Analytis, J. G., Chu, J.-H., Liu, Z. K., Mo, S.-K., Qi, X. L., Zhang, H. J., Lu, D. H., Dai, X., Fang, Z., Zhang, S. C., Fisher, I. R., Hussain, Z., and Shen, Z.-X. (2009b). “Experimental Realization of a Three-Dimensional Topological Insulator, Bi₂Te₃”. *Science* **325**, 5937, pp. 178–181 (cit. on pp. 3, 13, 16, 62, 64, 77).
- Chiang, C.-T., Winkelmann, A., Yu, P., and Kirschner, J. (08/2009). “Magnetic Dichroism from Optically Excited Quantum Well States”. *Physical Review Letters* **103**, 7, p. 077601 (cit. on pp. 31, 68).
- Chiang, C.-T., Winkelmann, A., Yu, P., Kirschner, J., and Henk, J. (03/2010). “Spin-orbit coupling in unoccupied quantum well states: Experiment and theory for Co/Cu(001)”. *Physical Review B* **81**, 11, p. 115130 (cit. on p. 31).
- Chulkov, E. V. (2012). *private communication* (cit. on pp. 65, 68, 73, 74, 89).
- Collins, G. P. (2006). “Computing with Quantum Knots”. *Scientific American* **294**, 4, pp. 56–63 (cit. on p. 2).
- Conrad, H., Küppers, J., Nitschké, F., and Plagge, A. (1977). “Oxidation of Ir(111) surfaces; a combined LEED/UPS study”. *Surface Science* **69**, 2, pp. 668 –676 (cit. on pp. 9, 36).
- Coraux, J., N’Diaye, A. T., Engler, M., Busse, C., Wall, D., Buckanie, N., Heringdorf, F.-J. Meyer zu Gastel, R. van, Poelsema, B., and Michely, T. (2009). “Growth of graphene on Ir(111)”. *New Journal of Physics* **11**, 2, p. 023006 (cit. on pp. 9, 36, 44, 47, 58).
- Crepaldi, A., Ressel, B., Cilento, F., Zacchigna, M., Grazioli, C., Berger, H., Bugnon, P., Kern, K., Grioni, M., and Parmigiani, F. (11/2012). “Ultrafast photodoping and effective Fermi-Dirac distribution of the Dirac particles in Bi₂Se₃”. *Physical Review B* **86**, 20, p. 205133 (cit. on pp. 20, 21, 30).
- Dadap, J., Kralj, M., Petrović, M., Knox, K., Zaki, N., Bhandari, R., Yeh, P. C., and Osgood, R. M. (2011). *Characterization of Image States in Graphene on Ir(111)*. Bulletin of the American Physical Society APS March Meeting 2011 Volume 56, Number 1 (cit. on p. 46).
- Das, A., Pisana, S., Chakraborty, B., Piscanec, S., Saha, K. S., Waghmare, U. V., Novoselov, K. S., Krishnamurthy, H. R., Geim, A. K., Ferrari, A. C., and Sood, A. K. (04/2008). “Monitoring dopants by Raman scattering in an electrochemically top-gated graphene transistor”. *Nature Nanotechnology* **3**, 4, pp. 210–215 (cit. on p. 83).
- Datta, S. and Das, B. (02/1990). “Electronic analog of the electro-optic modulator”. *Applied Physics Letters* **56**, 7, pp. 665–667 (cit. on p. 16).

- Davis, S., Zaera, F., Gordon, B., and Somorjai, G. (1985). “Radiotracer and thermal desorption studies of dehydrogenation and atmospheric hydrogenation of organic fragments obtained from [¹⁴C]ethylene chemisorbed over Pt(111) surfaces”. *Journal of Catalysis* **92**, 2, pp. 240–246 (cit. on p. 37).
- Dedkov, Y. S., Fonin, M., and Laubschat, C. (2008a). “A possible source of spin-polarized electrons: The inert graphene/Ni(111) system”. *Applied Physics Letters* **92**, 5, p. 052506 (cit. on p. 40).
- Dedkov, Y. S., Fonin, M., Rudiger, U., and Laubschat, C. (2008b). “Graphene-protected iron layer on Ni(111)”. *Applied Physics Letters* **93**, 2, p. 022509 (cit. on p. 40).
- Dedkov, Y. S., Fonin, M., Rüdiger, U., and Laubschat, C. (03/2008c). “Rashba Effect in the Graphene/Ni(111) System”. *Physical Review Letters* **100**, 10, p. 107602 (cit. on p. 35).
- Dirac, P. A. M. (02/1928). “The Quantum Theory of the Electron”. *Proceedings of the Royal Society of London. Series A, Containing Papers of a Mathematical and Physical Character* **117**, 778, pp. 610–624 (cit. on p. 6).
- Dresselhaus, M. S., Dresselhaus, G., Saito, R., and Jorio, A. (2005). “Raman spectroscopy of carbon nanotubes”. *Physics Reports* **409**, 2, pp. 47–99 (cit. on pp. 83, 85).
- Dresselhaus, M. S., Jorio, A., and Saito, R. (04/2010). “Characterizing Graphene, Graphite, and Carbon Nanotubes by Raman Spectroscopy”. *Annual Review of Condensed Matter Physics* **1**, p. 89 (cit. on pp. 5, 6).
- Driel, H. M. van (05/1987). “Kinetics of high-density plasmas generated in Si by 1.06- and 0.53- μ m picosecond laser pulses”. *Physical Review B* **35**, 15, pp. 8166–8176 (cit. on p. 75).
- Dütemeyer, T., Quitmann, C., Kitz, M., Dörnemann, K., O., J. S., and Reihl, B. (2001). “Photoelectron imaging using an ellipsoidal display analyzer”. *Review of Scientific Instruments* **72**, 6, pp. 2638–2648 (cit. on p. 34).
- Eastman, D. E., Donelon, J. J., Hien, N. C., and Himpfel, F. J. (1980). “An ellipsoidal mirror display analyzer system for electron energy and angular measurements”. *Nuclear Instruments and Methods* **172**, 1–2, pp. 327–336 (cit. on p. 34).
- Echenique, P. and Pendry, J. (1978). “The existence and detection of Rydberg states at surfaces”. *Journal of Physics C: Solid State Physics* **11**, 10, p. 2065 (cit. on pp. 30, 31, 42, 44, 54, 55, 57).
- Echenique, P. and Uranga, M. (1991). “Image potential states at surfaces”. *Surface Science* **247**, 2–3, pp. 125–132 (cit. on p. 31).
- Echenique, P., Berndt, R., Chulkov, E., Fauster, T., Goldmann, A., and Höfer, U. (2004). “Decay of electronic excitations at metal surfaces”. *Surface Science Reports* **52**, 7–8, pp. 219–317 (cit. on pp. 30, 31, 45).
- Eickhoff, C. (2010). *Zeitaufgelöste Zweiphotonen-Photoemission an der Si(001)-Oberfläche, Dynamik heißer Elektronen und zweidimensionaler Fano-Effekt*. Doctoral Thesis, Department of Physics, Freie Universität Berlin (cit. on p. 41).
- Emtsev, K. V., Speck, F., Seyller, T., Ley, L., and Riley, J. D. (04/2008). “Interaction, growth, and ordering of epitaxial graphene on SiC(0001) surfaces: A comparative photoelectron spectroscopy study”. *Physical Review B* **77**, 15, p. 155303 (cit. on pp. 10, 11, 40, 54).
- Emtsev, K. V., Bostwick, A., Horn, K., Jobst, J., Kellogg, G. L., Ley, L., McChesney, J. L., Ohta, T., Reshanov, S. A., Röhrl, J., Rotenberg, E., Schmid, A. K., Waldmann, D., Weber, H. B., and Seyller, T. (03/2009). “Towards wafer-size graphene layers by atmospheric pressure graphitization of silicon carbide”. *Nature Materials* **8**, 3, pp. 203–207 (cit. on pp. 1, 11, 37, 53, 54).
- Eremeev, S. (2012). *private communication* (cit. on pp. 71, 94).
- Falkovsky, L. A. and Varlamov, A. A. (2007). “Space-time dispersion of graphene conductivity”. *The European Physical Journal B* **56**, 4, pp. 281–284 (cit. on p. 7).
- Fann, W. S., Storz, R., Tom, H. W. K., and Bokor, J. (05/1992a). “Direct measurement of nonequilibrium electron-energy distributions in subpicosecond laser-heated gold films”. *Physical Review Letters* **68**, 18, pp. 2834–2837 (cit. on p. 30).

- (11/1992b). “Electron thermalization in gold”. *Physical Review B* **46**, 20, pp. 13592–13595 (cit. on p. 30).
- Fauster, T. (1994). “Calculation of surface states using a one-dimensional scattering model”. *Applied Physics A* **59**, 6, pp. 639–643 (cit. on p. 30).
- Fauster, T., Himpfel, F. J., Fischer, J. E., and Plummer, E. W. (08/1983). “Three-Dimensional Energy Band in Graphite and Lithium-Intercalated Graphite”. *Physical Review Letters* **51**, 5, pp. 430–433 (cit. on p. 56).
- Fauster, T. and Steinmann, W. (1995). “Two-photon photoemission spectroscopy of image states”. In: *Electromagnetic Waves: Recent Developments in Research*. Editor: P. Halevi, Elsevier (Amsterdam) (cit. on pp. 42, 54, 55).
- Fauster, T., Reuß, C., Shumay, I. L., and Weinelt, M. (2000). “Femtosecond two-photon photoemission studies of image-potential states”. *Chemical Physics* **251**, 1 - 3, pp. 111–121 (cit. on p. 31).
- Ferrari, A. C. and Robertson, J. (05/2000). “Interpretation of Raman spectra of disordered and amorphous carbon”. *Physical Review B* **61**, 20, pp. 14095–14107 (cit. on p. 83).
- Ferrari, A. C., Meyer, J. C., Scardaci, V., Casiraghi, C., Lazzeri, M., Mauri, F., Piscanec, S., Jiang, D., Novoselov, K. S., Roth, S., and Geim, A. K. (10/2006). “Raman Spectrum of Graphene and Graphene Layers”. *Physical Review Letters* **97**, 18, p. 187401 (cit. on pp. 7, 83).
- Ferstl, P. (2010). *Wachstum von Graphen auf der Iridium(100)-Oberfläche*. Bachelor thesis, Lehrstuhl für Festkörperphysik, Department für Physik der Universität Erlangen-Nürnberg (cit. on pp. 36, 39, 47, 49, 58).
- Ferstl, P., Gubo, M., Hammer, L., and Schneider, M. A. (2011). *Growth of Graphene on Ir(100)*. Verhandlungen der Deutschen Physikalischen Gesellschaft (cit. on pp. 39, 47–49, 58, 79, 82).
- Filleter, T., Emtsev, K. V., Seyller, T., and Bennewitz, R. (09/2008). “Local work function measurements of epitaxial graphene”. *Applied Physics Letters* **93**, 13, p. 133117 (cit. on pp. 9, 35, 54, 57).
- Fischer, R., Schuppler, S., Fischer, N., Fauster, T., and Steinmann, W. (02/1993). “Image states and local work function for Ag/Pd(111)”. *Physical Review Letters* **70**, 5, pp. 654–657 (cit. on pp. 31, 44, 49).
- Fischer, R. and Fauster, T. (03/1995). “Coupling of image states to quantum-well states for Au on Pd(111)”. *Physical Review B* **51**, 11, pp. 7112–7115 (cit. on p. 31).
- Fischer, R., Fauster, T., von der Linden, W., and Dose, V. (1996). “Island-Size Distributions of Ag on Pd(111)”. *Surface Review and Letters* **3**, 3, pp. 1393–1402 (cit. on p. 31).
- Fromm, F. (2011). *private communication* (cit. on p. 37).
- Fu, L. (12/2009). “Hexagonal Warping Effects in the Surface States of the Topological Insulator Bi_2Te_3 ”. *Physical Review Letters* **103**, 26, p. 266801 (cit. on pp. 25, 26).
- Fu, L., Kane, C. L., and Mele, E. J. (03/2007a). “Topological Insulators in Three Dimensions”. *Physical Review Letters* **98**, 10, p. 106803 (cit. on pp. 3, 13, 14, 16, 59).
- Fu, L. and Kane, C. L. (07/2007b). “Topological insulators with inversion symmetry”. *Physical Review B* **76**, 4, p. 045302 (cit. on pp. 3, 13, 16).
- (03/2008). “Superconducting Proximity Effect and Majorana Fermions at the Surface of a Topological Insulator”. *Physical Review Letters* **100**, 9, p. 096407 (cit. on pp. 2, 16).
- Gao, M., Pan, Y., Huang, L., Hu, H., Zhang, L. Z., Guo, H. M., Du, S. X., and Gao, H.-J. (2011). “Epitaxial growth and structural property of graphene on Pt(111)”. *Applied Physics Letters* **98**, 3, p. 033101 (cit. on pp. 9, 11, 36, 39).
- Gastel, R. van, N’Diaye, A. T., Wall, D., Coraux, J., Busse, C., Buckanie, N. M., Meyer zu Heringdorf, F.-J., Horn-von Hoegen, M., Michely, T., and Poelsema, B. (2009). “Selecting a single orientation for millimeter sized graphene sheets”. *Applied Physics Letters* **95**, 12, p. 121901 (cit. on pp. 9, 36, 38, 47, 58).
- Geim, A. K. and Novoselov, K. S. (2007). “The rise of graphene”. *Nature Materials* **6**, pp. 183–191 (cit. on pp. 35, 48).

- Geim, A. K. and Novoselov, K. S. (2010). *The Nobel Prize in Physics*. http://www.nobelprize.org/nobel_prizes/physics/laureates/2010/ (cit. on pp. 1, 5).
- Gierz, I., Suzuki, T., Weitz, R. T., Lee, D. S., Krauss, B., Riedl, C., Starke, U., Höchst, H., Smet, J. H., Ast, C. R., and Kern, K. (06/2010). “Electronic decoupling of an epitaxial graphene monolayer by gold intercalation”. *Physical Review B* **81**, 23, p. 235408 (cit. on p. 11).
- Giesen, K., Hage, F., Himpfel, F. J., Riess, H. J., and Steinmann, W. (04/1986). “Hydrogenic image-potential states: A critical examination”. *Physical Review B* **33**, 8, pp. 5241–5244 (cit. on pp. 28, 29, 43, 53).
- Giesen, K., Hage, F., Himpfel, F. J., Riess, H. J., Steinmann, W., and Smith, N. V. (01/1987). “Effective mass of image-potential states”. *Physical Review B* **35**, 3, pp. 975–978 (cit. on p. 31).
- Giovannetti, G., Khomyakov, P. A., Brocks, G., Karpan, V. M., Brink, J. van den, and Kelly, P. J. (07/2008). “Doping Graphene with Metal Contacts”. *Physical Review Letters* **101**, 2, p. 026803 (cit. on pp. 11, 12, 35, 52, 54, 58, 79, 81).
- Gland, J. L., Sexton, B. A., and Fisher, G. B. (1980). “Oxygen interactions with the Pt(111) surface”. *Surface Science* **95**, 2 - 3, pp. 587–602 (cit. on pp. 9, 36).
- Goldman, J. R. and Prybyla, J. A. (02/1994). “Ultrafast dynamics of laser-excited electron distributions in silicon”. *Physical Review Letters* **72**, 9, pp. 1364–1367 (cit. on p. 30).
- Göppert-Mayer, M. (2009). “Elementary processes with two quantum transitions”. *Annalen der Physik* **18**, 7 - 8, pp. 466–479 (cit. on p. 104).
- Göppert-Mayer, M. (1931). “Über Elementarakte mit zwei Quantensprüngen”. *Translated reprint in Reference Göppert-Mayer (2009). Annalen der Physik* **401**, 3, pp. 273–294 (cit. on p. 28).
- Graphene Industries Limited, M. (2012). <http://grapheneindustries.com> (cit. on p. 7).
- Gubo, M. (2006). *Messung von Elektronen aus Bildpotentialzuständen mit einem Display-Analysator*. Diploma thesis, Lehrstuhl für Festkörperphysik, Department für Physik der Universität Erlangen-Nürnberg (cit. on p. 34).
- (2009). *private communication* (cit. on p. 36).
 - (2010). *Epitaktische Kobaltoxid-Filme auf Ir(100)*. Dissertation, Lehrstuhl für Festkörperphysik, Department für Physik der Universität Erlangen-Nürnberg (cit. on pp. 33, 36).
- Güdde, J., Rohleder, M., Meier, T., Koch, S. W., and Höfer, U. (2007). “Time-Resolved Investigation of Coherently Controlled Electric Currents at a Metal Surface”. *Science* **318**, 5854, pp. 1287–1291 (cit. on p. 43).
- Gugel, D. (2011). *Zweiphotonen-Photoemissionsspektroskopie von Graphen auf Siliziumkarbid SiC(0001)*. Diploma thesis, Lehrstuhl für Festkörperphysik, Department für Physik der Universität Erlangen-Nürnberg (cit. on pp. 37, 38, 50, 53).
- Gugel, D., Niesner, D., Speck, F., Seyller, T., and Fauster, T. (2011). *Two-photon photoelectron spectroscopy of graphene on SiC(0001)*. Verhandlungen der Deutschen Physikalischen Gesellschaft (cit. on pp. 50, 53).
- Gusynin, V. P. and Sharapov, S. G. (09/2005). “Unconventional Integer Quantum Hall Effect in Graphene”. *Physical Review Letters* **95**, 14, p. 146801 (cit. on p. 1).
- Gusynin, V. P., Sharapov, S. G., and Carbotte, J. P. (06/2006). “Unusual Microwave Response of Dirac Quasiparticles in Graphene”. *Physical Review Letters* **96**, 25, p. 256802 (cit. on p. 7).
- Hadjarab, F. and Erskine, J. (1985). “Image properties of the hemispherical analyzer applied to multichannel energy detection”. *Journal of Electron Spectroscopy and Related Phenomena* **36**, 3, pp. 227–243 (cit. on p. 33).
- Haines, L. K. and Roberts, D. H. (11/1969). “One-Dimensional Hydrogen Atom”. *American Journal of Physics* **37**, 9, pp. 1145–1154 (cit. on p. 31).
- Hajlaoui, M., Papalazarou, E., Mauchain, J., Lantz, G., Moisan, N., Boschetto, D., Jiang, Z., Miotkowski, I., Chen, Y. P., Taleb-Ibrahimi, A., Perfetti, L., and Marsi, M. (2012). “Ultrafast Surface Carrier Dynamics in the Topological Insulator Bi₂Te₃”. *Nano Letters* **12**, 7, pp. 3532–3536 (cit. on pp. 20, 21, 29, 75, 77).

- Hamada, I. and Otani, M. (10/2010). “Comparative van der Waals density-functional study of graphene on metal surfaces”. *Physical Review B* **82**, 15, p. 153412 (cit. on p. 9).
- Hämäläinen, S. K., Sun, Z., Boneschanscher, M. P., Uppstu, A., Ijäs, M., Harju, A., Vanmaekelbergh, D., and Liljeroth, P. (11/2011). “Quantum-Confined Electronic States in Atomically Well-Defined Graphene Nanostructures”. *Physical Review Letters* **107**, 23, p. 236803 (cit. on p. 9).
- Hamilton, J. and Blakely, J. (1980). “Carbon segregation to single crystal surfaces of Pt, Pd and Co”. *Surface Science* **91**, 1, pp. 199–217 (cit. on pp. 7, 9, 11, 38).
- Han, G. H., Shin, H.-J., Kim, E. S., Chae, S. J., Choi, J.-Y., and Lee, Y. H. (2011). “Poly(ethylene co-vinyl Acetate)-Assisted One-Step Transfer of Ultra-Large Graphene”. *Nano* **06**, 01, pp. 59–65 (cit. on p. 1).
- Hanfland, M., Beister, H., and Syassen, K. (06/1989). “Graphite under pressure: Equation of state and first-order Raman modes”. *Physical Review B* **39**, 17, pp. 12598–12603 (cit. on p. 83).
- Hao, Z., Dadap, J. I., Knox, K. R., Yilmaz, M. B., Zaki, N., Johnson, P. D., and Osgood, R. M. (07/2010). “Nonequilibrium Band Mapping of Unoccupied Bulk States below the Vacuum Level by Two-Photon Photoemission”. *Physical Review Letters* **105**, 1, p. 017602 (cit. on p. 41).
- Hasan, M. Z. and Kane, C. L. (11/2010). “Colloquium: Topological insulators”. *Review of Modern Physics* **82**, 4, pp. 3045–3067 (cit. on pp. 2, 13, 14).
- Hattab, H., N’Diaye, A. T., Wall, D., Jnawali, G., Coraux, J., Busse, C., Gastel, R. van, Poelsema, B., Michely, T., Meyer zu Heringdorf, F.-J., and Horn-von Hoegen, M. (2011). “Growth temperature dependent graphene alignment on Ir(111)”. *Applied Physics Letters* **98**, 14, p. 141903 (cit. on pp. 36, 38, 47).
- Hattab, H., N’Diaye, A. T., Wall, D., Klein, C., Jnawali, G., Coraux, J., Busse, C., Gastel, R. van, Poelsema, B., Michely, T., Meyer zu Heringdorf, F.-J., and Horn-von Hoegen, M. (2012). “Interplay of Wrinkles, Strain, and Lattice Parameter in Graphene on Iridium”. *Nano Letters* **12**, 2, pp. 678–682 (cit. on pp. 36, 47).
- He, H.-T., Wang, G., Zhang, T., Sou, I.-K., Wong, G. K. L., Wang, J.-N., Lu, H.-Z., Shen, S.-Q., and Zhang, F.-C. (04/2011). “Impurity Effect on Weak Antilocalization in the Topological Insulator Bi_2Te_3 ”. *Physical Review Letters* **106**, 16, p. 166805 (cit. on p. 17).
- Hermann, V. (2012). *Bandstrukturmessungen an Topologischen Isolatoren mittels Zwei-Photonen-Photoemission*. Bachelor thesis, Lehrstuhl für Festkörperphysik, Department für Physik der Universität Erlangen-Nürnberg (cit. on pp. 64, 74).
- Hertel, S., Waldmann, D., Jobst, J., Albert, A., Albrecht, M., Reshanov, S., Schöner, A., Krieger, M., and Weber, H. (07/2012). “Tailoring the graphene/silicon carbide interface for monolithic wafer-scale electronics”. *Nature Communications* **3**, pp. 957– (cit. on pp. 5, 7, 11).
- Hertel, T., Knoesel, E., Wolf, M., and Ertl, G. (01/1996). “Ultrafast Electron Dynamics at Cu(111): Response of an Electron Gas to Optical Excitation”. *Physical Review Letters* **76**, 3, pp. 535–538 (cit. on p. 30).
- Hikami, S., Larkin, A. I., and Nagaoka, Y. (1980). “Spin-Orbit Interaction and Magnetoresistance in the Two Dimensional Random System”. *Progress of Theoretical Physics* **63**, 2, pp. 707–710 (cit. on p. 16).
- Hild, K., Maul, J., Schönhense, G., Elmers, H. J., Amft, M., and Oppeneer, P. M. (02/2009). “Magnetic Circular Dichroism in Two-Photon Photoemission”. *Physical Review Letters* **102**, 5, p. 057207 (cit. on p. 68).
- Höfer, U., Shumay, I. L., Reuß, C., Thomann, U., Wallauer, W., and Fauster, T. (1997). “Time-Resolved Coherent Photoelectron Spectroscopy of Quantized Electronic States on Metal Surfaces”. *Science* **277**, 5331, pp. 1480–1482 (cit. on pp. 31, 45, 46).
- Hong, S. S., Cha, J. J., Kong, D., and Cui, Y. (03/2012). “Ultra-low carrier concentration and surface-dominant transport in antimony-doped Bi_2Se_3 topological insulator nanoribbons”. *Nature Communications* **3**, pp. 757– (cit. on p. 17).
- Horák, J., Sary, Z., Lošt’ák, P., and Pancfř, J. (1990). “Anti-site defects in n- Bi_2Se_3 crystals”. *Journal of Physics and Chemistry of Solids* **51**, 12, pp. 1353–1360 (cit. on p. 63).

- Hotzel, A., Wolf, M., and Gauyacq, J. P. (2000). “Phonon-Mediated Intraband Relaxation of Image-State Electrons in Adsorbate Overlayers: $N_2/Xe/Cu(111)$ ”. *The Journal of Physical Chemistry B* **104**, 35, pp. 8438–8455 (cit. on p. 29).
- Hsieh, D., Qian, D., Wray, L., Xia, Y., Hor, Y. S., Cava, R. J., and Hasan, M. Z. (04/2008). “A topological Dirac insulator in a quantum spin Hall phase”. *Nature* **452**, 7190, pp. 970–974 (cit. on pp. 3, 13, 16, 17, 77).
- Hsieh, D., Xia, Y., Qian, D., Wray, L., Dil, J. H., Meier, F., Osterwalder, J., Patthey, L., Checkelsky, J. G., Ong, N. P., Fedorov, A. V., Lin, H., Bansil, A., Grauer, D., Hor, Y. S., Cava, R. J., and Hasan, M. Z. (08/2009a). “A tunable topological insulator in the spin helical Dirac transport regime”. *Nature* **460**, 7259, pp. 1101–1105 (cit. on pp. 3, 13, 16, 18, 64, 77).
- Hsieh, D., Xia, Y., Qian, D., Wray, L., Meier, F., Dil, J. H., Osterwalder, J., Patthey, L., Fedorov, A. V., Lin, H., Bansil, A., Grauer, D., Hor, Y. S., Cava, R. J., and Hasan, M. Z. (09/2009b). “Observation of Time-Reversal-Protected Single-Dirac-Cone Topological-Insulator States in Bi_2Te_3 and Sb_2Te_3 ”. *Physical Review Letters* **103**, 14, p. 146401 (cit. on pp. 13, 16, 73, 77).
- Hsieh, D., Mahmood, F., McIver, J. W., Gardner, D. R., Lee, Y. S., and Gedik, N. (08/2011). “Selective Probing of Photoinduced Charge and Spin Dynamics in the Bulk and Surface of a Topological Insulator”. *Physical Review Letters* **107**, 7, p. 077401 (cit. on pp. 17, 19, 20).
- Huang, M., Yan, H., Chen, C., Song, D., Heinz, T. F., and Hone, J. (2009). “Phonon softening and crystallographic orientation of strained graphene studied by Raman spectroscopy”. *Proceedings of the National Academy of Sciences* **106**, 18, pp. 7304–7308 (cit. on p. 83).
- Ichibayashi, T., Tanaka, S., Kanasaki, J., Tanimura, K., and Fauster, T. (12/2011). “Ultrafast relaxation of highly excited hot electrons in Si: Roles of the L-X intervalley scattering”. *Physical Review B* **84**, 23, p. 235210 (cit. on p. 75).
- Ignatiev, A., Jones, A., and Rhodin, T. (1972). “Leed investigations of xenon single crystal films and their use in studying the Ir(100) surface”. *Surface Science* **30**, 3, pp. 573–591 (cit. on p. 36).
- Imamura, G. and Saiki, K. (2011). “Synthesis of Nitrogen-Doped Graphene on Pt(111) by Chemical Vapor Deposition”. *The Journal of Physical Chemistry C* **115**, 20, pp. 10000–10005 (cit. on pp. 83, 84).
- International Technology Roadmap for Semiconductors (2011). *Emerging Research Materials*. <http://www.itrs.net/Links/2011ITRS/2011Chapters/2011ERM.pdf> (cit. on p. 1).
- Ishida, Y., Kanto, H., Kikkawa, A., Taguchi, Y., Ito, Y., Ota, Y., Okazaki, K., Malaeb, W., Mulazzi, M., Okawa, M., Watanabe, S., Chen, C.-T., Kim, M., Bell, C., Kozuka, Y., Hwang, H. Y., Tokura, Y., and Shin, S. (08/2011). “Common Origin of the Circular-Dichroism Pattern in Angle-Resolved Photoemission Spectroscopy of $SrTiO_3$ and $Cu_xBi_2Se_3$ ”. *Physical Review Letters* **107**, 7, p. 077601 (cit. on pp. 27, 94).
- Iwai, H. (06/2009). “Technology roadmap for 22nm and beyond”. In: *Electron Devices and Semiconductor Technology, 2009. IEDST '09. 2nd International Workshop on*, pp. 1–4 (cit. on p. 1).
- Jacobsen, J., Pleth Nielsen, L., Besenbacher, F., Stensgaard, I., Lægsgaard, E., Rasmussen, T., Jacobsen, K. W., and Nørskov, J. K. (07/1995). “Atomic-Scale Determination of Misfit Dislocation Loops at Metal-Metal Interfaces”. *Physical Review Letters* **75**, 3, pp. 489–492 (cit. on p. 52).
- Jang, C., Adam, S., Chen, J.-H., Williams, E. D., Das Sarma, S., and Fuhrer, M. S. (10/2008). “Tuning the Effective Fine Structure Constant in Graphene: Opposing Effects of Dielectric Screening on Short- and Long-Range Potential Scattering”. *Physical Review Letters* **101**, 14, p. 146805 (cit. on p. 57).
- Jha, S. S. (05/1966). “Second-Order Optical Processes and Harmonic Fields in Solids”. *Physical Review* **145**, 2, pp. 500–506 (cit. on p. 28).
- Jung, W., Kim, Y., Kim, B., Koh, Y., Kim, C., Matsunami, M., Kimura, S.-i., Arita, M., Shimada, K., Han, J. H., Kim, J., Cho, B., and Kim, C. (12/2011). “Warping effects in the band and

- angular-momentum structures of the topological insulator Bi_2Te_3 ". *Physical Review B* **84**, 24, p. 245435 (cit. on pp. 25, 27, 68).
- Kane, C. L. and Mele, E. J. (09/2005). " Z_2 Topological Order and the Quantum Spin Hall Effect". *Physical Review Letters* **95**, 14, p. 146802 (cit. on pp. 2, 13, 16, 59).
- Kang, B. J., Mun, J. H., Hwang, C. Y., and Cho, B. J. (2009). "Monolayer graphene growth on sputtered thin film platinum". *Journal of Applied Physics* **106**, 10, p. 104309 (cit. on p. 83).
- Katsiev, K., Losovyj, Y., Zhou, Z., Vescovo, E., Liu, L., Dowben, P. A., and Goodman, D. W. (05/2012). "Graphene on Ru(0001): Evidence for two graphene band structures". *Physical Review B* **85**, 19, p. 195405 (cit. on p. 48).
- Katsnelson, M. I., Novoselov, K. S., and Geim, A. K. (09/2006). "Chiral tunnelling and the Klein paradox in graphene". *Nature Physics* **2**, 9, pp. 620–625 (cit. on pp. 1, 6).
- Khomyakov, P. A., Giovannetti, G., Rusu, P. C., Brocks, G., Brink, J. van den, and Kelly, P. J. (05/2009). "First-principles study of the interaction and charge transfer between graphene and metals". *Physical Review B* **79**, 19, p. 195425 (cit. on pp. 9, 11, 12, 52, 54, 58, 81).
- Kim, D., Cho, S., Butch, N. P., Syers, P., Kirshenbaum, K., Adam, S., Paglione, J., and Fuhrer, M. S. (06/2012). "Surface conduction of topological Dirac electrons in bulk insulating Bi_2Se_3 ". *Nature Physics* **8**, 6, pp. 459–463 (cit. on p. 17).
- Kim, K. S., Zhao, Y., Jang, H., Lee, S. Y., Kim, J. M., Kim, K. S., Ahn, J.-H., Kim, P., Choi, J.-Y., and Hong, B. H. (02/2009). "Large-scale pattern growth of graphene films for stretchable transparent electrodes". *Nature* **457**, 7230, pp. 706–710 (cit. on pp. 5, 7).
- King, P. D. C., Hatch, R. C., Bianchi, M., Ovsyannikov, R., Lupulescu, C., Landolt, G., Slomski, B., Dil, J. H., Guan, D., Mi, J. L., Rienks, E. D. L., Fink, J., Lindblad, A., Svensson, S., Bao, S., Balakrishnan, G., Iversen, B. B., Osterwalder, J., Eberhardt, W., Baumberger, F., and Hofmann, P. (08/2011). "Large Tunable Rashba Spin Splitting of a Two-Dimensional Electron Gas in Bi_2Se_3 ". *Physical Review Letters* **107**, 9, p. 096802 (cit. on pp. 16, 17).
- Kirchmann, P. S., Wolf, M., Dil, J. H., Horn, K., and Bovensiepen, U. (06/2007). "Quantum size effects in Pb/Si(111) investigated by laser-induced photoemission". *Physical Review B* **76**, 7, p. 075406 (cit. on p. 31).
- Kirchmann, P. S. and Bovensiepen, U. (07/2008). "Ultrafast electron dynamics in Pb/Si(111) investigated by two-photon photoemission". *Physical Review B* **78**, 3, p. 035437 (cit. on pp. 29, 31).
- Kirchmann, P. S., Rettig, L., Zubizarreta, X., Silkin, V. M., Chulkov, E. V., and Bovensiepen, U. (10/2010). "Quasiparticle lifetimes in metallic quantum-well nanostructures". *Nature Physics* **6**, 10, pp. 782–785 (cit. on p. 31).
- Kittel, C. (1987). *Quantum theory of solids*. Ed. by 2nd. Wiley, New York (cit. on p. 83).
- (2005). *Introduction to Solid State Physics*. 8th ed. Wiley (cit. on p. 57).
- Knoesel, E., Hertel, T., Wolf, M., and Ertl, G. (1995). "Femtosecond dynamics of electronic excitations of adsorbates studied by two-photon photoemission pulse correlation: Co/Cu(111)". *Chemical Physics Letters* **240**, 5–6, pp. 409–416 (cit. on p. 66).
- Kohn, W. (05/1959). "Image of the Fermi Surface in the Vibration Spectrum of a Metal". *Physical Review Letters* **2**, 9, pp. 393–394 (cit. on p. 5).
- Kokh, K., Nenashev, B., Kokh, A., and Shvedenkov, G. (2005). "Application of a rotating heat field in Bridgman-Stockbarger crystal growth". *Journal of Crystal Growth* **275**, 1 - 2. Proceedings of the 14th International Conference on Crystal Growth and the 12th International Conference on Vapor Growth and Epitaxy, e2129 –e2134 (cit. on p. 60).
- Kong, D., Cha, J. J., Lai, K., Peng, H., Analytis, J. G., Meister, S., Chen, Y., Zhang, H.-J., Fisher, I. R., Shen, Z.-X., and Cui, Y. (2011). "Rapid Surface Oxidation as a Source of Surface Degradation Factor for Bi_2Se_3 ". *ACS Nano* **5**, 6, pp. 4698–4703 (cit. on p. 63).
- König, M., Wiedmann, S., Brüne, C., Roth, A., Buhmann, H., Molenkamp, L. W., Qi, X.-L., and Zhang, S.-C. (2007). "Quantum Spin Hall Insulator State in HgTe Quantum Wells". *Science* **318**, 5851, pp. 766–770 (cit. on pp. 2, 13, 15).

- Kotov, V. N., Uchoa, B., Pereira, V. M., Guinea, F., and Castro Neto, A. H. (07/2012). “Electron-Electron Interactions in Graphene: Current Status and Perspectives”. *Rev. Mod. Phys.* **84**, 3, pp. 1067–1125 (cit. on p. 57).
- Kralj, M., Pletikosić, I., Petrović, M., Pervan, P., Milun, M., N’Diaye, A. T., Busse, C., Michely, T., Fujii, J., and Vobornik, I. (08/2011). “Graphene on Ir(111) characterized by angle-resolved photoemission”. *Physical Review B* **84**, 7, p. 075427 (cit. on pp. 9, 10, 36, 44).
- Krueckl, V. and Richter, K. (08/2011). “Switching Spin and Charge between Edge States in Topological Insulator Constrictions”. *Physical Review Letters* **107**, 8, p. 086803 (cit. on p. 3).
- Kuzmenko, A. B., Heumen, E. van, Carbone, F., and Marel, D. van der (03/2008). “Universal Optical Conductance of Graphite”. *Physical Review Letters* **100**, 11, p. 117401 (cit. on pp. 7, 8).
- Kwon, S.-Y., Ciobanu, C. V., Petrova, V., Shenoy, V. B., Bareño, J., Gambin, V., Petrov, I., and Kodambaka, S. (12/2009). “Growth of Semiconducting Graphene on Palladium”. *Nano Letters* **9**, 12, pp. 3985–3990 (cit. on p. 9).
- LaShell, S., McDougall, B. A., and Jensen, E. (10/1996). “Spin Splitting of an Au(111) Surface State Band Observed with Angle Resolved Photoelectron Spectroscopy”. *Physical Review Letters* **77**, 16, pp. 3419–3422 (cit. on pp. 9, 14, 79, 81).
- Lang, N. D. and Kohn, W. (04/1973). “Theory of Metal Surfaces: Induced Surface Charge and Image Potential”. *Physical Review B* **7**, 8, pp. 3541–3550 (cit. on p. 57).
- Langer, T., Förster, D. F., Busse, C., Michely, T., Pfnür, H., and Tegenkamp, C. (2011). “Sheet plasmons in modulated graphene on Ir(111)”. *New Journal of Physics* **13**, 5, p. 053006 (cit. on p. 47).
- Larciprete, R., Ulstrup, S., Lacovig, P., Dalmiglio, M., Bianchi, M., Mazzola, F., Hornekær, L., Orlando, F., Baraldi, A., Hofmann, P., and Lizzit, S. (2012). “Oxygen Switching of the Epitaxial Graphene-Metal Interaction”. *ACS Nano* **6**, 11, pp. 9551–9558 (cit. on p. 84).
- Lauffer, P., Emtsev, K. V., Graupner, R., Seyller, T., Ley, L., Reshanov, S. A., and Weber, H. B. (04/2008). “Atomic and electronic structure of few-layer graphene on SiC(0001) studied with scanning tunneling microscopy and spectroscopy”. *Physical Review B* **77**, 15, p. 155426 (cit. on p. 58).
- Lauffer, P. (2009). *Rastertunnelmikroskopie und Rastertunnelspektroskopie an Kohlenstoffnanoröhren und epitaktischem Graphen*. Doctoral thesis, Lehrstuhl für Technische Physik, Department für Physik der Universität Erlangen-Nürnberg (cit. on p. 58).
- Lehmann, J., Merschdorf, M., Thon, A., Voll, S., and Pfeiffer, W. (12/1999). “Properties and dynamics of the image potential states on graphite investigated by multiphoton photoemission spectroscopy”. *Physical Review B* **60**, 24, pp. 17037–17045 (cit. on pp. 7, 56).
- Lerch, D., Klein, A., Schmidt, A., Müller, S., Hammer, L., Heinz, K., and Weinert, M. (02/2006). “Unusual adsorption site of hydrogen on the unreconstructed Ir(100) surface”. *Physical Review B* **73**, 7, p. 075430 (cit. on p. 48).
- Li, X., Cai, W., An, J., Kim, S., Nah, J., Yang, D., Piner, R., Velamakanni, A., Jung, I., Tutuc, E., Banerjee, S. K., Colombo, L., and Ruoff, R. S. (2009). “Large-Area Synthesis of High-Quality and Uniform Graphene Films on Copper Foils”. *Science* **324**, 5932, pp. 1312–1314 (cit. on pp. 7, 83).
- Li, X., Magnuson, C. W., Venugopal, A., An, J., Suk, J. W., Han, B., Borysiak, M., Cai, W., Velamakanni, A., Zhu, Y., Fu, L., Vogel, E. M., Voelkl, E., Colombo, L., and Ruoff, R. S. (2010). “Graphene Films with Large Domain Size by a Two-Step Chemical Vapor Deposition Process”. *Nano Letters* **10**, 11, pp. 4328–4334 (cit. on pp. 1, 7, 55).
- Lin, Y.-M., Dimitrakopoulos, C., Jenkins, K. A., Farmer, D. B., Chiu, H.-Y., Grill, A., and Avouris, P. (2010). “100-GHz Transistors from Wafer-Scale Epitaxial Graphene”. *Science* **327**, 5966, p. 662 (cit. on pp. 1, 5, 7).
- Linder, J., Yokoyama, T., and Sudbø, A. (11/2009). “Anomalous finite size effects on surface states in the topological insulator Bi₂Se₃”. *Physical Review B* **80**, 20, p. 205401 (cit. on pp. 77, 80, 82).

- Link, S., Dürr, H. A., Bihlmayer, G., Blügel, S., Eberhardt, W., Chulkov, E. V., Silkin, V. M., and Echenique, P. M. (2001a). “Femtosecond electron dynamics of image-potential states on clean and oxygen-covered Pt (111)”. *Physical Review B* **63**, 11, p. 115420 (cit. on pp. 53, 54).
- Link, S., Sievers, J., Dürr, H., and Eberhardt, W. (2001b). “Lifetimes of image-potential states on the clean and hydrogen-covered Ni(111) surface”. *Journal of Electron Spectroscopy and Related Phenomena* **114 - 116**, 0. Proceeding of the Eight International Conference on Electronic Spectroscopy and Structure, pp. 351–355 (cit. on p. 53).
- Liu, M., Chang, C.-Z., Zhang, Z., Zhang, Y., Ruan, W., He, K., Wang, L.-L., Chen, X., Jia, J.-F., Zhang, S.-C., Xue, Q.-K., Ma, X., and Wang, Y. (04/2011a). “Electron interaction-driven insulating ground state in Bi₂Se₃ topological insulators in the two-dimensional limit”. *Physical Review B* **83**, 16, p. 165440 (cit. on p. 17).
- Liu, N., Fu, L., Dai, B., Yan, K., Liu, X., Zhao, R., Zhang, Y., and Liu, Z. (2011b). “Universal Segregation Growth Approach to Wafer-Size Graphene from Non-Noble Metals”. *Nano Letters* **11**, 1, pp. 297–303 (cit. on p. 9).
- Loginova, E., Nie, S., Thürmer, K., Bartelt, N. C., and McCarty, K. F. (08/2009). “Defects of graphene on Ir(111): Rotational domains and ridges”. *Physical Review B* **80**, 8, p. 085430 (cit. on p. 38).
- Loudon, R. (1959). “One-Dimensional Hydrogen Atom”. *American Journal of Physics* **27**, 9, pp. 649–655 (cit. on p. 31).
- Malard, L. M., Pimenta, M. A., Dresselhaus, G., and Dresselhaus, M. S. (2009). “Raman spectroscopy in graphene”. *Physics Reports* **473**, 5–6, pp. 51–87 (cit. on pp. 83, 85).
- Marchenko, D., Varykhalov, A., Rybkin, A., Shikin, A. M., and Rader, O. (2011). “Atmospheric stability and doping protection of noble-metal intercalated graphene on Ni(111)”. *Applied Physics Letters* **98**, 12, p. 122111 (cit. on p. 55).
- Marchenko, D., Varykhalov, A., Scholz, M. R., Bihlmayer, G., Rashba, E. I., Rybkin, A., Shikin, A. M., and Rader, O. (11/2012). “Giant Rashba splitting in graphene due to hybridization with gold”. *Nature Communications* **3**, pp. 1232– (cit. on pp. 9, 10, 48).
- Marchini, S., Günther, S., and Wintterlin, J. (08/2007). “Scanning tunneling microscopy of graphene on Ru(0001)”. *Physical Review B* **76**, 7, p. 075429 (cit. on p. 9).
- Martin, J., Akerman, N., Ulbricht, G., Lohmann, T., Smet, J. H., Klitzing, K. von, and Yacoby, A. (02/2008). “Observation of electron-hole puddles in graphene using a scanning single-electron transistor”. *Nature Physics* **4**, 2, pp. 144–148 (cit. on p. 11).
- Massalski, T. B., Okamoto, H., Subramanian, P. R., and Kacprzak, L. (1990). *Binary Alloy Phase Diagrams. Second Edition. Vol. 3*. ASM International (cit. on p. 7).
- Mathew, S., Chan, T. K., Zhan, D., Gopinadhan, K., Barman, A. R., Breese, M. B. H., Dhar, S., Shen, Z. X., Venkatesan, T., and Thong, J. T. L. (2011). “Mega-electron-volt proton irradiation on supported and suspended graphene: A Raman spectroscopic layer dependent study”. *Journal of Applied Physics* **110**, 8, p. 084309 (cit. on p. 84).
- Mathias, S., Ruffing, A., Deicke, F., Wiesenmayer, M., Aeschlimann, M., and Bauer, M. (04/2010a). “Band structure dependence of hot-electron lifetimes in a Pb/Cu(111) quantum-well system”. *Physical Review B* **81**, 15, p. 155429 (cit. on p. 31).
- Mathias, S., Ruffing, A., Deicke, F., Wiesenmayer, M., Sakar, I., Bihlmayer, G., Chulkov, E. V., Koroteev, Y. M., Echenique, P. M., Bauer, M., and Aeschlimann, M. (02/2010b). “Quantum-Well-Induced Giant Spin-Orbit Splitting”. *Physical Review Letters* **104**, 6, p. 066802 (cit. on p. 31).
- Mattausch, A. and Pankratov, O. (08/2007). “*Ab Initio* Study of Graphene on SiC”. *Physical Review Letters* **99**, 7, p. 076802 (cit. on pp. 11, 40, 53, 54).
- McCann, E. and Fal’ko, V. I. (03/2006). “Landau-Level Degeneracy and Quantum Hall Effect in a Graphite Bilayer”. *Physical Review Letters* **96**, 8, p. 086805 (cit. on p. 6).

- McCarty, K. F., Feibelman, P. J., Loginova, E., and Bartelt, N. C. (2009). “Kinetics and thermodynamics of carbon segregation and graphene growth on Ru(0001)”. *Carbon* **47**, 7, pp. 1806–1813 (cit. on p. 9).
- McIver, J. W., Hsieh, D., Steinberg, H., Jarillo-Herrero, P., and Gedik, N. (02/2012). “Control over topological insulator photocurrents with light polarization”. *Nature Nanotechnology* **7**, 2, pp. 96–100 (cit. on pp. 17, 20, 77).
- Meindl, J. D., Chen, Q., and Davis, J. A. (2001). “Limits on Silicon Nanoelectronics for Terascale Integration”. *Science* **293**, 5537, pp. 2044–2049 (cit. on p. 1).
- Menshchikova, T. V., Ereemeev, S. V., and Chulkov, E. V. (2012). “Electronic structure of SnSb₂Te₄ and PbSb₂Te₄ topological insulators”. *Applied Surface Science* **In press**, -, pp. – (cit. on pp. 73–75, 77).
- Mirhosseini, H. and Henk, J. (07/2012). “Spin Texture and Circular Dichroism in Photoelectron Spectroscopy from the Topological Insulator Bi₂Te₃: First-Principles Photoemission Calculations”. *Physical Review Letters* **109**, 3, p. 036803 (cit. on pp. 26, 27).
- Miyamoto, K., Kimura, A., Okuda, T., Miyahara, H., Kuroda, K., Namatame, H., Taniguchi, M., Ereemeev, S. V., Menshchikova, T. V., Chulkov, E. V., Kokh, K. A., and Tereshchenko, O. E. (2012). *Topological Surface States with Persistent High Spin Polarization across Dirac Point in Bi₂Te₂Se and Bi₂Se₂Te*. arXiv:1203.4439v1, arXiv pre-print (cit. on p. 64).
- Mohr, M., Maultzsch, J., Dobardžić, E., Reich, S., Milošević, I., Damnjanović, M., Bosak, A., Krisch, M., and Thomsen, C. (07/2007). “Phonon dispersion of graphite by inelastic x-ray scattering”. *Physical Review B* **76**, 3, p. 035439 (cit. on pp. 84–86).
- Moore, G. (01/1998). “Cramming More Components Onto Integrated Circuits”. *Proceedings of the IEEE* **86**, 1, pp. 82–85 (cit. on p. 1).
- Moore, J. E. and Balents, L. (03/2007). “Topological invariants of time-reversal-invariant band structures”. *Physical Review B* **75**, 12, p. 121306 (cit. on p. 13).
- Moritz, W., Wang, B., Bocquet, M.-L., Brugger, T., Greber, T., Wintterlin, J., and Günther, S. (04/2010). “Structure Determination of the Coincidence Phase of Graphene on Ru(0001)”. *Physical Review Letters* **104**, 13, p. 136102 (cit. on pp. 35, 46).
- Murakami, S., Nagaosa, N., and Zhang, S.-C. (2003). “Dissipationless Quantum Spin Current at Room Temperature”. *Science* **301**, 5638, pp. 1348–1351 (cit. on p. 2).
- N’Diaye, A. T. (2004). *Epitaxial Graphene and Cluster Lattices on Iridium(111)*. Doctoral thesis, Fakultät für Mathematik, Informatik und Naturwissenschaften der RWTH Aachen University (cit. on pp. 7, 8).
- N’Diaye, A. T., Bleikamp, S., Feibelman, P. J., and Michely, T. (11/2006). “Two-Dimensional Ir Cluster Lattice on a Graphene Moiré on Ir(111)”. *Physical Review Letters* **97**, 21, p. 215501 (cit. on pp. 9, 36, 47).
- N’Diaye, A. T., Coraux, J., Plasa, T. N., Busse, C., and Michely, T. (2008). “Structure of epitaxial graphene on Ir(111)”. *New Journal of Physics* **10**, 4, p. 043033 (cit. on pp. 38, 46).
- N’Diaye, A. T., Gastel, R. van, Martínez-Galera, A. J., Coraux, J., Hattab, H., Wall, D., Meyer zu Heringdorf, F.-J., Horn-von Hoegen, M., Gómez-Rodríguez, J. M., Poelsema, B., Busse, C., and Michely, T. (2009). “In situ observation of stress relaxation in epitaxial graphene”. *New Journal of Physics* **11**, 11, p. 113056 (cit. on pp. 36, 38, 56, 58).
- Nagashima, A., Tejima, N., and Oshima, C. (12/1994). “Electronic states of the pristine and alkali-metal-intercalated monolayer graphite/Ni(111) systems”. *Physical Review B* **50**, 23, pp. 17487–17495 (cit. on p. 9).
- Nakagawa, T., Yamamoto, I., Takagi, Y., Watanabe, K., Matsumoto, Y., and Yokoyama, T. (05/2009). “Two-photon photoemission magnetic circular dichroism and its energy dependence”. *Physical Review B* **79**, 17, p. 172404 (cit. on p. 68).
- Nakamura, J., Hirano, H., Xie, M., Matsuo, I., Yamada, T., and Tanaka, K. ichi (1989). “Formation of a hybrid surface of carbide and graphite layers on Ni(100) but no hybrid surface on Ni(111)”. *Surface Science Letters* **222**, 1, pp. L809–L817 (cit. on pp. 36, 37).

- Nakano, H., Ogawa, J., and Nakamura, J. (2002). "Growth mode of carbide from C₂H₄ or Co on Ni(111)". *Surface Science* **514**, 1 – 3, pp. 256 –260 (cit. on p. 36).
- Neto, A. C., Kotov, V., Nilsson, J., Pereira, V., Peres, N., and Uchoa, B. (2009). "Adatoms in graphene". *Solid State Communications* **149**, 27 - 28. <ce:title>Recent Progress in Graphene Studies</ce:title>, pp. 1094 –1100 (cit. on p. 57).
- Neupane, M., Xu, S.-Y., Wray, L. A., Petersen, A., Shankar, R., Alidoust, N., Liu, C., Fedorov, A., Ji, H., Allred, J. M., Hor, Y. S., Chang, T.-R., Jeng, H.-T., Lin, H., Bansil, A., Cava, R. J., and Hasan, M. Z. (06/2012). "Topological surface states and Dirac point tuning in ternary topological insulators". *Physical Review B* **85**, 23, p. 235406 (cit. on p. 64).
- Newns, D. M. (1969). "Fermi-Thomas Response of a Metal Surface to an External Point Charge". *The Journal of Chemical Physics* **50**, 10, pp. 4572–4575 (cit. on p. 57).
- Nie, S., Walter, A. L., Bartelt, N. C., Starodub, E., Bostwick, A., Rotenberg, E., and McCarty, K. F. (2011). "Growth from Below: Graphene Bilayers on Ir(111)". *ACS Nano* **5**, 3, pp. 2298–2306 (cit. on pp. 38, 83).
- Niesner, D., Fauster, T., Dadap, J. I., Zaki, N., Knox, K. R., Yeh, P.-C., Bhandari, R., Osgood, R. M., Petrović, M., and Kralj, M. (02/2012a). "Trapping surface electrons on graphene layers and islands". *Physical Review B* **85**, 8, 081402(R) (cit. on pp. 7, 9, 38, 41–45, 79, 81).
- Niesner, D., Fauster, T., Eremeev, S. V., Menshchikova, T. V., Koroteev, Y. M., Protogenov, A. P., Chulkov, E. V., Tereshchenko, O. E., Kokh, K. A., Alekperov, O., Nadjafov, A., and Mamedov, N. (11/2012b). "Unoccupied topological states on bismuth chalcogenides". *Physical Review B* **86**, 20, p. 205403 (cit. on pp. 64–69).
- Niesner, D., Bierlein, T., and Fauster, T. (2010). *Two-Photon Photoelectron Spectroscopy using a Display Analyzer*. Verhandlungen der Deutschen Physikalischen Gesellschaft (cit. on p. 34).
- Nieuwenhuys, B., Bouwman, R., and Sachtler, W. (1974). "The changes in work function of group Ib and VIII metals on xenon adsorption, determined by field electron and photoelectron emission". *Thin Solid Films* **21**, 1, pp. 51 –58 (cit. on p. 44).
- Nieuwenhuys, B., Hagen, D., Rovida, G, and Somorjai, G. (1976). "LEED, AES and Thermal Desorption Studies of Chemisorbed Hydrogen and Hydrocarbons (C₂H₂, C₂H₄, C₆H₆, C₆H₁₂) on the (111) and Stepped [6(111) × (100)] Iridium Crystal Surfaces; comparison with Platinum". *Surface Science* **59**, 1, pp. 155 –176 (cit. on pp. 36, 47).
- Nobis, D. (2011). *Graphen auf Platin (111), Präparation und Photoemission*. Bachelor thesis, Lehrstuhl für Festkörperphysik, Department für Physik der Universität Erlangen-Nürnberg (cit. on pp. 37, 39, 50, 53).
- Nobis, D., Niesner, D., and Fauster, T. (2012). *Photoemission studies of graphene on Pt(111)*. Verhandlungen der Deutschen Physikalischen Gesellschaft (cit. on pp. 50, 53).
- Nobis, D., Potenz, M., Niesner, D., and Fauster, T. (2013a). *Image potential states of graphene on noble metal surfaces*. to be published (cit. on pp. 35, 38, 50, 52, 53).
- Nobis, D., Niesner, D., Fauster, T., Kralj, M., Petrović, M., Yeh, P. C., Hong, S. Y., Jin, W., Dadap, J., and Osgood, R. M. (2013b). *Two-photon photoemission studies of graphene on Ir(111)*. Verhandlungen der Deutschen Physikalischen Gesellschaft (cit. on pp. 46, 58, 79, 81).
- Novoselov, K. S., Geim, A. K., Morozov, S. V., Jiang, D., Zhang, Y., Dubonos, S. V., Grigorieva, I. V., and Firsov, A. A. (2004). "Electric Field Effect in Atomically Thin Carbon Films". *Science* **306**, 5696, pp. 666–669 (cit. on pp. 1, 5, 7, 35).
- Novoselov, K. S., Jiang, D., Schedin, F., Booth, T. J., Khotkevich, V. V., Morozov, S. V., and Geim, A. K. (2005a). "Two-dimensional atomic crystals". *Proceedings of the National Academy of Sciences of the United States of America* **102**, 30, pp. 10451–10453 (cit. on p. 7).
- Novoselov, K. S., Geim, A. K., Morozov, S. V., Jiang, D., Katsnelson, M. I., Grigorieva, I. V., Dubonos, S. V., and Firsov, A. A. (11/2005b). "Two-dimensional gas of massless Dirac fermions in graphene". *Nature* **438**, 7065, pp. 197–200 (cit. on p. 1).

- Novoselov, K. S., McCann, E., Morozov, S. V., Fal'ko, V. I., Katsnelson, M. I., Zeitler, U., Jiang, D., Schedin, F., and Geim, A. K. (03/2006). "Unconventional quantum Hall effect and Berry's phase of 2π in bilayer graphene". *Nature Physics* **2**, 3, pp. 177–180 (cit. on p. 6).
- Ogawa, S., Nagano, H., Petek, H., and Heberle, A. P. (02/1997). "Optical Dephasing in Cu(111) Measured by Interferometric Two-Photon Time-Resolved Photoemission". *Physical Review Letters* **78**, 7, pp. 1339–1342 (cit. on p. 30).
- Ohta, T., Gabaly, F. E., Bostwick, A., McChesney, J. L., Emtsev, K. V., Schmid, A. K., Seyller, T., Horn, K., and Rotenberg, E. (2008). "Morphology of graphene thin film growth on SiC(0001)". *New Journal of Physics* **10**, 2, p. 023034 (cit. on p. 40).
- Osgood, R. M. and Wang, X. (1997). "Image States on Single-Crystal Metal Surface". In: ed. by H. Ehrenreich and F. Spaepen. Vol. 51. *Solid State Physics*. Academic Press, pp. 1–80 (cit. on p. 30).
- Pankratov, O. (01/1987). "Supersymmetry in heterojunctions: Band-inverting contact on the basis of $\text{Pb}_{1-x}\text{Sn}_x\text{Te}$ and $\text{Hg}_{1-x}\text{Cd}_x\text{Te}$ ". *Solid State Communications* **61**, 2, pp. 93–96 (cit. on pp. 2, 13, 15).
- Papaconstantopoulos, D. A. (1986). *Handbook of the Band Structure of Elemental Solids*. Plenum, New York (cit. on p. 42).
- Parga, A. L. Vázquez de, Calleja, F., Borca, B., Passeggi, M. C. G., Hinarejos, J. J., Guinea, F., and Miranda, R. (02/2008). "Periodically Rippled Graphene: Growth and Spatially Resolved Electronic Structure". *Physical Review Letters* **100**, 5, p. 056807 (cit. on p. 35).
- Park, C.-H. and Louie, S. G. (08/2012a). "Spin Polarization of Photoelectrons from Topological Insulators". *Physical Review Letters* **109**, 9, p. 097601 (cit. on p. 26).
- Park, J.-W., Eom, S. H., Lee, H., Da Silva, J. L. F., Kang, Y.-S., Lee, T.-Y., and Khang, Y. H. (09/2009). "Optical properties of pseudobinary GeTe, $\text{Ge}_2\text{Sb}_2\text{Te}_5$, GeSb_2Te_4 , GeSb_4Te_7 , and Sb_2Te_3 from ellipsometry and density functional theory". *Physical Review B* **80**, 11, p. 115209 (cit. on p. 17).
- Park, S. R., Han, J., Kim, C., Koh, Y. Y., Kim, C., Lee, H., Choi, H. J., Han, J. H., Lee, K. D., Hur, N. J., Arita, M., Shimada, K., Namatame, H., and Taniguchi, M. (01/2012b). "Chiral Orbital-Angular Momentum in the Surface States of Bi_2Se_3 ". *Physical Review Letters* **108**, 4, p. 046805 (cit. on pp. 18, 25–27, 68).
- Passek, F. and Donath, M. (08/1992). "Spin-split image-potential-induced surface state on Ni(111)". *Physical Review Letters* **69**, 7, pp. 1101–1104 (cit. on p. 53).
- Patrick, L. and Choyke, W. J. (09/1970). "Static Dielectric Constant of SiC". *Physical Review B* **2**, 6, pp. 2255–2256 (cit. on p. 55).
- Peng, H., Lai, K., Kong, D., Meister, S., Chen, Y., Qi, X.-L., Zhang, S.-C., Shen, Z.-X., and Cui, Y. (03/2010). "Aharonov-Bohm interference in topological insulator nanoribbons". *Nature Materials* **9**, 3, pp. 225–229 (cit. on p. 17).
- Perdereau, J., Biberian, J. P., and Rhead, G. E. (05/1974). "Adsorption and surface alloying of lead monolayers on (111) and (110) faces of gold". *Journal of Physics F: Metal Physics* **4**, 5, pp. 798–806 (cit. on p. 52).
- Petek, H. and Ogawa, S. (1997). "Femtosecond time-resolved two-photon photoemission studies of electron dynamics in metals". *Progress in Surface Science* **56**, 4, pp. 239–310 (cit. on pp. 29, 45, 72).
- Phark, S.-H., Borme, J., Vanegas, A. L., Corbetta, M., Sander, D., and Kirschner, J. (05/2012). "Scanning tunneling spectroscopy of epitaxial graphene nanoisland on Ir(111)". *Nanoscale Research Letters* **7**, p. 255 (cit. on p. 9).
- Phark, S.-H., Borme, J., Vanegas, A. L., Corbetta, M., Sander, D., and Kirschner, J. (07/2012). "Atomic structure and spectroscopy of graphene edges on Ir(111)". *Physical Review B* **86**, 4, p. 045442 (cit. on p. 9).
- Philipp, H. R. and Taft, E. A. (1960). *Silicon Carbide - A High Temperature Semiconductor*. Ed. by J. O'Connor and J. Smiltens. Pergamon Press, Oxford - London - Paris (cit. on pp. 11, 55).

- Piscanec, S., Lazzeri, M., Mauri, F., Ferrari, A. C., and Robertson, J. (10/2004). “Kohn Anomalies and Electron-Phonon Interactions in Graphite”. *Physical Review Letters* **93**, 18, p. 185503 (cit. on p. 5).
- Pivetta, M., Patthey, F., Barke, I., Hövel, H., Delley, B., and Schneider, W.-D. (04/2005). “Gap opening in the surface electronic structure of graphite induced by adsorption of alkali atoms: Photoemission experiments and density functional calculations”. *Physical Review B* **71**, 16, p. 165430 (cit. on p. 48).
- Pletikosić, I., Kralj, M., Pervan, P., Brako, R., Coraux, J., N’Diaye, A. T., Busse, C., and Michely, T. (02/2009). “Dirac Cones and Minigaps for Graphene on Ir(111)”. *Physical Review Letters* **102**, 5, p. 056808 (cit. on pp. 9, 10, 35, 47, 48, 53–55, 85).
- Pletikosić, I., Kralj, M., Šokčević, D., Brako, R., Lazić, P., and Pervan, P. (2010). “Photoemission and density functional theory study of Ir(111); energy band gap mapping”. *Journal of Physics: Condensed Matter* **22**, 13, p. 135006 (cit. on pp. 9, 42).
- Politano, A., Marino, A. R., and Chiarello, G. (2012). “Phonon dispersion of quasi-freestanding graphene on Pt(111)”. *Journal of Physics: Condensed Matter* **24**, 10, p. 104025 (cit. on p. 85).
- Posternak, M., Baldereschi, A., Freeman, A. J., Wimmer, E., and Weinert, M. (03/1983). “Prediction of Electronic Interlayer States in Graphite and Reinterpretation of Alkali Bands in Graphite Intercalation Compounds”. *Physical Review Letters* **50**, 10, pp. 761–764 (cit. on p. 56).
- Potenz, M. (2012). *Photoemissionsspektroskopie von stark gebundenem und quasi freistehendem Graphen auf Nickel (111)*. Diploma thesis, Lehrstuhl für Festkörperphysik, Department für Physik der Universität Erlangen-Nürnberg (cit. on pp. 33, 36–39, 50, 53).
- Qi, X.-L., Hughes, T. L., and Zhang, S.-C. (11/2008). “Topological field theory of time-reversal invariant insulators”. *Physical Review B* **78**, 19, p. 195424 (cit. on p. 77).
- Qi, X.-L., Li, R., Zang, J., and Zhang, S.-C. (02/2009). “Inducing a Magnetic Monopole with Topological Surface States”. *Science* **323**, 5918, pp. 1184–1187 (cit. on pp. 16, 77).
- Qu, D.-X., Hor, Y. S., Xiong, J., Cava, R. J., and Ong, N. P. (2010). “Quantum Oscillations and Hall Anomaly of Surface States in the Topological Insulator Bi_2Te_3 ”. *Science* **329**, 5993, pp. 821–824 (cit. on p. 17).
- Ramakrishna, S., Willig, F., and Knorr, A. (2004). “Time-resolved two-photon photoemission spectroscopy of semiconductor bulk states”. *Applied Physics A* **78**, 2, pp. 247–252 (cit. on p. 30).
- Rashba, E. I. (1960). “Properties of semiconductors with an extremum loop. 1. Cyclotron and combinational resonance in a magnetic field perpendicular to the plane of the loop”. *Soviet Physics, Solid State* **2**, pp. 1224–1238 (cit. on p. 42).
- Rashba, E. I. (1965). “Combined Resonance in Semiconductors”. *Soviet Physics Uspekhi* **7**, 6, p. 823 (cit. on p. 2).
- (12/2003). “Spin currents in thermodynamic equilibrium: The challenge of discerning transport currents”. *Physical Review B* **68**, 24, p. 241315 (cit. on p. 2).
- Reich, S., Maultzsch, J., Thomsen, C., and Ordejón, P. (07/2002). “Tight-binding description of graphene”. *Physical Review B* **66**, 3, p. 035412 (cit. on pp. 5, 35, 48).
- Reich, S., Thomsen, C., and Maultzsch, J. (2004). *Carbon Nanotubes*. Wiley-VCH, New York (cit. on p. 83).
- Reihl, B., Gimzewski, J. K., Nicholls, J. M., and Tosatti, E. (04/1986). “Unoccupied electronic states of graphite as probed by inverse-photoemission and tunneling spectroscopy”. *Physical Review B* **33**, 8, pp. 5770–5773 (cit. on p. 56).
- Reina, A., Jia, X., Ho, J., Nezhich, D., Son, H., Bulovic, V., Dresselhaus, M. S., and Kong, J. (2009). “Large Area, Few-Layer Graphene Films on Arbitrary Substrates by Chemical Vapor Deposition”. *Nano Letters* **9**, 1, pp. 30–35 (cit. on pp. 1, 7, 83).
- Ren, Z., Taskin, A. A., Sasaki, S., Segawa, K., and Ando, Y. (12/2010). “Large bulk resistivity and surface quantum oscillations in the topological insulator $\text{Bi}_2\text{Te}_2\text{Se}$ ”. *Physical Review B* **82**, 24, p. 241306 (cit. on pp. 17, 64).

- Reuß, C., Wallauer, W., and Fauster, T. (1996). “Image States of Ag on Au(111)”. *Surface Review and Letters* **3**, p. 1547 (cit. on pp. 52–54).
- Reuß, C., Shumay, I. L., Thomann, U., Kutschera, M., Weinelt, M., Fauster, T., and Höfer, U. (01/1999). “Control of the Dephasing of Image-Potential States by Co Adsorption on Cu(100)”. *Physical Review Letters* **82**, 1, pp. 153–156 (cit. on pp. 31, 45).
- Rieder, K. (1978). “A combined SIMS-AES/LEED study of the room-temperature oxidation of Ni(110) and Ni(111) surfaces”. *Applications of Surface Science* **2**, 1, pp. 74–84 (cit. on p. 36).
- Riedl, C., Coletti, C., Iwasaki, T., Zakharov, A. A., and Starke, U. (12/2009). “Quasi-Free-Standing Epitaxial Graphene on SiC Obtained by Hydrogen Intercalation”. *Physical Review Letters* **103**, 24, p. 246804 (cit. on p. 11).
- Rieger, D., Schnell, R., Steinmann, W., and Saile, V. (1983). “A display-type analyzer with an image-processing system for angle-resolved photoelectron spectroscopy”. *Nuclear Instruments and Methods in Physics Research* **208**, 1–3, pp. 777–784 (cit. on p. 34).
- Ristein, J., Mammadov, S., and Seyller, T. (06/2012). “Origin of Doping in Quasi-Free-Standing Graphene on Silicon Carbide”. *Physical Review Letters* **108**, 24, p. 246104 (cit. on pp. 11, 54).
- Röhrl, J., Hundhausen, M., Emtsev, K. V., Seyller, T., Graupner, R., and Ley, L. (05/2008). “Raman spectra of epitaxial graphene on SiC(0001)”. *Applied Physics Letters* **92**, 20, p. 201918 (cit. on pp. 83, 85).
- Rojas, R. (04/1997). “Konrad Zuse’s Legacy: The Architecture of the Z1 and Z3”. *IEEE Annals of the History of Computing* **19**, 2, pp. 5–16 (cit. on p. 1).
- Roushan, P., Seo, J., Parker, C. V., Hor, Y. S., Hsieh, D., Qian, D., Richardella, A., Hasan, M. Z., Cava, R. J., and Yazdani, A. (08/2009). “Topological surface states protected from backscattering by chiral spin texture”. *Nature* **460**, 7259, pp. 1106–1109 (cit. on pp. 2, 17, 19).
- Rowe, M. W., Liu, H., Williams, G. P., and Williams, R. T. (01/1993). “Picosecond photoelectron spectroscopy of excited states at Si(111) $\sqrt{3} \times \sqrt{3}$ R30°-B, Si(111) 7×7 , Si(100) 2×1 , and laser-annealed Si(111) 1×1 surfaces”. *Physical Review B* **47**, 4, pp. 2048–2064 (cit. on p. 75).
- Sacépé, B., Oostinga, J. B., Li, J., Ubal dini, A., Couto, N. J., Giannini, E., and Morpurgo, A. F. (12/2011). “Gate-tuned normal and superconducting transport at the surface of a topological insulator”. *Nature Communications* **2**, pp. 575– (cit. on p. 17).
- Saito, R. and Dresselhaus, M. S. (1998). *Physical properties of carbon nanotubes*. Imperial College Presse, London (cit. on p. 5).
- Sánchez-Barriga, J., Varykhalov, A., Scholz, M. R., Rader, O., Marchenko, D., Rybkin, A., Shikin, A. M., and Vescovo, E. (2010). “Chemical vapour deposition of graphene on Ni(111) and Co(0001) and intercalation with Au to study Dirac-cone formation and Rashba splitting”. *Diamond and Related Materials* **19**, 7–9. Proceedings of Diamond 2009, pp. 734–741 (cit. on p. 11).
- Sánchez-Barriga, J., Varykhalov, A., Marchenko, D., Scholz, M. R., and Rader, O. (05/2012a). “Minigap isotropy and broken chirality in graphene with periodic corrugation enhanced by cluster superlattices”. *Physical Review B* **85**, 20, p. 201413 (cit. on p. 48).
- Sánchez-Barriga, J., Scholz, M. R., Marchenko, D., Varykhalov, A., Rader, O., Vloykhov, A., Yashina, L. V., Braun, J., Minár, J., and Ebert, H. (2012b). *Origin of the strong circular dichroism of the topological surface state of Bi₂Te₃*. Verhandlungen der Deutschen Physikalischen Gesellschaft (cit. on pp. 27, 68).
- Sandin, A., Pronschinske, A., Rowe, J. E., and Dougherty, D. B. (2010). “Incomplete screening by epitaxial graphene on the Si face of 6H-SiC(0001)”. *Applied Physics Letters* **97**, 11, p. 113104 (cit. on pp. 57, 58, 88).
- Schäfer, I., Schlüter, M., and Skibowski, M. (05/1987). “Conduction-band structure of graphite studied by combined angle-resolved inverse photoemission and target current spectroscopy”. *Physical Review B* **35**, 14, pp. 7663–7670 (cit. on p. 56).
- Schmuttenmaer, C. A., Aeschlimann, M., Elsayed-Ali, H. E., Miller, R. J. D., Mantell, D. A., Cao, J., and Gao, Y. (09/1994). “Time-resolved two-photon photoemission from Cu(100): Energy dependence of electron relaxation”. *Physical Review B* **50**, 12, pp. 8957–8960 (cit. on p. 30).

- Schmittenmaer, C. A., Cameron Miller, C., Herman, J. W., Cao, J., Mantell, D. A., Gao, Y., and Miller, R. J. D. (1996). “Femtosecond time-resolved photoemission study of hot electron relaxation at the GaAs(100) surface”. *Chemical Physics* **205**, 1 - 2. Surface Reaction Dynamics, pp. 91 –108 (cit. on p. 30).
- Scholz, R., Sánchez-Barrige, J., Marchenko, D., Varykhalov, A., Volykhov, A., Yashina, L., and Rader, O. (2011). *High spin polarization and circular dichroism of topological surface states on Bi₂Te₃*. arXiv:1108.1053v2, arXiv pre-print (cit. on p. 68).
- Schuppler, S., Fischer, N., Steinmann, W., Schneider, R., and Bertel, E. (11/1990). “Image-potential states on Ni(111): A two-photon-photoemission study”. *Physical Review B* **42**, 15, pp. 9403–9408 (cit. on p. 53).
- Seibel, C., Maaß, H., Ohtaka, M., Fiedler, S., Jünger, C., Min, C.-H., Bentmann, H., Kazuyuki, S., and Reinert, F. (2012). *Single Dirac-cone on the Cs-covered topological insulator surface Sb₂Te₃(0001)*. arXiv:1209.4263v1 [cond-mat.mes-hall], arXiv pre-print (cit. on p. 73).
- Sharapov, S. G., Gusynin, V. P., and Beck, H. (02/2004). “Magnetic oscillations in planar systems with the Dirac-like spectrum of quasiparticle excitations”. *Physical Review B* **69**, 7, p. 075104 (cit. on p. 1).
- Shelton, J. C., Patil, H. R., and Blakely, J. M. (1974). “Equilibrium segregation of carbon to a nickel (111) surface: A surface phase transition”. *Surface Science* **43**, 2, pp. 493 –520 (cit. on pp. 7, 9, 11, 36, 37).
- Shikin, A. M., Farías, D., Adamchuk, V. K., and Rieder, K.-H (1999). “Surface phonon dispersion of a graphite monolayer adsorbed on Ni(111) and its modification caused by intercalation of Yb, La and Cu layers”. *Surface Science* **424**, 1, pp. 155 –167 (cit. on p. 5).
- Shikin, A. M., Prudnikova, G. V., Adamchuk, V. K., Moresco, F., and Rieder, K.-H. (11/2000). “Surface intercalation of gold underneath a graphite monolayer on Ni(111) studied by angle-resolved photoemission and high-resolution electron-energy-loss spectroscopy”. *Physical Review B* **62**, 19, pp. 13202–13208 (cit. on p. 36).
- Shockley, W. B., Bardeen, J., and Brattain, W. H. (1956). *The Nobel Prize in Physics*. http://www.nobelprize.org/nobel_prizes/physics/laureates/1956/ (cit. on p. 1).
- Shockley, W. and Read, W. T. (09/1952). “Statistics of the Recombinations of Holes and Electrons”. *Physical Review* **87**, 5, pp. 835–842 (cit. on p. 1).
- Shumay, I. L., Höfer, U., Reuß, C., Thomann, U., Wallauer, W., and Fauster, T. (11/1998). “Lifetimes of image-potential states on Cu(100) and Ag(100) measured by femtosecond time-resolved two-photon photoemission”. *Physical Review B* **58**, 20, pp. 13974–13981 (cit. on p. 30).
- Silkin, V. M., Zhao, J., Guinea, F., Chulkov, E. V., Echenique, P. M., and Petek, H. (09/2009). “Image potential states in graphene”. *Physical Review B* **80**, 12, p. 121408 (cit. on pp. 2, 6, 7, 35, 46, 54, 56–58).
- Singh, H. P. (07/1968). “Determination of thermal expansion of germanium, rhodium and iridium by X-rays”. *Acta Crystallographica Section A* **24**, 4, pp. 469–471 (cit. on p. 39).
- Sławińska, J., Wlasny, I., Dabrowski, P., Klusek, Z., and Zasada, I. (06/2012). “Doping domains in graphene on gold substrates: First-principles and scanning tunneling spectroscopy studies”. *Physical Review B* **85**, 23, p. 235430 (cit. on pp. 9, 35, 54, 57).
- Smith, N. V. (09/1985). “Phase analysis of image states and surface states associated with nearly-free-electron band gaps”. *Physical Review B* **32**, 6, pp. 3549–3555 (cit. on p. 31).
- Sobota, J. A., Yang, S., Analytis, J. G., Chen, Y. L., Fisher, I. R., Kirchmann, P. S., and Shen, Z.-X. (03/2012). “Ultrafast Optical Excitation of a Persistent Surface-State Population in the Topological Insulator Bi₂Se₃”. *Physical Review Letters* **108**, 11, p. 117403 (cit. on pp. 3, 17, 19, 20, 75, 76).
- Speck, F., Ostler, M., Röhr, J., Jobst, J., Waldmann, D., Hundhausen, M., Ley, L., Weber, H. B., and Seyller, T. (2010). “Quasi-Freestanding Graphene on SiC(0001)”. *Materials Science Forum* **645 - 648**, pp. 629–632 (cit. on p. 11).

- Stander, N., Huard, B., and Goldhaber-Gordon, D. (01/2009). “Evidence for Klein Tunneling in Graphene p - n Junctions”. *Physical Review Letters* **102**, 2, p. 026807 (cit. on pp. 1, 6, 55).
- Starke, U. and Riedl, C. (2009). “Epitaxial graphene on SiC(0001) and SiC(0001) : from surface reconstructions to carbon electronics”. *Journal of Physics: Condensed Matter* **21**, 13, p. 134016 (cit. on p. 40).
- Starodub, E., Bostwick, A., Moreschini, L., Nie, S., Gabaly, F. E., McCarty, K. F., and Rotenberg, E. (03/2011). “In-plane orientation effects on the electronic structure, stability, and Raman scattering of monolayer graphene on Ir(111)”. *Physical Review B* **83**, 12, p. 125428 (cit. on pp. 9, 38, 83, 85).
- Steinberg, H., Gardner, D. R., Lee, Y. S., and Jarillo-Herrero, P. (2010). “Surface State Transport and Ambipolar Electric Field Effect in Bi₂Se₃ Nanodevices”. *Nano Letters* **10**, 12, pp. 5032–5036 (cit. on p. 17).
- Steinmann, W. (1989). “Spectroscopy of image-potential states by two-photon photoemission”. *Applied Physics A* **49**, 4, pp. 365–377 (cit. on pp. 28, 29).
- Strayer, R. W., Mackie, W., and Swanson, L. (1973). “Work function measurements by the field emission retarding potential method”. *Surface Science* **34**, 2, pp. 225–248 (cit. on p. 44).
- Subramaniam, D., Libisch, F., Li, Y., Pauly, C., Geringer, V., Reiter, R., Mashoff, T., Liebmann, M., Burgdörfer, J., Busse, C., Michely, T., Mazzarello, R., Pratzner, M., and Morgenstern, M. (01/2012). “Wave-Function Mapping of Graphene Quantum Dots with Soft Confinement”. *Physical Review Letters* **108**, 4, p. 046801 (cit. on p. 9).
- Sun, D., Divin, C., Berger, C., Heer, W. A. de, First, P. N., and Norris, T. B. (04/2010). “Spectroscopic Measurement of Interlayer Screening in Multilayer Epitaxial Graphene”. *Physical Review Letters* **104**, 13, p. 136802 (cit. on p. 57).
- Sutter, P. W., Flege, J.-I., and Sutter, E. A. (05/2008). “Epitaxial graphene on ruthenium”. *Nature Materials* **7**, 5, pp. 406–411 (cit. on pp. 9, 83).
- Sutter, P. W., Hybertsen, M. S., Sadowski, J. T., and Sutter, E. A. (2009a). “Electronic Structure of Few-Layer Epitaxial Graphene on Ru(0001)”. *Nano Letters* **9**, 7, pp. 2654–2660 (cit. on p. 9).
- Sutter, P. W., Sadowski, J. T., and Sutter, E. A. (12/2009b). “Graphene on Pt(111): Growth and substrate interaction”. *Physical Review B* **80**, 24, p. 245411 (cit. on pp. 9, 11, 35, 36, 39, 53–55, 57).
- Terekhov, I. S., Milstein, A. I., Kotov, V. N., and Sushkov, O. P. (02/2008). “Screening of Coulomb Impurities in Graphene”. *Physical Review Letters* **100**, 7, p. 076803 (cit. on p. 57).
- Thompson, S. E. and Parthasarathy, S. (2006). “Moore’s law: the future of Si microelectronics”. *Materials Today* **9**, 6, pp. 20–25 (cit. on p. 1).
- Tsang, D., Marsden, B., Fok, S., and Hall, G. (2005). “Graphite thermal expansion relationship for different temperature ranges”. *Carbon* **43**, 14, pp. 2902–2906 (cit. on p. 39).
- Tuinstra, F. and Koenig, J. L. (1970). “Raman Spectrum of Graphite”. *The Journal of Chemical Physics* **53**, 3, pp. 1126–1130 (cit. on pp. 83, 85).
- Ulstrup, S., Bianchi, M., Hatch, R., Guan, D., Baraldi, A., Alfè, D., Hornekær, L., and Hofmann, P. (10/2012). “High-temperature behavior of supported graphene: Electron-phonon coupling and substrate-induced doping”. *Physical Review B* **86**, 16, p. 161402 (cit. on p. 48).
- Umezawa, K., Nakanishi, S., and Gibson, W. M. (1999). “Surface structure and metal epitaxy: impact collision ion scattering spectroscopy studies on Au/Ni(111)”. *Surface Science* **426**, 2, pp. 225–234 (cit. on p. 39).
- Van Bommel, A., Crombeen, J. E., and Van Tooren, A. (1975). “LEED and Auger electron observations of the SiC(0001) surface”. *Surface Science* **48**, 2, pp. 463–472 (cit. on pp. 11, 40).
- Varchon, F., Feng, R., Hass, J., Li, X., Nguyen, B. N., Naud, C., Mallet, P., Veuillen, J.-Y., Berger, C., Conrad, E. H., and Magaud, L. (09/2007). “Electronic Structure of Epitaxial Graphene Layers on SiC: Effect of the Substrate”. *Physical Review Letters* **99**, 12, p. 126805 (cit. on pp. 9, 35, 54, 57).

- Varykhalov, A., Sánchez-Barriga, J., Shikin, A. M., Biswas, C., Vescovo, E., Rybkin, A., Marchenko, D., and Rader, O. (10/2008). “Electronic and Magnetic Properties of Quasifreestanding Graphene on Ni”. *Physical Review Letters* **101**, 15, p. 157601 (cit. on pp. 9–11, 35, 39, 53, 54).
- Varykhalov, A. and Rader, O. (07/2009). “Graphene grown on Co(0001) films and islands: Electronic structure and its precise magnetization dependence”. *Physical Review B* **80**, 3, p. 035437 (cit. on p. 9).
- Varykhalov, A., Scholz, M. R., Kim, T. K., and Rader, O. (09/2010). “Effect of noble-metal contacts on doping and band gap of graphene”. *Physical Review B* **82**, 12, p. 121101 (cit. on p. 9).
- Veen, J. F. van der, Himpsel, F. J., and Eastman, D. E. (01/1980). “Structure-Dependent $4f$ —Core-Level Binding Energies for Surface Atoms on Ir(111), Ir(100)-(5 × 1), and Metastable Ir(100)-(1 × 1)”. *Physical Review Letters* **44**, 3, pp. 189–192 (cit. on p. 36).
- Vidano, R. P., Fischbach D. B. and Willis, L. J, and Loehr, T. M. (1981). “Observation of Raman band shifting with excitation wavelength for carbons and graphites”. *Solid State Communications* **39**, 2, pp. 341–344 (cit. on p. 83).
- Visscher, P. B. and Falicov, L. M. (04/1971). “Dielectric Screening in a Layered Electron Gas”. *Physical Review B* **3**, 8, pp. 2541–2547 (cit. on p. 57).
- Volkov, B. A. and Pankratov, O. A. (08/1985). “Two-dimensional massless electrons in an inverted contact”. *ZhETF Pis ma Redaktsiiu* **42**, p. 145 (cit. on pp. 2, 13, 15).
- Waldmann, D., Jobst, J., Speck, F., Seyller, T., Krieger, M., and Weber, H. B. (05/2011). “Bottom-gated epitaxial graphene”. *Nature Materials* **10**, 5, pp. 357–360 (cit. on pp. 5, 7, 11).
- Wallace, P. R. (05/1947). “The Band Theory of Graphite”. *Physical Review* **71**, 9, pp. 622–634 (cit. on pp. 1, 5, 6, 11, 35, 47, 48).
- Wallauer, W. and Fauster, T. (1995). “Growth of Ag, Au, and Co on Cu(111) studied by high-resolution spectroscopy of image states”. *Surface Science* **331 - 333, Part A**, 0. Proceedings of the 14th European Conference on Surface Science, pp. 731–735 (cit. on pp. 31, 66).
- Wang, G., Zhu, X., Wen, J., Chen, X., He, K., Wang, L., Ma, X., Liu, Y., Dai, X., Fang, Z., Jia, J., and Xue, Q. (2010). “Atomically smooth ultrathin films of topological insulator Sb_2Te_3 ”. *Nano Research* **3**, 12, pp. 874–880 (cit. on pp. 16, 18).
- Wang, J. (2005). *Generation and application of Ultrashort Laser Pulses*. Doctoral thesis, Lehrstuhl für Festkörperphysik, Department für Physik der Universität Erlangen-Nürnberg (cit. on p. 32).
- Wang, X., Zhi, L., and Müllen, K. (2008). “Transparent, Conductive Graphene Electrodes for Dye-Sensitized Solar Cells”. *Nano Letters* **8**, 1, pp. 323–327 (cit. on pp. 5, 7).
- Wang, Y. H. (2012b). *Laser-based Angle-resolved Photoemission Spectroscopy of Topological Insulators*. Doctoral thesis, Department of Physics, Harvard University Cambridge, Massachusetts (cit. on p. 26).
- Wang, Y. H., Hsieh, D., Pilon, D., Fu, L., Gardner, D. R., Lee, Y. S., and Gedik, N. (11/2011a). “Observation of a Warped Helical Spin Texture in Bi_2Se_3 from Circular Dichroism Angle-Resolved Photoemission Spectroscopy”. *Physical Review Letters* **107**, 20, p. 207602 (cit. on pp. 26, 67, 68).
- (11/2011b). “Observation of a Warped Helical Spin Texture in Bi_2Se_3 from Circular Dichroism Angle-Resolved Photoemission Spectroscopy”. *Supplementary online material, Physical Review Letters* **107**, 20, p. 207602 (cit. on p. 27).
- Wang, Y. H., Hsieh, D., Sie, E. J., Steinberg, H., Gardner, D. R., Lee, Y. S., Jarillo-Herrero, P., and Gedik, N. (09/2012a). “Measurement of Intrinsic Dirac Fermion Cooling on the Surface of the Topological Insulator Bi_2Se_3 Using Time-Resolved and Angle-Resolved Photoemission Spectroscopy”. *Physical Review Letters* **109**, 12, p. 127401 (cit. on pp. 20, 21, 26, 27, 30).
- Wehling, T. O., Grigorenko, I., Lichtenstein, A. I., and Balatsky, A. V. (11/2008). “Phonon-Mediated Tunneling into Graphene”. *Physical Review Letters* **101**, 21, p. 216803 (cit. on p. 54).
- Weinelt, M. (2002). “Time-resolved two-photon photoemission from metal surfaces”. *Journal of Physics: Condensed Matter* **14**, 43, R1099 (cit. on pp. 29, 46).

- Wiets, M. (2004). *Photoelektronen-Spektroskopie besetzter und unbesetzter Zustände hexagonaler Siliziumkarbid-Oberflächen*. Doctoral thesis, Lehrstuhl für Festkörperphysik, Department für Physik der Universität Erlangen-Nürnberg (cit. on p. 53).
- Wiets, M., Weinelt, M., and Fauster, T. (09/2003). “Electronic structure of SiC(0001) surfaces studied by two-photon photoemission”. *Physical Review B* **68**, 12, p. 125321 (cit. on p. 53).
- Wintterlin, J. and Bocquet, M.-L. (2009). “Graphene on metal surfaces”. *Surface Science* **603**, 10–12. Special Issue of Surface Science dedicated to Prof. Dr. Dr. h.c. mult. Gerhard Ertl, pp. 1841–1852 (cit. on p. 7).
- Wolf, M., Hotzel, A., Knoesel, E., and Velic, D. (02/1999). “Direct and indirect excitation mechanisms in two-photon photoemission spectroscopy of Cu(111) and Co/Cu(111)”. *Physical Review B* **59**, 8, pp. 5926–5935 (cit. on pp. 30, 31, 46).
- Wöll, C., Chiang, S., Wilson, R. J., and Lippel, P. H. (04/1989). “Determination of atom positions at stacking-fault dislocations on Au(111) by scanning tunneling microscopy”. *Physical Review B* **39**, 11, pp. 7988–7991 (cit. on p. 52).
- Woodruff, D. P., Royer, W. A., and Smith, N. V. (07/1986). “Empty surface states, image states, and band edge on Au(111)”. *Physical Review B* **34**, 2, pp. 764–767 (cit. on p. 53).
- Wu, J., Agrawal, M., Becerril, H. A., Bao, Z., Liu, Z., Chen, Y., and Peumans, P. (2010). “Organic Light-Emitting Diodes on Solution-Processed Graphene Transparent Electrodes”. *ACS Nano* **4**, 1, pp. 43–48 (cit. on pp. 5, 7).
- Wu, X., Hu, Y., Ruan, M., Madiomanana, N. K., Hankinson, J., Sprinkle, M., Berger, C., and Heer, W. A. de (2009). “Half integer quantum Hall effect in high mobility single layer epitaxial graphene”. *Applied Physics Letters* **95**, 22, p. 223108 (cit. on pp. 1, 7, 55).
- Xia, Y., Qian, D., Hsieh, D., Wray, L., Pal, A., Lin, H., Bansil, A., Grauer, D., Hor, Y. S., Cava, R. J., and Hasan, M. Z. (06/2009). “Observation of a large-gap topological-insulator class with a single Dirac cone on the surface”. *Nature Physics* **5**, 6, pp. 398–402 (cit. on pp. 16–18, 62, 77).
- Xu, S., Cao, J., Miller, C. C., Mantell, D. A., Miller, R. J. D., and Gao, Y. (01/1996). “Energy Dependence of Electron Lifetime in Graphite Observed with Femtosecond Photoemission Spectroscopy”. *Physical Review Letters* **76**, 3, pp. 483–486 (cit. on p. 72).
- Yang, H., Heo, J., Park, S., Song, H. J., Seo, D. H., Byun, K.-E., Kim, P., Yoo, I., Chung, H.-J., and Kim, K. (2012). “Graphene Barristor, a Triode Device with a Gate-Controlled Schottky Barrier”. *Science* **336**, 6085, pp. 1140–1143 (cit. on pp. 1, 5, 7).
- Yu, Q., Lian, J., Siriponglert, S., Li, H., Chen, Y. P., and Pei, S.-S. (09/2008). “Graphene segregated on Ni surfaces and transferred to insulators”. *Applied Physics Letters* **93**, 11, p. 113103 (cit. on p. 9).
- Zhang, H., Liu, C.-X., Qi, X.-L., Dai, X., Fang, Z., and Zhang, S.-C. (06/2009a). “Topological insulators in Bi₂Se₃, Bi₂Te₃ and Sb₂Te₃ with a single Dirac cone on the surface”. *Nature Physics* **5**, 6, pp. 438–442 (cit. on pp. 15–17, 20, 59, 73).
- Zhang, Y., He, K., Chang, C.-Z., Song, C.-L., Wang, L.-L., Chen, X., Jia, J.-F., Fang, Z., Dai, X., Shan, W.-Y., Shen, S.-Q., Niu, Q., Qi, X.-L., Zhang, S.-C., Ma, X.-C., and Xue, Q.-K. (08/2010). “Crossover of the three-dimensional topological insulator Bi₂Se₃ to the two-dimensional limit”. *Nature Physics* **6**, 8, pp. 584–588 (cit. on p. 77).
- Zhang, Y., Tan, Y.-W., Stormer, H. L., and Kim, P. (11/2005). “Experimental observation of the quantum Hall effect and Berry’s phase in graphene”. *Nature* **438**, 7065, pp. 201–204 (cit. on p. 1).
- Zhang, Y., Tang, T.-T., Girit, C., Hao, Z., Martin, M. C., Zettl, A., Crommie, M. F., Shen, Y. R., and Wang, F. (06/2009b). “Direct observation of a widely tunable bandgap in bilayer graphene”. *Nature* **459**, 7248, pp. 820–823 (cit. on p. 3).
- Zhu, X.-Y. (10/2002). “Electron transfer at molecule-metal interfaces: A two-photon photoemission study”. *Annual Review of Physical Chemistry* **53**, pp. 221–247 (cit. on p. 29).

Danksagung

Selbstverständlich wäre die Durchführung dieser Arbeit nicht möglich gewesen ohne die Mithilfe der Mitarbeiter und Studenten am Lehrstuhl für Festkörperphysik, der Kollaborationspartner und die Unterstützung aus dem privaten Umfeld. Mein besonderer Dank gilt

Herrn Prof. Dr. **Thomas Fauster**, dessen Türe mir immer offen stand, und der selbst tatkräftiges Anpacken im Labor nicht scheute. Für die vielen Kommentare und Anregungen, konstruktive Kritik und Denkanstöße. Aber auch für das hohe Maß an Freiheit, das ich in den vergangenen Jahren genießen durfte und das entgegengebrachte Vertrauen.

Herrn Dr. **Lutz Hammer**, der stets gerne bereit war, seine langjährige Erfahrung in verschiedensten Bereichen weiterzugeben. Er hat damit einen Grundpfeiler für eine erfolgreiche Durchführung nicht nur dieser Arbeit gesetzt, auch die Betreuung von Studenten wäre ohne ihn in dieser Form nicht möglich gewesen.

Frau Dr.ⁱⁿ **Kerstin Biedermann**, für ihren unermüdlichen Einsatz für Arbeit und Gruppe. Für die über Jahre hinweg hervorragende, motivierende Zusammenarbeit und ihre immer durchdachten Ratschläge zu Wissenschaft und Technik, Lehre und Sozialem.

Ein großer Dank gilt den Diplom-, Master und Bachelorkandidaten, die ich auf ihrer Laufbahn ein Stück weit begleiten durfte. Mit einem hohen Maß an Einsatzbereitschaft und Neugierde haben sie nicht nur erste wissenschaftliche Fragestellungen beantwortet, sondern häufig auch wichtige Fragen aufgeworfen. Ich danke

Herrn Dipl.-Phys. **Marco Potenz**, der sich trotz zeitinsiver Lehrtätigkeit mit großer Leidenschaft Graphen, Nickel, Gold und Auger hingegeben hat. Nicht zu vergessen: Philosophische Exkurse und sein Einsatz an der Grillzange.

Herrn Dipl.-Phys. **Dieter Gugel**, dem eisernen Mann, der stets energiegeladen nicht nur in Erlangen, sondern auch am MBI Berlin Graphen auf SiC bearbeitet hat. Für die gemeinsame Zeit an Orten wie Mausdorf, Neunhof oder Hund.

Herrn Dipl.-Phys. **Tobias Bierlein**, der in der gemeinsamen frühen Zeit am Lehrstuhl für Festkörperphysik an der Au(100)-Oberfläche die Möglichkeiten des Ellipsoidanalysators ausgelotet hat.

Herrn B. Sc. **David Nobis** für seine Arbeit an Graphen in Erlangen und New York. Für seine Verdienste um die Kultur im Allgemeinen und das Theater im Speziellen.

Herrn B. Sc. **Florian Rühl**, der mit viel Eifer und Hartnäckigkeit die Automatisierung der Anlage vorangetrieben und Systeme mit Rashba-Aufspaltung untersucht hat.

Herrn B. Sc. **Volker Hermann** für seine ausgezeichnete Arbeit an topologischen Isolatoren, klare Analysen, abendliche Ausdauer und seine Pünktlichkeit.

Herrn Dipl.-Phys. Ulrich **Philip Ries**, der mich nicht umhinkommen ließ, mich mit Si(111) anzufreunden. Für diplomatisches Schweigen, scharfe Pointen, Unermüdlichkeit und für mancherlei Spezialwissen.

Das konstruktives und freundliches Arbeitsumfeld am Lehrstuhl wird natürlich durch seine Mitarbeiter bestimmt. Ich bedanke mich herzlich bei

Herrn M. Sc. **Sebastian Otto** für die großzügige Unterstützung zu jeder Tageszeit bei der Betreuung von Bachelorstudenten, bei Messungen an topologischen Isolatoren und bei der Erstellung und Beseitigung von technischen Problemen.

Frau Dipl.-Phys. **Rebecca Pöschel** und Frau Dipl.-Phys. **Ellen Fischermeier** für die gute kollegiale Zusammenarbeit im Mittellabor.

Herrn Dr. **Andreas Dobler** für die Einführung in die Ultrahochvakuumtechnik, die Vorlesungsassistenz und einen guten Start in die Arbeitsgruppe.

Herrn Dr. **Jingxiong Wang** für das Einlernen in die Femtosekunden-Lasertechnik und für seine Hilfe bei akuten Laserproblemen.

Herrn Prof. Dr. **Alexander Schneider** und seiner Gruppe für den kontinuierlichen Austausch von Wissen und Material sowie Hilfe, wenn sie benötigt wurde. Herrn M. Sc. **Pascal Ferstl** für die Zusammenarbeit zu Graphen auf Metallen. Für anregende Diskussionen zu Physik, Imkerei, klassischer Antike, Maschinenbau, Geographie, lokalem Brauchtum uvm. Für seine freundliche, aufmunternde Art sowie konstruktive Kritik an nicht nur meinen Fremdsprachenkenntnissen. Herrn Dipl.-Phys. **Tobias Schmitt** und Frau M. Sc. **Anastasia Sokolova** für die angenehme gemeinsame Zeit im Doktorandenzimmer. Herrn Dr. **Carsten Tröppner** für die vermittelten Kenntnisse zu UHV-Technik und Rastertunnelmikroskopie, für actionreiche Runden auf der Kartbahn und entspannte morgendliche Diskussionen.

für Anregungen seitens Herrn Prof. Dr. **Klaus Heinz** und seiner Gruppe, auch wenn ich diese zu Beginn meiner Tätigkeit am Lehrstuhl für Festkörperphysik nur kurz kennenlernen durfte. Insbesondere Herrn Dr. **Matthias Gubo** für die Einführung in die Handhabung des Displayanalysators und die Physik der Iridium-Oberfläche, und Herrn Dr. **Daniel Lerch** für die Einarbeitung in „sonstige Tätigkeiten“.

Prof. Dr. **Stefan Müller** und seiner Theorie-Gruppe, insbesondere Dr. **Tobias Kerscher**, Dr. **Nils Schindzielorz** und Dipl.-Phys. **Wolfgang Heckel**, die zeitweise den Lehrstuhl mit Leben füllten und um zusätzliche Sichtweisen bereichert haben.

Den Mitarbeitern der mechanischen Werkstatt, Herrn **Jürgen Linzmayer** und Herrn **Klaus Wölfel** die mit großem Einsatz, Geschick und Fachwissen für jedes Problem die beste individuelle Lösung gefunden haben. Dasselbe gilt für den Elektroniker Herrn **Adam Schneider**, der selbst seine private Habe zur Verfügung stellte.

Nicht zuletzt dem Sekretariat, Frau **Christine Staudt**, Frau **Rosemarie Feldner** und Frau **Ursula Müller**, die so viel bürokratischen Aufwand wie möglich fernhielten und zudem stets ein offenes Ohr und einen guten Ratschlag für „die jungen Leute“ hatten.

Darüberhinaus gilt mein Dank den Kollaborationspartnern außerhalb des Lehrstuhls, namentlich

Den Mitarbeitern des **Lehrstuhl für Technische Physik** für die langjährige freundschaftliche Zusammenarbeit. Herrn Prof. Dr. **Thomas Seyller** und den Herren Dipl.-Phys. **Florian Speck, Felix Fromm, Markus Ostler, Roland Koch, Peter Wehrfritz** und **Samir Mamedov** für Präparation und Charakterisierung von Graphen/SiC sowie für zahlreiche Diskussionen. Prof. **Martin Hundhausen** für die Möglichkeit, Raman-Spektroskopie durchzuführen.

Herrn Dr. **Marko Kralj**, Herrn M. Sc. **Marin Pletikosić** und Frau M. Sc. **Iva Šrut** für ARPES und Raman-Messungen an Graphen/Ir sowie für die Hilfe bei der Präparation des Systems. Außerdem für die Gastfreundschaft am **Institut za fiziku, Zagreb**.

Herrn Prof. **Richard M. Osgood** und seiner Oberflächenphysik-Gruppe an der **Columbia University**, New York City für die kooperative Zusammenarbeit bei der 2PPE an Graphen/Ir, insbesondere Herrn Dr. **Jerry Dadap**.

Herrn Prof. **Martin Weinelt** und Dr. **Christian Eickhoff** für die Möglichkeit, Zwei-photonen-Photoemission-Messungen an Graphen/SiC am **Max-Born-Institut, Berlin** durchzuführen. Außerdem Herrn Dipl.-Ing. **Rainer Schumann** für Rat und Tat bei Laserproblemen.

Prof. **Evgueni Chulkov, DIPC, San Sebastián/Donostia** für die fruchtbare Kollaboration im Bereich der topologischen Isolatoren.

Den Mitarbeitern des **Institute of Physics, Baku** für die Kristallzucht von topologischen Isolatoren, insbesondere Prof. **Nazim Mamedov**. Zudem den Gruppen an der **Azerbaijan National Academy of Science** und am General and Inorganic Chemistry Department der **Baku State University**.

Dr. **Konstantin Kokh**, Institute of Geology and Mineralogy und Dr. **Oleg Tereshchenko**, Institute of Semiconductor Physics aus **Tomsk** für das Wachstum von Wismuth-Chalcogenid-Einkristallen. Außerdem den Theoretikern der **Tomsk State University**, insbesondere Herrn Dr. **Sergej Eremeev**.

Herrn Prof. **Philipp Hofmann, Aarhus University** und Herrn M. Sc. **Marco Bianchi** für zusätzliche Wismuthselenid-Proben.

Herrn Prof. **Matthias Bode, Universität Würzburg** und Herrn Dr. **Paolo Sessi** für die Zusammenarbeit und die experimentelle Unterstützung bei den Systemen mit Rashba-Aufspaltung. Herrn Dr. **Gustav Bihlmayer, Forschungszentrum Jülich** und Frau Dr. **Simona Achilli, Università degli studi di Milano** für Theorie-Unterstützung.

Herrn Prof. **Markus Donath, Universität Münster**, für Diskussion zu den topologischen Isolatoren.

Herrn **Johannes Montag**, Herrn **Alexander Winkler** und Frau **Irene Schärf** für die freundliche Hilfe in der Hörsaalvorbereitung.

Dem Springer Verlag, Elsevier, Macmillan, der American Physical Society, der American Chemical Society, Annual Reviews, Prof. Daniel Dessau, Dr. Yihua Wang und Prof. Evgueni Chulkov für die zur Verfügung gestellten Abbildungen.

Frau **Beate Gresser** und Frau **Eva Volleth** von FAU university press für die Hilfe bei der Veröffentlichung der Arbeit, sowie Herrn Prof. Dr. **Klaus Mecke** als Herausgeber.

Allen, die durch Anregungen und Diskussion zu dieser Arbeit beigetragen haben.

Zu guter Letzt möchte ich ein herzliches Dankeschön an meine Freunde und Familie richten, allen voran an meine Eltern **Gottfried** und **Agnes**, die mir einen erfolgreichen Start ins Leben ermöglicht haben. Natürlich auch an meine Schwestern **Marie** und **Cornelia**, die sich immer wieder für erschöpfende Diskussionen am Telefon Zeit genommen haben. Und an meine Lebensgefährtin **Cindy**, die - selbst von diversen Fachvorträgen, die sie anhören musste, nicht verschreckt - diese Arbeit korrekturgelesen hat.

Ich bitte zu entschuldigen, falls **Sie** in dieser Danksagung vergessen wurden.

Daniel Niesner

Curriculum Vitae

Nürnberger Str. 113
D-91052 Erlangen
☎ 0176 23244659
✉ dniesner@gmx.net



Personal data

Born on **04.06.1982**
in **Nürnberg**
Nationality **German**
Marital status **single**

Doctoral work

since 10/2008 **Universität Erlangen-Nürnberg**, Lehrstuhl für Festkörperphysik,
Supervisor: Prof. Dr. Thomas Fauster

University education

10/2003–09/2008 **Universität Erlangen-Nürnberg**, Department für Physik,
Graduated with a diploma degree in physics
Subject of the Diplom thesis: Raman spectroscopy of carbon nanotubes
Supervisor: Prof. Dr. Martin Hundhausen

Obligatory military service

09/2002–06/2003 **Civil service**, nursing, Kreiskrankenhaus Haßfurt

School education

09/1993–05/2002 **Regiomontanus-Gymnasium**, Haßfurt
09/1989–05/1993 **Primary school**, Haßfurt

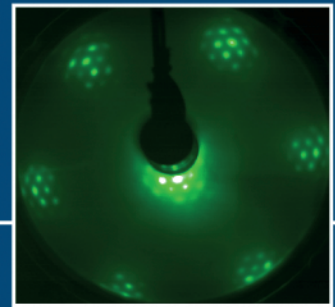
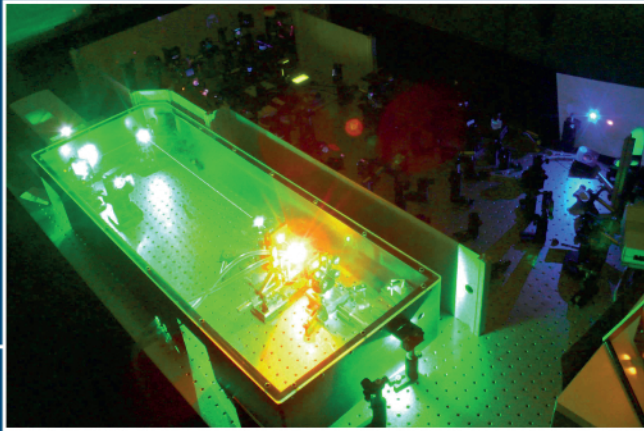
Publications

D. Niesner, Th. Fauster, S. V. Ereemeev, T. V. Menshchikova, Yu. M. Koroteev, A. P. Protogenov, E. V. Chulkov, O. E. Tereshchenko, K. A. Kokh, O. Alekperov, A. Nadjafov, and N. Mamedov. Unoccupied topological states on bismuth chalcogenides. *Phys. Rev. B*, 86:205403, Nov 2012.

D. Niesner, Th. Fauster, J. I. Dadap, N. Zaki, K. R. Knox, P.-C. Yeh, R. Bhandari, R. M. Osgood, M. Petrović, and M. Kralj. Trapping surface electrons on graphene layers and islands. *Phys. Rev. B*, 85:081402(R), Feb 2012.

D. Nobis, M. Potenz, D. Niesner, and Th. Fauster. Image-potential states of graphene on noble metal surfaces. submitted.

F. Fromm, D. Niesner, J. Röhrli, R. Graupner, Th. Seyller, and M. Hundhausen. Temperature dependence of the intermediate frequency modes of single walled carbon nanotubes. close to submission.



After an introduction to the systems under study and the applied experimental techniques, the following topics are discussed:

- Surface states of metal- and SiC-supported graphene around $\bar{\Gamma}$
- Charge screening in graphene and charge transfer to the substrate
- Unoccupied, energetically high-lying Dirac cones of bismut chalcogenides
- Electron dynamics in the surface state of Sb_2SnTe_4 , an intrinsically p-type topological insulator

ISBN 978-3-944057-07-1



9 783944 057071 >